UNIVERSITY TRANSPORTATION CENTER
FOR UNDERGROUND TRANSPORTATION INFRASTRUCTURE

ENGINEERING FEASIBILITY STUDY ON THE FUTURE EXTENSION OF THE EISENHOWER-JOHNSON MEMORIAL TUNNEL

FINAL PROJECT REPORT

by
Gauen Alexander
Ashton Krajnovich
Marte Gutierrez

University Transportation Center for
Underground Transportation Infrastructure
(UTC-UTI)
Colorado School of Mines

Sponsorship
US Department Transportation
Contract/Grant No. 69A355174711

Colorado Department of Transportation
PO # 471001372

October 31, 2022

COLORADO SCHOOL OF MINES
EARTH • ENERGY • ENVIRONMENT

Disclaimer

The contents of this report reflect the views of the authors, who are responsible for the facts and the accuracy of the information presented herein. This document is disseminated in the interest of information exchange. The report is funded, partially or entirely, by grants from the Colorado Department of Transportation and the U.S. Department of Transportation's University Transportation Centers Program. However, the U.S. Government assumes no liability for the contents or use thereof.

1. Report No. 12	2. Government Accession No.	3. Recipient's Catalog No.	
4. Title and Subtitle Engineering feasibility study on the future extension of the Eisenhower-Johnson Memorial Tunnel		5. Report Date October 31, 2020 6. Performing Organization Code	
7. Author(s) Gauen Alexander (Orcid.org/0000-0002-6078-7488) Ashton Krajnovich Marte Gutierrez (Orcid.org/0000-0001-5070-8726)		8. Performing Organization Report No: UTC-UTI 005	
9. Performing Organization Name and Address University Transportation Center for Underground Transportation Infrastructure (UTC-UTI) Tier 1 University Transportation Center Colorado School of Mines Coolbaugh 308, 1012 14th St., Golden, CO 80401		10. Work Unit No. (TRAIS) 11. Contract or Grant No. 69A355174711	
12. Sponsoring Agency Name and Address United States of America Department of Transportation Research and Innovative Technology Administration		13. Type of Report and Period Covered Final Project Report 14. Sponsoring Agency Code	
15. Supplementary Notes Report also available at: https://zenodo.org/communities/utc-uti			
16. Abstract A 3D implicit geological model was developed for the Eisenhower-Johnson Memorial Tunnel (EJMT) in Colorado for the purpose of selecting potential new tunnel bores that will extend the vehicular capacity of the existing tunnels. The 3D implicit geological model includes engineering geologic parameters of interest, such as rock mass classification parameters, rock mass quality index (Q), and rock mass rating (RMR). This model includes quantified uncertainty in each parameter. Using this probabilistic geologic model, a new alignment optimization algorithm, which seeks the best possible tunnel alignment through a given volume is developed. Further, a numerical finite difference model was calibrated to available EJMT case study data. This calibrated model validates the results of the alignment optimization algorithm. The result is a novel and useful tool and methodology, which can effectively evaluate and compare many plausible alignments and select the best possible option for further design studies.			
17. Key Words tunneling, rock mass classification, back analysis, case study, probabilistic analysis		18. Distribution Statement No restrictions.	
19. Security Classification (of this report) Unclassified	20. Security Classification (of this page) Unclassified	21. No of Pages 141	22. Price NA

EXECUTIVE SUMMARY

Transportation tunnels are heavily studied and debated before they are eventually constructed. The lead time on tunnel projects is typically years and sometimes decades. During the early phases of tunnel planning, it is often necessary to evaluate a wide range of alignment, excavation method, and support system options to find those which are technically feasible and cost-effective. However, comparing a wide or infinite range of alignment, excavation method, and support system options can be time–consuming, tedious, and expensive. Tunnel alignments are frequently selected not based on any quantitative evaluation and comparison of feasibility but on professional judgment or political whim. There are many components to a tunnel's feasibility including highly uncertain ground conditions, many possible excavation methods, and variable support options. The goal of this research project is to bring some quantifiable metrics to the comparison of alternative tunnel options.

To accomplish this goal, the author has developed a 3D implicit geological model of the Eisenhower-Johnson Memorial Tunnel (EJMT) case study in Colorado which includes engineering geologic parameters of interest such as rock mass classification parameters rock mass quality index (Q) and rock mass rating (RMR). This model includes quantified uncertainty in each parameter. Using this probabilistic geologic model a new alignment optimization algorithm which seeks the best possible tunnel alignment through a given volume is developed. Further, a numerical finite difference model was calibrated to available EJMT case study data. This calibrated model validates the results of the alignment optimization algorithm. The result is a novel and useful tool and methodology which can effectively evaluate and compare many plausible alignments and select the best possible option for further design studies.

TABLE OF CONTENTS

EXECUTIVE SUMMARY i

LIST OF FIGURES v

LIST OF TABLES xiv

GLOSSARY xvi

CHAPTER 1 INTRODUCTION 1
1.1 Motivation 1
1.2 Goals and Objectives 2
1.3 Report Organization 4
1.4 Computer Hardware and Software 5
1.5 Funding 5

CHAPTER 2 LITERATURE REVIEW 6
2.1 Geotechnical Baseline Reports 6
2.2 Risk and Reliability 7
2.3 Rock Mass Classifications 8
2.4 Correlations to Rock Mass Classifications 27
2.5 State of Practice in Tunnel Alignment Selection 54
2.6 Probability Distributions and Statistics 62
2.7 Probability Distribution Transformations and Convolutions 64

CHAPTER 3 DEVELOPMENT OF A THREE-DIMENSIONAL GEOLOGICAL AND GEOTECHNICAL DATABASE FROM THE EISENHOWER-JOHNSON MEMORIAL TUNNEL CASE STUDY 65
3.1 Collaborative Effort 66
3.2 Introduction 66

3.3 Geologic Setting 67
3.4 Project Description 69
3.5 Data Evaluation 79
3.6 Implications 149
3.7 Summary and Conclusions 171

CHAPTER 4 TUNNEL ALIGNMENT OPTIMIZATION THROUGH A THREE-DIMENSIONAL GEOLOGIC MODEL WITH UNCERTAINTY 175
4.1 Introduction 175
4.2 Methodology 175
4.3 Results 188
4.4 Discussion 194
4.5 Summary and Conclusions 198

CHAPTER 5 CALIBRATION OF FINITE DIFFERENCE MODEL BY BACK ANALYSIS OF THE EJMT PILOT BORE 203
5.1 Introduction 203
5.2 Project Description 204
5.3 Histogram Fit Methodology 206
5.4 Stress Field 207
5.5 FLAC Modeling 216
5.6 Summary and Conclusions 235

CHAPTER 6 MONTE CARLO SIMULATION WITH A FINITE DIFFERENCE MODEL FOR RAPID COMPARISON OF TUNNEL ALIGNMENT ALTERNATIVES 237
6.1 Introduction 237
6.2 Methodology 238
6.3 Results 242
6.4 Discussion 246
6.5 Summary and Conclusions 253

CHAPTER 7 SUMMARY, CONCLUSIONS, AND RECOMMENDATIONS 255
7.1 Summary 255
7.2 Conclusions 256

7.3 Recommendations to CDOT . . . 258
7.4 Future Work . . . 259

REFERENCES . . . 260

APPENDIX A SUPPLEMENTAL ELECTRONIC FILES . . . 285

APPENDIX B HOW TO APPLY THE ALIGNMENT OPTIMIZATION METHODOLOGY . . . 286

APPENDIX C ROCK MASS DEFORMATION MODULUS CORRELATIONS . . . 290

APPENDIX D TECHNOLOGY TRANSFER ACTIVITIES . . . 302
D.1 Accomplishments . . . 302
D.2 Participants and Collaborating Organizations . . . 302
D.3 Outputs . . . 303
D.4 Outcomes . . . 304
D.5 Impacts . . . 305

APPENDIX E PROJECT DATA . . . 307
E.1 Introduction . . . 307

LIST OF FIGURES

2.1 Unconfined compressive strength component of RMR_{14} (RMR_{14UCS}) correlation as proposed by Lowson and Bieniawski (2013) with regressed function for calculating the RMR component score based on unconfined compressive strength or uniaxial compressive strength (UCS). 12
2.2 Joint frequency component of RMR_{14} ($RMR_{14\lambda}$) correlation as proposed by Lowson and Bieniawski (2013) with regressed function for calculating the RMR component score based on joint frequency. 13
2.3 NGI (2015) Table 6b correlation points between stress state and stress reduction factor (SRF) with piecewise linear function fit. 20
2.4 Equations from Gutierrez and Xia (2009), Arora et al. (2020), and this study which are proposed as the dividing line between squeezing and non-squeezing behavior for clay-rich sedimentary and metasedimentary rocks. Data points from the EJMT pilot and Eisenhower bores have been binned by UCS and major principal stress with the percent of identified squeeze zones in each bin identified by color. 32
2.5 Correlation between excavation span, stand up time, and RMR as proposed by Bieniawski (1989). The numbers next to the data points indicate the RMR value recorded for that data point. 34
2.6 Correlation between excavation span, RMR and stand up time based on multi-linear regression to the database of Bieniawski (1989). Circles indicate data points, size indicates the depth of the data point. The multi-linear regression surface has been trimmed to only show the area where the distance between the 98% confidence intervals is less than 1.5 log cycles. 36
2.7 Limits of practical applicability of Lowson and Bieniawski (2013) recommendations for rock bolt support. 44
2.8 Correlation between RMR and rock bolt pattern strength as published by Lowson and Bieniawski (2013) and assuming a 250 kN rock bolt. 45

2.9 Correlation between RMR, excavation span, rock bolt strength, shotcrete strength, and overburden pressure after Lowson and Bieniawski (2013). 47
2.10 Limits of applicability of the RMR based support design for a given shotcrete strength (30 MPa) and rock bolt strength (250 kN) after Lowson and Bieniawski (2013). 48
2.11 Correlation between excavation span, excavation support ratio, Q value, and recommended preliminary design as published by NGI (2015). 49
2.12 Correlation between Q value and recommended preliminary design spacing of rock bolts as digitized for this report after NGI (2015). 51
2.13 Correlation between Q value and recommended preliminary design spacing of reinforced rib supports as digitized for this report after NGI (2015). 53
2.14 Correlation between excavation span, excavation support ratio, Q value, and recommended preliminary design as digitized for this report after NGI (2015). 56

3.1 A detailed section of the pilot bore geologic map used in this study, showing overlays of the digitized 3D format of lithological contacts (shaded intervals), structural orientation data (disks) and fault zone traces (polylines). 68
3.2 Typical Design Cross-Sections of Pilot Bore after Mattei (1965). 70
3.3 Isometric view of tunnel support system in Zone III by Bonnema (1972). . . 74
3.4 Zone II cross-section showing multi-drift system. Redrafted by the author after Colorado Department of Transportation (CDOT) historical as-built plans (CDOT 1973). 76
3.5 EJMT traffic data projected by Pavlo (1960) and recorded by CDOT (2018b). 78
3.6 Young's modulus data for the fault gouge materials tested by United States Bureau of Reclamation (USBR) with fitted statistical distributions. 86
3.7 Poisson's ratio data for the fault gouge materials tested by USBR with fitted statistical distributions. 87
3.8 Data from USBR and historical Mohr-Coulomb yield envelopes developed by USBR for the fault gouge material, as compared to new probabilistic Mohr-Coulomb envelope developed for this research. 90
3.9 Mohr-Coulomb yield envelopes showing the tested data points and the actual range of estimated in-situ stresses in the squeeze zone. 91
3.10 Axial-volumetric strain data from USBR for fault gouge materials showing dilation at end of curves. Note that dilation angles are relatively low for most samples. 92

3.11 Histogram of dilation angles from axial-volumetric strain data from USBR for fault gouge materials with fitted statistical distributions. 93
3.12 Idaho Springs Formation (ISF) Young's modulus from historical United States Geological Survey (USGS) data and current laboratory testing plotted versus confining stress. 97
3.13 ISF Poisson's ratio from historical USGS data and current laboratory testing plotted versus confining stress. 98
3.14 ISF Young's modulus from historical USGS data and current laboratory testing plotted versus angle of foliation from vertical. 99
3.15 Histogram of ISF Young's modulus from historical USGS data and current laboratory testing with fitted distributions. 100
3.16 Histogram of ISF Poisson's ratio from historical USGS data and current laboratory testing with fitted distributions. 102
3.17 ISF deviator stress at failure versus failure mode from historical USGS data and current laboratory testing. With a single exception, the failure modes divide into two groups with a change in failure mode at 34.5°. For the transversely isotropic yield model the samples were divided into foliation and non-foliation failures and yield envelopes developed separately for each mode. 103
3.18 ISF Mohr-Coulomb yield envelopes from historical USGS data and current laboratory testing regressed separately to sliding and non-sliding (foliation and non-foliation) failure modes. 104
3.19 ISF Hoek-Brown yield envelopes from historical USGS data and current laboratory testing regressed separately to sliding and non-sliding (foliation and non-foliation) failure modes. 105
3.20 ISF Hoek-Brown and Mohr-Coulomb yield envelopes regressed to all data points regardless of failure mode (sliding/folation or non-sliding/non-foliation). . . 107
3.21 Variation of Silver Plume Granite (SPG) Young's modulus with confining stress based on current and historical laboratory testing. 110
3.22 Variation of SPG Poisson's ratio with confining stress based on current and historical laboratory testing. 111
3.23 Histogram of SPG Young's modulus data based on current and historical laboratory testing with fitted distributions. 112
3.24 Silver Plume Granite yield envelopes (Mohr–Coulomb and Hoek–Brown) with 68% prediction intervals based on current and historical laboratory testing. . 113

3.25 Face flow data recorded in the pilot bore vs. various other data recorded in the pilot bore. 116
3.26 Face flow predicted by the developed correlation (Equation 3.4) compared to recorded face flow measured in the pilot bore. Face flow presented in log scale. Note that the zero flow data have been plotted as 10^{-2} in log space. 118
3.27 Face flow predicted by the developed correlation (Equation 3.4) in the Eisenhower bore compared to recorded groundwater descriptions. 119
3.28 Histograms of RMR_{14} probabilistic and deterministic estimates for the entire Eisenhower and pilot bores of the EJMT. All 2000 Monte Carlo realizations at each station along each bore have been aggregated for the probabilistic histogram of the entire bore. The deterministic estimates from each station are aggregated together for the entire bore , as well, to provide a histogram of deterministic estimates for the entire bore. Note that the probabilistic estimates are significantly smoother and lower than the deterministic estimates. 121
3.29 Histograms of RMR_{14} at each station presented as a heatmap slice at each station along the EJMT and compared to deterministic estimates (dotted line) at each station. 123
3.30 Mixture distribution of SPG and ISF unconfined compressive strength probability density functions (PDFs). 124
3.31 Heatmap of Q along the pilot and Eisenhower bores. 131
3.32 Histogram of Q along the pilot and Eisenhower bores. 132
3.33 Heatmap of rock mass quality index without stress factors (Q') along the pilot and Eisenhower bores. 133
3.34 Histogram of Q' for the pilot and Eisenhower bores. 134
3.35 Most likely rock quality designation (RQD) and range along the pilot and Eisenhower bores. 135
3.36 Most likely joint set number (J_n) and range along the pilot and Eisenhower bores. 137
3.37 Most likely joint roughness (J_r) and range along the pilot and Eisenhower bores. 140
3.38 Most likely joint alteration (J_a) and range along the pilot and Eisenhower bores. 141
3.39 Most likely joint water reduction factor (J_w) and range along the pilot and Eisenhower bores. 142

3.40 Depth vs. Q' for data points along the EJMT pilot and Eisenhower bores with percent squeeze zones binned and color coded. The squeeze prediction correlation by Singh et al. (1992) has a 90.2% accuracy at predicting squeezing and non-squeezing conditions in the EJMT dataset. The recalibrated criterion has a 93.5% accuracy at the same prediction. 144
3.41 Identified squeeze zones, squeeze predictions by Equation 2.14, and squeeze predictions by Equation 3.7. 145
3.42 Most likely SRF and range along the pilot and Eisenhower bores. 146
3.43 Heatmaps of various versions of RMR (rock mass rating (RMR_{14}), base rock mass rating (RMR_{14b}), and rock condition rating (RCR)) versus various versions of Q (Q, rock mass number (N), and Q') in the Eisenhower bore. Warmer colors indicate more correlations in a given bin. Note that the best correlation between the two systems in this case appears to be between RMR_{14b} and N, with RMR_{14b} versus Q' a close second. The A and B parameters of the RMR_{14b}-N fit line are 11.4 and 43.0, respectively, with $r^2 = 0.72$. 151
3.44 Heatmaps of various versions of RMR (RMR_{14}, RMR_{14b}, and RCR) versus various versions of Q (Q, N, and Q') in the pilot bore. Warmer colors indicate more correlations in a given bin. Note that the best correlation between the two systems in this case appears to be between RMR_{14b} and Q', with RMR_{14} versus Q a close second and RMR_{14b} versus N a reasonable comparison. The A and B parameters of the RMR_{14b}-Q' fit line are 10.9 and 35.5, respectively, with $r^2 = 0.73$. 152
3.45 Heatmaps of RMR_{14}, RMR_{14b}, RCR, Q, N, and Q' versus geological strength index (GSI) in the Eisenhower bore. Warmer colors indicate more correlations in a given bin. Note that the best correlation appears to be between N and GSI. However, this correlation is somewhat weak with $r^2 = 0.59$ and very wide scatter in the data. 153
3.46 Heatmaps of RMR_{14}, RMR_{14b}, RCR, Q, N, and Q' versus GSI in the pilot bore. Warmer colors indicate more correlations in a given bin. Note that GSI was estimated from Q parameters for the pilot bore by multi-linear regression, leading to the relatively good correlation here. 154
3.47 EJMT pilot bore weekly average advance rate data (m/working hour) after Mattei (1965) compared to most likely estimated Q-value from Monte Carlo simulation. 155

3.48 EJMT pilot bore weekly average advance rate data (m/working hour) after Mattei (1965) compared to most likely estimated Q'-value from Monte Carlo simulation. 156
3.49 EJMT pilot bore weekly average advance rate data (m/working hour) after Mattei (1965) compared to most likely estimated RMR_{14}-value from Monte Carlo simulation. 157
3.50 Correlations between recorded advance rates in the EJMT pilot bore and estimated rock mass rating (RMR_{89}). Note low r^2 values indicating little correlation (or very high scatter) between RMR_{89} and advance rate. Correlations between advance rate and other rock mass classifications were also poor. . . 159
3.51 Suite of geologic models created to characterize the subsurface geology around the EJMT. (a) shows the lithological model based on pilot bore mapping, (b) shows the fault zone network model based on pilot bore mapping, and (c) shows a regional scale composite model combining the detailed information from (a) and (b) with interpreted structures from surficial mapping. 161
3.52 Generation of an RBF interpolant structural trend from a fault zone geologic model. (a) structural orientation data are extracted from the geologic model based on vertices of key geologic surfaces. (b) Initialization of a structural trend in Leapfrog, with parameter options including the strength of the trend and whether the trend is non-decaying. 162
3.53 Comparison of RBF interpolants for an example rock mass classification parameter (GSI) using (a) an isotropic interpolant and (b) the fault zone derived structural trend. Areas where the interpolant returns erroneous values are colored bright red. (c) and (d) show the composite model combining both interpolants in section and plan view, respectively. 165
3.54 Final composite interpolants for GSI, RMR_{14} and Q. 166
3.55 Histogram of most likely RMR values from the pilot and Eisenhower bores compared to the same metric calculated at each block of the implicit geologic model. 168
3.56 Histogram of the range of most likely RMR values normalized by most likely RMR from the pilot and Eisenhower bores compared to the same metric calculated at each block of the implicit geologic model. 169

4.1 EJMT vicinity with elevation contours. 177
4.2 Locations of plausible portals (red dots) evaluated on a 100-m grid. There are 104 west portals and 79 east portals arranged on a 100 m grid with non-constructable areas (such as the alignment of Clear Creek) blocked out. 178

4.3 2065 remaining plausible alignments after filtering for grade requirements. . 182
4.4 438 remaining plausible alignments after filtering for ground surface conflicts. 183
4.5 320 remaining plausible alignments after filtering for intersections with the existing bores. 184
4.6 89 remaining possible alignments after filtering out alignments which cross the existing alignments in plan view. For a new roadway tunnel crossing would complicate the traffic pattern. For a rail tunnel, crossing the existing alignment may not be a problem. 185
4.7 89 remaining possible alignments after the various initial filtering criteria have been applied (grade requirements, ground surface conflicts, intersections with the existing bores, and excluding alignments which cross North-to-South or South-to-North across the existing bores) presented in three dimensions. 186
4.8 Interquartile range of Q. 189
4.9 Median absolute deviation of RMR_{14}. 190
4.10 Median RMR_{14}. 191
4.11 Estimated required volume of shotcrete based on Q. 192
4.12 Highest scoring alignments by various metrics. 195
4.13 Lowest scoring alignments by various metrics. 196

5.1 Ground response factor (GRF) versus RMR_{14} and Q for the instrumented stations in the EJMT pilot bore. Pilot bore data from data from Robinson et al. (1974). GRF is defined as load measured on the tunnel support at a given station divided by the total overburden on the tunnel at that station. 209
5.2 GRF versus RMR_{14} as recorded in the pilot bore by Robinson et al. (1974) along with a least-squares regression to an exponential function and the prediction model by Goel and Jethwa (1991). 211
5.3 GRF versus Q as recorded in the pilot bore by Robinson et al. (1974) along with a least-squares regression to an exponential function and the prediction model by Barton et al. (1974). Note that the predictions by the Barton et al. (1974) model are much higher than the recorded ground loads in the pilot bore. . . 212
5.4 Implied active height (IAH) versus RMR_{14} with the multi-linear regression fit surface. Data from Robinson et al. (1974). 213
5.5 Implied active height (IAH) versus depth below ground surface with the multi-linear regression fit surface. Data from Robinson et al. (1974). 214

5.6 Implied active height (IAH) versus depth below ground surface and RMR_{14} with the multi-linear regression fit surface. Data from Robinson et al. (1974). . . 215
5.7 Vertical deflections of the pilot bore through the squeeze zone (Mattei 1965). 217
5.8 Horizontal deflections of the pilot bore through the squeeze zone (Mattei 1965). 218
5.9 Histogram of crown, invert, maximum and minimum wall displacements from $N = 4320$ elastic Monte Carlo simulations in FLAC of the pilot bore squeeze zone with the calibrated parameters of $E = 38$ MPa and $H/V = 0.18$ to 0.35 compared to reported data by Mattei (1965). 219
5.10 Empirical correlations between rock mass classifications and rock mass modulus evaluated for the pilot bore rock mass classification data. 220
5.11 Radial meshing used in the elastic and elastic-perfectly-plastic FLAC models of the pilot bore. Axes are in units of meters. 222
5.12 Typical FLAC result showing the deviator stress (principal stress difference, $\sigma_1 - \sigma_3$) around the tunnel. Axes are in units of meters. Contours of deviator stress are in units of pascals. 224
5.13 Typical FLAC result showing the axial thrust in the tunnel liner. Axes are in units of meters. Forces in units of newtons. Forces plotted on the deformed liner shape without deformation exaggeration. 225
5.14 Calibration of the standup stress factor in the elastic and elastic-perfectly-plastic numerical models of the EJMT pilot bore. 226
5.15 Histogram of recorded leg thrust data in the pilot bore (Robinson et al. 1974) vs. histogram of elastic FLAC model leg thrust results. 227
5.16 Coefficient of determination versus number of Monte Carlo realizations of the elastic FLAC model used. Note that above approximately 25 Monte Carlo realizations the coefficient of determination is essentially constant. 228
5.17 Histogram of recorded leg thrust data in the pilot bore (Robinson et al. 1974) vs. histogram of plastic FLAC model leg thrust results. 229
5.18 Coefficient of determination versus number of Monte Carlo realizations of the plastic FLAC model used. 230
5.19 Histogram of recorded invert thrust data in the pilot bore (Robinson et al. 1974) vs. histogram of plastic FLAC model invert thrust results. 232
5.20 Histogram of recorded crown displacement data in the pilot bore (Robinson et al. 1974) vs. histogram of plastic FLAC model crown displacement results. . 233
5.21 Histogram of recorded horizontal convergence data in the pilot bore (Robinson et al. 1974) vs. histogram of plastic FLAC model horizontal convergence results. 234

6.1 Calculated axial, moment and shear loads at the crown and springline plotted versus liner capacity for one Monte Carlo realizations of alignment 5448 at Station 7+68. Tunnel lining design for this model estimated using the Q-system. Left figure is axial-moment interaction. Right figure is axial-shear interaction. 244
6.2 Calculated axial, moment and shear loads at the crown and springline plotted versus liner capacity for one Monte Carlo realizations of alignment 5448 at Station 9+50. Tunnel lining design for this model estimated using the RMR-system. Left figure is axial-moment interaction. Right figure is axial-shear interaction. 245
6.3 Design reliability for each alignment by the Q and RMR systems. 247
6.4 Calculated factor of safety versus estimated Q value for seven alignments modeled in FLAC. 251
6.5 Calculated factor of safety versus estimated RMR value for seven alignments modeled in FLAC. 252

LIST OF TABLES

2.1 Published correlations between RMR and Q. 25
2.2 Grimstad's Q-advance rate correlation for drill-and-blast tunnels. 38
2.3 Bieniawski et al. (2008) recommendations for applicability of TBM-excavation as a function of rock mass excavatability (RME) and intact UCS. 40
2.4 Table for estimating RME parameters after Bieniawski and Galera (2007). . 41
2.5 Table of fitting points defining piecewise boundaries between support categories for the NGI (2015) Q-system support chart. 54
2.6 Descriptions of recommended supports per NGI (2015) based on the Q-system support chart. 55

3.1 In-situ stresses in the EJMT cross-passages reported by Hoskins et al. (1974). 82
3.2 Fault gouge material properties summary. 85
3.3 Idaho Springs Formation material properties summary. 94
3.4 Silver Plume Granite material properties summary. 109
3.5 Coefficients of determination, r^2, for face flow predictions based on correlation to depth, joint frequency, excavation month, and distance to the nearest mapped fault. 115
3.6 Correlations assumed for this report between flow rate, RMR14(groundwater), Jw, and historical descriptions. 126
3.7 Correlations adopted for this study between historical blockiness and seaminess index; historical decomposition and alteration index; and Q system joint roughness number. 138
3.8 Correlations adopted for this study between historical blockiness and seaminess index; historical decomposition and alteration index; and Q system joint alteration number. 139
3.9 Pilot bore advance rate data correlations. 158
3.10 Interpolant basis applied to each rock mass classification component. 167

4.1 Initial alignment filtering by grade requirements, surface conflicts, and intersection with existing bores based on a 100 m net of portal locations on each side of the Continental Divide with 104 east portals and 79 west portals. 181
4.2 Calculated Optimization Parameters of Best Seven Alignments 199
4.3 Best Alignments By Various Optimization Metrics 202

5.1 Lowest plausible estimated rock mass moduli by various empirical correlations. 221

6.1 Correlations between compressive and tensile strength of concrete from literature. 242
6.2 Forward modeling results for RMR–system based liner models. 248
6.3 Forward modeling results for Q–system based liner models. 249

A.1 Supplemental Electronic Files 285

C.1 Rock mass deformation modulus correlations 291

GLOSSARY

F_s	stress adjustment factor for RMR
K_0-TXC	consolidated-lateral strain controlled triaxial compression
J_a	joint alteration
J_n	joint set number
J_r	joint roughness
J_w	joint water reduction factor
Q_{tbm}	rock mass quality index for TBM tunneling
RMR_{14Alt}	alterability component of RMR_{14}
RMR_{14GW}	groundwater component of RMR_{14}
$RMR_{14JCond}$	joint condition component of RMR_{14}
RMR_{14UCS}	unconfined compressive strength component of RMR_{14}
$RMR_{14\lambda}$	joint frequency component of RMR_{14}
RMR_{14b}	base rock mass rating
RMR_{14}	rock mass rating
RMR_{89}	rock mass rating
r^2–value	coefficient of determination
*.csv	comma-separated values
3D	three-dimensional

AACE	American Association of Cost Engineering
AISC	American Institute of Steel Construction
AR	advance rate
ASTM	American Society for Testing and Materials
BTS	British Tunneling Society
CDF	cumulative distribution function
CDOH	Colorado Division of Highways
CDOT	Colorado Department of Transportation
CEVP	cost estimate validation process
CHILE	continuous, homogeneous, isotropic, and linear elastic
CU-TXC	consolidated-undrained triaxial compression
D&B	drill-and-blast
DAT	Decision Aids for Tunneling
DBN	dynamic Bayesian networks
DEM	digital elevation model
DRB	dispute resolution or review board
DRI	drilling rate index
EJMT	Eisenhower-Johnson Memorial Tunnel
EPP	elastic-perfectly-plastic
ESR	excavation support ratio

ESRI	Environmental Systems Research Institute
FDM	finite difference method
FISH	FLACish
FLAC	Fast Lagrangian Analysis of Continua
FORM	the First-Order Reliability Method
GBR	Geotechnical Baseline Report
GDR	Geotechnical Data Report
GIS	geographic information system
GPa	gigapascals
GPM	gallons per minute
GRC	ground reaction curve
GRF	ground response factor
GSI	geological strength index
H-B	Hoek-Brown
I-70	Interstate 70
IAH	implied active height
ICE	*indice de comportamiento elastico*
IQR	interquartile range
ISF	Idaho Springs Formation
ISRM	International Society of Rock Mechanics

ITA	International Tunnelling Association
ITIG	International Tunnelling Insurance Group
kPa	kilopascals
ksi	kips per square inch
LiDAR	Light Detection and Ranging
LPM	liters per minute
LRFD	Load and Resistance Factor Design
M-C	Mohr-Coulomb
MAD	median absolute deviation
MC	Monte Carlo
Mines	the Colorado School of Mines
MIT	Massachusetts Institute of Technology
MPa	megapascals
N	rock mass number
NATM	New Austrian Tunneling Method
NEPA	National Environmental Policy Act
NGI	Norwegian Geotechnical Institute
NGMDB	National Geologic Map Database
NTNU	Norwegian University of Science and Technology

PACT	probabilistic analysis of cost and time in tunneling
PDF	probability density function
PEIS	programmatic environmental impact statement
PR	penetration rate
psi	pounds per square inch
Q	rock mass quality index
Q'	rock mass quality index without stress factors
RBF	radial basis function
RCR	rock condition rating
RME	rock mass excavatability
RMR	rock mass rating
RQD	rock quality designation
RSR	rock structure rating
SDSM	South Dakota School of Mines
SHANSEP	stress history and normalized soil engineering properties
SORM	the Second-Order Reliability Method
SPG	Silver Plume Granite
SRF	stress reduction factor
TBM	tunnel boring machine
TCE	tunnel cost estimator

TXC	triaxial compression
UCS	unconfined compressive strength or uniaxial compressive strength
USBR	United States Bureau of Reclamation
USDOT	United States Department of Transportation
USGS	United States Geological Survey
UTC-UTI	University Transportation Center for Underground Transportation Infrastructure
UTM	Universal Transverse Mercator
UU-TXC	unconsolidated-undrained triaxial compression
VBA	Visual Basic for Applications
WSDOT	Washington State Department of Transportation

CHAPTER 1

INTRODUCTION

Transportation tunnels are heavily studied and debated before they are eventually constructed. The lead time on tunnel projects is typically years and sometimes decades. During the early phases of tunnel planning, it is often necessary to evaluate a wide range of alignment, excavation method, and support system options to find those which are technically feasible and cost-effective. However, comparing a wide or infinite range of alignment, excavation method, and support system options can be time-consuming, tedious, and expensive. There are many components to a tunnel's feasibility including highly uncertain ground conditions, many possible excavation methods, and variable support options. The goal of this research project is to move from a quantifiably uncertain geologic model to a quantifiably uncertain estimate of technical feasibility for excavation and support of alternative alignments. By quantifying the feasibility of each alignment, excavation method, and support system considered, the options can be readily compared, and favorable alternatives carried forward to design.

1.1 Motivation

As shown in the Literature Review in Chapter 2 of this report, at present, tunnel selection is rarely based on a detailed analysis of technical feasibility. Most alignment choices are based on the expert opinion of experienced professionals. While professional opinion and experience are certainly valuable, the methodology for probabilistic quantification of feasibility produced by this research will allow for validation of professional experience and a deeper understanding of the parameters which are critical to a tunnel's design and construction.

Probabilistic back-analysis of tunnels is still largely theoretical, rather than applied. Current commonly employed methodologies for tunnel feasibility studies are based around ultimate tunnel costs (BTS and ICE 2004; Efron and Read 2012; HM Treasury and Infrastructure UK 2010; Rostami et al. 2013). Final tunnel costs are unitized and

compared to some simple metric of tunnel alignment (e.g. length, diameter, volume). Curves are fit through the resulting data, and then forward predictions are made about the costs of future projects. These methods are typically not probabilistic. Moreover, they are based fundamentally in cost as a metric, and ignore significant technical parameters such a rock mass quality, excavatability, and support requirements.

The Decision Aids for Tunneling (DAT) system, while an improvement on these simple methods, still has significant flaws. The DAT geologic module is based largely in expert opinion (Einstein et al. 1992) rather than a mathematical extrapolation from the known data with a definable uncertainty. In addition, the DAT geologic module is defined along a single alignment. Evaluation of a new alignment would require starting the process from the beginning and getting additional expert input.

Based on review of the currently available methods for tunnel feasibility studies, there are four major gaps in existing research:

1. Published probabilistic back-analyses of tunnels (Miro et al. 2015; Mirzaeian et al. 2015; Oggeri and Oreste 2012; Oreste 2015) are based on theoretical models, not project data. The published work neglects the fitting of model response to real-world distributions of tunnel stresses and deformations;
2. Current tunnel feasibility studies require pre-determined alignments, excavation methods, and support systems rather than leaving these as variables to be considered during the feasibility study;
3. Current tunnel feasibility studies handle geology, excavation method, and support system as deterministic variables rather than addressing the uncertainty in these values probabilistically;
4. Current tunnel feasibility studies typically estimate project costs based on deterministic geologic models and geometric tunnel parameters (e.g. length, volume) while neglecting the probabilistic uncertainty in the geologic model and the possibility for cost optimization based on alternative alignments; and,
5. No research has been published on the impacts of new parallel or skew tunnels adjacent to existing tunnels for hard-rock conditions with squeezing ground.

This report addresses items (1), (2), and (3), makes progress towards the consideration of (4), and leaves item (5) for further research.

1.2 Goals and Objectives

The fundamental engineering problem to be solved by this research is the selection of an optimal tunnel alignment through an uncertain geological model. This is not a trivial

problem, but it is a common one. All tunnels are designed under uncertainty as ground conditions cannot be known precisely before construction. Many tunnel designs go through significant revision and iteration as new data become available, even while construction is under way. The selection of the alignment to be tunneled is critical to the success of the project, but this decision is often made early in a project when uncertainty is highest. Tools to improve the tunnel alignment selection at an early stage under high uncertainty will be highly valuable to the tunneling industry and society as a whole by increasing reliability and reducing costs of tunneling projects.

Therefore, the main objective of this research is to develop a methodology for making tunnel alignment selection, excavation method, and support system decisions under great uncertainty. The methodology must respect the underlying uncertainty and allow the user some idea of the reliability of any given combination of alignment, excavation methodology, and support system. The largest uncertainty in underground construction typically comes from the highly variable geologic parameters. Therefore, addressing geologic uncertainty at the technical feasibility stage allows the project to begin with a risk-based methodology. The goal of this work is not to specify an excavation method, support system, or final design but to provide probabilistic information which quantifies uncertainty to the owner, designer, and contractor. Such information can then inform decisions about excavation method, support system, and design.

In furtherance of this overall goal, the following steps and objectives were identified for this project.

1. Review the state of practice in tunnel alignment selection and early-stage (feasibility- or scoping-stage) tunnel design methodologies (Chapter 2).
2. Evaluate a case study in a probabilistic fashion to determine likely engineering properties and their reasonable ranges (Chapter 3).
3. Propagate the data from the above case study in a three-dimensional model, including probabilistic engineering and geologic properties, to serve as a test bed for alignment optimization methodologies (Chapter 3).
4. Develop a methodology for determining the best possible alignment through the probabilistic three-dimensional geological model (Chapter 4).
5. Develop a numerical model-based design technique for estimating the effectiveness of a given tunnel lining design applied to a given probabilistic geologic condition. Calibrate the technique using back analysis to the previously developed case study. Reduce the model as much as possible to improve the efficiency of wide-scale evaluation of many possible alternatives in an efficient fashion (Chapter 5).
6. Evaluate the relative effectiveness of the rock mass quality index (Q) and rock

mass rating (RMR) systems in recommending initial tunnel designs by applying the empirically recommended designs within the calibrated numerical model to new alignments adjacent to the calibration alignment (Chapter 6).

7. Validate and refine the alignment optimization methodology given the outcomes from the forward modeling of new alignments adjacent to the calibration case study (Chapter 6).

This report details the achievement of these objectives and their application to a specific case study, the Eisenhower-Johnson Memorial Tunnel (EJMT). The case study used in this project was suggested by Colorado Department of Transportation (CDOT), one of the primary funding agencies for this project, and has several useful advantages:

1. It was well documented at the time of construction.
2. It contains a wide range of geologic conditions and encountered significant construction difficulties due to these geologic conditions. Due to the quantity of construction data available, the geologic uncertainties are quantifiable.
3. It is nearby the Colorado School of Mines (Mines).
4. The results of this study will be of practical use to CDOT in future potential expansions of the EJMT.

1.3 Report Organization

The author systematically stepped through the goals outlined above in pursuit of answers.

1. Chapter 2 presents a broad literature review on the current state of the art and practice in tunnel alignment selection and design. This included methodologies for tunnel alignment selection, analysis, design, excavation, and support as well as the underlying methodologies of rock mass classification and rock mechanics.
2. Chapter 3 lays out the available data on the EJMT case study. This work also blends from geotechnical engineering into geology and data science in the development of the probabilistic data model. Chapter 3 was co-authored with Ashton Krajnovich from the Department of Geological Engineering.
3. Chapter 4 presents a framework for optimizing alignments through the uncertain geologic model developed in Chapter 3, discusses overall trends in the data in the vicinity of the EJMT and presents the most favorable options determined by this analysis.
4. Chapter 5 returns to the underlying data of the EJMT pilot bore and presents a back analysis which is used to calibrate a numerical model of the tunnel lining

system for the vicinity of the EJMT. The author reduced the model complexity in order to achieve a reasonable balance between model accuracy and modeling efficiency.

5. Finally, Chapter 6 uses the calibrated and reduced numerical model to validate the alignment optimization of Chapter 4 and to gain insight into the utility of the Q and RMR systems as empirical design heuristics.

1.4 Computer Hardware and Software

Models were run on a computer purchased expressly for this research project. The processor for this computer is an Intel Core i7-9700k CPU with a nominal processing speed of 3.60GHz. The computer has 32 GB of RAM. The operating system is Windows 10 Home, 64-bit version.

The finite difference method (FDM) numerical modeling software used was FLAC 8.0.

The calculation software used for preparing model run code and post-processing model data was MatLab versions 2019 and later. MatLab was also used for:

1. Beam-spring modeling;
2. Digitizing, processing, and interpreting historical data; and,
3. Statistical analyses of data.

Leapfrog Geo (Seequent 2020) was used to create the 3D implicit geological model.

Microsoft Excel was used to create spreadsheets of data for input to MatLab.

The freeware programs Tabula (Aristaran et al. 2013) and Plot Digitizer (Huwaldt 2015) were instrumental in the digitization of historical data.

1.5 Funding

The research project was conducted at the University Transportation Center for Underground Transportation Infrastructure (UTC-UTI) at Mines. Funding for this research project was provided by the United States Department of Transportation (USDOT) under Grant No. 69A3551747118. Matching funding was also provided by CDOT under PO number 471001372. The opinions expressed in this report are those of the author and not the USDOT or CDOT.

CHAPTER 2

LITERATURE REVIEW

2.1 Geotechnical Baseline Reports

Most tunnel projects begin with a Geotechnical Baseline Report (GBR). This report presents an in-depth study of the geological and geotechnical conditions in the area of the desired tunnel. The report aims to synthesize a large amount of geotechnical data, sometimes provided in its raw form as a Geotechnical Data Report (GDR), into a concise evaluation of the geological and geotechnical parameters tunnel construction will encounter. There is a continuing debate in the geotechnical engineering community about evaluating reliability, risk, and uncertainty in the GBR. Some engineers believe that the GBR should contain only a single set of deterministic parameters representing the engineer's best estimate of the most likely conditions to be encountered, with any uncertainty inherent in the GDR left up to the reader to interpret. Some engineers, owners, and contractors suggest that the GBR is virtually meaningless (Smith 2012). Others feel that the GBR should explicitly contain probabilistic metrics expressing the inherent uncertainty in the underlying data. A critical limitation of the GBR is that critical design details are often not known at the time of the development of the GBR. The ground-structure interaction problem inherent in tunnel design means that sometimes, interpretations presented in the GBR may be irrelevant or inaccurate if the final design differs from initial assumptions. One example would be a GBR that focuses on the soil or rock properties at a specific depth estimated as the final structure's location. Relocation of the tunnel vertically within the ground may invalidate assumptions made in the GBR which may or may not have been explicitly stated. Part of the goal of this report is the demonstration of probabilistic implicit geologic modeling techniques as a supplement to a traditional GBR. This methodology, presented in Chapter 3, circumvents some of the shortcomings of a traditional deterministic GBR and allows for flexibility in future design.

2.2 Risk and Reliability

The evaluation of tunnel project risk and reliability is an area of research that has received much attention recently (Brown 2012; Goodfellow et al. 2014; ITIG 2006; Min 2014; Sousa and Einstein 2012; Suorineni 2014b; WSDOT 2018). As discussed in Section 2.1, there continues to be a debate about the appropriate means of addressing geotechnical uncertainty and risk. Many techniques exist for evaluating risk and reliability.

Probably the simplest way of evaluating risk is parametric analysis. Deterministic parameters can vary across their expected range of values and the design's sensitivity to the parameters can be assessed. The parametric analysis can allow for a better understanding of the conservatism of the design and a deeper understanding of which variables are critical to study further.

Parametric analysis tends to lack a rigorous metric for risk and reliability. One better step is to evaluate the limit states of failure through techniques such as the First-Order Reliability Method (FORM) (Chen et al. 2019; Christian et al. 1994; Hasofer and Lind 1974; Low and Tang 2007, 2008; Zhang and Goh 2012). FORM can also be extended to second–order analyses, which is called the Second-Order Reliability Method (SORM) (Breitung 1984; Zhao and Ono 1999a,b; Zhao and Ono 1999c). Load and Resistance Factor Design (LRFD) can generally be viewed as a particular application of FORM or SORM.

Other methods for developing probabilistic outputs based on uncertain inputs include dynamic Bayesian networks (DBN) (Špačková and Straub 2013), Markov chains (Lu et al. 2018), and Monte Carlo (MC) analysis Lu et al. 2019; Miro et al. 2015; Oreste 2015; Shen 2012. Each of the different methods has been applied to tunnel design problems with varying degrees of success.

Although the above highly-quantitative approaches are popular in the academic realm, there have been few applications to actual tunnel projects. A much more widely adopted approach to risk analysis in tunnel engineering is the semi-quantitative risk technique (Goodfellow et al. 2014) which has been specifically endorsed by the International Tunnelling Insurance Group (ITIG), the British Tunneling Society (BTS), and the International Tunnelling Association (ITA) in a model code of practice (ITIG 2006). A risk register is created in a joint meeting of tunnel project stakeholders and involves the creation of a list of everything that participants envision could go wrong with the project. Expert opinion is used to generate simple hazard, exposure, and risk metrics for each identified scenario. The stakeholders can then determine in a semi-quantitative fashion which risks deserve additional mitigation, which risks are unavoidable or acceptable, and

how to apportion financial responsibility for each risk appropriately.

2.3 Rock Mass Classifications

Tunnels are commonly designed and constructed according to empirical rock mass classification systems. These systems are generally based on observed material properties and rock mass conditions. The systems vary from almost entirely based on judgement to being largely quantitative and based on measurable properties. However, their application to tunnel excavation and support system design is still largely based on semi-theoretical or empirical correlations. There is significant debate in the engineering community as to the comparative usefulness of the various systems or the appropriateness of these systems at all (Palmstrom and Broch 2006; Pells 2008; Pells and Bertuzzi 2007). Nevertheless, rock mass classifications are standard-of-practice in tunnel design and provide a simple and useful tool for the particular focus of this research, early stage feasibility studies. However, they are rarely applied probabilistically and there is room for improvement in their application to tunnel engineering feasibility studies and risk characterization.

Of the numerous rock mass classification systems available, the three most popular and widely used are the geomechanics classification or rock mass rating (RMR) system (Bieniawski 1976, 1989, 1973; Celada et al. 2014), the rock mass quality index (Q)-system (Barton 2002; Barton et al. 1974; NGI 2015), and the geological strength index (GSI) (Hoek and Brown 2018; Hoek 1965; Hoek et al. 2002, 1995). Several authors have published extensive reviews and comparisons of the various available systems. The textbook of Singh and Goel (2011) is an excellent summary of developments in rock mass classifications through the date of that textbook. More recently, Rehman et al. (2018) published another relatively complete literature review and summary of rock mass classification systems.

2.3.1 Rock Quality Designation

The rock quality designation (RQD) was first introduced by Deere (1963) for the development of underground shafts, tunnels, and chambers at the Nevada Test Site, it was incorporated into the RMR and Q-systems when each was initially developed. It is a simple method of classifying the quality of rock by measuring the length of intact rock core as compared to the total length of coring. The method was applied, refined, and evaluated for applicability through the late 1960s and early 1970s by Deere and others (Deere et al. 1967; Deere and Miller 1966; Deere et al. 1969, 1970). It was incorporated as an input parameter in Bieniawski's geomechanics classification system and Barton's

Q-system in 1973 and 1974, respectively (Barton et al. 1974; Bieniawski 1973). It has been used extensively in rock mechanics, and is still used today. The system was applied to tunnel lining design as early as 1967 (Deere et al. 1967). In 1989, Deere re-evaluated the system based on twenty years of experience using it (Deere and Deere 1989). Deere found that the system was still generally satisfactory, but that earlier correlations between RQD and tunnel lining design systems should be ignored in favor of Bieniawski's or Barton's system, each of which include RQD as one of several parameters considered.

RQD has been deprecated as a component of RMR but is still included in the Q-system (NGI 2015). In its original form, RQD was simply the sum of the lengths of all pieces of core over 4 inches long in a given core run divided by the total length of the core run. Today, it is often estimated based on correlations with linear (Priest and Hudson 1976) or volumetric (Palmstrom 2005) joint counts.

Recently, it has been argued that it is time for RQD to "rest in peace" (Pells et al. 2017) in favor of the GSI, but the RQD system continues to be used because of its simplicity and industry wide experience with it.

2.3.2 Geomechanics Classification or Rock Mass Rating System

Bieniawski (1973) introduced the Geomechanics Classification System, better known as the RMR system. Bieniawski's system uses RQD as one of its inputs, but also includes seven other input parameters. The inputs to the original RMR system were:

1. RQD;
2. state of weathering;
3. unconfined compressive strength or uniaxial compressive strength (UCS) of intact rock;
4. spacing of joints or bedding;
5. strike and dip orientations;
6. separation of joints;
7. continuity of joints; and
8. ground water inflow.

In the original system presented by Bieniawski (1973), each of these eight parameters is assigned a rating from 1 to 5 (very good to very poor) based on the description or quantitative value of the parameter. For example, an RQD between 50 and 75 gets a rating of 3 (fair). This rating is related to a point system; for an RQD described as 3 (fair), the rock mass gets 12 points. The points for all eight parameters are summed for a total RMR score between zero and 100. The overall class of the rock is then determined

from this score, again ranging from 1 to 5 (very good to very poor). The RMR score and rock mass class are related directly to anticipated stand-up time, active unsupported span, and recommended support system. Bieniawski gives recommendations for rock bolts, shotcrete, and steel sets. For a rock class of 1, support is not generally required, while for a rock class of 5 the recommended steel support was "heavy sets with lagging, immediately 80mm shotcrete". This is clearly not intended to be a constructable steel design; one cannot go to a steel fabricator and request "heavy sets", but rather a guideline for a good starting point. It is also important to remember that Bieniawski's recommendations are based on a typical 10-meter span horseshoe tunnel excavated by drill-and-blast, in a rock mass subject to a vertical stress less than 25 megapascals (MPa) (approximately 900 meters of overburden). Again, the tunnel design engineer must consider the basis of the recommendations, and the change in tunnel construction practice since Bieniawski's recommendations were first published in 1973. Bieniawski made some tweaks to the system, evaluated its usefulness against a database of case studies, and re-presented the rock mass rating (RMR_{89}) system in 1989 (Bieniawski 1989). This is the most widely used version of the system.

Recognizing the need to update the system over time, Lowson and Bieniawski (2013) updated the RMR system. The revised system simplifies some of the parameters, removes RQD as an input in favor joint frequency, and provides graphs of continuous functions of RMR scores versus input parameters. Unfortunately, Lowson and Bieniawski (2013) do not provide equations for these graphs, so applying them is still a graphical solution.

Celada et al. (2014) provided a significant revision to the RMR system, incorporating the Lowson and Bieniawski (2013) removal of RQD, revising factors for joint condition, and adding new factors for excavation method and in-situ stress state. This revised system is referred to as rock mass rating (RMR_{14}) with the subscript 14 to distinguish it from the original 1973 system or the 1989 revision.

RMR_{14} still ranges between 0 and 100 and is the sum of several component scores. There are five components of the base RMR_{14}, sometimes denoted base rock mass rating ($\text{RMR}_{14\text{b}}$). There is one subtractive and two multiplicative factors which are applied to the base score to achieve the final RMR_{14} score.

$$RMR_{89} = RMR_{UCS} + RMR_{RQD} + RMR_{JSpac} + RMR_{JCond} + RMR_{GW} \tag{2.1}$$

$$RMR_{14b} = RMR_{14UCS} + RMR_{14\lambda} + RMR_{14JCond} + RMR_{14GW} + RMR_{14Alt} \tag{2.2}$$

$$RMR_{14} = (RMR_{14b} + F_O) \cdot F_e \cdot F_s \tag{2.3}$$

$$RCR = RMR_{JFreq} + RMR_{JCond} + RMR_{GW} + RMR_{Alt} \tag{2.4}$$

where RMR_{89} is the RMR as published by Bieniawski (1989), RMR_{14b} is the base RMR score before application of the F_0, F_e, and F_s factors, RMR_{14} is the RMR as published by Celada et al. (2014), RCR is the rock condition rating as suggested by Singh and Goel (2011), RMR_{UCS} is the UCS component of the RMR score, RMR_{RQD} is the RQD component of the RMR score, RMR_{JSpac} is the joint spacing component of the RMR score, RMR_{JCond} is the joint condition component of the RMR score, RMR_{GW} is the groundwater component of the RMR score, RMR_{JFreq} is the joint frequency component of the RMR score, RMR_{Alt} is the rock mass alterability component of the RMR score, F_0 is the discontinuity orientation factor, F_e is the excavation method factor, and F_s is the in-situ stress state factor.

2.3.2.1 Unconfined Compressive Strength

The function relating UCS to its RMR component score is presented as a graph in several papers (Celada et al. 2014; Lowson and Bieniawski 2013; Pells et al. 2017) but the underlying function is not given. This presents a problem for the quantification of the system in any kind of spreadsheet or calculation software, as graphical lookup requires direct user input. The author contacted Lowson to inquire if the underlying function is available. Lowson stated that they had never seen an equation for this graph and they were given the graph as a flat image during the writing of the 2013 paper with Bieniawski (Lowson, personal communication, 2020). In accordance with Lowson's advice, the author digitized this graph, sampled points along the given curves, and regressed functions to these points. Several functional forms were tried including polynomial (parabolic), logarithmic, and power functions. The power function fit the given curve the best, with a coefficient of determination (r^2–value) value in excess of 0.9999, suggesting that this was the likely functional form originally used to develop the graph. The regressed power functions is given as Equation 2.5 and shown in Figure 2.1.

$$RMR_{14UCS} = 0.415\sigma_{ci}^{0.651} \leq 15 \tag{2.5}$$

where σ_{ci} is the uniaxial compressive strength of the rock mass in MPa.

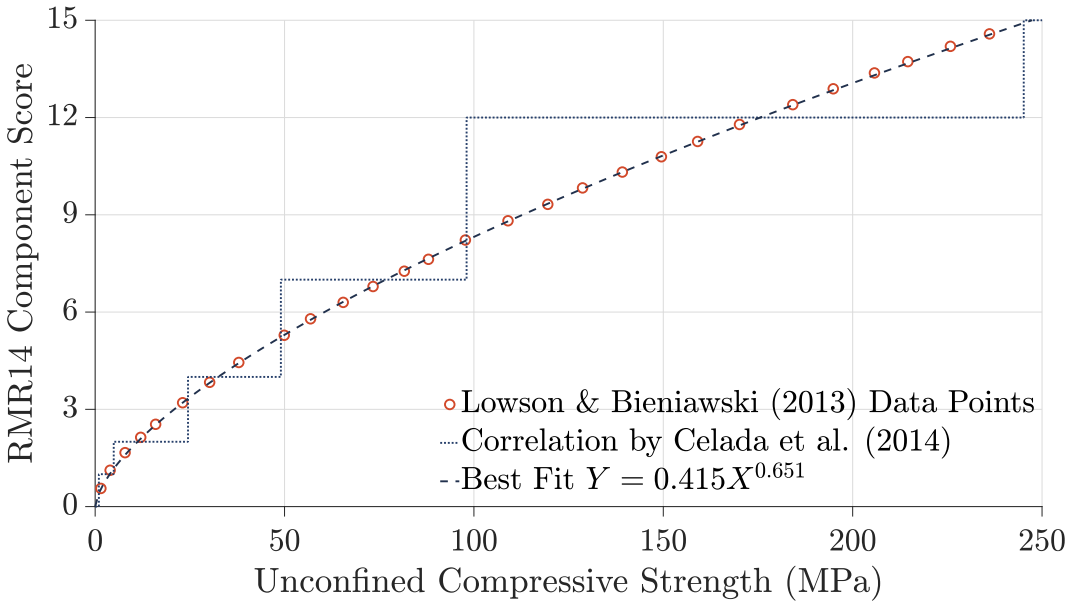

Figure 2.1: Unconfined compressive strength component of RMR_{14} (RMR_{14UCS}) correlation as proposed by Lowson and Bieniawski (2013) with regressed function for calculating the RMR component score based on UCS.

2.3.2.2 Fracture Spacing and Discontinuity Density

Similar to the function for uniaxial compressive strength, the function relating discontinuity density to its component score is presented as a graph in several papers (Celada et al. 2014; Lowson and Bieniawski 2013; Pells et al. 2017) but the underlying functions is not given. As with the uniaxial compressive strength relationship, the author digitized this graph, sampled points along the given curves, and regressed functions to these points. Several functional forms were tried including polynomial (parabolic), exponential, and power functions. The power function fit the given curve the best, with an r^2–value value in excess of 0.9999, suggesting that this was the likely functional form originally used to develop the graphs. The regressed power function is given as Equation 2.6 and shown in Figure 2.2.

$$RMR_{14\lambda} = 40 \geq -6.36\lambda^{0.467} \geq 0 \tag{2.6}$$

where λ is the discontinuity density of the rock mass in joints per meter. Note that the range of scores is limited to between 0 and 40.

Note that if one assumes that $RMR_{14\lambda}$ should only be reported in whole numbers, it is possible to estimate a minimum joint frequency and thus a maximum joint spacing. Rearranging the $RMR_{14\lambda}$ function for JPM and putting in an $RMR_{14\lambda}$ score of 39.5

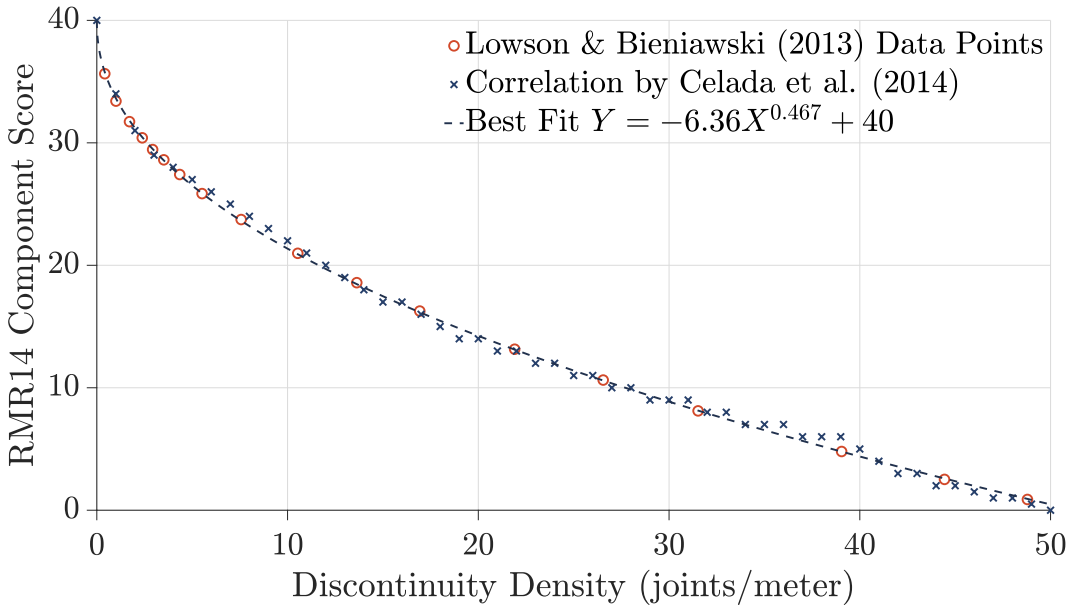

Figure 2.2: Joint frequency component of RMR_{14} ($RMR_{14\lambda}$) correlation as proposed by Lowson and Bieniawski (2013) with regressed function for calculating the RMR component score based on joint frequency.

gives a JPM of 0.0043 joints per meter. This equates to a joint spacing of 232 meters. Measuring a joint spacing of that magnitude is unrealistic and impractical under most field conditions. For example: Assume that a 20-meter diameter tunnel is to be excavated, which is significantly larger than anything currently being excavated. By face mapping, the widest joint spacing that could conceivably be measured is 20 meters. By wall mapping, larger joint spacings could conceivably be mapped, but there is a question of practicality and usefulness of the data when mapping joint spacings more than a few diameters behind the advancing face. Assume, generously, that 100 meters is the largest joint spacing that could practically be mapped. This would mean that a length equivalent to an American football field has been excavated underground and one joint has been mapped in the entire length of the field. This joint spacing would correlate to a joint frequency of 0.01 m^{-1} and an $RMR_{14\lambda}$ score of 39. More practically, a joint spacing of 20 meters (i.e., one joint in the entire face of an extremely large excavated tunnel) correlates to a joint frequency of 0.05 m^{-1} and an $RMR_{14\lambda}$ of 38. The RMR system was designed for use in-situ during excavation and construction of tunnels. However, under the current recommended methodology for RMR_{14} it appears to be impossible under practical construction conditions to achieve the highest possible $RMR_{14\lambda}$ score. This would seem to be a flaw in the system worth correcting, or at least discussing. What is the usefulness of a system which includes unrealistic or non-physical results within its defined range?

How does one calibrate a semi-empirical curve outside of the range of practically available data? For practical application to more typically sized tunnels in the 3- to 10-meter range, the maximum possible $RMR_{14\lambda}$ score based on face mapping drops to 36 to 38. Note that this system is also, therefore, estimating worse ground conditions for smaller tunnels, the inverse of the typically assumed relationship. In general, smaller tunnels are more stable, not less.

2.3.2.3 Groundwater Conditions

The RMR component score for the presence of water has five qualitative descriptions of the moisture conditions in the tunnel. These descriptions are dry, slightly wet, wet, dripping, and water flow. Scores range from 15 to 0 for these descriptions. No quantitative descriptions of groundwater flow are given. The RMR component score for groundwater is intended to reflect excavation and support difficulties associated with groundwater inflow conditions including worker safety, outwash of joint fillings, hydraulic jacking of joints, hydraulic pressure on supports, and face collapse. Any continuous water inflow into the excavation immediately moves this score to the last category, water flow, and sets the score to zero. For this reason, the RMR groundwater score has significantly lower granularity at the upper end than the Q-system J_w score which includes six categories of qualitative groundwater flow, four of which describe conditions of water flow. On the other hand, the Q-system has less granularity on the lower end, where the two lowest J_w descriptions roughly correlate to the four lower RMR groundwater score descriptions. Neither of these systems provide any quantitative correlation to the range of groundwater inflow which would correlate to any given score.

2.3.2.4 Stress-Strain Behavior

Bieniawski et al. (2011) suggested that the *indice de comportamiento elastico* (ICE) be used to adjust the RMR for inelastic behavior of underground openings (Celada et al. 2014; Celada and Bieniawski 2020). The piecewise equation for computing ICE is a function of the in-situ stress ratio, RMR, uniaxial compressive strength, tunnel depth, overburden weight, and tunnel shape. Bieniawski et al. (2011) derived Equation 2.7 based on the Kirsch equations (Kirsch 1898; Timoshenko and Goodier 1951), an assumed overburden unit weight, a relationship between intact uniaxial compressive strength and rock mass compressive strength originally developed for coal mines by Kalamaras and

Bieniawski (1995), and a factor of 100 to normalize the range of ICE.

$$ICE = \begin{cases} K_0 \leq 1 & \dfrac{3704 S \sigma_{ci} \exp\left(\dfrac{RMR_{14b} - 100}{24}\right)}{(3 - K_0)\, H} \\ K_0 > 1 & \dfrac{3704 S \sigma_{ci} \exp\left(\dfrac{RMR_{14b} - 100}{24}\right)}{(3K_0 - 1)\, H} \end{cases} \tag{2.7}$$

where K_0 is the in-situ horizontal/vertical stress ratio, S is a shape factor, $\sigma_c i$ is the uniaxial compressive strength of the intact rock in MPa, H is the tunnel depth, meters, and RMR_{14b} is the rock mass rating before the application of F_e, F_s, or F_0.

The stress adjustment factor for RMR (F_s) is then computed from the ICE by the further piecewise function Equation 2.8:

$$F_s = \begin{cases} ICE < 15 & F_s = 1.3 \\ 15 \leq ICE \leq 70 & F_s = \dfrac{2.3\sqrt{100 - ICE}}{7.1 + \sqrt{100 - ICE}} \\ ICE > 70 & F_s = 1 \end{cases} \tag{2.8}$$

Bieniawski et al. (2011) provide a table of shape factors based on regression to a set of 1152 FLAC3D models. These shape factors are:

1. Circular tunnel, 6-meter diameter, S = 1.3;
2. Circular tunnel, 13-meter diameter, S = 1.0;
3. Conventional tunnel (oval with flat invert), 14-meter diameter, S = 0.75; and,
4. Chambers 25 meters wide by 60 meters high, S = 0.55.

Bieniawski et al. (2011) hypothesize that any case where estimated elastic strength exceeds estimated elastic stress should behave elastically.

The derivation based on the Kirsch equations is a fundamental assumption of elastic behavior, and in theory the ICE is intended to predict the line between elastic and inelastic behavior. The idea behind this assumption is that ICE will indicate where the boundary of elastic behavior is, though the actual in-situ stresses may not be elastic.

There are several significant shortcomings to the Bieniawski et al. (2011) ICE factor:

1. In deriving the equation for ICE, Bieniawski et al. (2011) used a typical overburden weight of 0.027 meganewtons per cubic meter because they were looking at generic

cases. For specific cases, there is no need for this generalization and the estimated in-situ overburden pressure based on project data can be used.

2. The use of the Kalamaras and Bieniawski (1995) relationship for rock mass compressive strength is arguable, especially as this relationship was developed and intended for the evaluation of coal mine pillar and roof stability. The correlation to in-situ strength of coal mine overburden units (generally low-strength horizontally bedded sedimentary formations) is likely unrealistic for many other geologic formations.
3. Bieniawski et al. (2011) compute the maximum compressive stress but neglect the fact that at very low stress ratios ($K_0 < \frac{1}{3}$) or very high stress ratios ($K_0 > 3$) the controlling stress may be a tensile failure.
4. The Kirsch equations are derived from an assumed zero-stress condition at the excavation boundary. If the excavation were unsupported, this would be accurate. However, any support pressure holding the tunnel open will create a different stress distribution around the tunnel than that predicted by the Kirsch equations.
5. The shape factors are calibrated for a few very specific tunnel shapes and sizes. Issues of stress concentration at corners are significant for many tunnel shapes and should be evaluated more precisely than this method allows. Note that Bieniawski et al. (2011) only evaluated four excavation shapes and sizes. For shapes differing significantly from these descriptions, the shape factor may need to be recalibrated.

The shortcomings in the Bieniawski et al. (2011) ICE coefficient can be addressed by reformulating ICE. The in-situ uniaxial compressive strength can be calculated based on a Hoek-Brown (H-B) failure envelope. The in-situ stress can be estimated based on a more rigorous elastic analysis. While the calculation of stresses based on an assumed elastic rock mass behavior is still debatably accurate, an analysis which includes greater flexibility for the shape of the cross section is advisable. In the case of the Eisenhower-Johnson Memorial Tunnel (EJMT), tabulated results by Eissa (1980) based on the boundary element method are recommended. The Eissa (1980) method has been well documented and used for the identification of the boundary of elastic behavior previously by other authors (Hoek and Brown 1980; Palmstrom 1995a,b, 1996).

Even more rigorous approaches could be pursued. However, for the purposes of early stage probabilistic feasibility estimates of tunnel alignments, the simple refinements to the Bieniawski et al. (2011) described in Equation 2.9 are considered sufficient.

$$ICE = \frac{100\sigma_c}{\sigma_{max}} \tag{2.9}$$

where σ_c is the uniaxial compressive strength of the rock mass (not the uniaxial compres-

sive strength of intact rock), estimated from the H-B envelope of the rock mass reduced based on the GSI and σ_{max} is the maximum stress at the boundary of the excavation estimated via a closed form equation appropriate to the excavation shape such as that by Eissa (1980).

2.3.3 Q Rock Mass Rating System

A team of engineers from the Norwegian Geotechnical Institute (NGI), led by Nick Barton, also developed an empirical correlation to tunnel support systems, which they termed the rock mass quality index (Q) (Barton et al. 1974). The Q-system was based on a large number of case studies (>200). These case studies were heavily biased towards European and especially Scandinavian tunnel projects. In the 1974 paper, the authors state that:

> As a result of this European-Scandinavian bias, and the belief that shotcrete and bolting methods deserve most attention, many well-documented case records have been ignored. These include those describing steel rib support methods, free span concrete arch roofs, and pre-cast sectional linings. (Barton et al. 1974)

The Q-system has been well documented with many case studies of applications, occasionally refined, and updated as necessary. The most recent version of the system is documented in a handbook published by NGI (2015).

The Q-system is a combination of six parameters, related as shown in Equation 2.10. The first of these parameters is Deere's RQD, while the other five relate to joint set, joint roughness, joint alteration, water in joints, and the ratio of in-situ stress to rock strength. There are also three additional variants of the Q-system which are sometimes used: the rock mass quality index without stress factors (Q') (Equation 2.12), the rock mass number (N) (Equation 2.11), and the rock mass quality index for TBM tunneling (Q_{tbm}) (Equation 2.13).

$$Q = \frac{RQD}{J_n} \cdot \frac{J_r}{J_a} \cdot \frac{J_w}{SRF} \tag{2.10}$$

$$N = \frac{RQD}{J_n} \cdot \frac{J_r}{J_a} \cdot J_w \tag{2.11}$$

$$Q' = \frac{RQD}{J_n} \cdot \frac{J_r}{J_a} \tag{2.12}$$

$$Q_{TBM} = \frac{RQD_0}{J_n} \cdot \left(\frac{J_r}{J_a}\right)_c \cdot \frac{J_w}{SRF} \cdot \frac{SIGMA}{F^{10}/20^9} \cdot \frac{q}{CLI} \cdot \frac{\sigma_\theta}{5} \tag{2.13}$$

where RQD is the rock quality designation (Deere and Deere 1989), RQD_0 is the RQD oriented in tunneling direction (Barton 2000), J_n is the joint set number (NGI 2015), J_r is the joint roughness number (NGI 2015), J_a is the joint alteration number (NGI 2015), $\left(\frac{J_r}{J_a}\right)_c$ are the joint parameters most assisting or hindering cutter penetration (Barton 2000), J_w is the joint water reduction factor (NGI 2015), SRF is the stress reduction factor (NGI 2015), $SIGMA$ is the rock mass compressive or tensile strength (whichever controls) in MPa (Barton 2002), F is the tunnel boring machine (TBM) thrust force per cutter, tonnes, q is the rock quartz content expressed as a whole number fraction of 100, CLI is the cutter life index (Movinkel and Johannessen 1986), and σ_θ is the maximum excavation tangential stress (MPa) typically estimated by an elastic analytical solution, e.g., (Kirsch 1898).

NGI (2015) states that Q varies from 0.001 to 1000. Higher and lower values are possible with extreme combinations of parameters. NGI recommends setting a floor and a ceiling at 0.001 and 1000 respectively for practical purposes.

The Q-system is intended to provide recommendations for the design of the permanent roof support of tunnels. Some relation to wall support is also provided, although this is highly dependent on the in-situ stress ratio, and requires additional calibration. The Q-system does not provide recommendations for temporary support. Part of the rockbolt and shotcrete system is the idea that temporary tunnel support becomes permanent tunnel support. In general, the Q-system handbook suggests that shifting down and right on the included graph of Q vs. support is an appropriate estimate of required temporary support. Another method of estimating temporary support would be to apply a different excavation support ratio (ESR) than that used for the permanent support. The Q-system includes the ESR as a measure of the importance of the structure, and can be thought of as something like a factor of safety. The span of the tunnel is divided by the ESR when entering the Q-system chart to arrive at an effective span. ESR numbers below 1 increase the effective span, and thus the required support, while ESR numbers above 1 decrease the effective span and required support.

2.3.3.1 Stress Reduction Factor

The Q-system's stress reduction factor (SRF) is dependent on the stress condition, four broad geologic categories, maximum tangential stress estimated via elastic theory, and the likely failure mode of the ground (brittle or ductile). According to the NGI handbook

"SRF describes the relation between stress and rock strength around an underground opening" (NGI 2015). The SRF is thus somewhat analogous to ICE in the RMR system (Celada et al. 2014).

SRF distinguishes between four different failure modes: brittle failures (e.g., rock burst), ductile failures (squeezing), structurally controlled failures due to weak zones intersecting the excavation, and chemically swelling ground.

In order to estimate the transition from brittle to ductile behavior the correlation of Singh et al. (1992) is suggested by NGI (2015). This correlation estimates the depth of overburden which will cause squeezing as a function of Q, as shown in Equation 2.14.

$$H_{squeeze} = 350 \cdot Q^{\frac{1}{3}} \tag{2.14}$$

Based on the brittle-ductile behavior estimate of Equation 2.14 the user applies the NGI (2015) handbook Table 6. Table 6a is for "weak zones intersecting the underground opening, which may cause loosening of rock mass". This table should be applied for unique structural features, e.g., the locations where specific faults cross the alignment. Otherwise, the user turns to NGI (2015) Table 6b (for non-squeezing behavior) and NGI (2015) Table 6c (for squeezing behavior).

To efficiently implement the suggested SRF values of NGI Table 6b in a vectorized fashion, a piecewise linear function was written relating the input criteria $\frac{\sigma_c}{\sigma_1}$ and $\frac{\sigma_\theta}{\sigma_c}$ to SRF. Figure 2.3 shows the Table 6b correlation points, suggested boundary points, and the best fit piecewise line through these points. The equations of the piecewise functions shown on Figure 2.3 are:

$$\log_{10} SRF = \begin{cases} -3.29 \cdot \log_{10} \dfrac{\sigma_c}{\sigma_1} + 3.29 & for \quad \dfrac{\sigma_c}{\sigma_1} \leq 10 \\ \\ 0.306 \cdot \log_{10} \dfrac{\sigma_c}{\sigma_1} - 0.306 & for \quad \dfrac{\sigma_c}{\sigma_1} > 10 \end{cases} \tag{2.15}$$

$$\log_{10} SRF = \begin{cases} -0.269 \cdot \log_{10} \dfrac{\sigma_\theta}{\sigma_c} - 0.141 & for \quad \dfrac{\sigma_\theta}{\sigma_c} \leq 0.3 \\ \\ 4.40 \cdot \log_{10} \dfrac{\sigma_\theta}{\sigma_c} + 2.30 & for \quad \dfrac{\sigma_\theta}{\sigma_c} > 0.3 \end{cases} \tag{2.16}$$

where SRF is the stress reduction factor, σ_θ is the maximum tangential stress estimated from the Kirsch equations, σ_c is the unconfined compressive strength of the rock mass estimated by the H-B criterion, and σ_1 is the major principal stress at the point of interest. These functions have coefficients of determination of 0.94 and 0.95, respectively,

to the suggested correlation points in NGI (2015) Table 6b.

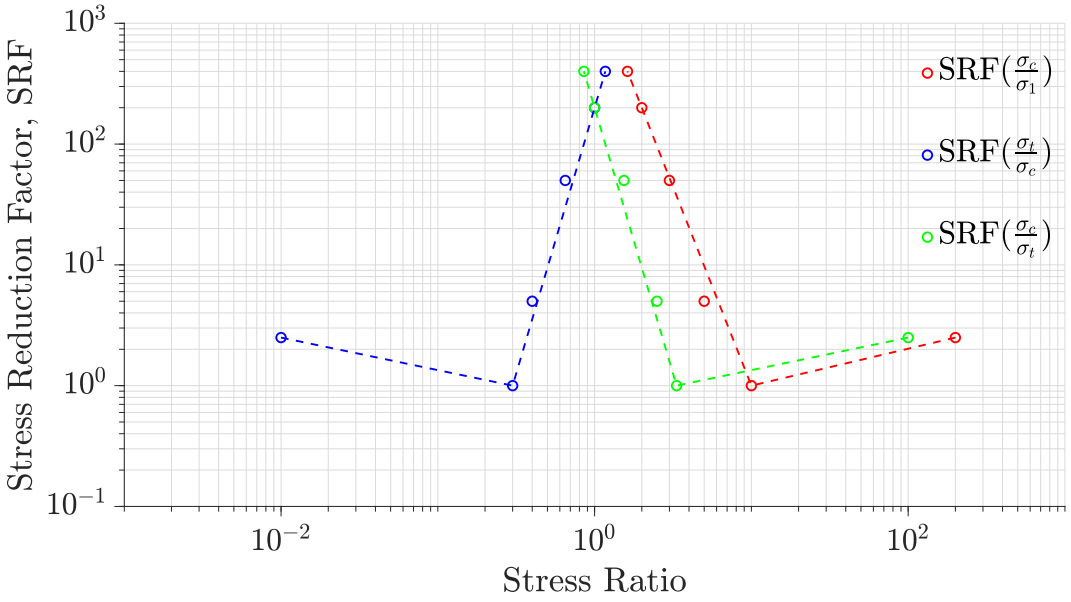

Figure 2.3: NGI (2015) Table 6b correlation points between stress state and SRF with piecewise linear function fit.

The NGI (2015) handbook Table 6c gives suggested values for SRF for squeezing rock as a function of $\frac{\sigma_\theta}{\sigma_c}$. The lowest listed value of $\frac{\sigma_\theta}{\sigma_c}$ is 1 and the recommended SRF for this value is 5. This raises the question: what SRF should be used for ductile rock materials below their compressive strength? To this author's knowledge, there is no explicit statement of how to handle this condition, though one imagines that $SRF = 1$ would be appropriate, i.e., no strength reduction for ductile materials in an elastic state.

From the listed values in NGI (2015) Table 6c, the following linear function was developed to estimate SRF values:

$$SRF = \frac{5}{4}\left(\frac{\sigma_\theta}{\sigma_c}\right) + \frac{15}{4} \tag{2.17}$$

This gives a value of $SRF = 5$ at $\frac{\sigma_\theta}{\sigma_c} = 1$ and a value of $SRF = 20$ at $\frac{\sigma_\theta}{\sigma_c} = 13$, which is the saturation value of SRF given in Table 6c. Presumably, for ductile materials below their compressive strength, SRF should be lower than 5, plausibly as low as 1 (i.e., no failure). Simple linear extrapolation of the above function to a value of $\frac{\sigma_\theta}{\sigma_c} = 0$ gives an SRF of 3.75, which seems unreasonably high for a material experiencing no stress. In order to reduce the value of SRF to 1, the following piecewise linear function is adopted for SRF

for ductile materials:

$$SRF = \left\{ \begin{array}{ccccc} 1 & for & & x & \leq 0.9 \\ 40x - 35 & for & 0.9 < & x & \leq 1.0 \\ \frac{5}{4}x + \frac{15}{4} & for & 1.0 < & x & \leq 13 \\ 20 & for & 13 < & x & \end{array} \right| \; x = \frac{\sigma_\theta}{\sigma_c} \tag{2.18}$$

2.3.4 Geological Strength Index

Hoek and Brown (1988) originally proposed the use of a rock mass classification to reduce the H-B failure criterion from an intact rock strength to a rock mass strength. At that time, they used RMR directly in their failure criterion, implying that $RMR = GSI$, at least for the 1976 definition of RMR (Bieniawski 1976). Hoek and Brown (1988) recommended assuming dry conditions (i.e., setting the groundwater component score to 10) and assuming favorable joint orientations (zero adjustment). The most recent descriptions of the use and application of the GSI system have been published by Hoek and Brown (2018) and Marinos and Carter (2018).

Hoek (1994) and Hoek et al. (1995) introduced GSI as a separate rock mass classification system from RMR. The original GSI chart was based on qualitative evaluation of a rock exposure in which the engineering geologist evaluated the rock structure (blocky, very blocky, blocky/seamy, or crushed) and surface condition (very good to very poor).

Hoek (1994) and Hoek et al. (1995) suggested a relationship between GSI and the 1989 version of RMR, again assuming dry conditions (i.e., setting the groundwater component score to 15) and favorable joint orientations (zero adjustment). Hoek et al. (1995) noted that the 1989 RMR values tended to be slightly higher than the 1976 RMR values, and hence provided Equation 2.19 relating RMR to GSI.

$$GSI = RMR_{89} - 5 \tag{2.19}$$

Hoek (1994) and Hoek et al. (1995) further suggested a relationship between GSI and Q' as shown in Equation 2.20. Note that Hoek (1994) and Hoek et al. (1995) set a minimum value of Q' at 0.0208. Below this, the correlation produces GSI less than 9 and is considered not applicable to most rocks. Note that the maximum GSI value in the H-B strength criterion is 100, but Q' values higher than 504 will return GSI values above 100. Q' values higher than 500 are fairly easily attainable for good rock conditions. Hoek

(1994) and Hoek et al. (1995) are silent on how to handle this issue.

$$Q' = e^{\frac{GSI-44}{9}} \tag{2.20}$$

Pells et al. (2017) note that this relationship is the same as that suggested by Bieniawski (1993) to correlate RMR to Q and note that "it seems illogical that the same equation relates Q' to GSI, and Q to RMR. The writers accept [Bieniawski's Q to RMR relationship] as being based on source data." One of the issues with the Hoek (1994) and Hoek et al. (1995) suggested RMR-GSI-Q relationship is that this creates an implied relationship between Q and RMR that is not necessarily supported by other research on these correlations (Abad et al. 1983; Barton 1995; Barton and Bieniawski 2008; Bieniawski 1976; Cameron-Clarke and Budavari 1981; Moreno Tallon 1980, 1982; Rutledge and Preston 1978).

Hoek and Brown (1997) provided further advice on the use of their strength criterion and GSI. This appears to be the first version of the GSI chart which included contours of GSI scores. These contours were hand drawn, not parallel, and unevenly spaced. The conversion from the original 20 categories of GSI to the contoured chart implied significant uncertainty and Hoek and Brown (1997) provided a clear admonition against excess precision: "Do not attempt to be too precise. Quoting a range of GSI from 36 to 42 is more realistic than stating that GSI = 38." Nonetheless, the contours of GSI values and the desire for a neat, closed-form, deterministic solution to all problems means that GSI is frequently quoted as a single discrete value, rather than a range.

Hoek and Marinos (2000a,b), Hoek et al. (1998), Marinos and Hoek (2001), Marinos and Hoek (2000), and Marinos et al. (2005) extensively discussed the application of GSI to weak, chaotic, and heterogeneous rock masses. During this work, they further updated the GSI chart by adding an extra row at the bottom for laminated and sheared rock masses.

In an open access textbook first published online in 2006 and subsequently occasionally updated, Hoek (2006) states that "GSI should be estimated directly by means of the chart, not from the RMR classification." Nonetheless, engineers have attempted to quantify the GSI chart including Cai et al. (2004), Cai and Kaiser (2006), and Russo (2009).

Following these other authors attempts to quantify the GSI chart Hoek et al. (2013) published their own quantification of the GSI chart. Noting that the original lines on the GSI chart were hand drawn, not parallel, and not evenly spaced, Hoek et al. "corrected" this by setting the lines parallel and evenly spaced. They also provided axes along the chart based on some of the parameters of RMR and Q. This resulted in equations for

estimating GSI based on the parameters of RMR (Equation 2.21) and Q (Equation 2.22).

$$GSI = 1.5 \cdot RMR_{JCond} + \frac{RQD}{2} \tag{2.21}$$

$$GSI = \frac{52\frac{J_r}{J_a}}{1 + \frac{J_r}{J_a}} + \frac{RQD}{2} \tag{2.22}$$

where RMR_{JCond} is the joint condition component of RMR from Bieniawski's 1989 definition of RMR, J_r is the joint roughness factor from the Q-system, J_a is the joint alteration factor from the Q-system, and RQD is the rock quality designation. Note that Hoek et al. (2013) have removed the correlation of the GSI score with the UCS of the material. This avoids double-consideration of the UCS value in reducing the strength of the intact material using the H-B failure criterion. Hoek et al. (2013) gave an r^2–value of 0.95 for Equation 2.21 based on correlation to data from a single drill-and-blast tunnel.

Pells et al. (2017) note that Equations 2.21 and 2.22 tend to give somewhat less consistent answers than simply having a trained engineering geologist use the GSI look-up chart and appropriate judgment. Further, Pells et al. (2017) suggest that the GSI value can be reasonably expected to deviate by as much as ±10 points when considering natural (aleatory) variation across a given exposure and epistemic variation between multiple trained engineering geologists classifying the exposure. Note that this ±10 point deviation is actually well in line with the implied variability across the 20 categories of the original GSI chart from 1995 (Hoek et al. 1995), which raises the question of whether this is a feature or a bug of the GSI system. However, Pells et al. (2017) note that "for zero confining stress ($\sigma_3 = 0$) it is shown that for a 10 point uncertainty in GSI, the uncertainty in the computed rock mass unconfined strength, ranges from 100% at true GSI of 15, to 75% at true GSI of 25, and [approx.] 56% for true GSI greater than 70." This uncertainty declines to 20% to 40% for confining stresses above 1 MPa.

2.3.5 Correlations Between Rock Mass Classifications

Many authors have attempted to find correlations between the various rock mass classification systems, with limited success. The inherently subjective nature of the classification systems combined with sometimes scant or inconsistent data make interpreting historical documents on rock mass classification particularly difficult. Inherent differences in the systems themselves and their application to different projects has also been a complication.

2.3.5.1 RMR and Q

Rehman et al. (2018) state that "there is no scientific basis to assume a universally valid regression between the two systems [Q and RMR]." Nevertheless, many authors have offered correlations between the Q and RMR systems. Some of these correlations have been tabulated in Table 2.1. Note that the RMR-Q correlations include a logarithmic function in order to convert from the Q-system, which spans six orders of magnitude, to the RMR system which ranges from 0 to 100. Some references list these logarithmic functions in base 10 log, while others give the reference in natural log. The issue is further confused by worldwide differences in notation, specifically in the use of the abbreviated notation $log(X)$ to indicate a base 10 logarithm in some places and a natural logarithm in others. However, all of the correlations can be placed in an equation of a single form with two variables, A and B, which are empirically calibrated. In Table 2.1, the RMR to Q correlations have been tabulated in this fashion. All correlations have been adjusted to natural logarithms. The basic form of the relationship is as shown in Equation 2.23.

$$RMR = A \cdot \ln Q + B \tag{2.23a}$$

$$Q = e^{(RMR-B)/A} \tag{2.23b}$$

The correlation listed in the first row of Table 2.1 is the most popular one, and has been specifically endorsed by both Barton and Bieniawski in a joint paper (Barton and Bieniawski 2008). The alternative correlation by Barton (1995) is also endorsed in the same paper. Mean values for A and B from Table 2.1 are 6.6 and 50.

Singh and Goel (2011) state that correlations between Q and RMR are not truly equivalent because the systems have fundamental differences in the way that they are determined and applied. Singh and Goel (2011) point primarily to the SRF factor on Q and the UCS and joint orientation factors on RMR. Singh and Goel (2011) suggest that removing these factors from Q and RMR make them much more amenable to correlation, and provide a correlation between some components of Q, denoted rock mass number (N), and other components of RMR, denoted rock condition rating (RCR). Equation 2.11 and Equation 2.4 show how N and RCR are calculated, respectively.

By correlating N and RCR rather than Q and RMR, Singh and Goel (2011) suggest that a relationship can be established as shown in Equation 2.24 (Goel et al. 1996). Note that Equation 2.24 preserves the same functional form as Equation 2.23.

$$RCR = 8 \ln N + 30 \tag{2.24}$$

Table 2.1: Published correlations between RMR and Q.

Papers Where Referenced	A	B	Notes
Barton and Bieniawski (2008), Bieniawski (1976, 1978, 1984, 1989, 1993), Jethwa (1981), and Moreno Tallon (1982)	9	44	Specifically endorsed by Barton and Bieniawski in a 2008 joint paper
Bieniawski (1993) and Rutledge and Preston (1978)	5.9	43	Calibrated against New Zealand rock mass classification experience
Bieniawski (1993), Kaiser et al. (1986), Moreno Tallon (1980, 1982), and Singh and Goel (2011)	5.4	55.2	Based on four tunneling projects in Spain
Cameron-Clarke and Budavari (1981)	5	60.8	Based on three tunnels in South Africa. Correlations based on in–situ mapping of the tunnel face. Authors found poor correlation and did not recommend using.
Abad et al. (1983) and Bieniawski (1993)	10.5	41.8	Calibrated against data from 187 coal mine roadways in Spain
Barton (2002), Barton (1995), Barton and Bieniawski (2008), and Barton (2000)	6.5	50	Specifically endorsed by Barton and Bieniawski in a 2008 joint paper
This report	4.69 to 5.47	51.4 to 55.8	Correlation between RMR_{14b} and Q with $r^2 = 0.32$ and $r^2 = 0.45$, respectively, for the pilot and Eisenhower bores of the EJMT. See Section 3.6.1 for further discussion.

Goel et al. (1996) report a r^2–value of 0.92 for this correlation based on 63 case histories, primarily in India.

2.3.5.2 Rock Mass Rating 1989 and 2014 Revisions

Because of several updates to the system over the years, historical values of RMR are not necessarily equivalent to values of RMR calculated by the current methodology. The two most common iterations of RMR are generally referred to as RMR_{89} (Bieniawski 1989) and RMR_{14} (Celada et al. 2014), although there were some incremental improvements between those two major updates.

RMR_{89} and RMR_{14} have the same 0 to 15 point scoring for UCS and this correlation is not generally assumed to have changed between the systems.

RMR_{89} has a 0 to 20 score for RQD and a 0 to 20 score for spacing of discontinuities. RMR_{14} combines these into a single 0 to 40 score based on joint frequency (inverse of joint spacing) per Lowson and Bieniawski (2013).

RMR_{89} has a 0 to 30 score for condition of discontinuities. RMR_{14} has a 0 to 20 score for condition of discontinuities that is further separated into four 0 to 5 point components for continuity, roughness, gouge infilling, and weathering. RMR_{14} also has a 0 to 10 point score for alterability of the intact material which is not present in RMR_{89}. It is reasonable to combine the RMR_{14} scores for alterability and discontinuity condition and consider these roughly equivalent to the RMR_{89} score for discontinuity condition, but there is likely some error inherent in this simplification.

RMR_{89} and RMR_{14} both have a 0 to 15 score based on groundwater. However, RMR_{89} provides different ways of determining this score, either based on quantitative inflow in liters per meter of tunnel, the ratio of joint water pressure to major principal stress, or a qualitative description of moisture conditions. RMR_{14} provides only 5 qualitative categories of moisture condition. Although there are certainly reasons to critique these quantitative metrics, such as liters per minute per length of tunnel failing to account for differences in tunnel diameter, the quantitative basis for the rating system provides better reproducibility. In this case, where data with the granularity required for the quantitative metrics are lacking, the qualitative descriptions are used. The RMR_{89} groundwater scores and RMR_{14} groundwater scores are therefore the same.

Celada et al. (2014) provide an empirical correlation between RMR_{89} and RMR_{14} based on a database of 2,298 mapped tunnel sections.

$$RMR_{14} = 1.1 \cdot RMR_{89} + 2 \tag{2.25a}$$

$$RMR_{89} = 0.91 \cdot (RMR_{14} - 2) \tag{2.25b}$$

2.4 Correlations to Rock Mass Classifications

In an attempt to leverage the available rock mass classification data, many correlations between rock mass classifications and various engineering properties, design inputs, and even complete design suggestions have been correlated to rock mass classifications. In particular, attempts to estimate rock mass deformation modulus are numerous.

2.4.1 Young's Modulus or Deformation Modulus

Table C.1 contains 50 published correlations from 40 separate references between various rock mass classification systems and the Young's modulus or deformation modulus of the rock mass. The term deformation modulus is commonly used in rock mechanics to refer to the ratio of axial deformation to axial load in an unconfined loading situation, i.e., the Young's modulus. However, the term deformation modulus is preferred by some experts in rock mechanics to imply a certain humility about the accuracy of this value. Although deformation moduli are used interchangeably in equations of elastic mechanics with Young's moduli, they are at best a convenient fiction. The actual deformational behavior of a rock mass is controlled by a complex interaction of continuous and discontinuous deformation within intact rock and across joints, bedding planes, faults, and other discontinuities. The deformation modulus is an approximation of the deformation behavior of the rock mass when it is treated as a continuous elastic solid. The avoidance of the term Young's modulus implies that the value being used is not truly a fundamental property of the material, but a convenient continuum elastic approximation.

When choosing a rock mass deformation modulus correlation, bear in mind the advice of Zhang (2017):

> Different empirical relations often give very different deformation modulus values even for rock masses at the same site...it is important that the estimation of rock mass deformation modulus should not rely only on a single empirical relation. Instead, various empirical relations should be used to get an idea on the possible range of the rock mass deformation modulus. Zhang (2017)

2.4.2 Poisson's Ratio

In laboratory triaxial testing of intact and jointed granite samples, Alejano et al. (2017) found that at high confining stresses ($>$ 10 MPa) the Poisson's ratio of the

specimens converged to a range of 0.1 to 0.2, regardless of jointing. This suggests that at high confining pressures the intact Poisson's ratio can be used in place of a rock mass Poisson's ratio. However, the area where the Poisson's ratio is of most importance is in evaluation of the tunnel wall deformation, an inherently unconfined condition. Alejano et al. (2017) clearly showed that the Poisson's ratio of the jointed specimens was significantly higher than the Poisson's ratio of the intact specimens for the unconfined condition.

Zhang (2017) states that although "the presence of discontinuities also influences the Poisson's ratio of rock masses...there seems to be no...correlation between the rock mass Poisson's ratio and the intact rock Poisson's ratio" citing Gercek (2007). Zhang (2017) suggests treating the rock mass as a continuum (where appropriate) and using the methodology of Kulhawy (1978), Fossum (1985), or Zhang (2010) to estimate the rock mass Poisson's ratio from the estimated deformation modulus and shear modulus of the rock mass.

Gercek (2007) provides an excellent summary of work on Poisson's ratios for rocks and rock masses. They also suggests some values for intact Poisson's ratio for several broad classes of rock.

> As it has also been shown in some studies...the rock mass deformation modulus (E_m) can be empirically correlated to the intact rock modulus (E_i). Unfortunately, there seems to be no such correlation between the values of Poisson's ratio for rock mass (ν_m) and intact rock (ν_i). Yet, theoretically, the intact rock (i.e., matrix) value constitutes a limit for the values that may be assumed by the jointed rock mass.

Logo and Vásárhelyi (2020), Vásárhelyi (2009), and Vásárhelyi and Kovács (2017) have explored the relationship of Poisson's ratio to various properties and offered two correlations. In addition, Logo and Vásárhelyi (2020) explicitly state that Poisson's ratio should be positively correlated with confining stress. Logo and Vásárhelyi (2020) also demonstrated that GSI is positively correlated with Poisson's ratio *under confined conditions* but not necessarily under unconfined conditions.

$$\nu_m = \nu_i + 0.2 - 0.002 \cdot GSI \tag{2.26}$$

$$\nu_m = 0.457 - 0.003 \cdot m_i - 0.002 \cdot GSI \tag{2.27}$$

where ν_m is the rock mass Poisson's ratio, ν_i is the intact rock Poisson's ratio, m_i is the Hoek-Brown slope parameter, and GSI is the geological strength index.

2.4.3 Deformation and Squeezing

Although the issue of tunnel deformation is a critical one for tunnel design, few authors have offered a correlation between rock mass classification and expected deformation. Looking at data from the EJMT, Monsees (1970) stated that they lacked deformation data of sufficient quality to evaluate a correlation between rock mass class and deformation.

Singh et al. (1992), Goel (1994), Goel et al. (1995), Goel et al. (1996), and Singh and Goel (2011) suggest a semi-empirical system for squeezing ground based on estimated percent closure, thereby implying a deformation for a given tunnel diameter. Their squeeze criterion is based on overburden depth, tunnel width, and rock mass number (equivalent to Q without the SRF).

Singh et al. (1992) suggested that squeezing be estimated via Equation 2.14. This correlation estimates the depth of overburden which will cause squeezing as a function of Q. However, the Singh et al. (1992) correlation is based upon Q, which requires SRF, which is based in part on estimating the squeezing behavior of the rock mass. This presents a recursion problem, i.e., it is necessary to estimate squeezing potential to estimate Q to estimate squeezing potential. Singh and Goel (2011) provided some clarification on this issue, suggesting that Q in this equation could be calculated with an assumed SRF of 2.5.

$$H_{squeeze} = 350 \cdot Q^{\frac{1}{3}} \qquad \text{(restatement of 2.14)}$$

More recently, Arora et al. (2020) suggested a different squeezing criterion for clay-rich rocks based on the stress history and normalized soil engineering properties (SHANSEP) concept for clay soils (Ladd and Foott 1974) based on previous work by Gutierrez et al. (1996) and Gutierrez and Xia (2009). The Arora et al. (2020) squeezing criterion is shown below.

$$S = \frac{\sigma'_v}{\sigma_{critical}} \tag{2.28}$$

$$\sigma_{critical} = \sigma'_y \cdot \left(\frac{F(n)}{aN} \right)^{1/b} \tag{2.29}$$

$$\sigma'_y = 5.4 \cdot UCS^{0.73} \text{ effective stress at which yield observed} \tag{2.30}$$

$$N = \frac{\sigma_v}{S_u} \tag{2.31}$$

$$F(n) = \frac{\gamma}{\gamma'} = \frac{\sigma_v}{\sigma'_v} = \frac{G_s(1-n)+n}{(G_s-1)(1-n)} \tag{2.32}$$

$$\frac{S_u}{\sigma'_v} = a \cdot OCR^b \tag{2.33}$$

$$a = 0.37$$

$$b = 0.87$$

$$OCR = \frac{\sigma'_y}{\sigma'_v} \tag{2.34}$$

By substitution of Equation 2.30, Equation 2.31, and Equation 2.32 into Equation 2.29:

$$\sigma_{critical} = 5.4 \cdot UCS^{0.73} \cdot \left(a \cdot \frac{S_u}{\sigma'_v} \right)^{1/b} \tag{2.35}$$

By substitution of Equation 2.33 into Equation 2.35:

$$\sigma_{critical} = 0.55 \cdot OCR \cdot UCS^{0.73} \tag{2.36}$$

By substitution of Equation 2.34 into Equation 2.36:

$$\sigma_{critical} = 0.55 \cdot \frac{\sigma'_y}{\sigma'_v} \cdot UCS^{0.73} \tag{2.37}$$

Once again substituting Equation 2.30 into Equation 2.37:

$$\sigma_{critical} = \frac{2.97 \cdot UCS^{1.46}}{\sigma'_v} \tag{2.38}$$

Substituting Equation 2.38 into Equation 2.28:

$$S = \frac{\sigma'^2_v}{2.97 \cdot UCS^{1.46}} \tag{2.39}$$

Setting $S = 1$, i.e., at the boundary of stability, and then rearranging and simplifying Equation 2.39:

$$\sigma'_v = 1.72 \cdot UCS^{0.73} \tag{2.40}$$

where $\sigma_{critical}$ is the critical stress at the point of interest beyond which squeezing is likely to occur, $F(n)$ is the ratio of total and effective unit weights or stresses at the point of interest, a is the empirical coefficient parameter of the $\log(S_u/\sigma'_v) - \log(OCR)$ linear relationship, b is the empirical exponent parameter of the $\log\left(\frac{S_u}{\sigma'_v}\right) - \log(OCR)$ linear relationship, γ is the total unit weight of the overburden, γ' is the effective (typically buoyant) unit weight of overburden, σ_v is the total overburden stress, σ'_v is the effective overburden stress, G_s is the specific gravity of soil solids, N is Peck's stability number, n is the poros-

ity of overburden, OCR is the overconsolidation ratio or apparent overconsolidation ratio, and UCS is the unconfined compressive strength of the intact rock.

Note that the above equations are based on the assumption that the vertical effective stress is the major principal stress. If the horizontal stress is greater than the vertical stress, the horizontal stress should be used in place of vertical stress.

Equation 2.40 essentially closes the loop to the underlying study by Gutierrez and Xia (2009) which set a stability criterion as a power-function relationship between UCS and effective vertical stress. Gutierrez and Xia (2009) had a coefficient of 1.05 and an exponent of 0.73 for their stability criterion, while Arora et al. (2020) implies values of 1.72 and 0.73. Gutierrez and Xia (2009) were calibrating their criterion to data by Bhasin (1991) focused on Himalayan clayshales. Arora et al. (2020) calibrated their criterion against data from the Stillwater Tunnel in Utah, USA; John Street Pumping Station in Toronto, Canada; Laodongshan Tunnel in China; and Uluabat Project in Turkey. These projects were tunneled through thinly bedded to laminar shale interspersed with sandstone and siltstone; thinly bedded shale interpersed with mudstones, silstones, sandstones, and limestones; mudstone; and fine-grained metasedimentary geologies, respectively.

When compared to the identified squeeze zones in the EJMT, the Gutierrez and Xia (2009) stability criterion has an approximately 66% accuracy. The Arora et al. (2020) equation improves this accuracy to approximately 75%. Recalibrating the coefficient and exponent of Equation 2.40 based on the current data from the EJMT it is possible to achieve an accuracy of 95% using Equation 2.41.

$$\sigma_v' = 9.63 \cdot UCS^{0.5} \tag{2.41}$$

All three criteria are shown in Figure 2.4 along with the data from the EJMT binned by UCS and major principal stress with squeeze zones identified by color. One possible explanation for the differences in the calibrated coefficients of the Gutierrez and Xia (2009), Arora et al. (2020), and Equation 2.41 criteria could be the degree of metamorphism of the geology being studied. Although the current study is far from conclusive, the three lines do appear to be moving left and becoming shallower in Figure 2.4 as the degree of metamorphism increases.

2.4.4 Stand-up Time

Terzaghi (1946) discussed the idea of stand-up time, though Terzaghi called it the "bridge-action period", implying that the increase in load on a tunnel with time is caused by the breakdown of arching action above the tunnel. Later, in the tunnelman's ground

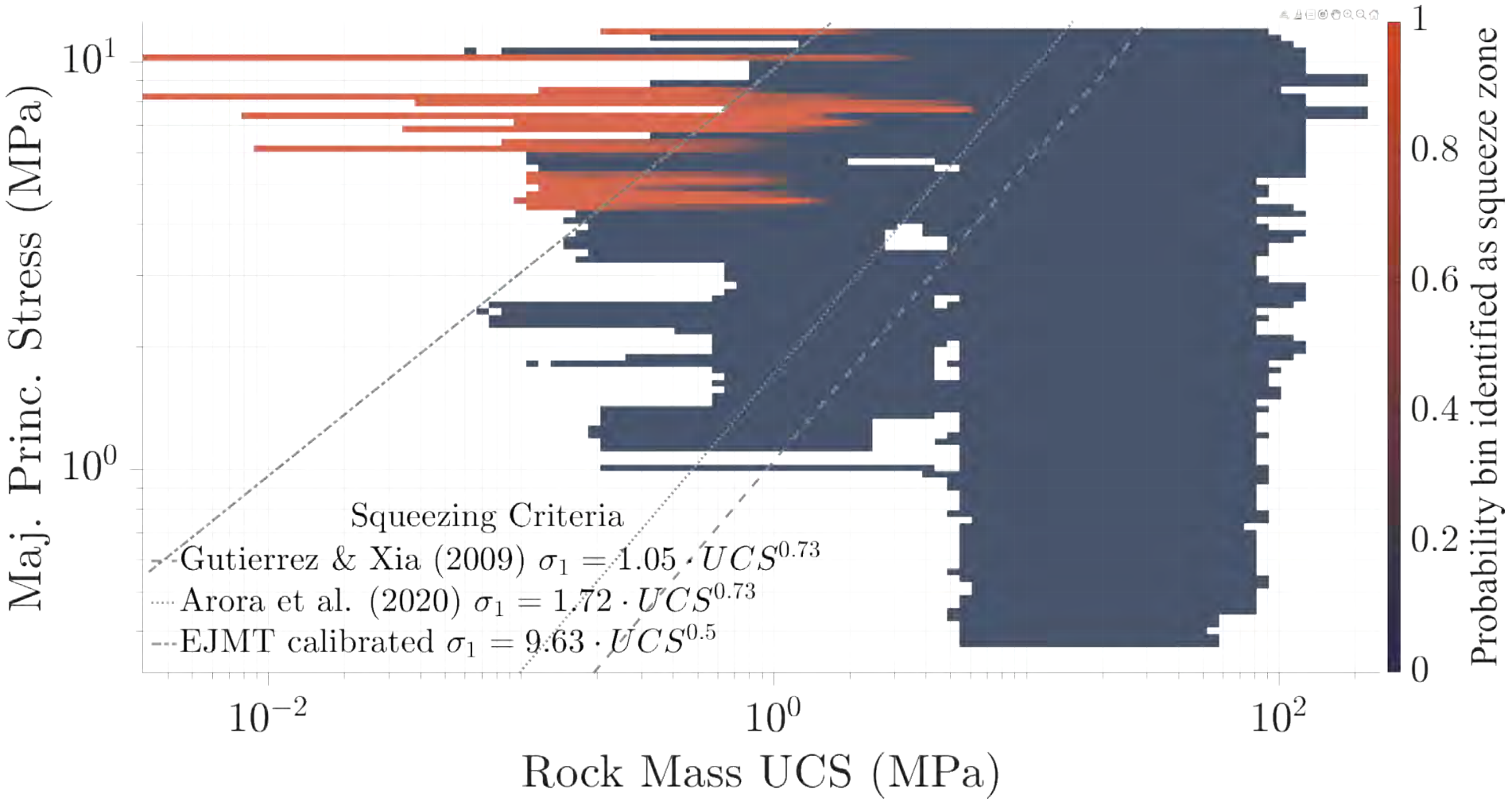

Figure 2.4: Equations from Gutierrez and Xia (2009), Arora et al. (2020), and this study which are proposed as the dividing line between squeezing and non-squeezing behavior for clay-rich sedimentary and metasedimentary rocks. Data points from the EJMT pilot and Eisenhower bores have been binned by UCS and major principal stress with the percent of identified squeeze zones in each bin identified by color.

classification system, Terzaghi (1950) started using the term "stand-up time". Terzaghi also provided six principal categories of soft-ground: firm, raveling, running, flowing, squeezing, and swelling. Terzaghi did not give a way of estimating the stand-up time quantitatively but provided broad ranges of common values for different soil textures and groundwater conditions.

The New Austrian Tunneling Method (NATM) is fundamentally based on the idea of standup time and ground reaction curves. However, NATM is implemented in practice based primarily on experience and professional opinion, rather than theoretical or empirical correlations. Lauffer (1958) was the first to quantify the relationship between stand-up time, tunnel span, and rock mass classification. Later, Bieniawski (1973) presented a figure relating unsupported span, RMR, and standup time based on Lauffer's work, reproduced here in Figure 2.5. Bieniawski (1989) updated that figure based on the work of Unal (1983). Barton joined Bieniawski in a 2008 article that recreated Bieniawski's 1989 figure and added estimated Q values, as well (Barton and Bieniawski 2008). Note that the Bieniawski (1989) database on which RMR_{89} is based is composed of 63% sedimentary rocks, 28% shale, and 29% coal mines. Also, Bieniawski's database is dominated by shallower tunnels, in general (Suorineni 2014a,b).

In order to implement a correlation between RMR and stand up time in a MC simulation, it is necessary to have a vectorizable function which can be repeatedly calculated efficiently by a computer. Therefore, the Bieniawski (1989) database of projects was digitized and a new multi-linear regression equation was fit to the data. For data with recorded stand up time, there are 123 entries. The database entries for coal mines were filtered out as being relatively dissimilar to the case of igneous and metamorphic hard rock civil infrastructure tunneling, leaving 63 remaining entries. These entries still contain numerous sedimentary cases, but a greater proportion of igneous and metamorphic cases and a greater focus on civil tunnel works. These 63 cases have a depth range from 8 to 897 meters, an RMR range from 9 to 91, a span range from 1 to 25 meters, and recorded stand-up times ranging from immediate collapse to 403,000 hours (approximately 46 years). Multi-linear regression to these 63 filtered data points provides the model calculated below with an r^2–value of 0.681. This function has been implemented by the author in MatLab and is visualized in Figure 2.6. Note that this function shows a much stronger correlation to RMR than to excavation span.

$$\log_{10} T = 0.02908 \cdot D + 0.06506 \cdot RMR - 1.441 \tag{2.42}$$

where T is the stand-up time in hours, RMR is the rock mass rating, and D is the

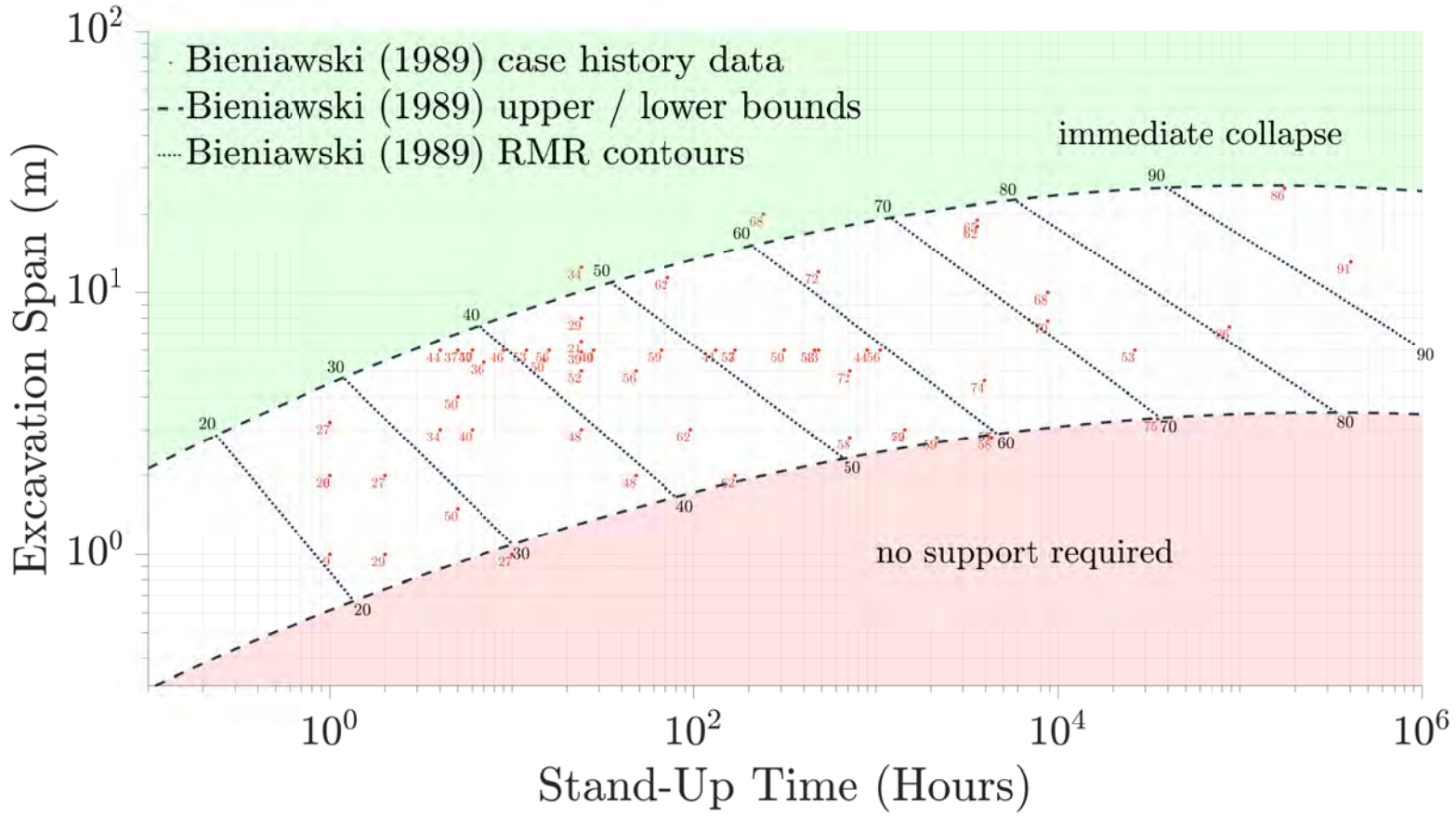

Figure 2.5: Correlation between excavation span, stand up time, and RMR as proposed by Bieniawski (1989). The numbers next to the data points indicate the RMR value recorded for that data point.

unsupported excavation span (m).

Note that this function does not contain the boundaries of "immediate collapse" and "no support required" suggested by Bieniawski (1989) and the data are very sparse over some ranges of RMR, span, and depth. It is left up to the engineer to judge appropriate ranges of applicability and cut-off points for this function. The surfaces in Figure 2.6 have been trimmed so that the 98% confidence intervals do not exceed a range of 1.5 log cycles which this author considers a reasonable starting point but not an engineering recommendation.

2.4.5 Advance Rate

The rate at which a tunnel excavation can be expected to advance has a strong impact on the cost and feasibility of a project. Many researchers have attempted to find correlations between rock mass classifications and tunnel advance rates, dating back to at least the 1970s (Ozdemir et al. 1977; Tarkoy 1979; Tarkoy and Hendron 1975). Nelson (1993) and Nelson et al. (1994) created a database of 630 projects and employed statistical analyses to simulate construction performance of TBMs. Researchers at TU Delft used Nelson's database and a combination of fuzzy logic and artificial neural networks to develop correlation parameters between ground conditions and TBM performance (Alvarez Grima et al. 2000).

Norwegian University of Science and Technology (NTNU) has developed a rigorous statistical model of the expected time and costs of drill-and-blast tunnel advance based on an extensive database of projects, primarily in Norway (Bruland 1998; Dahl et al. 2010, 2012; Zare and Bruland 2007, 2013; Zare and Bruland 2006). This method is commonly referred to as the NTH method, after the old name of NTNU. Unfortunately, this model does not include any simple correlations to rock mass classifications but requires a full model of the construction cycle.

In hard-rock TBM tunneling the penetration rate (PR) is the rate of tunnel advance while the TBM is actually in operation. The advance rate (AR) is the overall average rate of advance (per hour, per shift, per day, etc.) including downtime for maintenance and downtime during the construction cycle (e.g., regripping). The relationship between these two values (Equation 2.43) is the utilization rate, U, typically reported as percent utilization.

$$AR = U \cdot PR \tag{2.43}$$

In drill-and-blast tunneling or other forms of mechanical excavation other than TBM tunneling, the difference between AR and PR is not so clear. Advance rate is still measured,

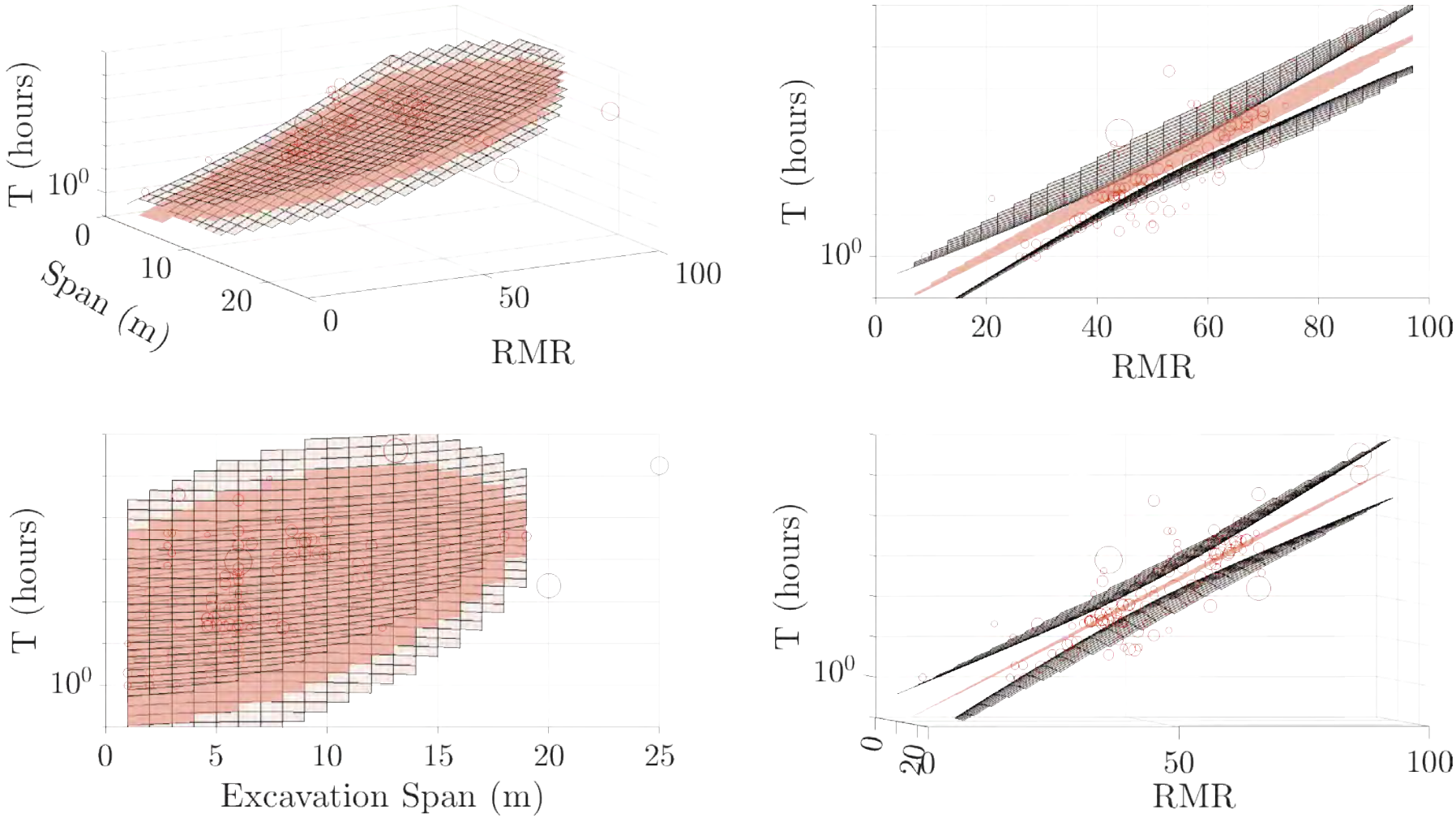

Figure 2.6: Correlation between excavation span, RMR and stand up time based on multi-linear regression to the database of Bieniawski (1989). Circles indicate data points, size indicates the depth of the data point. The multi-linear regression surface has been trimmed to only show the area where the distance between the 98% confidence intervals is less than 1.5 log cycles.

but the cyclical nature of the tunnel construction operation (e.g., drill, blast, vent, muck, support, repeat) means that PR is not really a relevant metric. Advance per round blasted is sometimes considered an equivalent metric. One way that utilization rate might be relevant is in measurement of time spent performing the actual primary operations of the construction cycle versus downtown spent repairing equipment, dealing with safety problems (e.g., disposing of an unexploded dud charge), or otherwise not directly advancing the primary construction operation.

The Colorado School of Mines (Mines) method, sometimes called the CSM method, was based on early work by Ozdemir et al. (1977) and first formally presented by Rostami and Ozdemir (1993). It has since been updated and refined several times (Hamidi et al. 2010; Ramezanzadeh et al. 2008; Rostami 2016; Rostami et al. 1994; Yagiz et al. 2012). Buchi (1984) suggested some improvements to the CSM method including a correction factor for anisotropic or schistose rock that varies from 1.0 to 1.33 and a correction for fractured rock masses that varies between 1.0 and 2.0. Rostami et al. (1996) also found that the Mines method achieves comparable results to the NTH method developed by the Norwegian University of Science and Technology.

Barton (2000) suggests that U can be estimated by Equation 2.44 where T is units of working hours per day and m is a decay coefficient.

$$U = T^m \tag{2.44}$$

Barton (2000) suggests that $m = -0.2$ is a typical mean estimate for TBM performance. Assuming that it is possible for the construction to proceed 24 hour days, 7 days a week the mean utilization rate of this correlation is 53%. Barton further suggests that optimizing TBM design might lead to decay coefficients of -0.15 to -0.17, while poor TBM design (or the use of an innapropriate TBM design) will lead to decay coefficients of -0.22 to -0.25. In extreme cases, temporary conditions of m from -0.7 to -0.9 are possible. Of course, a fully stuck TBM has an instantaneous utilization rate of zero.

Barton (2000) also suggests that PR and AR can estimated as by Equations 2.45 and 2.46.

$$PR = 5 \cdot Q_{tbm}^{-\frac{2}{9}} \tag{2.45}$$

$$AR = 5 \cdot Q_{tbm}^{-\frac{2}{9}} \cdot T^m \tag{2.46}$$

The Barton (2000) Q_{tbm} parameter has been heavily criticized by Sapigni et al. (2002), Bi-

Table 2.2: Grimstad's Q-advance rate correlation for drill-and-blast tunnels.

Q	AR per Round	Cycle Time	AR $\frac{meters}{hour}$	AR $\frac{meters}{100\ hours}$
0.001	1	30	0.03	3
0.01	2.25	23	0.095	9.5
0.1	3.25	13	0.25	25
1	4.5	9	0.55	55
10	5	5	1	100
100	5	4	1.2	120

eniawski et al. (2006), Palmstrom and Broch (2006), and Blindheim (2007). In particular, the Barton 2000 Q_{tbm} correlation to advance rate appears to provide, at best, an upper bound of achievable advance rates, rather than a strong correlation to typical advance rates (Sapigni et al. 2002). Several authors have strongly recommended not using Q_{tbm} as a method for estimating advance rates, as it does not appear to have a strong correlation to advance rate, and simply correlating to Q may actually be better in some cases.

Barton (2000), Grimstad (1981), and Grimstad and Barton (1993) provide a correlation between Q and the advance rate of drill-and-blast tunnels as a piecewise linear function, reproduced here as Table 2.2.

Sapigni et al. (2002) suggest that advance rates for TBMs follow a quadratic or Gaussian curve with the best advance rates occurring in moderately good rocks with RMR values in the range of 50 to 60. Weaker rocks present support difficulties while harder rocks present excavation difficulties. Sapigni et al. (2002) showed this central peak to be especially strong in the Varzo gneiss that they analyzed, and that their quadratic RMR correlation to PR was statistically significant but still imperfect. They found some improvement in the relationship by incorporating data on Mohs' hardness of the rocks, but Mohs' hardness is a somewhat problematic value to use because of its qualitative and non-linear scale. Sapigni et al. (2002) also noted that maintaining constant thrust of the TBM against the excavation face seems to be a significant problem leading to scatter in TBM PR and AR measurements. It should also be noted that the Sapigni et al. (2002) observation on TBM advance rates as a function of rock mass classification would not be expected to translate to drill-and-blast construction.

Innaurato et al. (1991, 1988) proposed a correlation between TBM penetration rate and rock structure rating (RSR) (Wickham and Tiedemann 1972, 1974) as shown in

Equation 2.47.

$$PR = 40.41 \cdot UCS^{-0.44} + 0.047 \cdot RSR + 3.15 \tag{2.47}$$

where PR is in millimeters per rotation and UCS is in MPa. Note the difference in units for PR: penetration rate is sometimes defined as length per time and sometimes defined as length per cutter head rotation, depending on the context.

Note that Bieniawski (1989) provides a correlation between RMR and RSR per Equation 2.48.

$$RSR = 0.77 \cdot RMR + 12.4 \tag{2.48}$$

Substituting Equation 2.48 into Equation 2.47 gives Equation 2.49 relating RMR to PR for a TBM.

$$PR = 40.41 \cdot UCS^{-0.44} + 0.06104 \cdot RMR - 12.95 \tag{2.49}$$

Bieniawski et al. (2006) developed the rock mass excavatability (RME) method of estimating tunnel advance rate (Bieniawski et al. 2011, 2007, 2008; Bieniawski and Galera 2007; Bieniawski and Grandori 2007; Bieniawski et al. 2006). This methodology provides a straightforward method for estimating the AR as a function of RME, which is a similar parameter to RMR, with a few important differences. The input parameters to RME are the UCS of the intact rock; the drilling rate index (DRI); the frequency, homogeneity, and orientation of joints in the advancing tunnel face; the estimated stand up time based on RMR; and the estimated groundwater flow in liters per minute. The table detailing the scoring based on the various parameters as presented by Bieniawski et al. (2007), Bieniawski and Galera (2007), Bieniawski and Grandori (2007), and Bieniawski et al. (2006) is reproduced here as Table 2.4. The simplest correlation between RME and estimated advance rate is given by Equation 2.50a. Bieniawski et al. (2008) also provide some recommendations for the most appropriate TBM type based on RME and intact UCS. These recommendations are reproduced here in Table 2.3.

$$AR = 0.213 \cdot RME \qquad for RME < 75 \tag{2.50a}$$

$$AR = 0.56 \cdot RME - 26 \qquad for RME > 75 \tag{2.50b}$$

$AR =$ advance rate, meters per day

$RME =$ rock mass excavatability

Table 2.3: Bieniawski et al. (2008) recommendations for applicability of TBM-excavation as a function of RME and intact UCS.

$RME < 45$	$UCS < 45$ MPa		45 MPa $< UCS$	
	$45 < RME < 77$	$77 < RME$	$45 < RME < 75$	$75 < RME$
TBM not advised	double shield	single shield	double shield	open or main beam

Table 2.4: Table for estimating RME parameters after Bieniawski and Galera (2007).

Uniaxial Compressive Strength of Intact Rock (0 to 25 points)					
σ_c (MPa)	$\leq$5	5 to 30	30 to 90	90 to 180	$\geq$180
Rating	4	14	25	14	0

Drillability					
DRI	$\geq$80	80 to 65	65 to 50	50 to 40	$\leq$40
Rating	15	10	7	3	0

Stand-up Time (0 to 25 points)					
Hours	$\leq$5	5 to 24	24 to 96	96 to 192	$\geq$192
Rating	0	2	10	15	25

Groundwater Inflow (0 to 5 points)					
Liters/sec	$\geq$100	70 to 100	30 to 70	10 to 30	$\leq$10
Rating	0	1	2	4	5

Discontinuities in front of the tunnel face (0 to 30 points)										
Homogeneity			Number of Joints per Meter					Orientation w.r.t. tunnel axis		
Homogeneous		Mixed	0-4	4-8	8-15	15-30	>30	Perpendicular	Oblique	Parallel
Rating	10	0	2	7	15	10	0	5	3	0

2.4.6 Direct Estimation of Support Requirements by RMR

Several of the rock mass classification systems have been correlated directly to estimated design of supports, beginning as early as the Terzaghi (1946) qualitative descriptions of rock mass correlating to supports, continuing with the Deere et al. (1969) RQD-based recommendations of tunnel support systems, and branching out into a variety of modern systems. In some cases, individual projects (especially large mines) develop their own internal system based on some underlying system calibrated to that particular project's history. The most popular methods of empirical design of underground civil infrastructure in the United States are the RMR and Q-systems. These systems are adopted for the purposes of this report for initial estimation of tunnel support requirements.

Bieniawski (1989) made broad recommendations of required supports with ranges of typical rock bolt patterns, shotcrete thicknesses, and steel set spacings, but no exact preliminary design recommendations. Lowson (2012) and Lowson and Bieniawski (2013) provided an updated set of design recommendations including equations specifically relating RMR to rock bolt spacing (Equation 2.51), rock bolt length (Equation 2.53), achievable rock bolt capacity (Equation 2.54), shotcrete strength reduced for RMR (Equation 2.56), required shotcrete thickness (Equation 2.58), shotcrete arch strength (Equation 2.57), required steel section capacity, and required supplemental shotcrete between steel sections. These recommendations are specifically based on circular excavations, but can be adapted to non-circular excavations with caution. Note that the Lowson (2012) recommendations for steel support design could also be replaced with the Carranza-Torres and Engen (2017) design method using the support pressure recommendation by Lowson and Bieniawski (2013) and achieve a substantially similar result.

$$S_b = \begin{cases} \text{spot bolting only} & for \quad 85 < RMR \leq 100 \\ 0.5 + \dfrac{2.5\,(RMR - 20)}{65} & for \quad 20 < RMR \leq 85 \\ 0.25 + \dfrac{(RMR - 10)^{1.5}}{140} & for \quad 10 < RMR \leq 20 \\ 0.25 & for \quad 0 < RMR \leq 10 \end{cases} \tag{2.51}$$

$$B = \frac{(L_b + 2.5)^{\frac{RMR+25}{52}}}{3.6} \tag{2.52}$$

$$L_b = e^{\frac{52 \ln 3.6W}{RMR + 25}} - 2.5 \tag{2.53}$$

$$F_{bd} = F_b \left(\frac{RMR}{85} \right)^{\frac{40}{RMR}} \tag{2.54}$$

$$P_{bd} = \frac{F_{bd}}{S_b^2} \tag{2.55}$$

$$P_{cd} = P_c \left[0.2 + 0.8 \cdot \left(\frac{RMR}{100} \right)^{1.5} \right] \tag{2.56}$$

$$P_v = \frac{tP_{cd}}{R} \tag{2.57}$$

$$t_{req} = \frac{P_v \cdot R}{P_{cd}} \tag{2.58}$$

where RMR is the rock mass rating, B is the excavation span (m), S_b is the bolt spacing (m), L_b is the embedded bolt length (m), F_b is the ultimate tensile capacity of the rock bolt, F_{bd} is the reduced tensile capacity of the rock bolt, P_{bd} is the achievable rock bolt capacity for a given bolt tensile strength bolt spacing, and RMR, P_c is the nominal strength of the shotcrete, P_{cd} is the design strength of the shotcrete liner, P_v is the vertical overburden stress on the liner, and t_{req} is the required shotcrete thickness for a given vertical overburden stress, shotcrete nominal capacity, and RMR.

Note that Equation 2.53 suggests bolts that are longer than the span for many cases, which may be impractical to install. Most rock bolting guides suggest limiting rock bolts to no more than one-half of the tunnel height (Li 2017; Stillborg 1994). Also, Equation 2.54 suggests that rock bolts become highly inefficient at low RMR values. Specifically, the reduction factor declines below 50% at an RMR of 41 and below 10% at an RMR of 22. These practical limits have been plotted in Figure 2.7. The unbounded rock bolt length recommendations of Lowson and Bieniawski (2013) may be unrealistically conservative, and thus some of the middle grey area of the graph may still be practical for rock bolt support, but as the Lowson and Bieniawski (2013) recommendations stand, only a very small portion of the RMR and span interaction present a practical application of rock bolts.

Figure 2.8 presents the reduced rock bolt strengths divided by the squared rock bolt spacings to achieve a rock bolt pattern strength. The resulting curve is approximately log-normal. Overall, the rock bolt design suggestions of Lowson and Bieniawski (2013) suggest that it may not be practical to use rock bolts at all below an RMR of approximately 15 or conservatively 22, again presenting a relatively narrow range of RMR and span values over which rock bolts are practical.

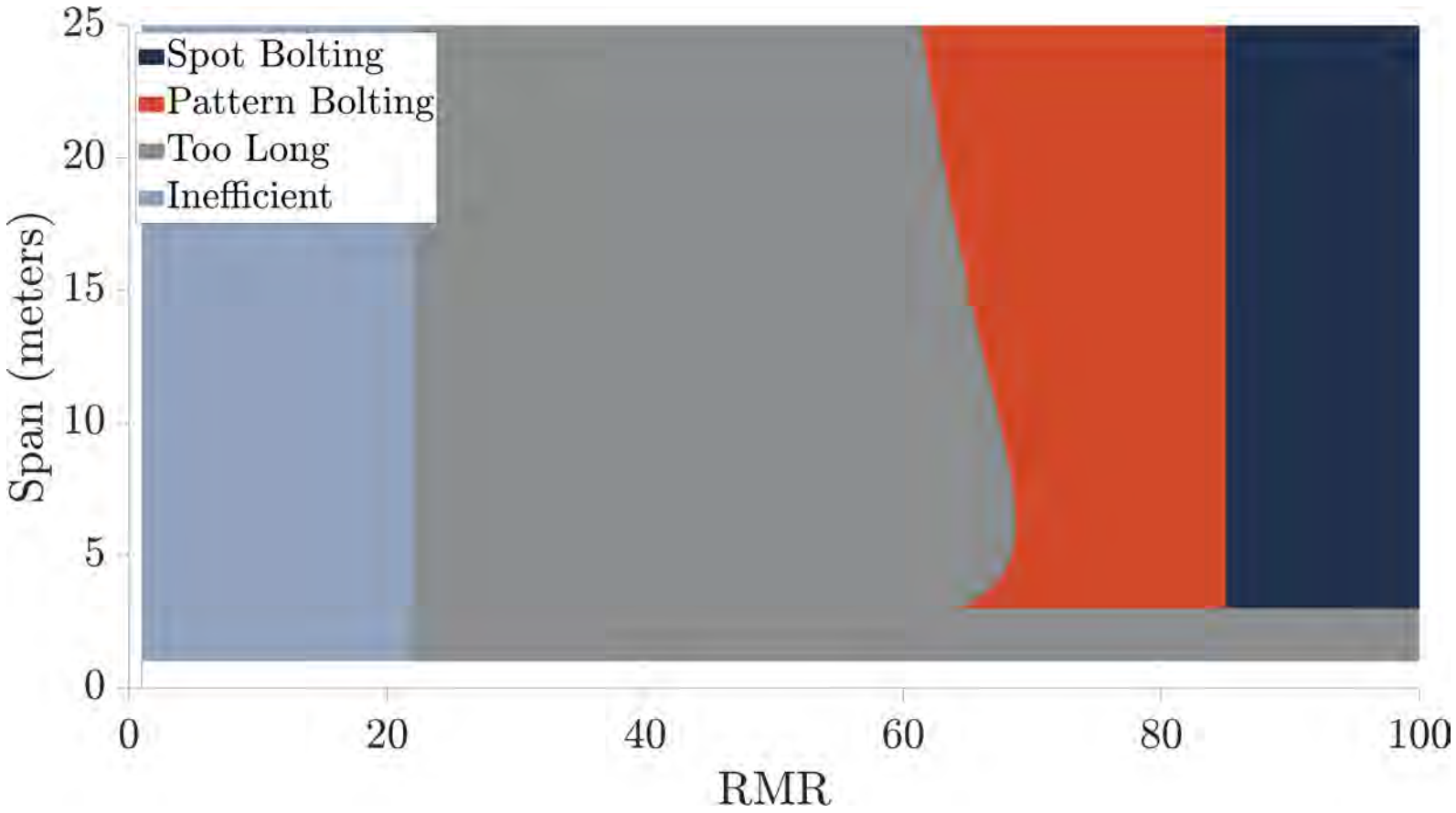

Figure 2.7: Limits of practical applicability of Lowson and Bieniawski (2013) recommendations for rock bolt support.

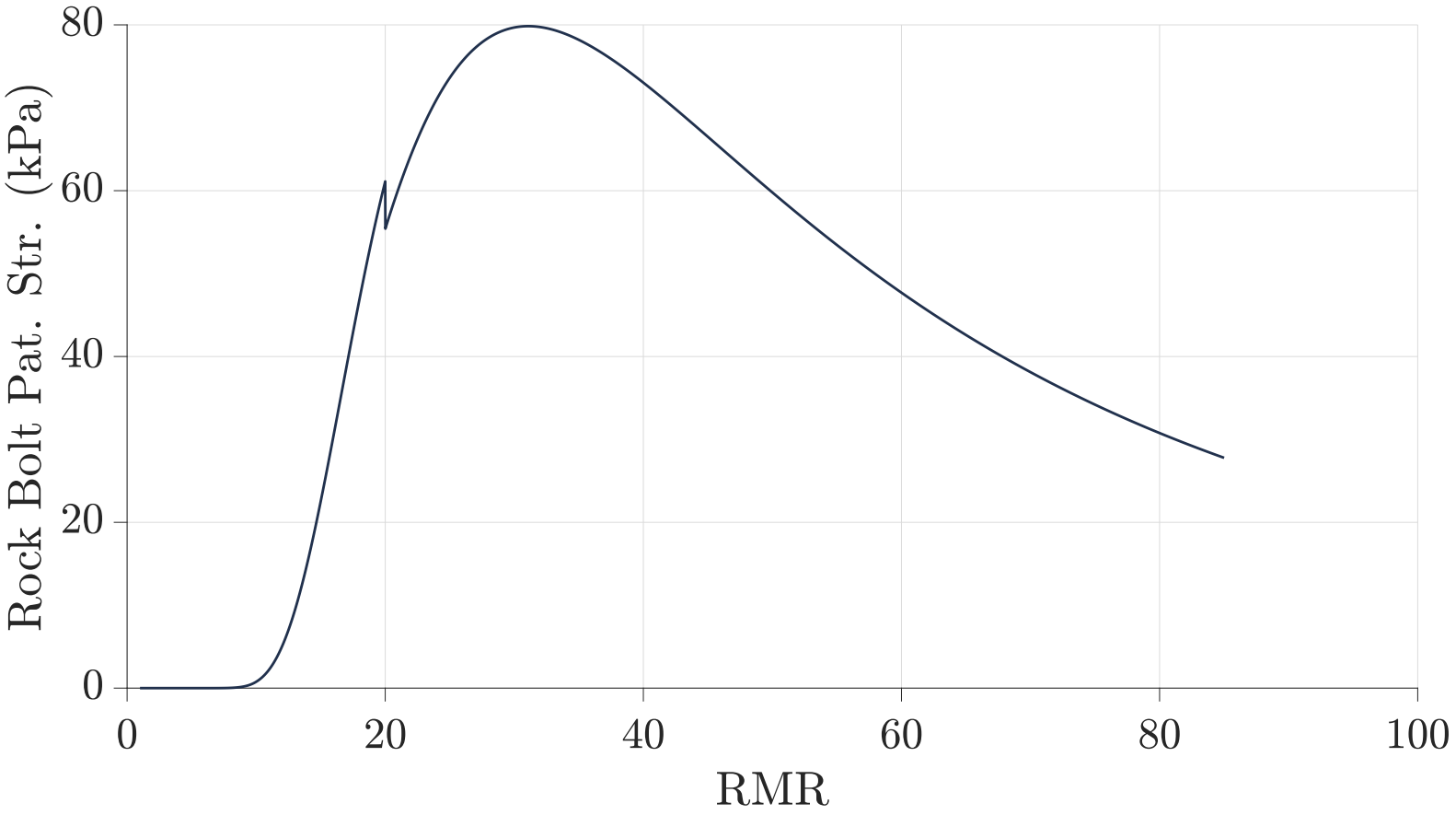

Figure 2.8: Correlation between RMR and rock bolt pattern strength as published by Lowson and Bieniawski (2013) and assuming a 250 kN rock bolt.

Equation 2.58 assumes that the shotcrete acts as an arch in compression, a condition only satisfied for some stress fields and excavation shapes, and that all of the vertical load is carried by the shotcrete. If a composite rock bolt shotcrete system is to be used, the shotcrete thickness would be calculated based on the overburden pressure reduced by the portion of the overburden supported by the rock bolts, Equation 2.59, still assuming that the shotcrete acts as an arch in compression.

$$t_{req} = \frac{(P_v - P_{bd}) \cdot R}{P_{cd}} \tag{2.59}$$

Figure 2.9 presents this interaction between RMR, excavation span, rock bolt strength, and required shotcrete thickness for a shotcrete nominal strength of 30 MPa and a rock bolt nominal tensile capacity of 250 kN. These values lead to a required shotcrete thickness in excess of 1300 millimeters in some locations. This is probably unrealistic for most tunnel applications, where rib supports would be added for most cases where required shotcrete thicknesses exceed 300 mm. Therefore, shotcrete thickness has been limited to 300 mm leading to some cases where the support system is not able to achieve the necessary capacity, shown in Figure 2.10 as unconservative cases. Further, shotcrete thickness has been truncated at a lower bound of 20 millimeters, leading to some cases where the design is conservative compared to overburden pressure. Note that for the purposes of this academic study these calculations have been performed without partial factors, allowable stress factors, load factors, or resistance factors.

2.4.7 Direct Estimation of Support Requirements by Q

Barton et al. (1974) developed the Q-system specifically for the empirical design of tunnel support systems. The Q-system calibration database, originally based largely on a dissertation by Cecil III (1970), has a strong bias towards tunnels in Scandinavia excavated by the drill-and-blast technique and supported by rock bolts and shotcrete. At the lower end of the Q values, the system also recommends steel reinforcement be embedded in the shotcrete for additional support. Since its initial publication in 1974, the Q-system has been revised and updated several times (Grimstad and Barton 1993; Grimstad et al. 2002). The current iteration of the system is the 2015 handbook published by NGI (NGI 2015). The design recommendations are summarized in a single rock support chart, Figure 2.11. Note that this database is not publicly available and, based on personal communications with NGI, there is no readily available systematically digitized database of the data upon which the Q-system is based, presenting a validation problem for the correlations presented.

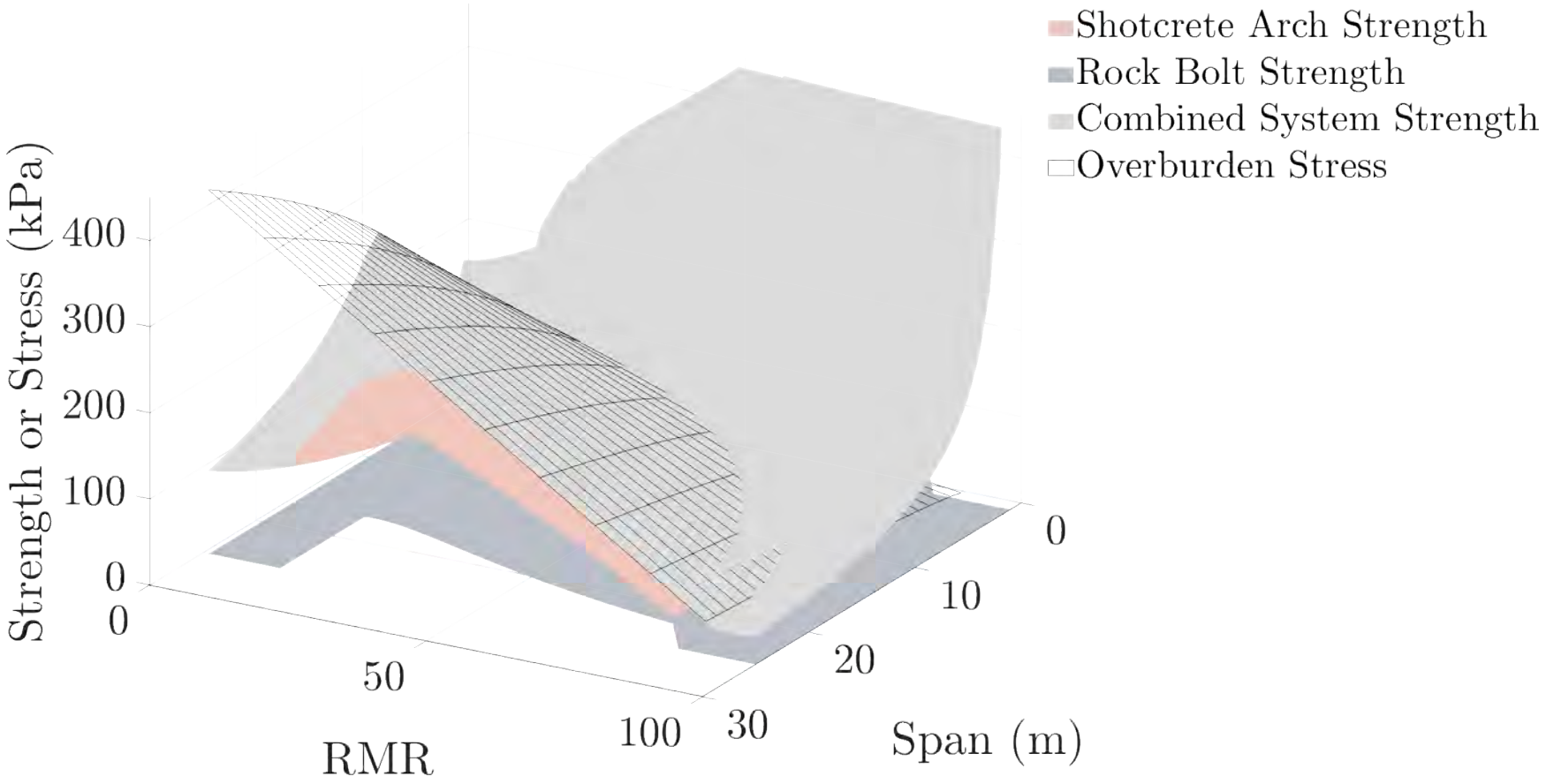

Figure 2.9: Correlation between RMR, excavation span, rock bolt strength, shotcrete strength, and overburden pressure after Lowson and Bieniawski (2013).

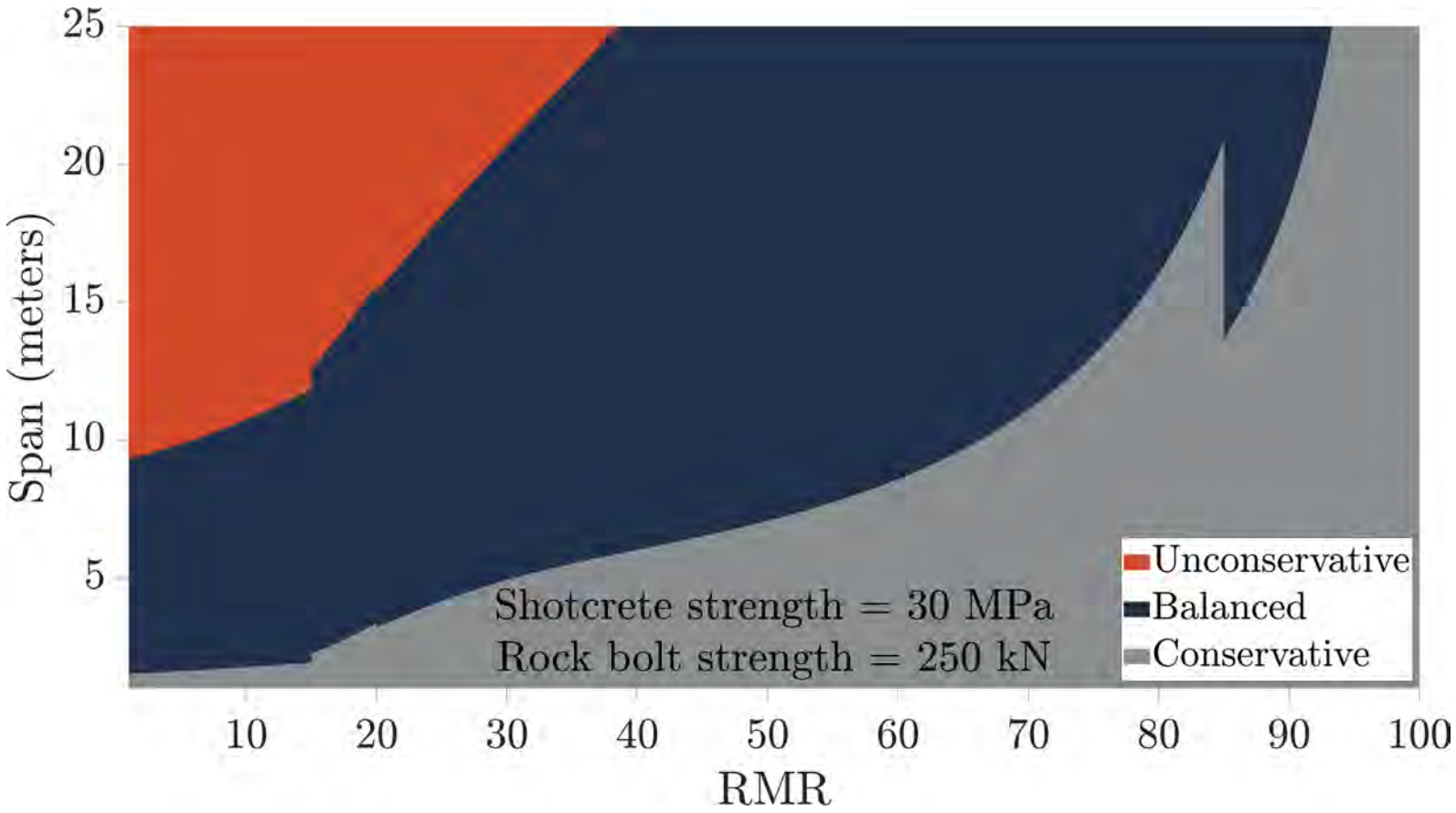

Figure 2.10: Limits of applicability of the RMR based support design for a given shotcrete strength (30 MPa) and rock bolt strength (250 kN) after Lowson and Bieniawski (2013).

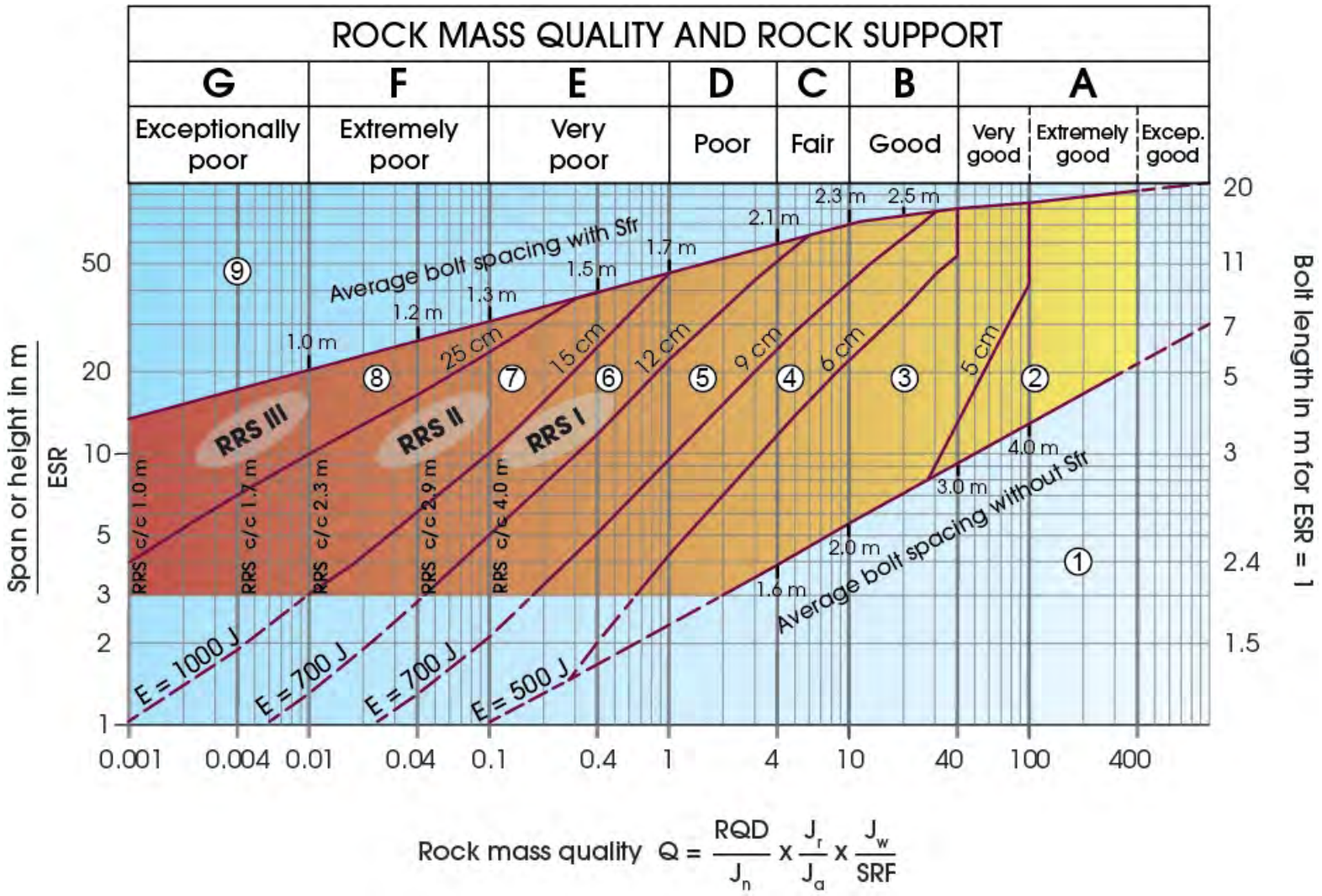

Figure 2.11: Correlation between excavation span, excavation support ratio, Q value, and recommended preliminary design as published by NGI (2015).

The left axis of the Q-system rock support chart is defined as span divided by ESR (similar in concept to a factor of safety or partial factor). The right axis of the chart is defined as the bolt length for an ESR of 1. An ESR of 1 is suggested by NGI (2015) for "power houses, storage rooms, water treatment plants, major road and railway tunnels, civil defense chambers, portals, intersections, etc." In other words, this system has been calibrated to an ESR of 1 for critical infrastructure. An ESR below 1 indicates high-hazard infrastructure, for example, the manual suggests an ESR of 0.5 for "very important caverns and underground openings with a long lifetime, 100 years, or without access for maintenance". The manual suggests an ESR of 0.8 for "underground nuclear power stations, railways stations, sports and public facilities, factories, etc.". In typical American civil engineering practice, it is uncommon to have any facility with a higher factor of safety or lower risk tolerance than a nuclear power station, and areas of public assembly or emergency refuge (such as a railway station or sports arena) would generally be grouped into the next lower category along with critical infastructure. For the purposes of this study, an ESR of 1 is assumed in keeping with the NGI manual's suggestion for "major road and railway tunnels". However, the logic in the categorization and assignment of ESR in this system should be reconsidered from an American risk management perspective before application of the NGI system in the United States.

Figure 2.11 gives estimates of required support directly for given values of excavation span, ESR, and Q. The earliest version of this chart was published by Barton et al. (1974) and it has since been updated and refined several times by Grimstad and Barton (1993), Barton (2002), Grimstad et al. (2002), Grimstad (2007), Barton and Grimstad (2014), and NGI (2015). While these refinements contain increasingly detailed charts and recommendations, none of these papers contains a set of explicit functions for implementing the Q-system empirical design recommendations. The only explicitly defined functions are the self-supprting line (lower bound of the recommendations) and the estimation of bolt lengths. Using this system in a MC analysis requires that support requirements be determined by some vectorizable function. Therefore, the author has approximated the lines of the Q-system chart by a series of functions. Note that as of 2014, there appears to be some disagreement in the correct trajectory of further development of the Q-system. Barton and Grimstad (2014) stated "that an unchecked version of Q with several errors has recently been promoted by NGI despite the present authors' lack of participation or approval. These younger authors were (clearly) not present during original development of Q, nor participated in its case record based update in 1993". As Barton and Grimstad (2014) do not specifically state what errors are present in the current NGI update of the Q-system, present no evidence of these errors, and

Barton has a notable penchant for *ad hominen* arguments in academic publications, this author chooses to ignore Barton's concerns and use the current NGI manual for the Q-system.

Based on Figure 2.11 the following functions defining the support recommendations of the Q-system have been developed. Equation 2.60 defines the lower boundary of support requirements based on Barton et al. (1974). Equation 2.61 defines the required bolt length for a given excavation span independent of Q value after Barton et al. (1974). Note that the NGI (2015) chart gives slightly different bolt length suggestions than those calculated per Equation 2.61. The new recommendations are somewhat more conservative for spans wider than 20 meters but somewhat less conservative for spans less than 20 meters. Given that the scale of typical civil infrastructure is less than 20 meters and that there is no clear explanation for this change this report adopts the original recommendations of Barton et al. (1974), i.e., Equation 2.61.

Figure 2.12 shows the rock bolt spacing recommendations plotted against Q. Note that these functions appear to be approximately linear in log-log space, suggesting a power function as an appropriate functional form for these correlations. Equation 2.62 and Equation 2.63 were regressed to the NGI (2015) recommendations.

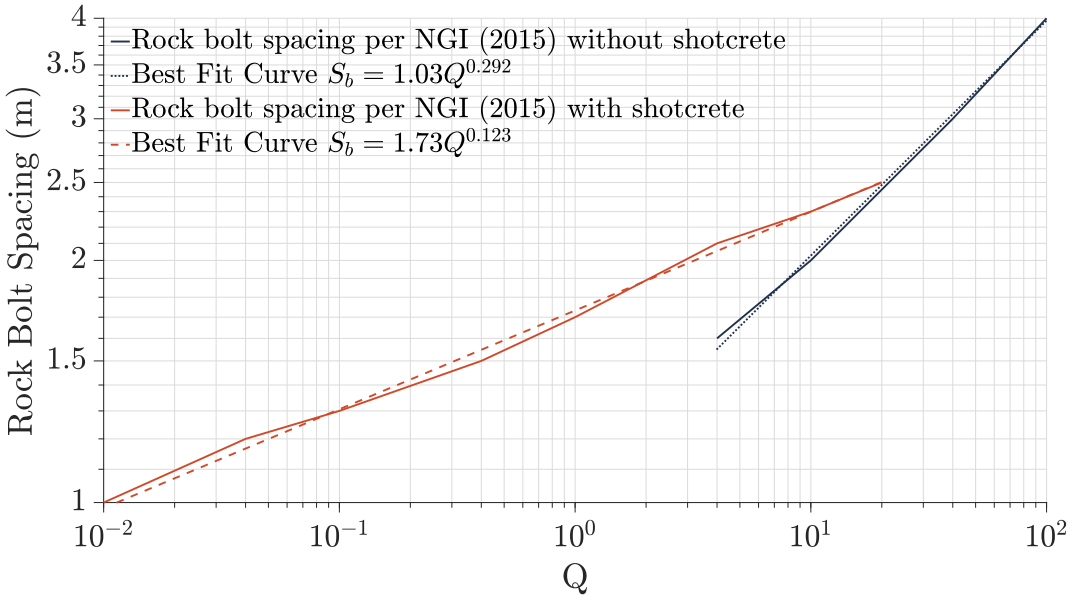

Figure 2.12: Correlation between Q value and recommended preliminary design spacing of rock bolts as digitized for this report after NGI (2015).

Equation 2.62 prescribes rock bolt spacing for spot-bolting without shotcrete. Note that the suggested spacing for spot bolting without shotcrete should not be taken as a recommendation of pattern bolting, but rather a rough estimate of the likely required

number of rockbolts. Spot bolting without shotcrete reinforcement must always be based on an individual analysis of the need and best use (including angle, tension, depth, and type) of any particular bolt. Equation 2.62 has an r^2–value of 0.998 when compared to the NGI (2015) recommendations.

Equation 2.63 prescribes spacing for pattern bolting with shotcrete. This is intended to be used as a prescribed regular bolt spacing, though care should still be taken to ensure that each bolt is in the most advantageous position and that any rock wedges in the roof are properly supported. This function has an r^2–value of 0.997 when compared to the NGI (2015) recommendations.

Equation 2.64 prescribes the spacing of steel-reinforced shotcrete ribs. Note that Grimstad (2007) and NGI (2015) give broad recommendations on the reinforcing steel design of the reinforced ribs of sprayed concrete but in practice this design needs to be based on anticipated pressure distribution on the tunnel lining, the reinforcement to be used, and a numerical or analytical (e.g., curved beam theory) model of the support. NGI (2015) suggests using bar reinforcement but another common practice is the use of lattice girders. I-beams are generally not recommended for this application because it can be difficult to thoroughly apply shotcrete around and behind them. This report limits the reinforcement recommendation to the spacing of rib supports on the assumption that a more detailed reinforcement design would occur later in the design process. Figure 2.13 shows the recommended rib support spacings given by NGI (2015) with a best fit exponential function for calculating the rib spacing value. This best fit function has an r^2–value of 1.0 because their are four coefficients of the exponential function and only five fitting points. Note that NGI (2015) suggests that reinforced shotcrete ribs be used up to a Q value of 0.4, while Grimstad (2007) suggests that reinforced shotcrete ribs be used up to a Q value of 1. Beyond that point they are likely inefficient and overly conservative. However, the last recommended rib spacing on the NGI (2015) chart is given as 4 meters at a Q value of 0.1. Extrapolating Equation 2.64 to $Q = 0.4$ gives a rib spacing of nearly 20 meters, likely well beyond the ability of the ground to arch between ribs. It is unclear from NGI (2015) how far this extrapolation was intended to be carried. However, Grimstad (2007) and Barton and Grimstad (2014) explicitly state that the maximum rib spacing should be 4 meters. Therefore, Equation 2.64 is truncated at a spacing of 4 meters and should be neglected for Q greater than 1.

$$W_{unsupported} = \frac{2Q^{0.4}}{ESR} \tag{2.60}$$

$$L_b = 2 + \frac{0.15W}{ESR} \tag{2.61}$$

$$S_b = 1.04Q^{0.292} \quad \text{for spot bolting without shotcrete} \tag{2.62}$$

$$S_b = 1.73Q^{0.123} \quad \text{for pattern bolting with shotcrete} \tag{2.63}$$

$$S_{RRS} = 2.35e^{5.34Q} - 1.70e^{-225Q} \qquad 1 \leq S_{RRS} \leq 4 \;\text{ and }\; Q \leq 1 \tag{2.64}$$

where Q is the rock mass quality index, W is the excavation span (m), ESR is the excavation support ratio, L_b is the bolt length (m), S_b is the spacing of bolts (m), and S_{RRS} is the center-to-center spacing of reinforced shotcrete rib supports (m).

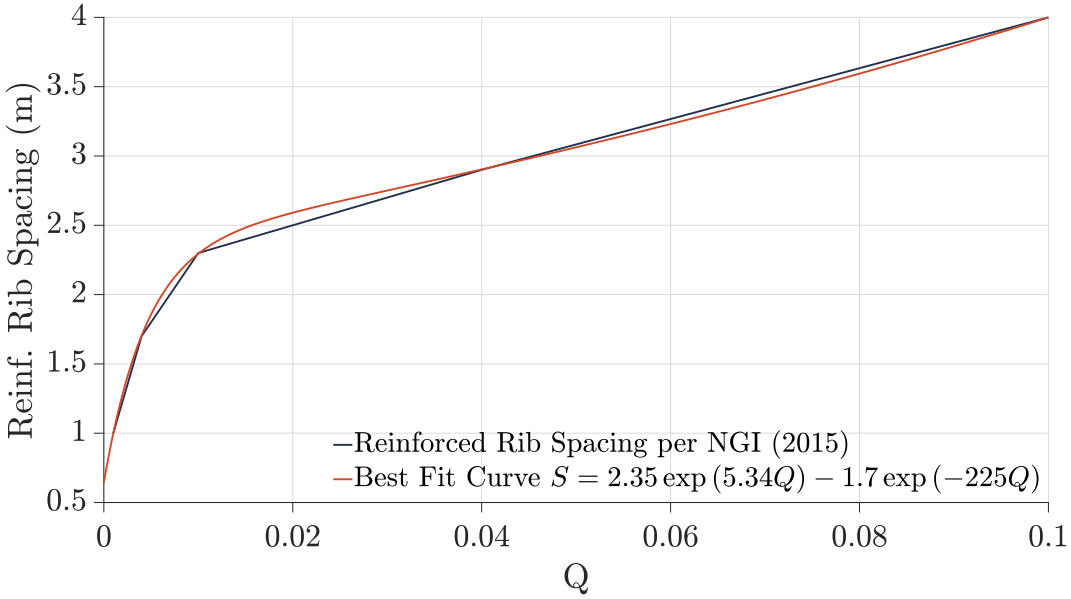

Figure 2.13: Correlation between Q value and recommended preliminary design spacing of reinforced rib supports as digitized for this report after NGI (2015).

The boundaries between support categories two through nine were defined as piecewise power functions based on points read from the NGI (2015) support chart. A power function is a straight line in log-log space, allowing for direct calculation of points along these lines without conversion from linear to log space. The fitting points defining each line are shown in Table 2.5 and Figure 2.14 shows the power functions describing each of the lines on the chart. Note that the boundaries between the support categories are also contours of recommended shotcrete support. This implies that there is a surface which is a function of Q and excavation span which defines the required shotcrete thickness. Rather than attempting to find an explicit function for this surface, the author simply linearly interpolated between the contours given on the NGI (2015) chart (in log-log space) to

develop a convenient table relating Q, excavation span, and shotcrete thickness. This table can then be referenced conveniently within a MC simulation loop to evaluate required support for a given tunnel parameterized by Q and excavation span. Note that although support category 2 does not specifically specify a shotcrete liner be incorporated, for the purposes of this research project the author specified a 25 mm minimum shotcrete liner at the boundary between support categories 1 and 2. This is included here as a matter of good practice and engineering judgement. It is rare that civil infrastructure tunnels open to the public would remain unlined. Even if the shotcrete is not strictly required for support, it will be applied to alleviate public concern. In addition, the litigous American construction environment also lends itself to such conservatism.

Equation 2.60 to Equation 2.64 and Table 2.5 are shown in Figure 2.14 and were implemented in a MatLab code which allows for the rapid estimation of Q-system based support requirements for a given excavation span, ESR, and Q value.

Table 2.5: Table of fitting points defining piecewise boundaries between support categories for the NGI (2015) Q-system support chart.

Support Category Boundary	Fitting Points (Q, W/ESR)		
2 - 3	27, 7.5	100, 40	100, 84
3 - 4	0.3, 1.24	40, 54	40, 78
4 - 5	0.023, 1	0.4, 5	30, 76
5 - 6	0.006, 1	0.02, 6	6, 64
6 - 7	0.001, 1	0.04, 6	1, 46
7 - 8	0.001, 4	0.3, 37.4	–
8 - 9	0.001, 13.5	10, 70	1000, 100

2.5 State of Practice in Tunnel Alignment Selection

There are many parameters which affect the selection of a tunnel alignment. Many of these factors are non-technical, having to do with the need for the tunnel. Many factors are difficult to identify or quantify. Many others are technical but extraneous to the geomechanical and structural concerns of the tunnel designer, such as environmental constraints. Other concerns relate directly to the constructability of the project, such as construction safety and resource availability. All these concerns are critical to the planning and construction of the project.

Table 2.6: Descriptions of recommended supports per NGI (2015) based on the Q-system support chart.

Support Category	Support System
1	unsupported or spot bolting only
2	spot bolting
3	systematic bolting, 50-60 mm fiber reinforced shotcrete
4	systematic bolting, 60-90 mm fiber reinforced shotcrete of 500 joule energy absorption grade
5	systematic bolting, 90-120 mm fiber reinforced shotcrete of 700 joule energy absorption grade
6	systematic bolting, 120-150 mm fiber reinforced shotcrete of 700 joule energy absorption grade, reinforced ribs of sprayed shotcrete with bolts
7	systematic bolting, >150 mm fiber reinforced shotcrete of 1000 joule energy absorption grade, reinforced ribs of sprayed shotcrete with bolts
8	systematic bolting, >150 mm fiber reinforced shotcrete of 1000 joule energy absorption grade, closely spaced reinforced ribs of sprayed shotcrete with bolts, consider cast-in-place reinforced concrete lining
9	special evaluation, may require extensive ground improvement, multi-drift system, or other excavation technique.

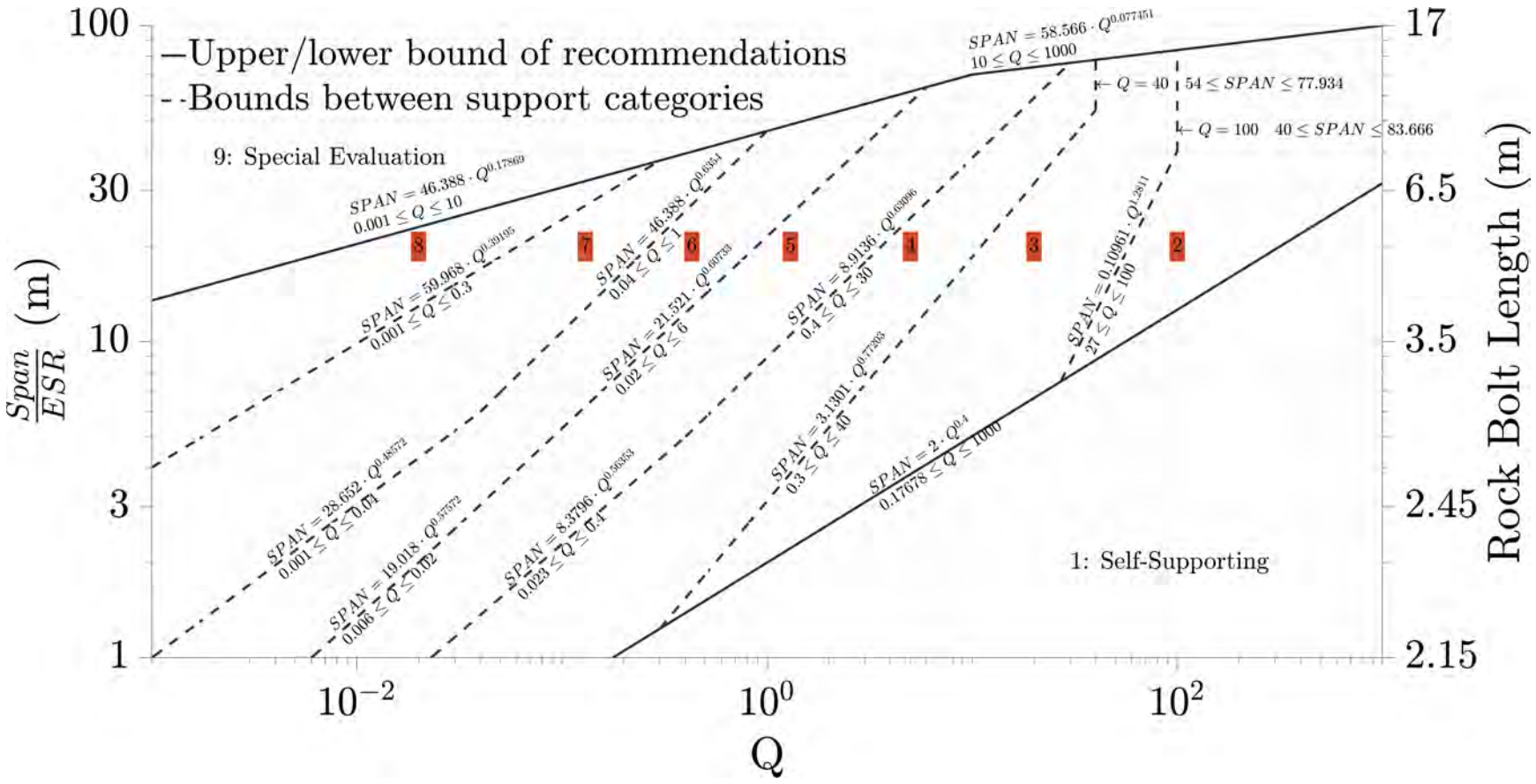

Figure 2.14: Correlation between excavation span, excavation support ratio, Q value, and recommended preliminary design as digitized for this report after NGI (2015).

Probabilistic design of tunnels is currently employed by application of the FORM (Mirzaeian et al. 2015), MC method (Miro et al. 2015; Oreste 2015), or LRFD (AASHTO 2017). Probabilistic techniques have also been applied to methods of discrete block stability (Jakubowski 2011a,b). Probabilistic back-analysis of tunnels has been employed for some projects (Miro et al. 2015; Mirzaeian et al. 2015; Oggeri and Oreste 2012; Oreste 2015). Each of these projects was theoretical, rather than applied to a practical case study.

Several techniques exist for estimating tunneling project costs. Current industry practice is largely based upon the professional experience of the estimator. Academia has developed several methods for more rigorously evaluating costs, but none of these techniques has gained widespread acceptance among contractors, owners, or design engineers.

Early stage cost estimating for tunnel projects has been studied by several researchers (BTS and ICE 2004; Efron and Read 2012; HM Treasury and Infrastructure UK 2010; Infrastructure and Projects Authority 2018; Rostami et al. 2013). Each of these reports relates total tunnel cost to simple geometric tunnel metrics (e.g., length, diameter, volume). Although valuable insights can be gleaned from these regressions, their simplicity neglects significant details about the geology, excavation system, support system, and other factors unique to each project.

Current industry practice is generally based upon the experience of a particular company. Unlike many other areas of construction, where tools and databases such as RS Means (Gordian Group 2019) are widely available and standardized across an industry, the tunneling industry is still largely focused on the experience and opinions of experts in the field. Great uncertainty is associated with cost estimates for tunnel projects, and projects frequently run well over budget.

In the broader construction industry in the United States, a system based on the American Association of Cost Engineering (AACE) and American Society for Testing and Materials (ASTM) is relatively common for many construction cost estimates (ASTM 2011; Christensen et al. 2020; Christensen and Dysert 1997). The AACE method defines cost estimates at levels from 5 (screening or feasibility level) to 1 (check estimate or bid/tender level). For conceptual, preliminary, screening, or feasibility studies of tunneling projects, a class 5 or 4 estimate is appropriate. A class 5 estimate will be based primarily on professional judgement and experience, with some background research performed. A class 4 estimate will be somewhat more detailed and often uses a probabilistic cost model based on previous work performed.

Cost estimates, like many other engineering analyses, can be performed in a deterministic or probabilistic fashion. Deterministic analyses find expected properties for the

necessary inputs and then compute the desired outputs. In a construction cost estimate this means that the project is broken down into its individual components, and the cost of each component is estimated. This estimate can be based upon experience, quotes from contractors, or costs for similar items on other projects. The unit costs are multiplied by quantities for each line item, and the subtotals are summed to find a total estimated cost for the project. These deterministic analyses require fairly detailed plans and specifications for the project considered, can be quite time consuming to produce, and require a high degree of input from experts. In a typical design-bid-build project, deterministic cost estimates are generally developed late in the design of a project by the engineering design team, hence the common term "engineer's estimate". These estimates are an AACE level 2 estimate. Even more detailed estimates are developed by the contractor as a part of the bidding process, with the end result of each contractor's estimate being the bid at an AACE level 2 or 1 with more detail than the engineer's estimate. Finally, an AACE level 1 cost estimate is developed based on final plans issued for construction and firm quotes from subcontractors.

An extension of the deterministic cost model is a probabilistic estimate where uncertainty in each line item is considered individually. If costs for concrete for the project are estimated at $250 per cubic yard, the uncertainty in that number can be expressed as lower- and upper-bounds, standard deviation, coefficient of variation, or some probability density function. By computing the uncertainty in each line item, the uncertainty in the overall cost can be determined. This form of probabilistic estimate requires the development of a deterministic cost estimate, and probabilities for each line item, and thus is at least as costly and time consuming as a deterministic estimate. For that reason, they are rarely performed.

An alternative form of probabilistic estimate is based on the gross properties of the desired tunnel. Generally, a database of previous projects relating tunnel dimensions or other properties to costs is required. A probabilistic study of this database finds the expected value and range of values for a given tunnel based upon some characteristic of the tunnel. For example, the database may show a curve relating tunnel cost per linear foot to tunnel diameter, and curves of a relevant set of confidence intervals (commonly 15% and 85%). By inputting the tunnel diameter, the cost per linear foot of tunnel can be determined at the 15%, 50%, and 85% confidence level. Both the Nelson et al. (1994) model and the tunnel cost estimator (TCE) (Rostami et al. 2013) are derived in this fashion.

Several researchers have also demonstrated that dynamic Bayesian networks (DBN)s and decision trees have significant utility in modeling tunnel excavation processes (Brown

2012; Sousa and Einstein 2012; Špačková and Straub 2013). A Bayesian network models each step in the construction process as a random variable, represented graphically as a node. The nodes are connected in a web of directed links demonstrating dependencies and the process of construction. By assigning a probability to each node, the outcome of the project can be determined probabilistically. A DBN is one which can be updated and adapted based upon new information (such as updated geologic data during construction). This technique is quite powerful, but also quite complex, and has not achieved widespread use in the tunneling industry.

Another method of probabilistic analysis of tunnel costs is the MC method. The Decision Aids for Tunneling (DAT) (Einstein 2004b) uses this method. In the MC method, a menu of options is prepared for various factors related to tunnel cost. For example, the cost per linear foot of tunnel for the proposed tunnel diameter may be estimated for a variety of rock classes with some probability density function. Many possible models of the variation of rock class along the alignment are prepared, generally in a probabilistic fashion based upon preliminary geologic mapping. A program then simulates the tunnel construction process by randomly selecting alignments and costs and computing the total cost of tunneling. This process repeats through many thousands of iterations. Each run creates a data point of cost; the entire population of potential costs can then be fitted with a probability density function.

2.5.1 Cost Estimate Validation Process (CEVP)

An excellent example of current practice in project cost risk management for transportation infrastructure is the Washington State Department of Transportation (WSDOT) cost estimate validation process (CEVP) (WSDOT 2018). This process brings stakeholders and experts to the table to determine a range of likely project costs based on an early design and cost estimate. However, the CEVP methodology is intended to be applied after many design and construction decisions have been made. Decisions about alignment, excavation method, support method, and construction sequencing have strong impacts on costs, and thus a true risk assessment for a tunnel project must begin before these decisions are made.

2.5.2 Preliminary Analysis of Costs and Time for Tunneling (PACT)

Oreste (2006) provided a framework termed probabilistic analysis of cost and time in tunneling (PACT) which is intended for probabilistically evaluating tunneling times and costs based on the expected time for each period of the tunneling cycle and normally

distributed variation of this expected time. As expected, Oreste (2006) showed a good correlation between tunneling time and costs. However, Oreste does not provide a specific correlation to be used for forward analysis between any rock mass classification system and tunneling times or costs.

2.5.3 Decision Aids for Tunneling (DAT)

Decision Aids for Tunneling (DAT) (Einstein 2004a,b; Einstein et al. 1992, 1999, 1978, 1987; Einstein and Vick 1974; Haas and Einstein 2002; Min and Einstein 2016; Min 2014; Moret and Einstein 2016) is a system for estimating tunnel construction costs and times. The system was developed by a team of researchers from the Massachusetts Institute of Technology (MIT) led by Herbert Einstein. Einstein's work on cost estimating and optimization for tunneling and underground construction projects dates to the 1970s (Einstein et al. 1978; Einstein and Vick 1974). Einstein et al. (1987) published a paper detailing the various computer programs, primarily written in Fortran, developed by the MIT tunneling group for decision making in underground construction (Einstein et al. 1987). The name Decision Aids in Tunneling first appears in a 1992 monograph which was the outcome of research collaboration between MIT and the Ecole Polytechnique Federale de Lausanne (EPFL) and funded by the Swiss Federal Office of Transportation (Einstein et al. 1992). The work leading to this monograph also updated the programming language for DAT from Fortran to C. The name "Decision Aids for Tunneling" has been used much more consistently than "Decision Aids in Tunneling" since that time. More recent versions of the code have been implemented in C++ and Java, with a more user-friendly graphical user interface and new resource-optimization features (Einstein 2004b; Einstein et al. 1999; Haas and Einstein 2002; Min et al. 2003, 2005, 2008; Min 2003, 2007; Min and Einstein 2016; Min 2014)

A significant drawback of the DAT is its use of expert opinion as the basis for costs, which are then used to develop triangular probability density functions (Haas and Einstein 2002). No database of historical costs or relation to quotes or current markets is used. Rather, unit costs are estimated based upon the opinions of experts in the field, ideally those with experience in the geographical area being considered (Einstein et al. 1992).

The greatest flaw in the DAT method is the relation between geology and cost or advance rate, which is defined as a simple probability distribution. The DAT methodology jumps over any consideration of different excavation methods, support requirements, and geomechanical design. Additionally, the DAT is designed around an assumed drill-and-blast tunneling method with rockbolt and shotcrete support. The DAT further convolves

these technical uncertainties with cost uncertainties into a single probability distribution. For a given ground class, the DAT relates directly to cost and excavation time by a single probabilistic function. While this is admirably simple and straightforward, this system can be improved by adding additional steps between the geologic model and the cost estimate which quantify the unique uncertainties of each step.

An extension of the DAT is a system of decision aids for tunnel exploration which seeks to optimize the amount of money spent on initial geologic investigations for tunnel projects. Einstein and Vick (1974) also contributed to the development of this system. The most recent version of this system is coded in Visual Basic for Applications (VBA) which runs behind a Microsoft Excel user-interface (Karam 2005).

Min et al. (2003) succinctly describe the way that the geologic model is developed in the DAT:

> The description of geology produces probabilistic geologic/geotechnical profiles. The input is based on geologic information provided by geologists and engineers obtained from typical geologic explorations. The profiles which indicate the probabilities of particular geologic conditions occurring at a particular tunnel location are usually obtained through a combination of objective information and subjective estimates of experts. Specifically, the average length of geologic (geotechnical) parameter states and their transition probabilities are estimated. For instance, for the parameter lithology, one estimates the average length of the parameter states granite, phyllite and schist as well as the probability that phyllite follows granite, schist follows granite, etc. Subsequently the DAT use this information to simulate a possible profile for each parameter. The profiles for all parameters are then combined in ground class profiles. A number of such profiles (each being different) are simulated to represent the whole range of geologic conditions. (Min et al. 2003)

From the probabilistic geologic model, the DAT proceeds through a MC simulation process. Different realizations of the geologic model are created, the construction process is simulated, and outputs of construction time and cost are generated. The construction process simulation "involves relating geologic conditions to construction classes or tunnelling methods" (Min et al. 2003).

Currently, DAT is not widely employed in the tunneling industry. The code is not publicly available, even for a fee, so application of the DAT requires the user to either manually code the system or contract with Einstein and MIT for consulting services. Einstein's research group continues to publish papers employing the DAT (Min and

Einstein 2016; Moret and Einstein 2016), but there does not appear to be a wide or consistent application within the tunneling industry.

2.5.4 Tunnel Cost Estimator (TCE)

Rostami et al. (2013) developed a database of approximately 270 projects, performed statistical analyses of this database, and developed a MatLab tool called the tunnel cost estimator (TCE). This tool takes inputs of tunnel length, tunnel diameter, excavation type, and tunnel application and returns an approximate construction cost and average unit cost for the tunnel based upon the cost of similar projects under similar conditions. Uncertainty is quantitatively handled via probability density functions, allowing for calculation of confidence intervals of cost. Ongoing work at Mines is focused on updating and expanding this database to improve the previous model.

2.6 Probability Distributions and Statistics

There are many metrics for evaluating the shape of a distribution. The simplest are the meaures of central tendency such as the mean, median, and mode. Other measures of central tendency include the trimean, midhinge, midsummary, trimmed mean, and truncated mean (Hoaglin et al. 2000; Tukey 1977). Variance and standard deviation are probably the two most widely known measures of dispersion but they are designed specifically for normal distributions and are considered non-robust measures of sample dispersion, i.e., they are highly sensitive to outliers. In addition, they perform poorly in evaluating skewed or kurtotic (heavy-tailed) distributions (Pearson 1893, 1895). For distributions which may be non-normal, skewed, or kurtotic the more commonly preferred measures of data dispersion are range, interquartile range (IQR), and median absolute deviation (MAD), as well as the skewness and kurtosis themselves.

The second order central moment of a distribution is the variance; the square root of the variance is the standard deviation. Third and fourth order central moments are similarly related to skewness and kurtosis, respectively, as shown in Equation 2.67 and Equation 2.68.

$$variance = \sum (x - \overline{x})^2 \tag{2.65}$$

$$standard\ deviation = \sqrt{\sum (x - \overline{x})^2} \tag{2.66}$$

$$skewness = \frac{\sum (x - \overline{x})^3}{\left[\sum (x - \overline{x})^2\right]^{1.5}} \tag{2.67}$$

$$kurtosis = \frac{\sum (x - \overline{x})^4}{\left[\sum (x - \overline{x})^2\right]^2} \tag{2.68}$$

where x is an observation of a variable, and $\overline{x}$ is the mean of the observations.

The IQR and MAD are considered robust measures of dispersion, i.e., they are relatively insensitive to outliers, although they still do not capture skewness or kurtosis of the distribution (Rousseeuw and Croux 1993). The IQR is simply defined as the difference between the 25^{th} and 75^{th} percentiles of the data set. The MAD is the median of the absolute values of the difference between each observation and the median observation.

Throughout this report the coefficient of determination (r^2–value) has been calculated per Equation 2.69.

$$r^2 = 1 - \frac{SSE}{SST} \tag{2.69}$$

where SSE is the sum of squared errors for the prediction and SST is the sum of squared errors for a baseline constant value (mean) prediction.

MatLab has several built in commands for random sampling from probability distributions. These functions generate a pseudo-random number from a uniform or normal distribution as appropriate and then scale the number as necessary to fit the desired distribution's probability density function. However, MatLab does not have a built-in function for random sampling from a triangular distribution. The method used in this report for sampling from a triangular distribution is that of Kotz and Van Dorp (2004) as shown in Equation 2.70. A MatLab subroutine was created to implement Equation 2.70.

$$R = \begin{cases} A + \sqrt{U\,(M-A)\,(B-A)} & for \quad 0 \quad \leq U \quad \leq \frac{M-A}{B-A} \\ \\ B - \sqrt{(1-U)\,(B-M)\,(B-A)} & for \quad \leq \frac{M-A}{B-A} \quad \leq U \quad 1 \end{cases} \tag{2.70}$$

where U is a random number drawn from a uniform distribution between 0 and 1, A is the lower bound of the desired triangular distribution, M is the peak of the desired triangular distribution, B is the upper bound of the desired triangular distribution, and R is a random number drawn from a triangular distribution with lower bound A, peak M, and upper bound B.

2.7 Probability Distribution Transformations and Convolutions

Random variables may be transformed (a random variable is operated on by some function) or convolved (two random variables are arithmetically combined). In general, the transformation or convolution of randomly distributed variables does not preserve the original distribution shape except in the simplest cases. Many algebraic operations on random variables, both transformations and convolutions, do not produce distributions with closed-form solutions (Hogg et al. 2019; Springer 1979). Many open problems in statistics exist within this research area, sometimes termed random variable algebra.

Adding together distributions which have different peaks generally leads to a multimodal distribution, often with significant skew and kurtosis. For these cases, MC simulation is a robust technique for estimating the distribution of results. Simply selecting the best estimate of each parameter and estimating a single deterministic result ignores the interaction effects of transforming and convolving distributions. Deterministic estimates can significantly over- or under-estimate the actual most likely parameters and provide no understanding of the uncertainty involved in the estimate.

In the particular case of the RMR and Q systems, each component of the system (each term in Equation 2.3 or Equation 2.10) is a random variable. Further, each of these components is based on underlying data which are themselves random variables. The components have been estimated via various functional transformations. The ultimate RMR or Q value is therefore a convolution of a transformation of several underlying random variables. It is therefore unsurprising that the resulting distribution of RMR_{14} and Q values may have a wildly abnormal distribution.

CHAPTER 3

DEVELOPMENT OF A THREE-DIMENSIONAL GEOLOGICAL AND GEOTECHNICAL DATABASE FROM THE EISENHOWER-JOHNSON MEMORIAL TUNNEL CASE STUDY

This chapter presents the background information on the Eisenhower-Johnson Memorial Tunnel (EJMT) case study which is later used as a testbed for the alignment optimization and probabilistic back analysis techniques of Chapter 4, Chapter 5, and Chapter 6. To improve the understanding of rock mass classification systems, the rock mass quality index (Q) and rock mass rating (RMR) systems were characterized probabilistically for the EJMT. Distributions of Q and RMR were developed both at discrete points along the tunnel with instrumentation data and along the entire alignment based on excavation mapping data. Interesting discrepancies were observed between the deterministic and probabilistic rock mass classifications, including bias of deterministic results away from peak probabilistic results. Numerical models using rock mass properties based on probabilistic rock mass classifications were found to provide a reasonable match to rock loads recorded during tunnel construction. This suggests that forward modeling of tunnels using probabilistic rock mass classifications may give a more realistic estimate of tunnel support requirements, costs, and risks than deterministic rock mass classifications. Further, the findings suggest that current deterministic geotechnical baseline reports may be inadequate at providing a complete picture of a proposed project and may bias design towards a single, potentially incorrect solution. Although this important distinction between probabilistic and deterministic rock mass classifications arises from fundamental properties of random variable algebra, it appears to be under-discussed in the geotechnical literature.

3.1 Collaborative Effort

This chapter of the report was written collaboratively with fellow the Colorado School of Mines (Mines) doctoral candidate Ashton Krajnovich. While significant threads of both our work are present throughout this chapter, the following sections and figures were authored primarily by Krajnovich:

1. Section 3.3
2. Section 3.6.3
3. Section 3.6.4
4. Section 3.6.5
5. Figure 3.1
6. Figure 3.51
7. Figure 3.52
8. Figure 3.53
9. Figure 3.54

In addition, Krajnovich participated in the collection, identification, characterization, and preparation of geologic samples described in Section 3.5.2, and led field geologic mapping activities.

3.2 Introduction

The EJMT is a pair of two-lane automobile tunnels located approximately 97 km west of Denver, Colorado. They are some of the highest highway tunnels in the world at 11,155 ft above mean sea level and carry Interstate 70 (I-70) from one side of the continental divide to the other. The first (westbound) bore opened in 1973 while the second (eastbound) bore opened in 1979. The EJMT is the primary thoroughfare for vehicles traveling west from Denver.

The tunnels were excavated by the drill-and-blast technique through the Silver Plume Granite (SPG) and the Idaho Springs Formation (ISF) (metasedimentary gneiss and schist). On the west side of the tunnel the rock is extremely massive and hard, and the tunnel was advanced rapidly without significant issues. At the east side of the tunnel the rock is heavily fractured and presented some problems with excavation leading to the use of a top-heading and bench excavation method. Near the center of the ridge the tunnels pass through the inactive Loveland Fault. Rock in this area became progressively more fractured until, for a portion in the middle, the rock was almost entirely weathered to fault gouge. This squeezing material presented extreme excavation difficulties.

The EJMT was very thoroughly studied and documented. The proximity of the tunnel to Mines, United States Geological Survey (USGS), and United States Bureau of Reclamation (USBR) made it convenient for all these organizations to use the construction of the tunnel as a laboratory and case study, while at the same time providing useful information to the designers and contractors. In addition, researchers from the South Dakota School of Mines (SDSM) contemporaneously studied the construction of the pilot bore and documented their findings on the in-situ stress field around the EJMT. The most heavily documented portion of the tunnel is the pilot bore.

As constructed, the EJMT are 115 ft apart at the east portal, 120 ft apart at the west portal, and 230 ft apart at the widest point of separation. The westbound tunnel curves to the left while the eastbound tunnel is approximately straight. Each tunnel is approximately 1.7 miles long; about 1100 ft of this distance is ventilation equipment, portal structures, and cut and cover tunnel at each portal. The mean elevation of the tunnels is approximately 11,112 ft above sea level. The Continental Divide above the tunnels is approximately 12,608 ft above mean sea level, or approximately 1500 ft above the tunnel roadway elevation at the point where the tunnel alignment crosses the divide. The western approach to the tunnel has a grade of approximately 7%, while the eastern approach has a grade of approximately 6%. These steep approaches contribute to traffic issues in the vicinity of the tunnel, especially when heavier trucks have difficulty climbing the approach grades. The passage through the tunnel has a shallow grade of 1.6% as the tunnel climbs slightly from east to west (CDOT n.d.; Mattei 1965; Robinson et al. 1974).

Many primary sources were reviewed to find relevant background information for the modeling of the existing tunnels and the surrounding geology. Relevant records of the EJMT's construction are contained at the libraries of the USGS and USBR at the Denver Federal Center, Colorado Department of Transportation (CDOT)'s geotechnical division library in Denver, the Russell L. and Lyn Wood Mining History Archive at the Arthur Lakes Library at Mines, and records archived at the EJMT's west portal.

3.3 Geologic Setting

The EJMT passes through Precambrian igneous and metamorphic rocks of the Colorado Rocky Mountains. These include the ∼1.42 Ga Silver Plume Granite (SPG) (Aleinikoff et al. 1993) and the ∼1.7 Ga Idaho Springs Formation (ISF) containing metasedimentary gneisses and schists (Kellogg et al. 2008). At the EJMT, the ISF appears as xenoliths in the SPG. The ISF is foliated and folded as a result of the ∼1.8–1.6 Ga Yavapai and Mazatzal orogenies (Whitmeyer and Karlstrom 2007) and possibly the

∼1.4 Ga Picuris orogeny (Daniel et al. 2013; Shaw et al. 2001). The SPG contains foliations that have been interpreted as flow foliations (Robinson et al. 1974). The foliations in the ISF and SPG are roughly parallel, which may be due to the SPG intrusions generally following the foliation of the ISF (Robinson et al. 1974). The ∼70–40 Ma Laramide orogeny led to regional uplift of the Colorado Rocky Mountains causing new faulting and potential reactivation of preexisting faults (Erslev et al. 2004; Kellogg et al. 2008). The limited extent of the EJMT limits the ability to interpret the observed structures in the context of these regional structures (Robinson et al. 1974). Robinson et al. (1974) identified northeast-trending folds along the EJMT while Lovering (1935) interpreted the EJMT to lie within the northeast–trending Laramide-age Loveland Pass fault zone. The geologic structures along the EJMT have uncertain origins (Daniel et al. 2013; Robinson et al. 1974; Shaw et al. 2001; Whitmeyer and Karlstrom 2007), though the brittle faults observed are believed to be Laramide age (∼70–40 Ma).

Two aspects of the subsurface geology that were of particular importance to the construction of the EJMT were the inclusions of the ISF and the subsurface fault zone network. 25% of the EJMT pilot bore alignment is in the ISF while 75% is in the SPG, and the pilot bore passes through 86 distinctly mapped fault zones with thicknesses ranging from less than 1 ft (0.3 m) to greater than 5 ft (1.5 m). A section of the EJMT pilot bore geologic map plan view with overlain digitized lithological contacts, fault zone traces and structural orientation disks is shown in Figure 3.1.

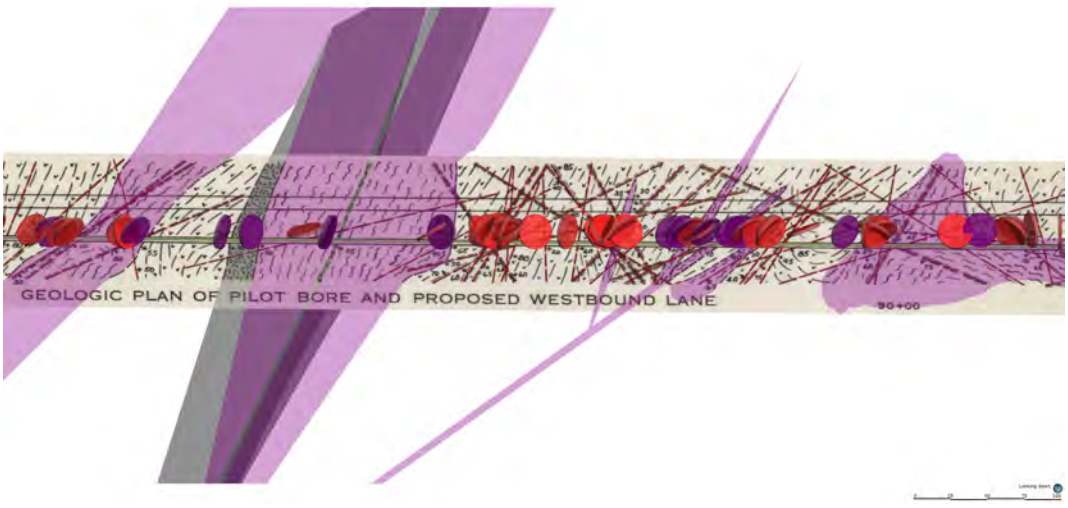

Figure 3.1: A detailed section of the pilot bore geologic map used in this study, showing overlays of the digitized 3D format of lithological contacts (shaded intervals), structural orientation data (disks) and fault zone traces (polylines).

Structural weakness may be expected along the foliation planes present in the ISF, and the aluminosilicate-rich rocks of this formation are heavily altered in faulted areas with groundwater flow. The most problematic sections of tunnel occurred where high densities of fault zones overlapped with large inclusions of the ISF.

Characterization of the fault zone network along the EJMT involved a structural analysis investigating the relationship between fault zones and foliations present in the SPG and ISF. Based on this analysis, the structural geology encountered by the EJMT can be roughly split into two structural domains around Station 75+00: The Western domain shows consistent foliation orientations in the SPG and very few inclusions of the ISF and intermittent faults, while the Eastern domain shows a higher density of faults, more inclusions of the ISF, and generally less consistent foliations in the SPG. With the data available, it is not possible to conclude whether faulting occurred preferentially through the ISF. The orientations of fault zones intersecting the EJMT generally resemble the regional Loveland Pass fault zone with faults predominantly dipping steeply to the southeast, though there is significant complexity resulting in a wide range of structural orientations and fault zone thicknesses.

3.4 Project Description

Crossing the Continental Divide has always been a challenge due to adverse weather and extreme elevations, but cross-Divide trade has made it economically desirable to have an expedient route through the mountains since at least the 19th century. The Moffat Tunnel, a rail line, was opened in 1928 and significantly improved the east-west rail system. After completion of the Moffat Tunnel, a similar road tunnel was considered several times. What was then the Colorado Division of Highways (CDOH) and is now CDOT officially began searching for the best route through the mountains in 1932 (CDOT 1953; Pavlo 1960; Robinson et al. 1974).

In 1960, a report by a New York based engineering firm, E. Lionel Pavlo, evaluated several possible locations and recommended an interstate alignment including a tunnel at Straight Creek to meet interstate highway requirements while crossing the Continental Divide (Pavlo 1960). Following Pavlo's report, CDOT began pursuing the construction of a tunnel at the site of the EJMT.

The pilot bore was begun in October 1963 and completed in December 1964. The total length of the pilot bore was approximately 8,350 ft. The contract was awarded to Mid-Valley Construction of Houston, Texas on October 9, 1963 for $1,291,920. The actual final cost of construction was approximately $1.4 million, an overrun of approximately 8%.

A report by CDOT's on-site project engineer, Fred Mattei, contains extensive descriptions of the excavation methodology and progress (Mattei 1965).

The original design cross-section was trapezoidal, 7 ft (2.1 m) wide at the top, 10 ft wide at the bottom, and 10 ft (3 m) high with timber supports. The support design was changed to a steel horseshoe early in the construction process at the request of the contractor. Three general support designs were used including 4-in steel sets, 6-in steel sets, and 6-in steel sets with invert struts. Typical cross–sections have been redrawn in Figure 3.2 based upon shop drawings contained in Mattei's report (Mattei 1965).

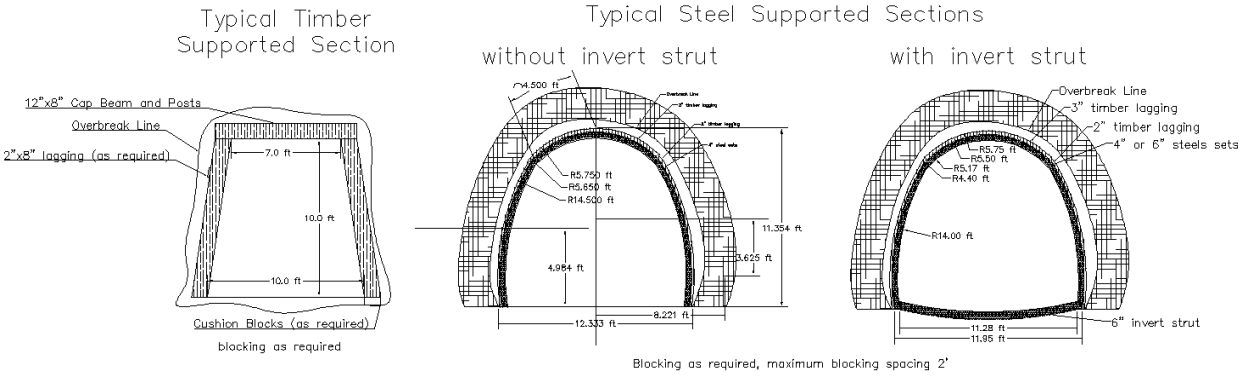

Figure 3.2: Typical Design Cross-Sections of Pilot Bore after Mattei (1965).

Water flow from the tunnel was measured at a flume at the east portal. Average daily water output at the flume varied from 40 to 680 gallons per minute (GPM) (150 to 2500 liters per minute (LPM)). Although a few water-bearing features were encountered which drained into the tunnel, water inflow to the tunnel did not present a great difficulty to construction.

The westbound bore is to the north of the pilot bore and was originally called the Straight Creek Tunnel. Construction of the westbound bore was started on March 15, 1968 and the bore was officially named the Eisenhower Memorial Tunnel by the Colorado state legislature in 1972 upon its completion. CDOT estimated that the project would take about three years and cost approximately $42.5 million. The winning bid from Straight Creek Contractors, a venture consisting of four contractors from across the United States, was accepted by CDOT on October 3, 1967 at a price of $54 million.

During the excavation of the east approach to the tunnel, a landslide was found to the northwest of the portal (Robinson et al. 1972). The excavation likely destabilized the toe of the slope. The slide was remediated by buttressing the toe with compacted fill, and the east portal was relocated approximately 150 ft south and 16 ft lower than its original planned location. The landslide occurred in highly fractured and faulted Precambrian

granite and metasedimentary gneiss and schist. In a paper from 1972, the USGS team who investigated and designed remediation for the landslide note that they have little information on the slide since 1965, but that they have anecdotal reports that the slide continued to move enough to load and deform some steel supports at the east portal (Robinson et al. 1972). Monitoring conducted by CDOT and reported in 1988 showed little or no movement since 1970 (Belknap et al. 1988). Additionally, CDOT has not reported any issues with this landslide since 1972, suggesting that landslide movement, if any, is negligible.

The excavated Eisenhower bore cross–section is approximately 50 ft high by 48 ft wide, the lined cross–section is approximately 48 ft high by 40 ft wide. The portion visible to drivers as they traverse the tunnel is much smaller, approximately 16 ft 4 in high with two 13-ft wide traffic lanes plus a tunnel maintenance walkway. Clearance through the tunnel is 13 ft 11 in due to hanging signs. For safety and maintenance reasons, three cross-passages connect the two tunnels at approximately 2,000-ft intervals. The tunnel cross-section varied along each alignment from horse-shoe shaped to ovoid due to changes in stress conditions, rock type, and unanticipated conditions (CDOT 1973, n.d.; Hopper et al. 1972).

The CDOT project engineers came up with a unique rock mass classification system for the construction of the EJMT. This system rated rocks from I to IV with subcategories of a and b within each category. Another researcher at Mines, Hui Lu, began the work to correlate these historical classifications to modern systems such as Q (NGI 2015), RMR (Bieniawski 1989; Lowson and Bieniawski 2013), and geological strength index (GSI) (Hoek and Brown 2018). Hui's work can be seen in their dissertation (Lu 2020).

Varying degrees and methods of support were required in the construction of the westbound bore to account for the varying quality of the rock as the tunnel crosses the Loveland Fault. A detailed paper by the CDOT District Engineer, R.C. Hopper, and two consultants to the project, T.A. Lang and A.A. Mathews, describes the construction methods and supports required to drive the westbound bore of the EJMT (Hopper et al. 1972). The tunnel was divided into five zones of similar conditions numbered by roman numerals from west to east. Construction began from the East portal in Zone V in January 1968 and from the West portal in Zone I in March 1968. The portals of the westbound bore were approximately 120 ft north of the initial pilot tunnel.

Hopper et al. (1972) present a detailed discussion of Terzaghi, Proctor, and White's semi-empirical tunnel support design method as it was applied to the EJMT (Proctor et al. 1946; Terzaghi 1946), although Abel noted that "in actual practice, steel supports were placed based on the experience of [the contractor's] personnel, at the discretion of the

contractor" (Abel 1966).

The Zone I excavation, measuring approximately 4,350 ft from the west portal, proceeded smoothly. Rock in this area was largely intact and competent. A top heading was excavated first, followed by removal of the bench. Temporary supports consisted of steel ribs with rockbolts for additional reinforcement (Hopper et al. 1972).

The Zone V, IV, and III excavations presented increasing difficulties as the tunnel proceeded from east to west approaching the Loveland Fault. The top heading and bench method was employed for this excavation. At the portal, the initial excavations proceeded through loose soil, including the stabilized edge of the Loveland Basin Landslide for approximately 500 ft. Once reached, the rock in Zone IV of the tunnel was described as "very blocky with weathered joints" and reinforcement by spiling was required (Hopper et al. 1972). Excavation of the top heading proceeded through Zone IV and Zone III for approximately another 1800 ft with continually worsening ground conditions, but no major problems. Steel supports, rockbolts, and spiling continued to be generally sufficient for support (Hopper et al. 1972).

In September 1969, several issues became apparent at roughly the same time. As the eastern portion of the tunnel approached Zone II the ground pressure on the supports began to exceed their capacity, and several supports in Zones III, IV, and V became seriously deformed. It was the opinion of the tunnel designers at the time that the use of Terzaghi's empirical method (Proctor et al. 1946; Terzaghi 1946) for design of steel sets had been extended beyond the data Terzaghi used to define the method. Terzaghi had data from much smaller tunnels than the Straight Creek Tunnel, and the coefficients Terzaghi (1946) suggested for smaller tunnels did not adequately scale up in a linear fashion (Hopper et al. 1972).

The worst cases occurred in the top heading of Zone III closest to Zone II. As Hopper et al. (1972) put it, "before completion of the eastern part of the tunnel could be considered, it was necessary to first stabilize the top heading. To perform bench excavation under an unstable arch would invite disaster". A concrete buttress was installed in Zone III at the base of the top heading supports to provide greater lateral stability to the arch, and additional supports and struts were installed. However, deformation of the tunnel continued. Further inspection determined that excessive overbreak and differential loading around the tunnel circumference was causing deflection of the steel ribs such that the arch could not mobilize its full strength. The solution to this problem was, at that time, a novel one in the United States. 20-ft long reinforcing bars were grouted into the rock on 5-ft centers, the entire tunnel wall was lined in concrete or shotcrete, and the overbreak voids were grouted (Hopper et al. 1972; Merten 1971; Post and Eastwood 1973). This

created a support system in much more intimate contact with the rock which successfully distributed the load on the tunnel to the concrete buttress. Today, rockbolts and shotcrete are a very common tunnel lining method, but, as Merten (1971) noted at the time, rockbolts and netting had been initially passed over as a support option due to the "hesitancy of workmen to work under this type of protection". The rockbolt and concrete lining approach was conservatively continued back through Zones IV and V in anticipation of potential issues during bench excavation (Bonnema 1972; Hopper et al. 1972).

After stabilization of the top heading, footing drifts were driven at the bottom corners of the Zone III, IV, and V cross-sections. This improved the speed of bench excavation and support installation through these zones. Additional rockbolt and spiling reinforcing was also used to resist horizontal loads. Spiling was drilled down into the Zone V sidewalls from the top heading, and 20-ft long #14 grouted reinforcing bars were installed radially (Bonnema 1972; Hopper et al. 1972).

Excavation of Zone II, the vicinity of the Loveland Fault, was the most difficult portion of the construction of the Straight Creek Tunnel. Rocks in this area were extremely faulted and fractured. In some areas, the rock had been turned almost completely to fault gouge with the consistency of stiff clay rather than rock. Zone II was approximately 1,900 ft long with approximately 1,000 ft of overburden and significant amounts of fault gouge. Where the rock was intact, it was extremely fractured. The tunnel tended to squeeze itself closed or collapse very quickly after excavation. Before construction of the Straight Creek Tunnel, no one had ever attempted such a large tunnel in such poor ground with that much overburden (Bonnema 1972; Hopper et al. 1972).

The contractor's initial plan was to advance the tunnel full-face with a horseshoe–shaped shield through the Zone II. To do this, the contractor had advanced smaller footing drifts at the bottom corners of the tunnel cross-section most of the way through Zone II. As the shield was advanced, and before it had reached Zone II, the contractor encountered difficulties with the roller system used to advance it. An alternative skid system was designed, but by this time (also September 1969), an evaluation of the ground conditions in the footing drifts and in Zone III led to the conclusion that the shield system likely would not work. The ground in Zone II was simply not capable of supporting itself sufficiently, and the shield was likely to get stuck. In addition, it was determined based on the required Zone III support system that a more robust tunnel lining would be required in Zone II than was originally planned (Bonnema 1972; Hopper et al. 1972).

To meet the support needs in Zone II, a multi-drift support system was devised as shown in Figure 3.3. Where geologic conditions were comparable to those previously encountered, five smaller drifts were bored. There were two footing drifts at the lower

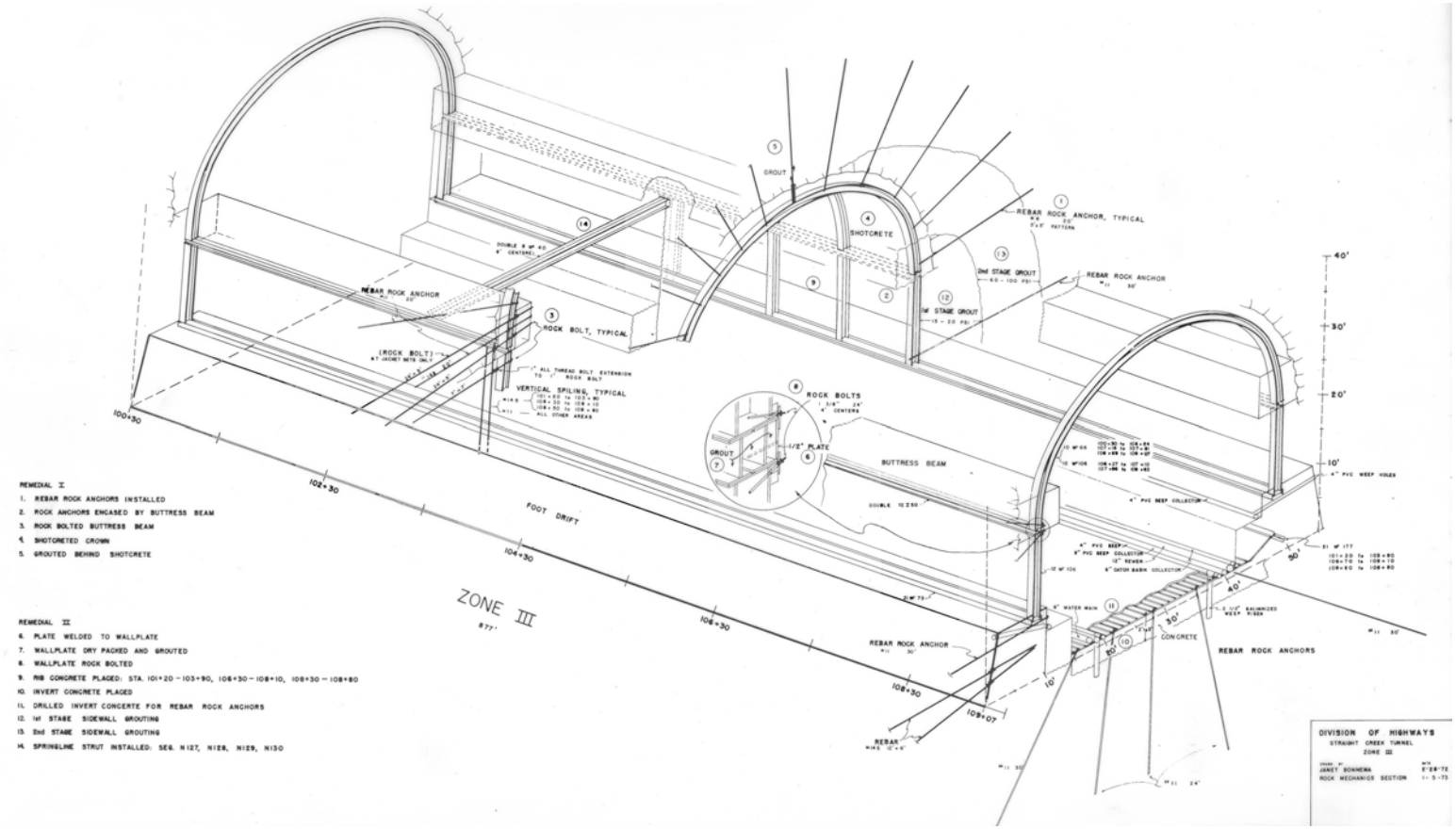

Figure 3.3: Isometric view of tunnel support system in Zone III by Bonnema (1972).

corners of the horseshoe section, two drifts at the tunnel springline, and one crown drift. From these drifts, spiling and rock bolts were installed. The drifts were then backfilled with concrete to create a series of stabilizing beams surrounding the tunnel. The project engineers noted that "portions of the arch drift which would project inside the final excavation line were blocked out with gravel and crushed rock" rather than using more traditional timber formwork, presumably because of the ready availability of the crushed rock material. The tunnel could then be excavated within this pre-installed protective framework by the top heading and bench method with minimal risk of collapse (Bonnema 1972; Hopper et al. 1972).

An Austrian tunnel engineer, Horst Ueblacker, was brought in to help analyze the squeezing problem and identify a solution for portions of Zone II where the rock had been turned almost entirely to fault gouge (approximately station 82+40 to 84+00) (Ueblacker 1971). After creating finite element and Winkler-beam models of the tunnel which were quite advanced for the time, Ueblacker and the design team came up with a stacked drift solution. The perimeter of the tunnel was excavated in a sequence of 13 stacked drifts.

The actual driving of the crown drift was a careful operation through the fault gouge zone. The material was described as "stiff clay containing blocks of decomposed, weak rock" (Hopper et al. 1972). The drift was 8 ft wide by 9 ft high (2.4 m by 2.7 m) and advanced approximately "6 to 7 ft per day by means of spading with some light blasting" (Hopper et al. 1972). Steel sets were used on 3-ft (0.9 m) centers with timber lagging and blocking between the steel and the earth. Deformation of the ground was enough to crush timber blocking, with ground squeezing of 1.5 to 2 ft (0.5 to 0.6 m). The crown drift required several iterations of re-timbering over a period of weeks while the drift was completed.

Each drift was supported by steel beams and was backfilled with concrete before the excavation of the main tunnel (Figure 3.4). The upper five drifts had longitudinal beams placed along them, as well. This protective arch allowed for the successful excavation of the tunnel by the top-heading and bench method even in rapidly collapsing and squeezing ground (Bonnema 1972; Hopper et al. 1972). Arch ribs and side legs were placed as each section was excavated. The invert was supported by another curved beam. The overburden at this section is approximately 992 ft and the excavated tunnel width and height are approximately 56 ft 2 in and 64 ft 8 in (17.1 m by 19.7 m), respectively (Bonnema 1972; CDOT 1973; Hopper et al. 1972; Ueblacker 1971).

After five years of difficult construction, the tunnel was opened to traffic on March 8, 1973 at a total cost of approximately $108 million. The Eisenhower bore has the ignominious distinction of being the single most expensive federal aid project in US

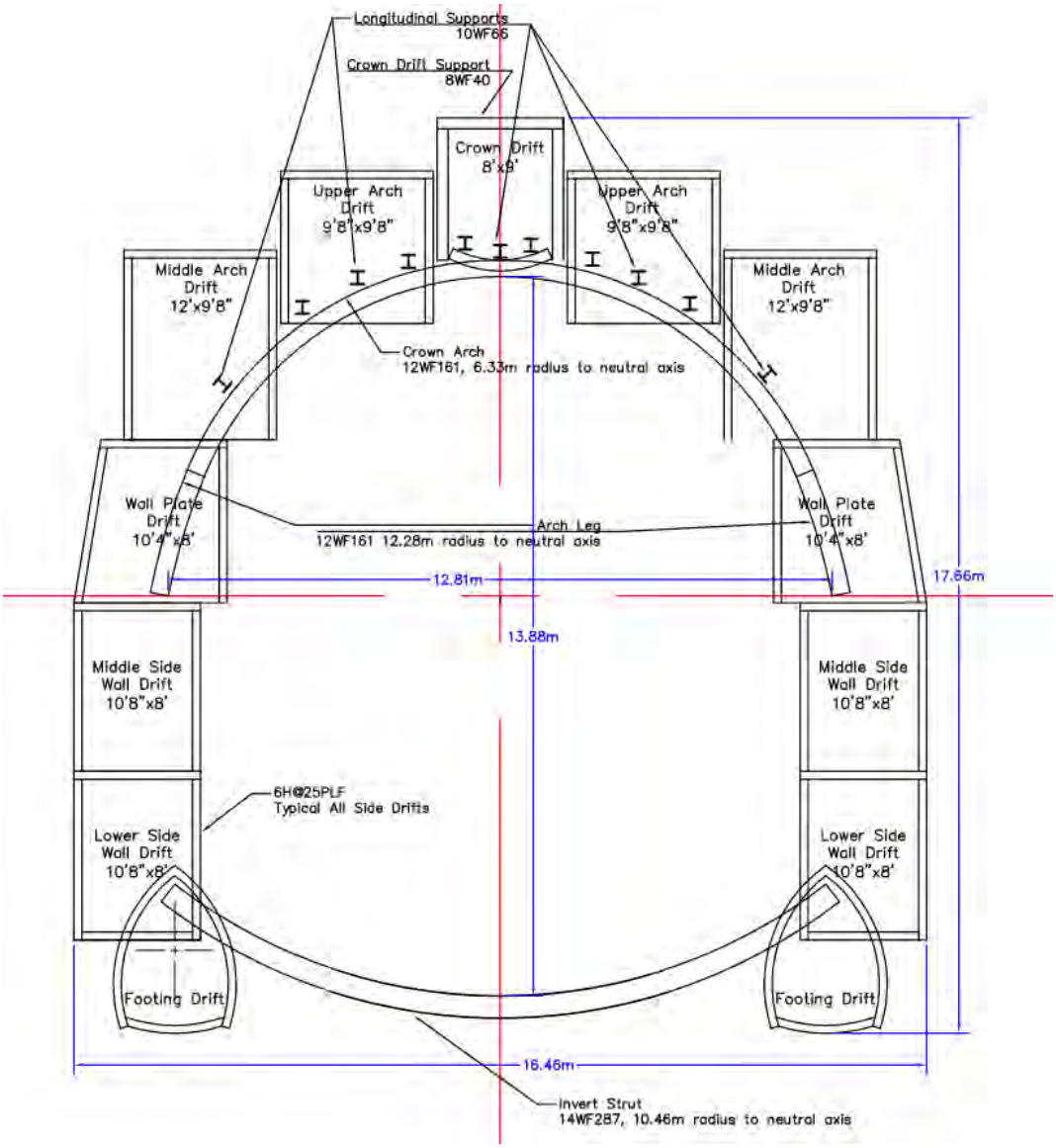

Figure 3.4: Zone II cross-section showing multi-drift system. Redrafted by the author after CDOT historical as-built plans (CDOT 1973).

history at the time of its construction, going 100% over bid. This cost overrun led to the Johnson bore being the first use of a dispute resolution or review board (DRB) on a US construction project (McOllough 1981; Technical Committee on Contracting Practices of the Underground Technology Research Council 1991).

Technical innovations on the Eisenhower bore included the use of rock bolts and shotcrete, which were previously not widely known or used in the United States (Hopper et al. 1972; Merten 1971; Post 1973). Ueblacker's use of a finite element model and a Winkler-beam model in the analysis of the squeezing ground conditions was quite innovative for the time (Ueblacker 1971). This analysis led to the implementation of the

stacked drift design, which introduced the sequential excavation method to the United States and presages the modern pipe arch (or umbrella arch) technique. Ueblacker's analysis also led to the curved bottom corners and invert of the tunnel, a common practice today for better load distribution around a tunnel lining.

The project was planned from the beginning as a pair of tunnels, one eastbound and one westbound. Plans for the eastbound bore, officially the Edwin C. Johnson Memorial Tunnel, were started as soon as the first bore was completed.

Construction on the eastbound bore was started on August 18, 1975 by a joint venture of Kiewit and Brown & Root. The second bore approximately follows the alignment of the pilot bore (CDOT 1979). Construction was completed on December 21, 1979 at a cost of $102.8 million (not including mechanical and electrical work), slightly cheaper than the westbound bore and below the engineer's estimate of $110.6 million.

The plans for the south tunnel (eastbound tunnel or the Johnson bore), accounted for the difficult ground conditions encountered in the Eisenhower bore. The western half of the tunnel, in solid and competent rock, was bored by the top heading and bench method with no additional support drifts required. The eastern half of the tunnel began with two foundation drifts and one crown drift, switching to a fully multi-drift encased system for approximately 500 ft (150 m) of the worst ground conditions. The as-built plans note that:

> The tunneling method that was used for excavation started with a 11x11-ft Crown Drift and a 12x12-ft North Foundation drift being driven from the east portal to a point about halfway through the tunnel. The pilot bore previously driven in 1964 was enlarged and used as a south foundation drift. Following the completion of the drifts and the insertion of receiver and crown beams, the main tunnel was excavated by a top heading and bench method from east and west headings. (CDOT 1979)

There are significantly fewer publications pertaining to the Johnson bore than the Eisenhower bore. This can be attributed in part to the experience gained in the construction of the pilot and Eisenhower bores and in part to the early adoption of the United States' first DRB. The DRB successfully resolved three disagreements between the contractors and CDOT, helping to keep the project on schedule and within budget (McOllough 1981; Technical Committee on Contracting Practices of the Underground Technology Research Council 1991).

Recent structural inspections have found the tunnel in remarkably good shape and suitable for years of continued service with ongoing maintenance and inspection (Trapani et al. 2010). CDOT continues to perform routine maintenance and update mechanical,

electrical, and plumbing systems as required.

The EJMT carries a large volume of traffic which continues to increase every year. Pavlo (1960) estimated traffic flows through the tunnel to 1990. As shown in Figure 3.5 the traffic through the EJMT has consistently exceeded these estimated flows since 1974, the year after the first tunnel opened. Today traffic far outstrips any traffic volume that could be imagined in 1960. Average daily traffic has more than quadrupled since the opening of the tunnel and is expected to continue to rise. Long traffic delays at the tunnels are common, and a metering system is enforced by CDOT for safety reasons.

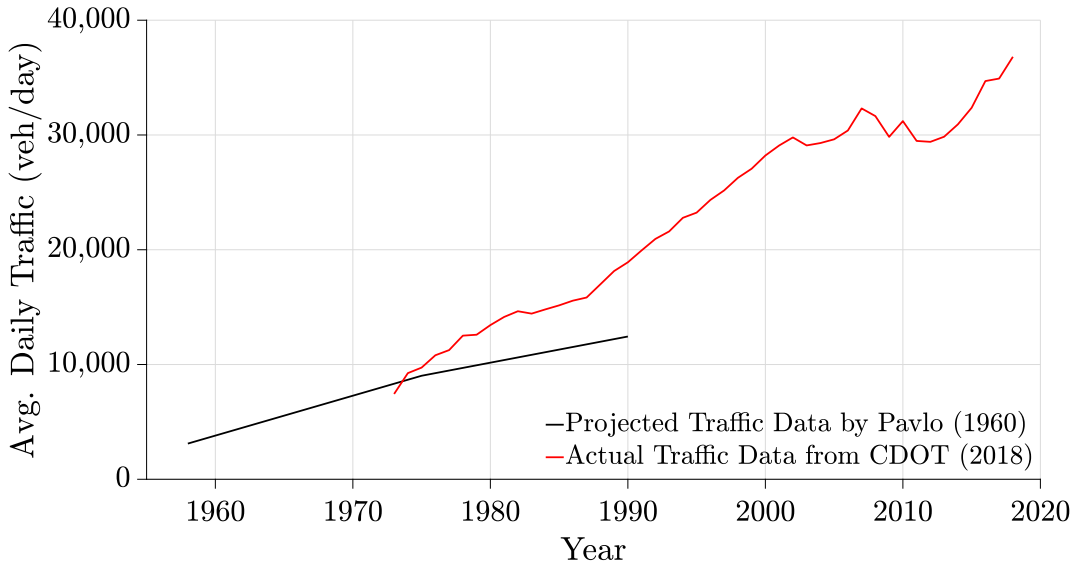

Figure 3.5: EJMT traffic data projected by Pavlo (1960) and recorded by CDOT (2018b).

The result is significant economic losses from the delay in the movement of commuters and passengers, goods and services, and tourism. To meet the growing traffic demand and to achieve a more efficient and economical traffic flow CDOT has made expansion of I-70 a priority. A programmatic environmental impact statement for the I-70 Mountain Corridor project was completed in 2011 (CDOT 2011). The Veterans Memorial Tunnel further east was recently widened, and further improvements are planned at various bottlenecks along the route between Denver and the Eagle County Airport.

The EJMT is a critical link in this chain of improvements. Expansion of the existing tunnels is generally considered to be a poor option as it would require long construction closures of one or both tunnels and has significant technical complications regarding the tunnel's structural stability. Therefore, the addition of a new tunnel or tunnels to increase the overall capacity of the system is the CDOT preferred option. To find the best solution to improve traffic flow and capacity through the EJMT, CDOT has sought the services of the Mines University Transportation Center for Underground Transportation

Infrastructure (UTC-UTI). Several graduate students are exploring various aspects of the feasibility of adding additional throughput capacity to I-70 at the Continental Divide. The goal of the research project described in this report is to develop a process for assessing tunnel feasibility, using the EJMT expansion case study as a real-world testbed.

3.5 Data Evaluation

A thorough review of historical data pertaining to the geology and geomaterial properties in the vicinity of the EJMT was performed. The original EJMT project was very thoroughly studied and documented. The proximity of the tunnels to Mines, USGS, and USBR made it convenient for all these organizations to use the construction of the tunnel as a laboratory and case study, while at the same time providing useful information to the designers and contractors. Many primary sources were reviewed to find relevant background information for the modeling of the existing tunnels and the surrounding geology. Data sources consulted include as-built plans, construction reports, laboratory reports, field test reports, and field geologic maps. Academic research published contemporaneously with the tunnel construction also provides a valuable insight into the tunnel design and construction process. In addition, data gaps pertaining to the properties of the ISF have been filled with new data collected by the EJMT research team. The data have been aggregated and analyzed to develop a conceptual geologic model and estimates of rock mass classifications, elastic parameters, and yield criteria.

3.5.1 Overview of Available Data Sources

CDOT maintains records of the EJMT in two locations: at the tunnel itself and at the geotechnical library in downtown Denver. The authors visited both of these locations to access available records and scanned documents into electronic format for further review.

The as-built plans for the EJMT are maintained primarily in electronic format though the resolution is somewhat low and some portions are illegible. Some physical copies of intermediate plan sets are in storage at the tunnel warehouse, but no complete physical copy of the as-built plans was identified during the record search.

An engineering technician with CDOT named Janet Bonnema was responsible for preparing a set of isometric drawings of the tunnel reinforcement system, including Figure 3.3 (Bonnema 1972). These are some of the best visualizations of the as-built tunnel support system available.

CDOT geologists John Post and Al Eastwood did extremely detailed mapping of the Eisenhower Bore during construction (Post and Eastwood 1973). Of particular interest

was Appendix 1 to Post and Eastwood (1973) which is labeled Geologic Map of the Straight Creek Tunnel, Showing the Pilot Bore, Scale 1 in = 100 ft. This detailed map covers the entire Eisenhower bore. Descriptions of the geology along the alignment include the historical rock mass class (Ia to IVb); decomposition and alteration (none, slight, moderate, or high); water zones (none, damp, wet, raining); joint spacing (1 ft or more, 0.5 to 1 ft, 0.5 ft or less); blockiness and seaminess (massive, blocky, moderately blocky and seamy, very blocky and seamy); and overbreak (given as a binary condition of overbreak or no overbreak with a cutoff at 3 ft of overbreak). Most of the data used in developing the rock mass classifications along the Eisenhower bore come from this appendix.

Post also wrote a report on the use of rock bolts in the Eisenhower bore construction (Post 1973). At the time, the use of rock bolts was a relatively new concept in the United States and their use in the Eisenhower bore was considered somewhat experimental. Post reported good success in the use of rock bolts in the Eisenhower bore.

The Russell L. and Lyn Wood Mining History Archive at Mines maintains a number of unique documents not available elsewhere. Fred Mattei, construction engineer for the EJMT pilot bore, donated personal files to the archive and these proved to be an invaluable data source for this project. In particular, Mattei's construction report (Mattei 1965) and the geology report co-written with George Miles (Miles and Mattei 1965) were particularly valuable. Miles and Mattei (1965) identified three distinct shear zones from 83+00 to 84+00, 89+20 to 92+45, and 105+35 to 107+35. Some of the detailed descriptions of Miles and Mattei (1965) are reproduced here verbatim because of their exceptional relevance to discussion of the material properties of the geomaterials encountered in the pilot bore.

> All the shear zones followed the same general pattern of slivers and slickensides at the contact points, diminishing size of the granulated particles as the intensity increased, grading to clay (fault gouge) at the point of most intense crushing, and reversing the gradation to the other contact...
>
> Many of the faults contained abundant clay gouge and showed clay alteration...the potential volume change of the swelling clays, while being a contributing factor to the heavy loads developed, played only a minor role in creating the demand for additional support; the loads being generated by squeezing rather than swelling ground...
>
> Some faults were water bearing while others showed variable thicknesses of wet gouge; others were filled with granulated quartz and feldspar grains; combinations of these characteristics, in some cases, produced heaving and

squeezing ground...

> Rock at the contacts are slivers, from less the 0.1 in to 1.0 in wide, confined by slickensided shear planes. As the intensity increases, the rock is crushed to a coarse to fine sand and the shear planes are less than 0.01 in to 0.5 in apart and lie in all directions. The most intense shearing, accompanied by some alteration, produces clay (fault gouge) with variable amounts of quartz and/or feldspar. The gouge, as disconnected streaks parallel to the trend of the shear zone, usually does not occur near the center of the zone but is most commonly adjacent to the footwall. (Miles and Mattei 1965)

USBR was contracted by CDOT during the original tunnel construction to perform in-situ and laboratory testing of materials along the tunnel alignment. USBR conducted plate jacking tests in the eastbound heading of the Eisenhower bore (Cohen 1970) and extensive laboratory testing on samples from the pilot bore during its construction (Cohen 1971a,b).

The USGS published several papers about the EJMT (Carroll et al. 1966; Lee and Nichols 1966; Monk and Farrow 1965; Nichols and Lee 1966). Robinson et al. (1974) provides a detailed summary of the USGS efforts on the construction of the pilot bore including geologic maps, geophysical surveys, engineering geology, hydrology, construction practices, and support design. The preface to this paper notes that "the proximity of this tunnel to the research center of the U.S. Geological Survey in Denver offered an unusual opportunity to utilize the personnel and facilities of the Survey on the problems of defining the environment of the proposed tunnel". In other words, many experts consulted on the EJMT project and provided a great deal of useful information before and during construction. The USGS also conducted an extensive series of laboratory tests on 54 samples from borings, the pilot bore, the surface, and a nearby quarry (Robinson et al. 1974) and conducted in-situ geophysical testing to determine elastic moduli of the rock mass (Carroll et al. 1966; Robinson et al. 1974).

SDSM Department of Mining Engineering performed in-situ investigations in the pilot bore of the EJMT before construction of the Johnson bore. The exact dates of the testing are not reported, but the date of the report is January 1974. That date and the reference to the cross-passageway implies that these tests were conducted after the construction of the Eisenhower bore. To determine in-situ stresses and elastic moduli around the tunnel, researchers used flat jacks in the north wall of the pilot bore and performed borehole strain relief tests in the center cross-passageway between the pilot bore and the Eisenhower bore of the EJMT (Hoskins et al. 1974). Based on their in-situ testing, the

Table 3.1: In-situ stresses in the EJMT cross-passages reported by Hoskins et al. (1974).

Stress Direction	Most Likely Value		Lower Bound		Upper Bound	
	psi	MPa	psi	MPa	psi	MPa
Vertical	900	6.2	700	4.8	1100	7.6
North-South	400	2.8	200	1.4	600	4.1
East-West	100	0.69	-100	-0.69	300	2.1

SDSM team suggested reasonable engineering estimates for the in-situ stresses near their test locations in and around the squeeze zone, as shown in Table 3.1.

These values suggest that the minimum and maximum in-situ horizontal/vertical stress ratios normal to the tunnel axis are approximately 2/11 and 6/7 or 0.18 and 0.86, respectively. Similarly, the minimum and maximum in-situ horizontal/vertical stress ratios longitudinal to the tunnel are approximately $-1/11$ and 3/7 or -0.09 and 0.43, respectively. Note that Hoskins et al. (1974) did not offer any comment on why they thought it likely that the east-west stress direction could possibly be negative (i.e. field stress in tension). This is mechanically possible but somewhat unlikely.

3.5.2 New Laboratory Testing Conducted for this Research

In reviewing the available data on the strength properties of the SPG and ISF the current research team determined that additional testing would be beneficial. The research team collected 29 test samples along the north side of I-70 at exit 216 US-6/Loveland Pass approximately one mile from the east portal of the EJMT. Intact samples of the SPG and ISF showing minimal weathering and fracturing were selected. Cores were drilled from block specimens, cut to appropriate lengths, and ends were ground smooth in general accordance with typical International Society of Rock Mechanics (ISRM) and American Society for Testing and Materials (ASTM) procedures for preparation of core samples (ASTM 2008, 2014; ISRM 2007). Samples were tested for unconfined compressive strength and triaxial shear strength at Mines research laboratories according to ASTM D 7012 (ASTM 2014). The current research team tested 17 samples of the ISF and 4 samples of the SPG.

3.5.3 Data Digitization and Processing

The data presented in tables and graphs in primary sources were digitized into Microsoft Excel (Microsoft 2008) tables using Plot Digitizer software (Huwaldt 2015) or Tabula software (Aristaran et al. 2013; Gioi et al. 2012). Data presented as narrative text was digitized into Excel tables by hand where appropriate. This digitization effort was conducted by graduate students Gauen Alexander, Ashton Krajnovich, and Hui Lu and by undergraduate research assistants Jacob Mellema and Cooper Carroway.

Surficial map data were georeferenced as raster images using ArcMap software (ESRI 2019). Universal Transverse Mercator (UTM) Zone 13 N was used as the common coordinate system for all data. When available, the known locations of map corners and coordinate grid overlays were used to calibrate the georeferencing. In addition, known landmarks such as the corners of the EJMT portal buildings were used to refine the georeferencing and provide maximal accuracy in the vicinity of the existing tunnel. Comparison with current satellite imagery from the Environmental Systems Research Institute (ESRI) Basemap catalog allowed for visual verification of the georeferencing accuracy. Surficial map data were digitized using ArcMap (boreholes and tunnel alignments) and Leapfrog (fault zones and lithological contacts). The high-resolution digital elevation model (DEM) from the National Geologic Map Database (NGMDB) provided topographic information for map data relevant to the ground surface (USGS 2016a,b).

Plan and section view geologic maps from the pilot bore were georeferenced according to known drawing dimensions (e.g., tunnel diameter) and the georeferenced pilot bore tunnel alignment polyline. The data from these maps were digitized using Leapfrog (Seequent 2020) and the Plot Digitizer (Huwaldt 2015) software to extract detailed polyline traces and structural orientations describing the encountered fault zones, lithological contacts, and foliations. Data that were digitized in terms of station readings from the pilot bore and Eisenhower bore were georeferenced to the common coordinate system using the relevant tunnel alignment polyline.

MatLab has a number of tools for processing linear, multi-linear, and non-linear regressions to data. In general, the term regression in this paper refers to a linear or non-linear (as required) least–squares regression algorithm as implemented in MatLab (Branch et al. 1999; Byrd et al. 1988; MathWorks 2019; Moré and Sorensen 1983).

Fit of several distributions were checked against the various material parameters using MatLab distribution fitting functions as described in Section 2.6. MatLab has a built-in algorithm for fitting statistical distributions to data which uses a maximum likelihood estimation methodology. The quality of each distribution fit to the data was tested using a

χ^2 goodness of fit test.

After data were brought into the digital realm, they were interpreted using a number of computational tools including MatLab (MathWorks 2019), Leapfrog Geo (Seequent 2020), and Python (Rossum 1995; Rossum and Python Software Foundation 2020). Interpretation of the data including an evaluation of the geologic setting, interpretation of the available geologic data via three-dimensional (3D) implicit geologic modeling, and evaluation of the mechanical properties of the geomaterials.

3.5.4 Fault Gouge Material Properties

An isotropic elastic model with a Mohr-Coulomb (M-C) yield criterion has been selected for the modeling of the fault gouge based upon analysis of historical in-situ and laboratory test data by the USBR. Rather than relaxing the continuous, homogeneous, isotropic, and linear elastic (CHILE) assumptions, this model uses stochastic uncertainty of the input variables to estimate a range of outputs by means of Monte Carlo (MC) simulation.

The material model required for input to a continuum numerical model of the fault gouge has five parameters: density, Young's modulus, Poisson's ratio, friction angle, and cohesion. Alternatively, bulk modulus and shear modulus can be substituted for Young's modulus and Poisson's ratio. An optional parameter for the material model is the dilation angle, which represents volumetric strain after yield. Table 3.2 summarizes these material properties.

As the fault gouge is a decomposition product of SPG and ISF which have been sheared, the bulk material model over a larger scale will grade from these fault gouge properties towards fractured and then intact SPG and ISF properties. In this sense, the fault gouge material properties represent a likely lower bound of material properties that one might expect to encounter in the EJMT vicinity.

3.5.4.1 Elastic Moduli

The USBR performed seven K_0-consolidated triaxial shear tests on fault gouge materials. In these tests, the lateral confining pressure was varied as necessary to maintain zero lateral strain in the specimen. From the K_0-consolidated test results, the USBR computed Young's modulus (secant form) and Poisson's ratio for the samples at several points along the stress-strain curve for each test. In addition, two unconfined compressive strength or uniaxial compressive strength (UCS) tests by the USBR on fault gouge samples provided data on Young's modulus of the material.

Table 3.2: Fault gouge material properties summary.

Property	Units	Median	Mean	Min	Max	Distribution	Distribution Parameters
Dry Bulk Density	g/cm^3	2.103	2.056	1.692	2.552	NA	discrete parameter
Saturated Bulk Density	g/cm^3	2.323	2.278	2.053	2.431	NA	discrete parameter
Porosity	unitless	0.235	0.243	0.168	0.366	NA	discrete parameter
Young's Modulus	MPa	7.55	9.59	4.79	20.8	Rice	$s = 0.932$, $\sigma = 7.56$
Poisson's Ratio	unitless	0.23	0.24	0.08	0.44	beta	$a = 2.80$, $b = 2.91$
Friction Angle	degrees	NA	21.1	NA	NA	NA	discrete parameter, uncertainty in Mohr-Coulomb envelope captured by cohesion
Cohesion	kPa	NA	31	NA	NA	normal	$\mu = 31$, $\sigma = 50$
Dilation Angle	degrees	0.796	1.02	0	2.85	half-normal	$\mu = 0$, $\sigma = 1.33$

Notes: s is the Rice distribution reference distance, σ is the Rice distribution scale or normal distribution standard deviation, μ is the mean of a normal distribution, and a and b are the first and second shape parameters of a beta distribution.

A lognormal distribution appeared to fit the fault gouge laboratory Young's modulus data the best as shown in Figure 3.6. The fit of the lognormal distribution is superior to that of a standard normal distribution because it is bounded between zero and positive infinity. The parameters of the lognormal distribution for Young's modulus data are $\mu = 2.15$ and $\sigma = 0.465$. The most likely value of Young's modulus from the lognormal distribution is 6.9 megapascals (MPa).

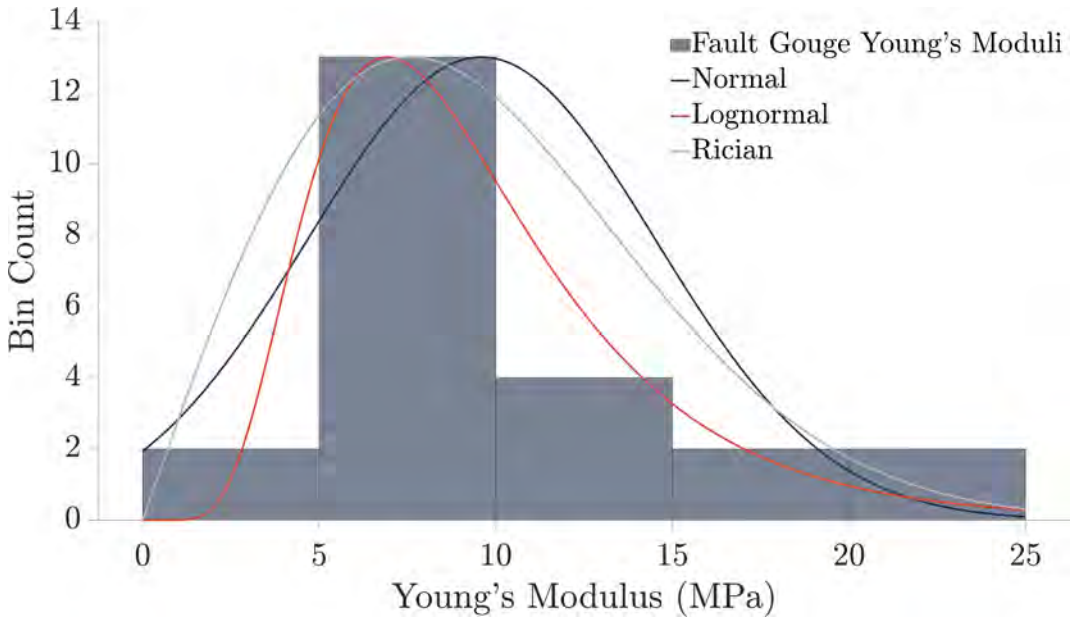

Figure 3.6: Young's modulus data for the fault gouge materials tested by USBR with fitted statistical distributions.

The Rician distribution has a slightly better fit than the lognormal distribution to the fault gouge laboratory Young's modulus data as determined by a χ^2 goodness-of-fit test. The most likely value of Young's modulus from the Rician distribution is 9.5 MPa.

For the fault gouge Poisson's ratio data, a Rayleigh distribution provided the best fit to the data as shown in Figure 3.7. A beta distribution also provided a better fit to the data than a normal distribution and was selected as the best fit for practical application because it is inherently bounded at either end. For the purposes of numerical stability, it is necessary to limit the input Poisson's ratio to a range between 0 and 0.5, exclusive. Therefore, a beta distribution can be applied without additional truncation or error trapping in the numerical modeling code. The most likely value of Poisson's ratio from the beta distribution is 0.245 while the most likely value of Poisson's ratio from the Rayleigh distribution is 0.185.

The USBR also conducted plate jacking tests in which a circular plate was pushed into the wall or ceiling of the tunnel using a hydraulic jack (Cohen 1970) between approx-

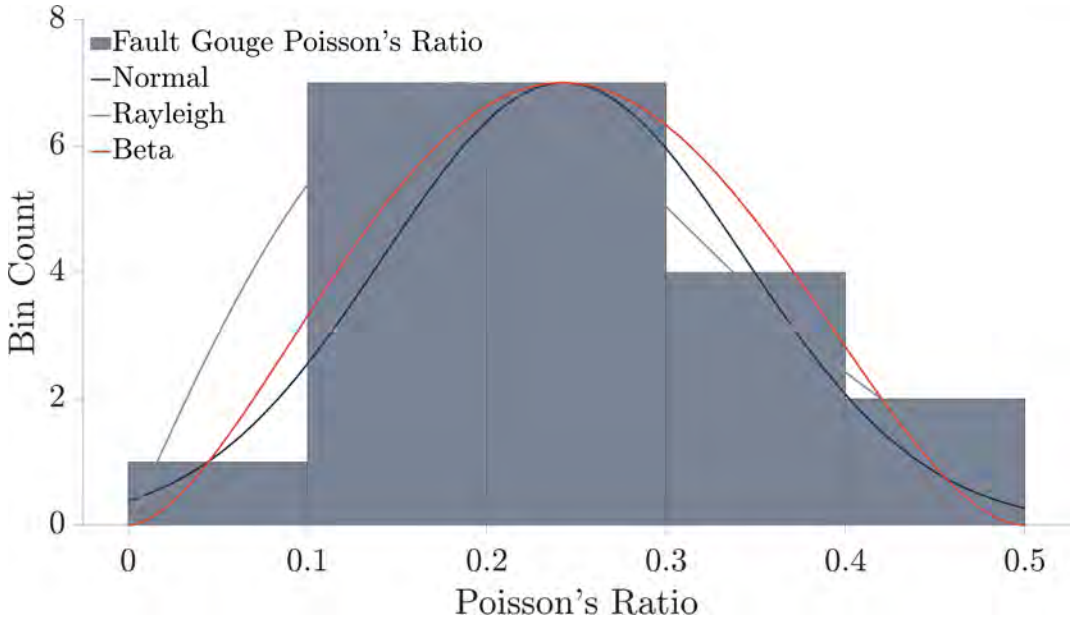

Figure 3.7: Poisson's ratio data for the fault gouge materials tested by USBR with fitted statistical distributions.

imately Station 83 and 84 and between Stations 89 and 90. The load-deformation curve recorded during this test can be used to determine in-situ elastic moduli given certain assumptions about stress distributions. Four such tests were reported in materials which can be identified as fault gouge based upon descriptions in the USBR report, their estimated locations, and descriptions of the testing in a paper by Hopper et al. (1972). Another two tests appear to be in more competent rock materials, but exact locations or geologic descriptions are not available.

USBR used a trapezoidal pressure distribution as described by Jumikis (1964) and an assumed Poisson's ratio of 0.2. This was the standard of practice at the time. However, more modern methods as recommended by ISRM (2007) provide slightly different elastic moduli.

The USBR report states that the equation used to calculate Young's modulus of the rock mass is Equation 3.1.

$$E = \frac{qR^2}{\delta}\left(\frac{1}{R} - \frac{1}{R+d}\right) \tag{3.1}$$

where E is Young's modulus of the rock mass, R is the radius of the loading plate, δ is the measured deflection of the loading plate, q is the pressure on the loading plate, and d is the depth of the altered material (assumed equal to 0.69 m).

The ISRM suggests an equation based upon a Boussinesq distribution which includes

Poisson's ratio as shown in Equation 3.2.

$$E = \frac{2(1-\nu^2)qR}{\delta} \tag{3.2}$$

Based upon the four plate jacking tests in fault gouge, the results as calculated by the USBR in 1970 have a mean Young's modulus of the rock mass of 4.7 MPa with a standard deviation of 2.1 MPa, indicating a coefficient of variation of 44%. Computing the mean Young's modulus of the rock mass using a Boussinesq pressure distribution as suggested by ISRM (2007) and using Poisson's ratio of 0.24 based upon the USBR K_0-consolidated and UCS tests gives a mean Young's modulus of the rock mass of 11 MPa with a standard deviation of 4.9 MPa, indicating a coefficient of variation of 44%. These values roughly bracket the most likely value of Young's modulus as determined from a lognormal distribution fit to lab testing data, 6.9 MPa.

The SDSM investigations included flat jack tests on varying materials, including one in the "softest, most unstable, squeezing ground that we could find in the pilot bore" (Hoskins et al. 1974). Hoskins et al. (1974) reported Young's modulus from that test of 130 MPa. This is an order of magnitude higher than any results from the USBR laboratory or in-situ tests. The SDSM flat jack test was conducted by an old method not in accordance with modern ISRM recommended practice. Because of the single test point, the lack of agreement with other measured data, the incomplete description of the geology at the test point, and the obsolete test method used, this data point is neglected in the determination of the elastic moduli to be used in modeling of the fault gouge material.

3.5.4.2 Mohr-Coulomb Failure Envelope

The USBR conducted strength tests on 30 specimens of fault gouge from the pilot bore of the EJMT including 2 UCS tests, 7 unconsolidated-undrained triaxial compression (UU-TXC), 7 consolidated-lateral strain controlled triaxial compression (K_0-TXC) (K_0-consolidated) tests, and 14 consolidated-undrained triaxial compression (CU-TXC) tests. USBR grouped these tests in various combinations and reported six different M-C strength envelopes for the fault gouge. By grouping the UCS, UU-TXC, and CU-TXC tests on a single plot of minor principal stress versus major principal stress at failure (Figure 3.8) the test results show a clear trend. Therefore, all the test results are analyzed together as a single material. As shown in Figure 3.8, regression to the test data results in an envelope with a passive earth pressure coefficient (slope of the regression) of 2.13 and an unconfined compressive strength of 89.4 kilopascals (kPa) (13.0 pounds per square inch (psi)). The coefficient of determination (r^2–value) of the regression is approximately 0.82

indicating a good fit to the data. The equivalent M-C failure envelope has a friction angle of 21.1° and a cohesion of 30.6 kPa (4.4 psi). The individual M-C envelopes as reported by USBR have friction angles ranging from 12° to 36° and cohesions ranging from 0 to 51 kPa (0 to 7.4 psi). The newly regressed failure envelope falls comfortably within these models as shown in Figure 3.8 and contains most of the models within a 68% prediction interval. Although the prediction interval does not have a constant width across the range of confining stresses, it varies in a narrow range of ±128 to 138 kPa (18.5 to 20 psi) from the regression line. A Hoek-Brown (H-B) envelope was considered for this material but was rejected because that failure criterion is intended for brittle materials and did not provide a significantly better fit to the data.

One shortcoming of the M-C failure envelope thus developed is the range of the test results. The highest confining stress used in the USBR laboratory testing was 459 kPa (66.5 psi) and the highest tested vertical stress on a sample was 1.28 MPa (186 psi). The estimated in-situ stresses in the vicinity of the pilot bore are a minor principal stress of 3.5 MPa (510 psi) and a major principal stress of 7.9 MPa (1150 psi) as shown in Figure 3.9. In general, it is poor engineering practice to use regression equations outside of the data range to which they were regressed. However, lacking any additional data or the ability to collect and test additional fault gouge samples, this research must progress with the M-C failure envelope as it is. It is strongly recommended that any future design work for the EJMT which builds upon this research be based on additional laboratory and in-situ tests.

3.5.4.3 Dilation Angle

Based on the reanalysis of the historical laboratory tests performed by Cohen (1971a,b), the dilation angle of the fault gouge material appears to be quite low, as one might expect for a normally consolidated soft clay (Lambe and Whitman 1969). Except for one test which dilated strongly after failure (52N-34-1 at 170 kPa (25 psi) confining pressure), the USBR-tested fault gouge specimens showed very small amounts of dilation (Figure 3.10). Excluding the single outlier data point and computing the dilation angle for the remaining 20 USBR tests gives dilation angles between zero and 6 degrees.

The best fit distribution to the dilation angle is debatable. By omitting the dilation angles equal to zero, it is possible to fit a lognormal or similar distribution to the data. However, a dilation angle of zero is a physically possible (and perhaps even likely) answer supported by the data. Alternatively, the single data point showing large dilation could reasonably be omitted as an outlier. Fitting a distribution to the data excluding the single

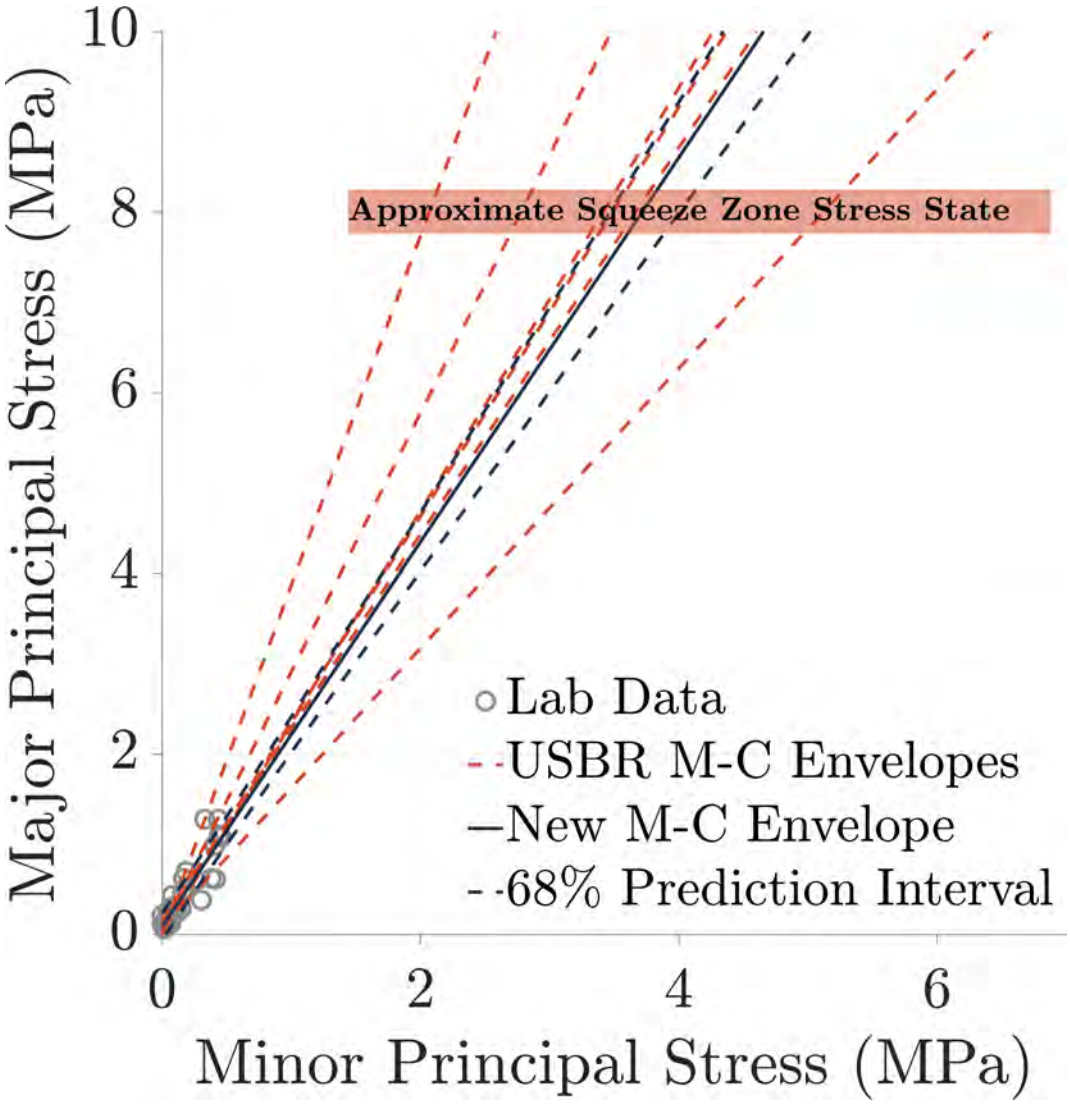

Figure 3.8: Data from USBR and historical Mohr-Coulomb yield envelopes developed by USBR for the fault gouge material, as compared to new probabilistic Mohr-Coulomb envelope developed for this research.

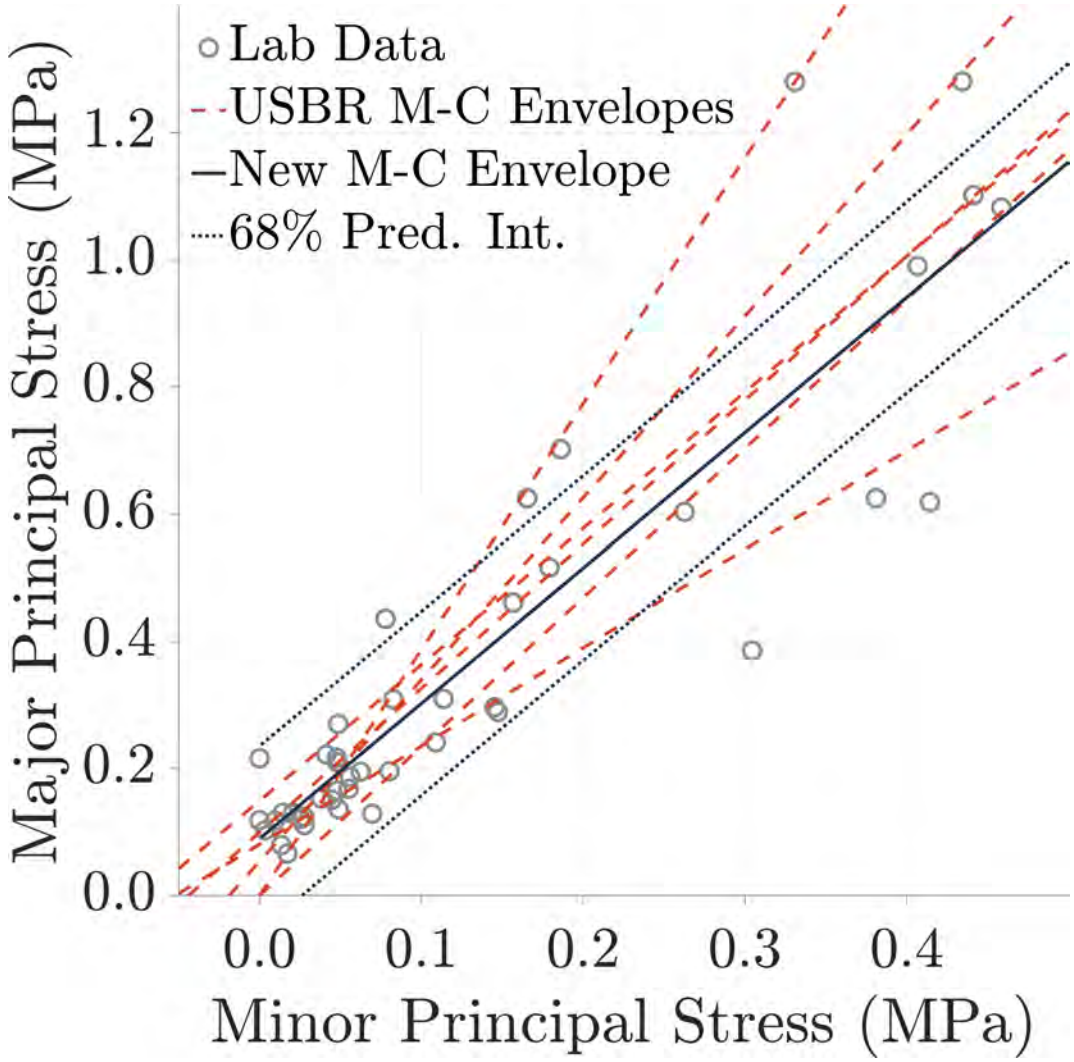

Figure 3.9: Mohr-Coulomb yield envelopes showing the tested data points and the actual range of estimated in-situ stresses in the squeeze zone.

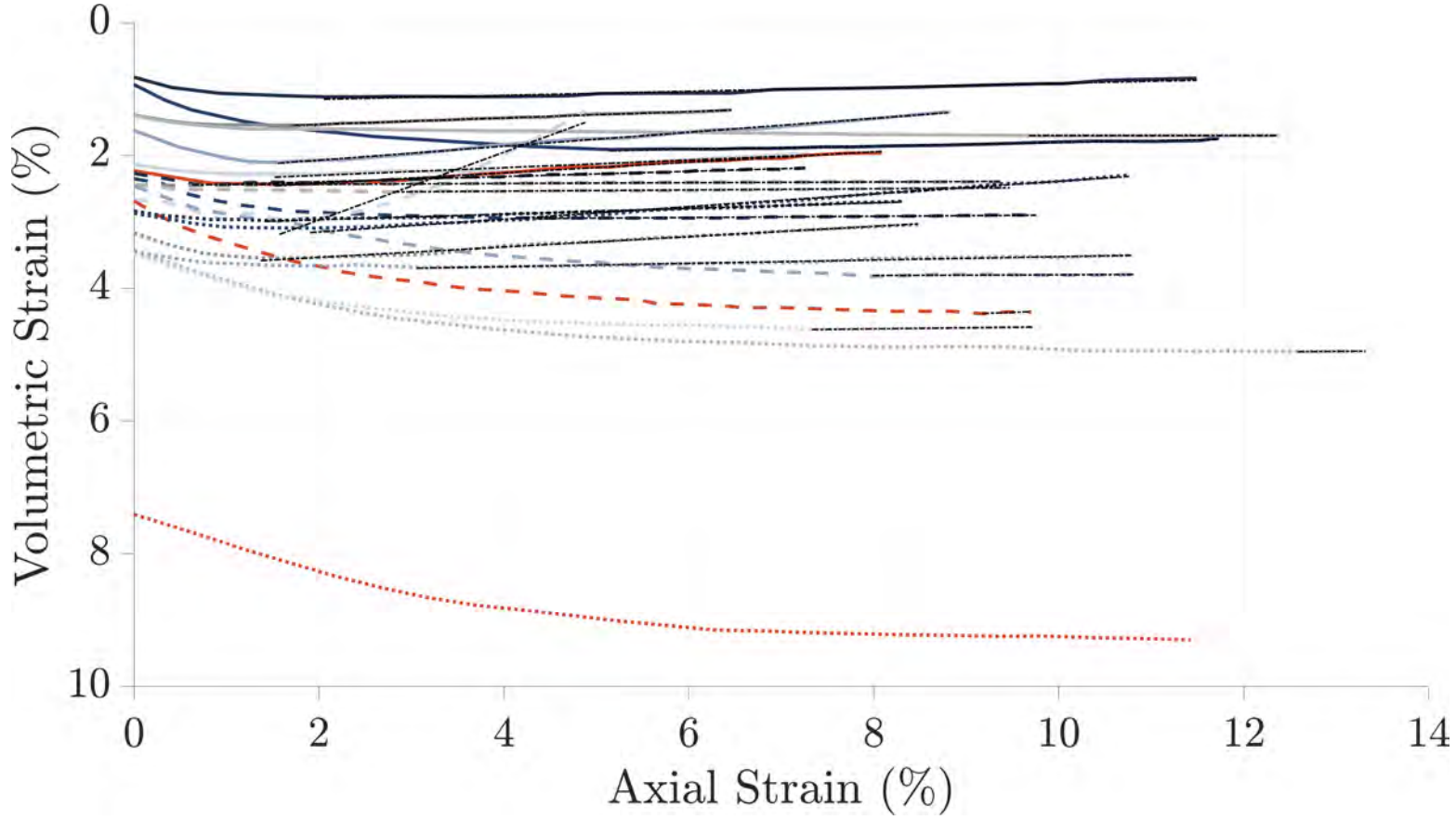

Figure 3.10: Axial-volumetric strain data from USBR for fault gouge materials showing dilation at end of curves. Note that dilation angles are relatively low for most samples.

large dilation point shows that a half-normal distribution fits the best (Figure 3.11). This gives the most likely value of the dilation angle as zero, with probability decaying rapidly for larger values of dilation angle. This half-normal distribution has a mean of 0° and a standard deviation of 1.33°.

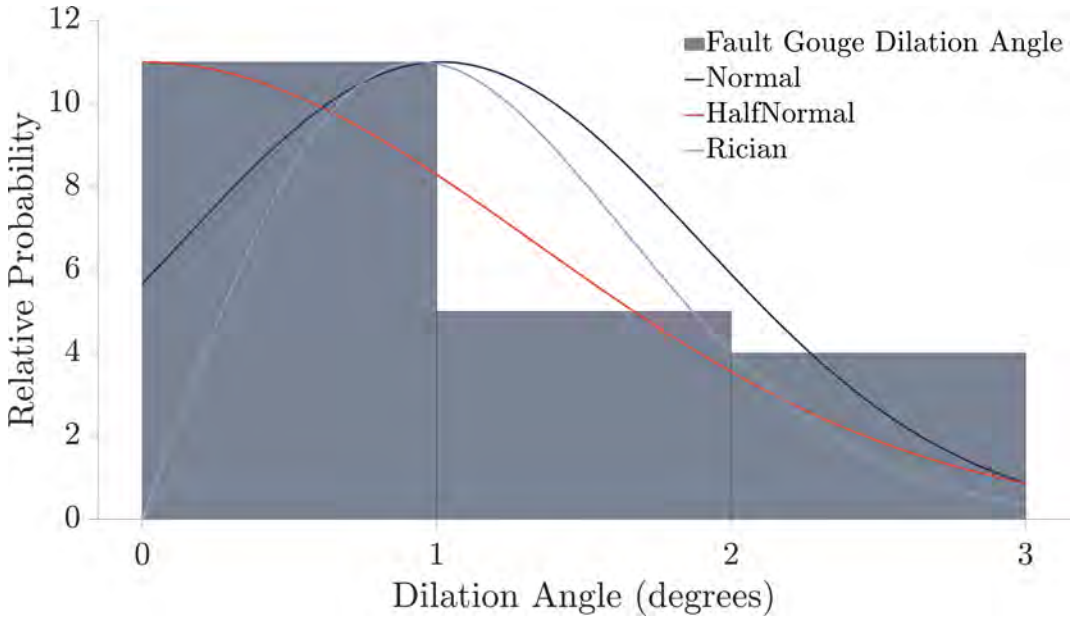

Figure 3.11: Histogram of dilation angles from axial-volumetric strain data from USBR for fault gouge materials with fitted statistical distributions.

3.5.5 Idaho Springs Formation Material Model

Two material models of the ISF are developed here. The first is a transversely isotropic material model developed in general accordance with the methodology recommended by Tien and Kuo (2001) and Tien et al. (2006). Samples that failed in a sliding failure mode (along the foliation) were grouped together to find a M-C strength envelope for the foliation. Samples that failed in a non-sliding failure mode (across the foliation) were grouped together. The non-sliding samples were evaluated first for the relationship between foliation angle and strength and then fitted with a H-B failure envelope and a M-C failure envelope.

The second material model is an isotropic model that is independent of ISF foliation angle and instead incorporates foliation angle uncertainty into the overall uncertainty associated with the model parameters. This reduced model allows for more efficient numerical model processing. Table 3.3 summarizes the material properties for this isotropic model.

Table 3.3: Idaho Springs Formation material properties summary.

Property	Units	Median	Mean	Min	Max	Distribution	Distribution Parameters
Dry Bulk Density	g/cm^3	2.684	2.691	2.57	2.830	NA	discrete parameter
Saturated Bulk Density	g/cm^3	2.720	2.722	2.590	2.840	NA	discrete parameter
Porosity	unitless	0.0175	0.0200	0.0060	0.0410	NA	discrete parameter
Young's Modulus	GPa	19.5	25.0	3.80	71.6	lognormal	$\mu = 3.035$, $\sigma = 0.6315$ truncated at 3 and 80 GPa, most likely value 14 GPa
Poisson's Ratio	unitless	0.16	0.18	0.11	0.37	beta	$a = 3.150$, $b = 5.259$
Friction Angle	degrees	NA	37.5	NA	NA	NA	discrete parameter, uncertainty in Mohr-Coulomb envelope captured by cohesion
Cohesion	MPa	NA	21.9	NA	NA	normal	$\mu = 21.9$, $\sigma = 10.4$

Notes: μ is the mean of a normal distribution, σ is the standard deviation of a normal distribution standard deviation, and a and b are the first and second shape parameters of a beta distribution.

There were 26 total test samples from the ISF. The USGS had nine samples from the ISF and an additional 17 samples were tested by the current research team. Two USGS samples were identified as gneiss, two samples were identified as schist, and five samples were identified as migmatite. Ten current samples were identified as gneiss and seven as migmatite. The samples were assumed to belong to various members of the ISF which grades from more schistose to more gneissic members; migmatite is considered a member of the gneissic end of this gradation.

One USGS sample (69+25.4N) has no information on whether the sample failed along or across foliation and was therefore excluded from this analysis. One USGS sample (6CR-62) had a strength 50% higher than the next highest sample and was excluded from the data set as an outlier. Of the remaining seven USGS samples 3 failed along the foliation, 3 failed across the grain of the foliation, and 1 failed partially along the foliation. The partial foliation failure was grouped with the non-foliation failures for this analysis on the assumption that the failure initiated at an angle to the foliation and then proceeded along the foliation.

One sample from the current study (04-03) had pre-existing fractures and inconsistent foliation orientation and was deemed un-testable. Data from another sample (23-03) were excluded from the analysis because the testing membrane ruptured during testing and the data were deemed unreliable. Of the new test samples 4 failed along the foliation and 13 failed across the foliation. Together with the historical data, there are 7 in the foliation failure mode analysis group and 17 samples in the non-foliation failure mode analysis group.

3.5.5.1 Elastic Moduli

The elastic moduli of foliated metamorphic rocks have been shown to be transversely isotropic by many researchers (Amadei 1988, 1996; Amadei and Savage 1993, 1989; Jaeger 1960; Ramamurthy 1993). In evaluating the variation of elastic moduli with foliation angle, various models have been proposed including polar, U-type, shoulder type, and undulatory type. This paper adopts the technique of Amadei (1996) in relating elastic moduli to foliation. Amadei suggests plotting elastic moduli on a polar graph where the angle is the foliation angle relative to vertical and the radius is the elastic modulus in question. An elliptical function is then fit to the data. The value of the elliptical function at any given angle is the anticipated value of the elastic modulus at that angle. Most importantly for this effort, the value of the elastic modulus at 0 and 90 degrees corresponds to the major and minor axis of the regressed elliptical function.

In keeping with the historical analysis by USGS, Young's modulus used in this analysis is a secant modulus. Santi et al. (2000) suggest using secant moduli modified for "strain offset from microfracture closing", sometimes referred to as "seating load", i.e. moving the origin of the coordinate system to account for variability in the initial portion of the stress-strain curve. The general assumption is that disturbance of the sample causes microfractures which are not representative of the in-situ material.

Note that USGS presented dynamic modulus data along with the static modulus data. Dynamic moduli are typically higher than static moduli, as with these samples. The regressed dynamic moduli are not directly relevant to the present work which seeks to calculate static load response.

The Young's modulus and Poisson's ratio of the ISF samples do not appear to be correlated to the confining pressure on the samples as demonstrated in Figure 3.12 and Figure 3.13. Therefore, elastic moduli presented in this section were calculated based on elastic moduli derived from both UCS and triaxial compression (TXC) tests.

As shown in Figure 3.14 the polar plot of Young's moduli versus foliation orientation shows a slightly stiffer material when loaded parallel to the foliation than when loaded perpendicular to the foliation. A similar pattern can be observed with Poisson's ratio. There is significant scatter of the data leading to wide prediction intervals. In general, the foliation dependence of the elastic moduli is far less than the variation of the material at any given angle. This suggests that an isotropic set of elastic properties with uncertainty may adequately represent this material, especially where foliation orientation in the ISF is unknown or uncertain. This is especially useful for application of the numerical model to positions within the broader 3D geologic model where foliation orientation is highly uncertain.

The best fit to Young's modulus data (irrespective of foliation angle or failure mode) as determined by a χ^2 goodness of fit test is a half-normal distribution (Figure 3.15). This would suggest that the most likely value for Young's modulus is zero. It seems likely in this case that the small number of data points is causing this non-intuitive fit. A lognormal fit is selected for the elastic moduli based on the best judgment of the author. A lognormal fit is commonly used for geomaterial properties in soil mechanics (Jones et al. 2002), and a normal distribution is sometimes assumed for rock moduli in practice. The ISF Young's modulus lognormal distribution is truncated at 3 gigapascals (GPa) and 80 GPa (the approximate upper and lower bounds of the data set for the ISF Young's modulus) to prevent unrealistically soft or stiff results from occurring in downstream modeling efforts. The lognormal distribution of ISF Young's moduli in units of MPa has parameters $\mu = 9.94$ and $\sigma = 0.632$. Based on this lognormal distribution of Young's

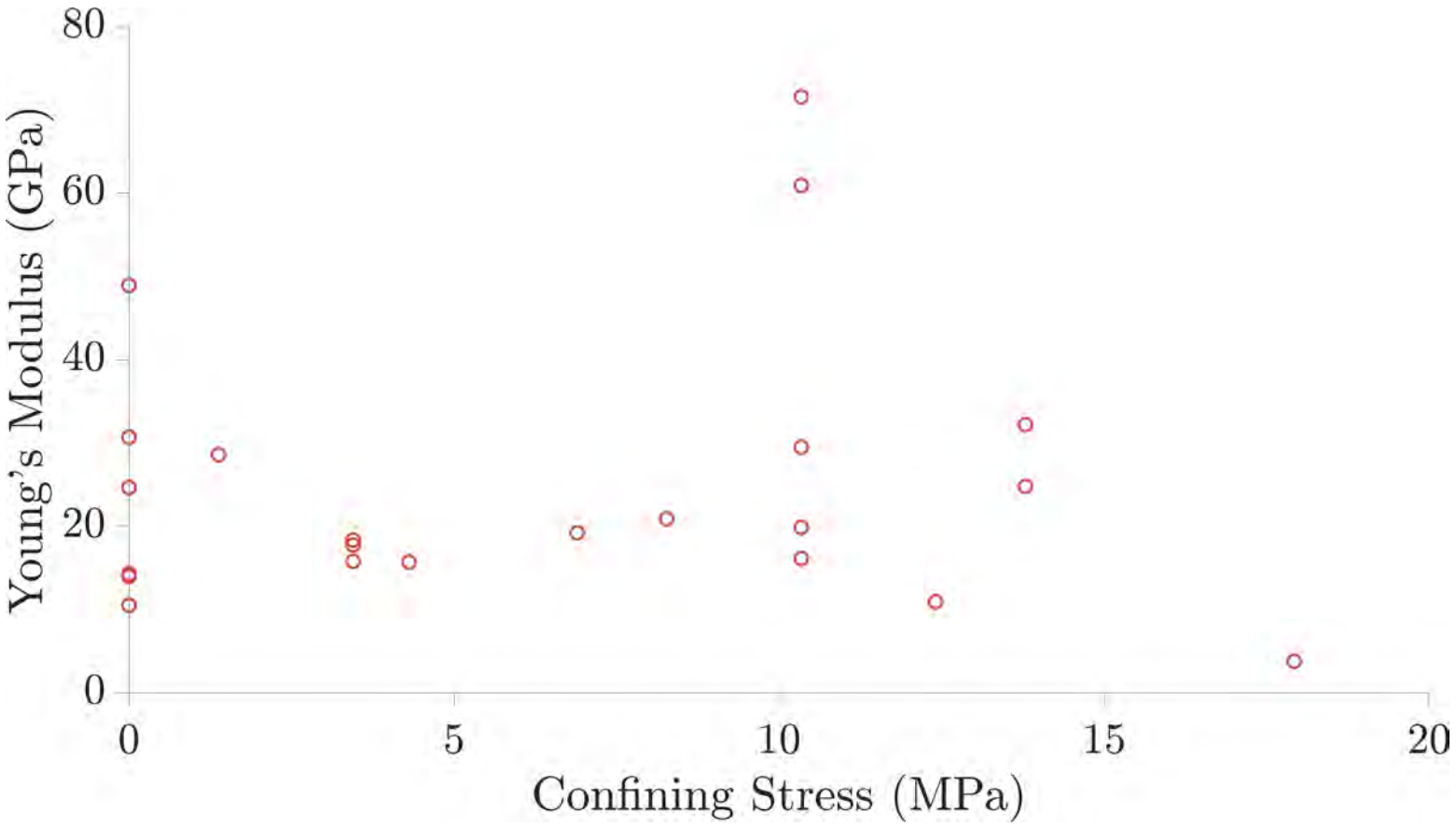

Figure 3.12: ISF Young's modulus from historical USGS data and current laboratory testing plotted versus confining stress.

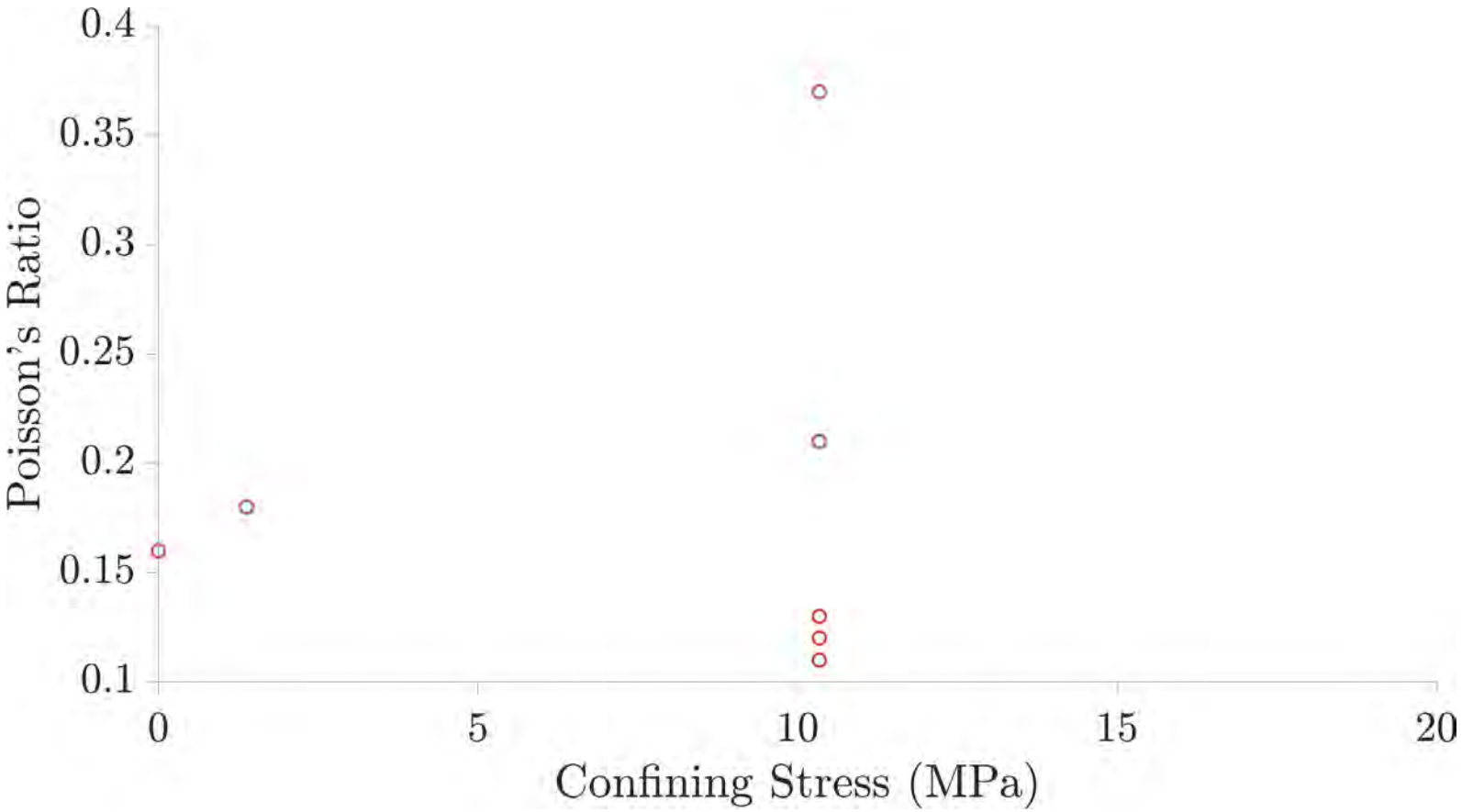

Figure 3.13: ISF Poisson's ratio from historical USGS data and current laboratory testing plotted versus confining stress.

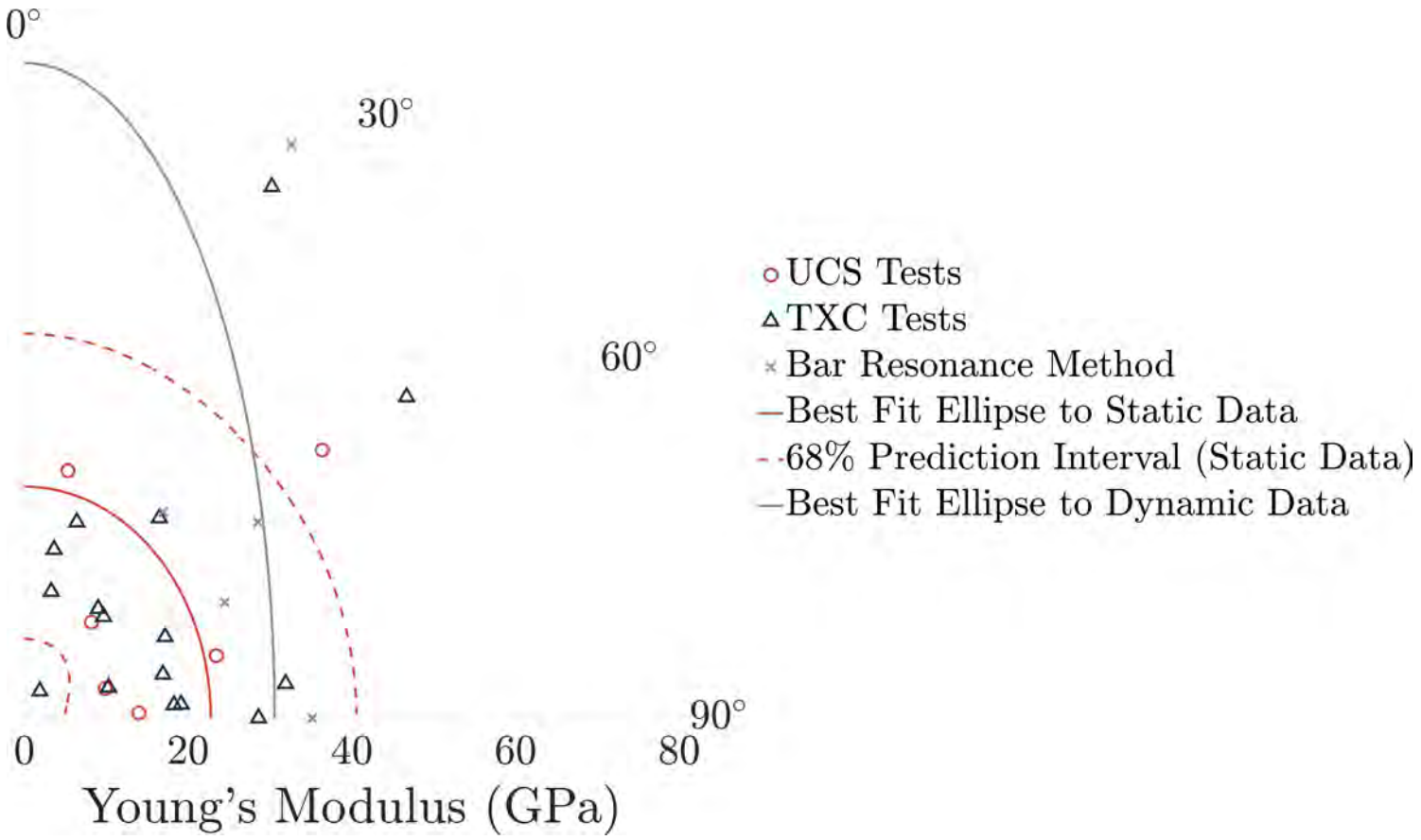

Figure 3.14: ISF Young's modulus from historical USGS data and current laboratory testing plotted versus angle of foliation from vertical.

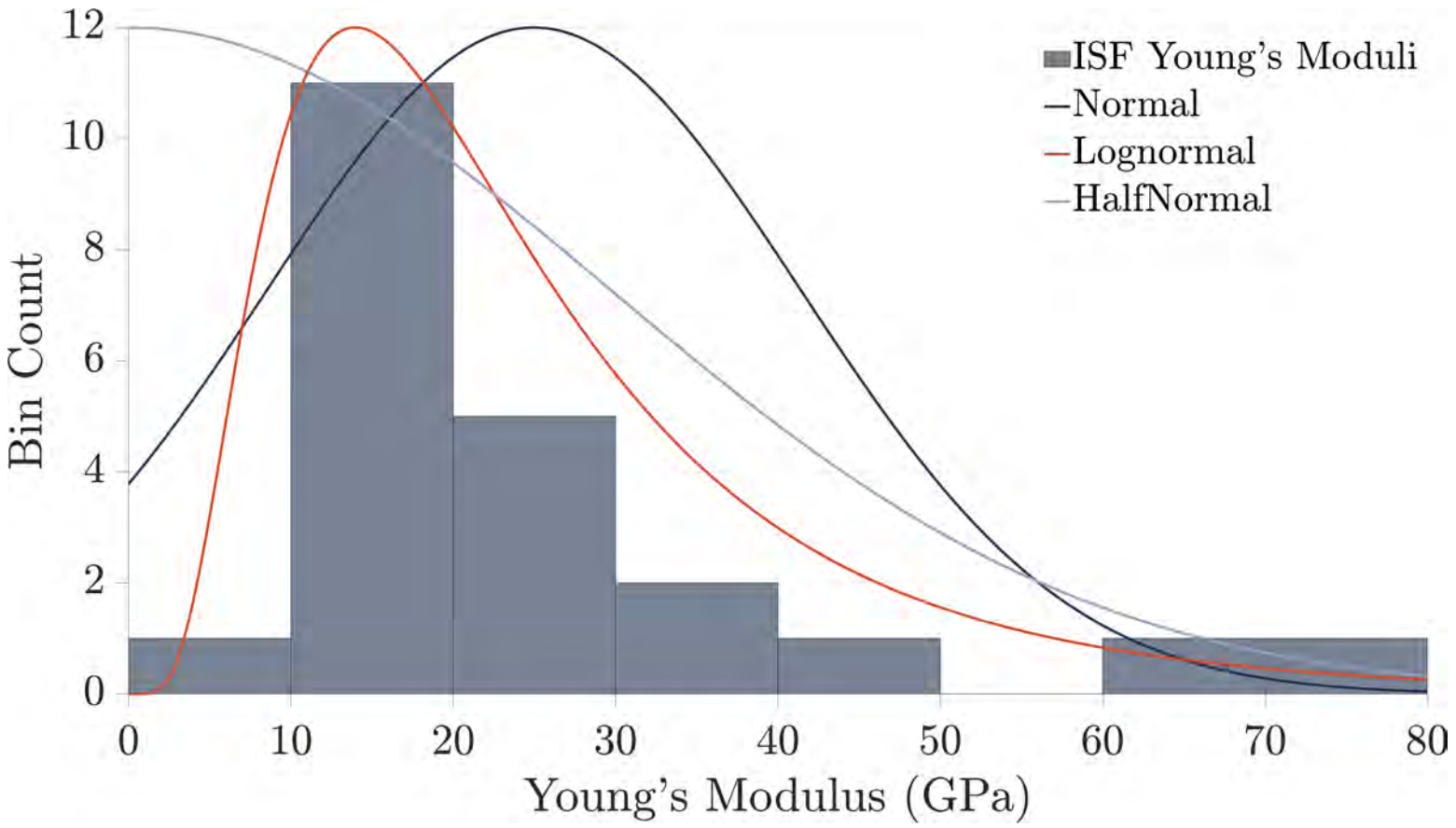

Figure 3.15: Histogram of ISF Young's modulus from historical USGS data and current laboratory testing with fitted distributions.

moduli, the most likely Young's modulus for the intact ISF is 14 GPa.

The best fit to the Poisson's ratio data (irrespective of foliation angle or failure mode) as determined by a χ^2 goodness of fit test is a Rician distribution (Figure 3.16). However, a beta distribution was selected as the best fit for practical application because it is inherently bounded at either end. For the purposes of numerical stability, it is necessary to limit the input Poisson's ratio to a range between 0 and 0.5, exclusive. Therefore, a beta distribution can be applied without additional truncation or error trapping in the numerical modeling code. The most likely value of Poisson's ratio from the beta distribution is 0.168 while the most likely value of Poisson's ratio from the Rician distribution is 0.178.

3.5.5.2 Foliation Yield Model

Figure 3.17 shows the failure modes of the ISF unconfined compression and triaxial compression tests plotted against their foliation orientations relative to vertical.

The stress state at the failure of the seven foliation failure mode samples was plotted in principal stress space as shown in Figure 3.18. The M-C envelope in Figure 3.18 has a slope and intercept in principal stress space of 5.05 and 61.7 MPa, respectively. These correspond to a friction angle of 42.0° and a cohesion of 13.7 MPa. The r^2–value of this correlation is 0.32, indicating the relatively wide scatter of the data.

A H-B envelope was also fit to the foliation failure mode data as shown in Figure 3.19. This envelope has parameters $m_i = 20.1$ and $\sigma_{ci} = 45.2$ and a r^2–value of 0.37. Because the r^2–value of the H-B envelope is not a great improvement over the M-C envelope, the M-C model is preferred for simplicity of analysis.

3.5.5.3 Cross-Foliation Yield Model

Because of the relatively high joint strength of this material, the angle of minimum strength (as measured from vertical) is 20.8°, on the low end of the Tien and Kuo (2001) and Tien et al. (2006) suggested typical range. This means that there are no TXC tests available with foliation sub-parallel loading with a failure through the bulk material (not along the foliation). The closest option is sample 21-05 where the angle of foliation is 10°. The next closest option is sample 02-06 where the angle of foliation is 35°. Moreover, as shown in Figure 3, the non-sliding failure mode samples do not show a clear trend of strength relative to foliation orientation. This suggests that the ISF material aside from the foliation behaves in a generally isotropic manner. Further laboratory testing to confirm this assumption may be warranted, but for the purposes of this study it is assumed that

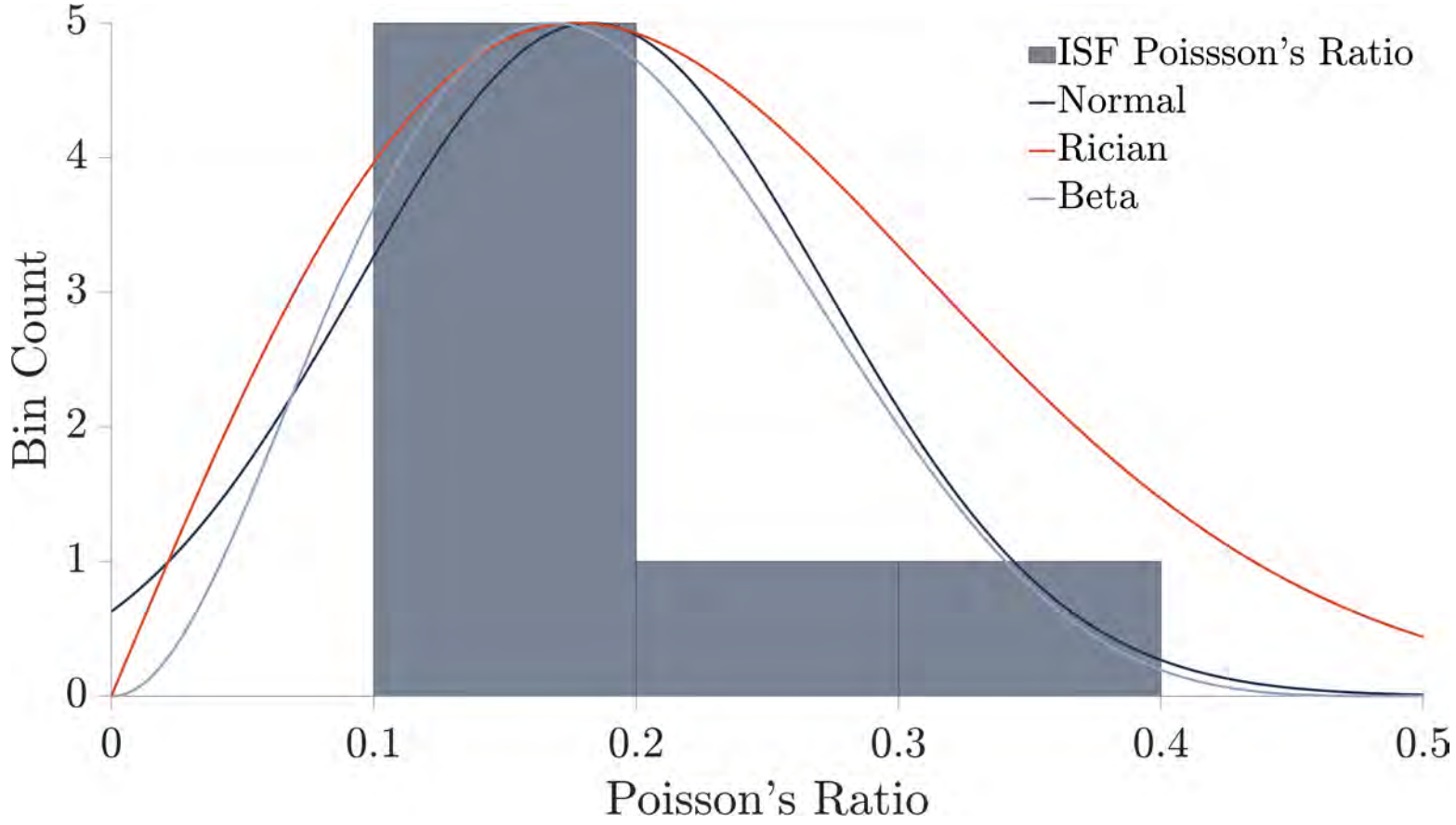

Figure 3.16: Histogram of ISF Poisson's ratio from historical USGS data and current laboratory testing with fitted distributions.

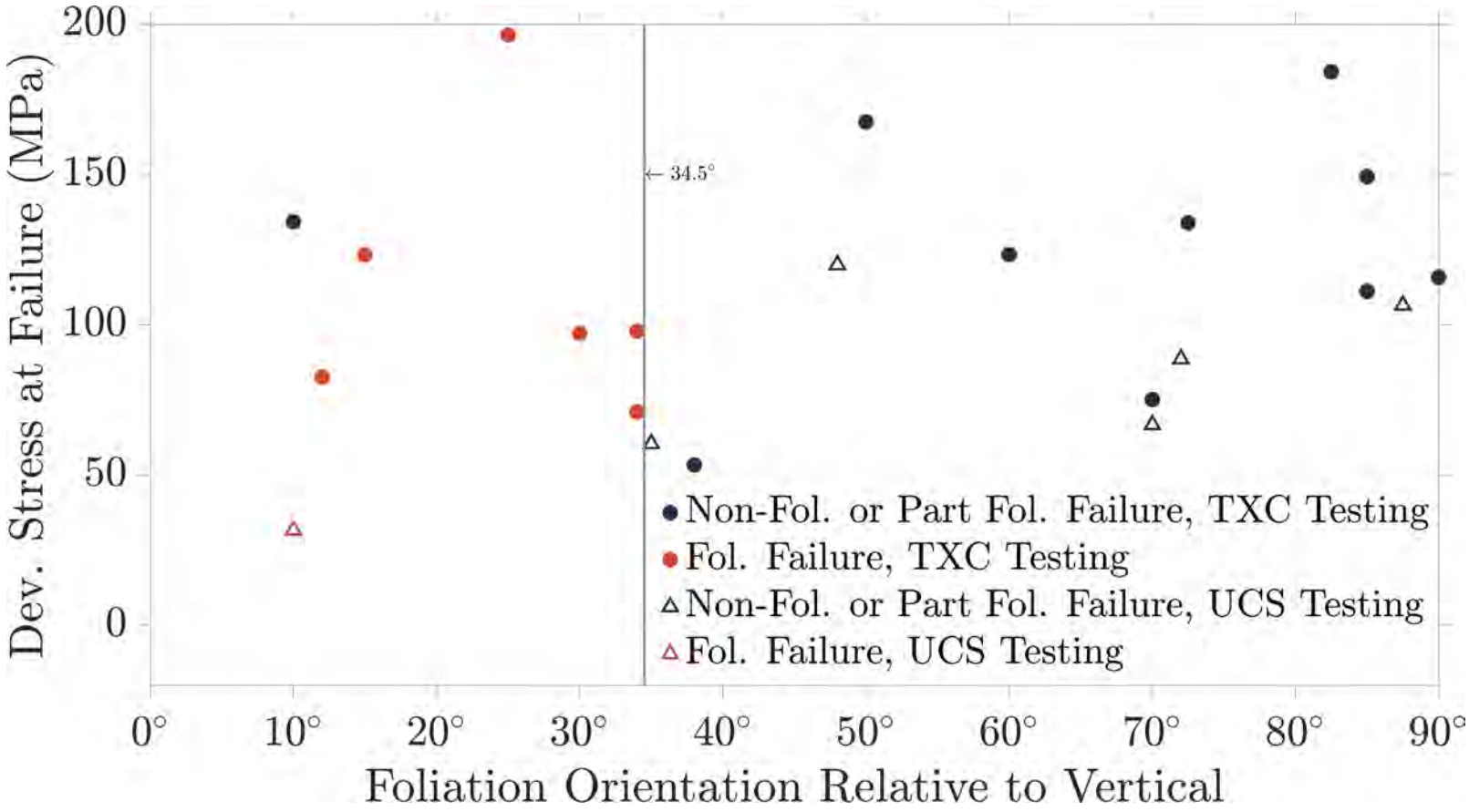

Figure 3.17: ISF deviator stress at failure versus failure mode from historical USGS data and current laboratory testing. With a single exception, the failure modes divide into two groups with a change in failure mode at 34.5°. For the transversely isotropic yield model the samples were divided into foliation and non-foliation failures and yield envelopes developed separately for each mode.

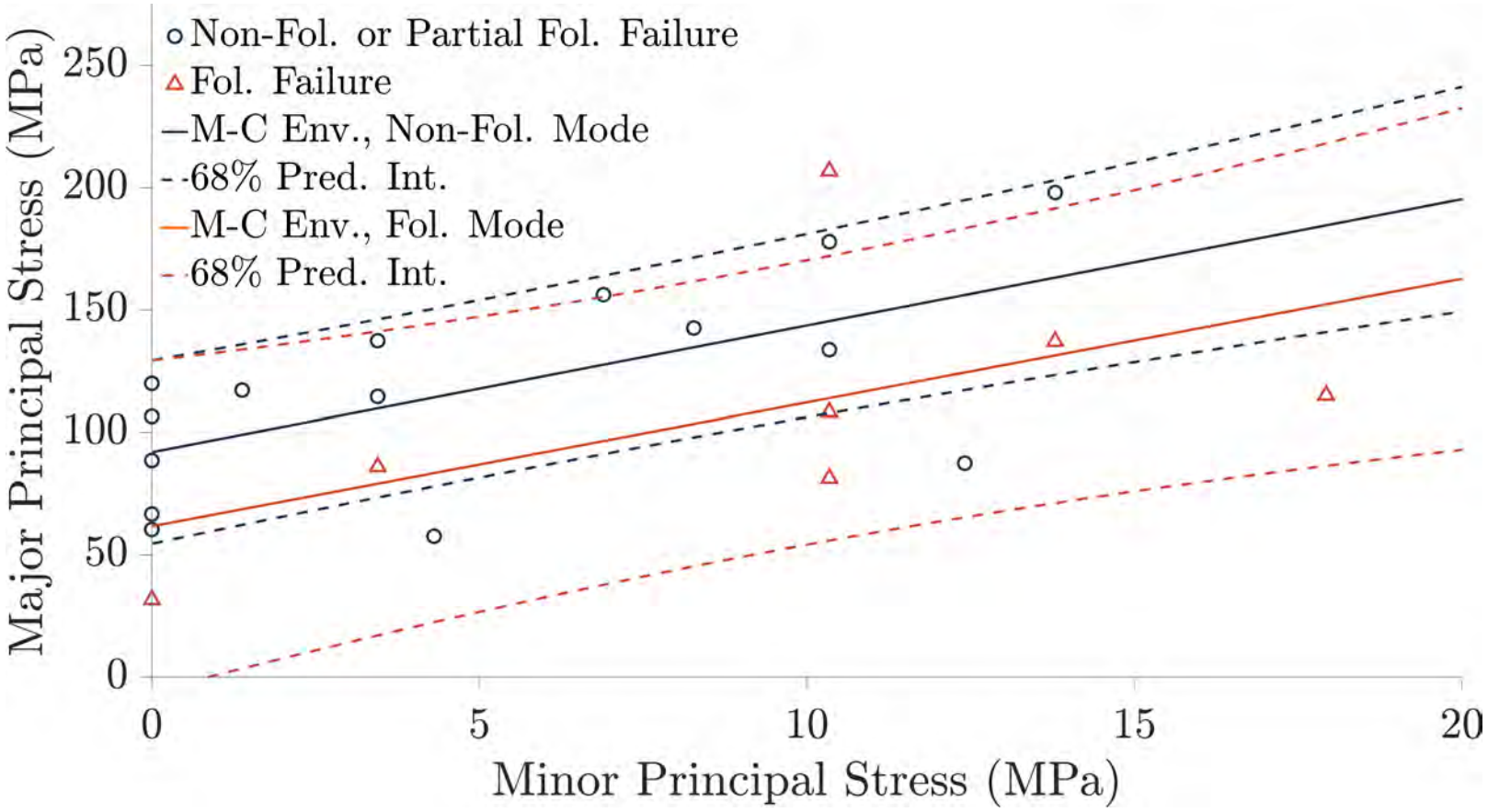

Figure 3.18: ISF Mohr-Coulomb yield envelopes from historical USGS data and current laboratory testing regressed separately to sliding and non-sliding (foliation and non-foliation) failure modes.

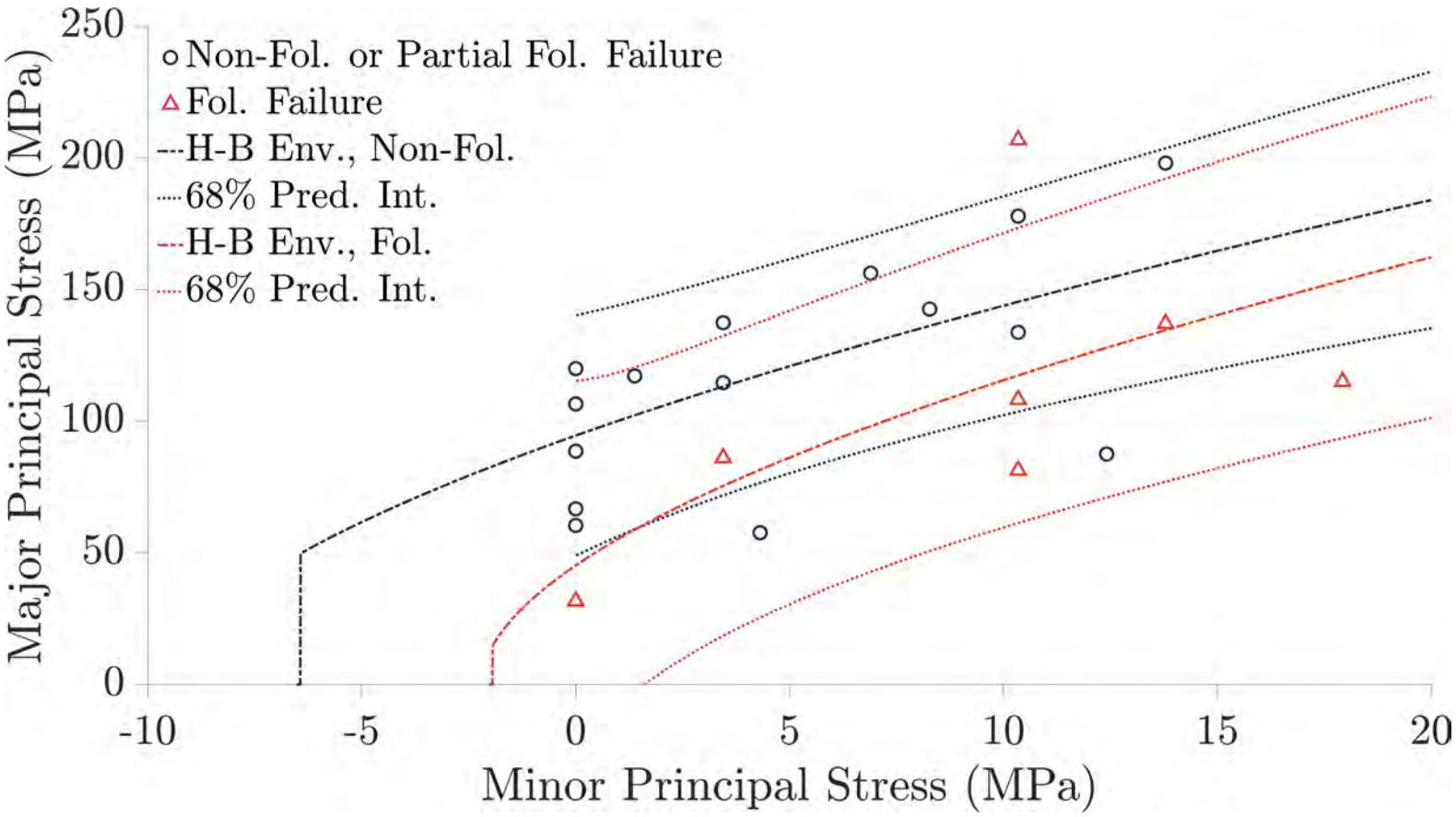

Figure 3.19: ISF Hoek-Brown yield envelopes from historical USGS data and current laboratory testing regressed separately to sliding and non-sliding (foliation and non-foliation) failure modes.

the bulk material is isotropic.

The stress state at the failure of the 17 non-foliation failure mode samples was plotted in principal stress space as shown in Figure 3.18. The M-C envelope in Figure 3.18 has a slope and intercept in principal stress space of 5.17 and 92.0 MPa, respectively. These correspond to a friction angle of 42.5° and a cohesion of 20.2 MPa. The r^2–value of this correlation is 0.34, indicating the relatively poor fit of this linear model to the data.

A H-B envelope was also fit to the non-foliation failure mode data as shown in Figure 3.19. This envelope has parameters $m_i = 9.50$ and $\sigma_{ci} = 94.6$ and a r^2–value of 0.28. Note that the use of the curved H-B envelope reduces the r^2–value of the curve fit, suggesting that a M-C envelope may actually be preferable for forward modeling.

3.5.5.4 Isotropic Yield Model

As can be seen in Figure 3.18 and Figure 3.19 there is significant scatter around the regressed envelopes to the foliation and non-foliation failure modes, the yield envelopes are close to parallel, and the confidence intervals for the yield envelopes have significant overlap. This uncertainty likely reflects the wide variability of the rocks making up the ISF which contains rocks ranging from schist to gneiss, with migmatite samples including some intrusions of the SPG into gneiss. Moreover, the use of the separate yield models requires knowledge of the local orientation of the ISF foliation. Foliation orientation can change rapidly and unexpectedly. There is also limited ability to propagate foliation orientation across the 3D geologic model with any reasonable level of certainty. Therefore, further analyses in this report reduce the yield model to a single envelope with uncertainty and model the ISF as an isotropic material for this preliminary level of analysis. This model reduction has the additional benefit of increasing the processing speed of forward models. Therefore M-C and H-B yield envelopes were regressed to the full data set of 24 samples without differentiation for foliation orientation or failure mode as shown in Figure 3.20.

The M-C envelope in Figure 3.20 has a slope and intercept in principal stress space of 4.12 and 88.7 MPa, respectively. These correspond to a friction angle of 37.5° and a cohesion of 21.9 MPa. The r^2–value of this correlation is 0.27, indicating the wide scatter in the data.

A H-B envelope was also fit to all 24 data points, also shown in Figure 3.20. This envelope has parameters $m_i = 5.48$ and $\sigma_{ci} = 97.4$ and a r^2–value of 0.14. Again, the use of the curved H-B envelope reduces the quality of the curve fit, suggesting that a M-C envelope is preferable for forward modeling. Although there remains significant scatter

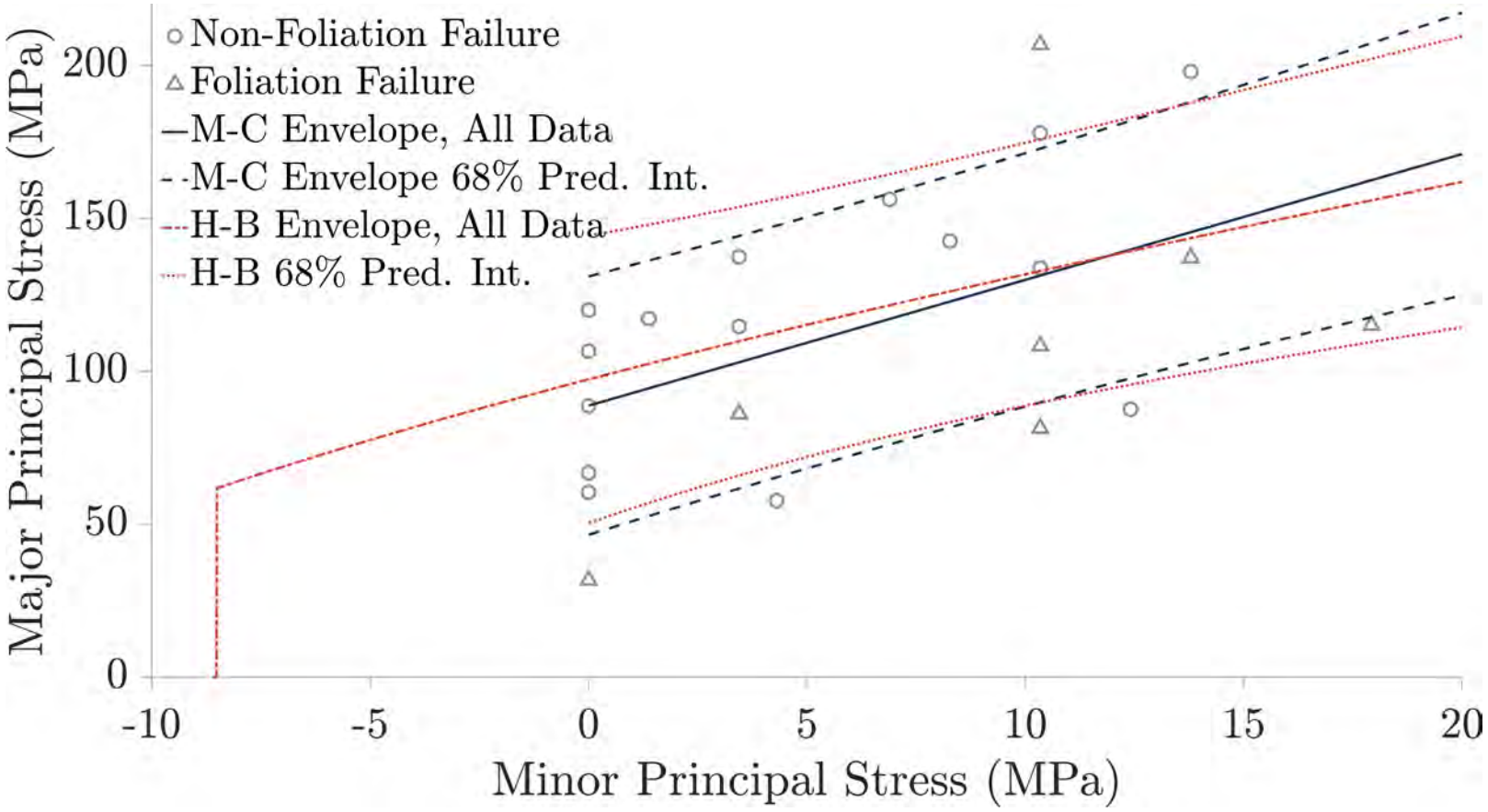

Figure 3.20: ISF Hoek-Brown and Mohr-Coulomb yield envelopes regressed to all data points regardless of failure mode (sliding/folation or non-sliding/non-foliation).

around the failure envelope, the reduction to a single isotropic M-C yield envelope with uncertainty is ideal for early-stage probabilistic modeling by application of MC simulation.

3.5.5.5 Unconfined Compressive Strength

There are six available unconfined compressive strength tests on the ISF with a range of results from 30 to 120 MPa. The mean unconfined compressive strength of these samples is 79 MPa and the standard deviation of the seven samples is 32 MPa. A normal distribution was constructed for predicting uniaxial compressive strength of the ISF with a mean of 97 MPa and a standard deviation of 47 MPa, truncated at 30 and 120 MPa. The mean of this distribution represents the intercept of the H-B failure envelope with $\sigma_3 = 0$ while the wider distribution was selected to better represent the prediction interval of the H-B failure envelope at zero confining stress. The distribution was truncated in forward modeling to prevent prediction of UCS values not represented by test data.

3.5.6 Silver Plume Granite Material Model

The material model used for the SPG in this research is based primarily upon the laboratory testing performed by the USGS during the construction of the pilot bore of the EJMT and reported by Nichols and Lee (1966) and Robinson et al. (1974). Of the reported laboratory tests, there are 30 TXC test results, 8 UCS test results, and 7 tensile test results on samples of the SPG. 17 of the TXC test results, 6 of the UCS test results, and 5 of the tensile test results indicate that the samples were not fractured, and that failure did not occur along any pre-existing plane of weakness, such as a healed fracture.

For confirmation, this research team also tested one UCS and three TXC specimens of SPG material collected from the surface in the vicinity of the tunnel. Results of the confirmation tests are generally in line with the historical data and are included in the regression analysis. Table 3.4 summarizes the material properties developed in this analysis.

3.5.6.1 Elastic Moduli

Young's modulus (Figure 3.21) and Poisson's ratio (Figure 3.22) of the SPG were plotted against confining stress to evaluate the dependence of these parameters on confinement. There does not appear to be a clear correlation between either of these elastic moduli and confining stress.

Several distributions were fit to the available Young's modulus data. Figure 3.23 shows normal and lognormal distributions for comparison. Overall, the Young's modulus data

Table 3.4: Silver Plume Granite material properties summary.

Property	Units	Median	Mean	Min	Max	Distribution	Distribution Parameters
Dry Bulk Density	g/cm^3	2.638	2.637	2.56	2.720	NA	discrete parameter
Saturated Bulk Density	g/cm^3	2.640	2.643	2.590	2.700	NA	discrete parameter
Porosity	unitless	0.0105	0.0130	0.0030	0.0330	NA	discrete parameter
Young's Modulus	GPa	59.0	55.0	21.1	77.9	normal	$\mu = 55.0$, $\sigma = 16.0$ truncated at 20 and 80 GPa
Poisson's Ratio	unitless	0.20	0.23	0.13	0.39	beta	$a = 5.202$, $b = 6.244$
H-B Slope Parameter m_i	unitless	NA	22.6	NA	NA	NA	discrete parameter, uncertainty in H-B envelope captured by UCS
Unconfined Compressive Strength σ_{ci}	MPa	NA	180	124	236	normal	$\mu = 180$, $\sigma = 55.9$, truncated at 100 and 230 GPa

Notes: μ is the mean of a normal distribution, σ is the standard deviation of a normal distribution standard deviation, and a and b are the first and second shape parameters of a beta distribution.

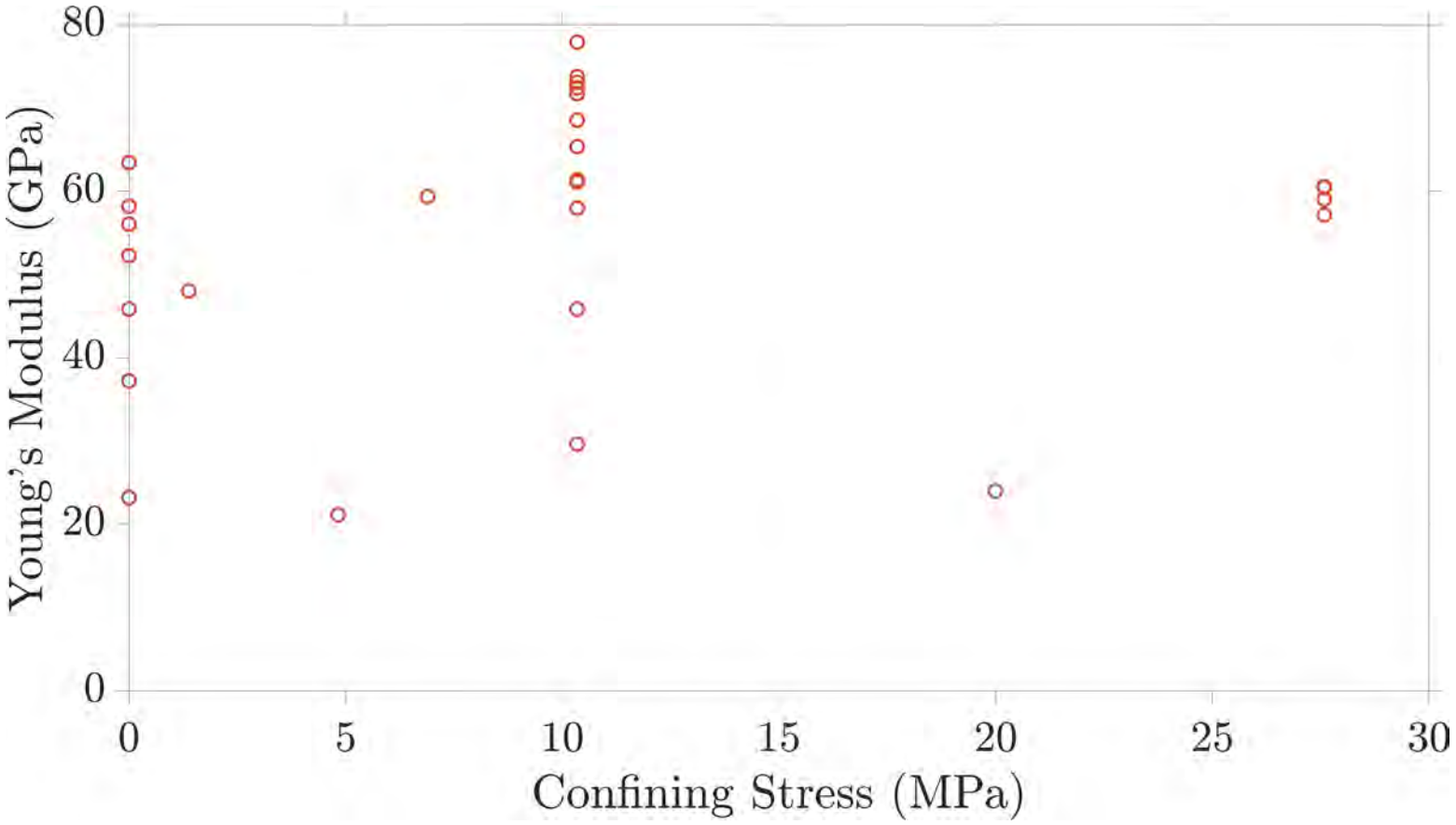

Figure 3.21: Variation of SPG Young's modulus with confining stress based on current and historical laboratory testing.

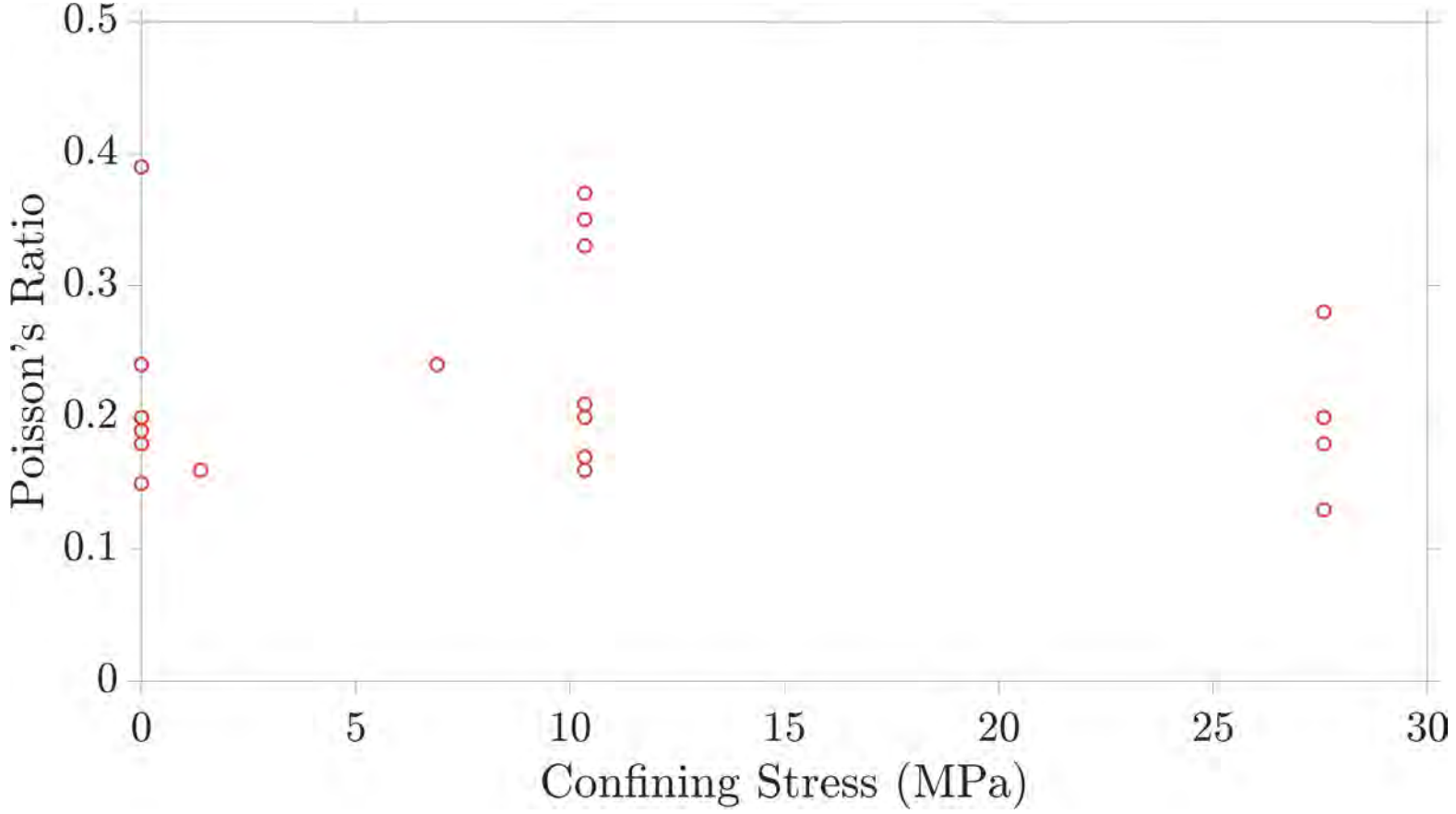

Figure 3.22: Variation of SPG Poisson's ratio with confining stress based on current and historical laboratory testing.

do not show a clear tendency towards any particular distribution. A normal distribution was selected as having the best χ^2 statistic and being a reasonable default scenario. The SPG Young's modulus normal distribution is truncated at 20 GPa and 80 GPa (the approximate upper and lower bounds of the data set for the SPG Young's modulus) to prevent unrealistically soft or stiff results from occurring in downstream modeling efforts. The normal distribution of Young's moduli has a mean of 55.0 GPa and a standard deviation of 16.0 GPa.

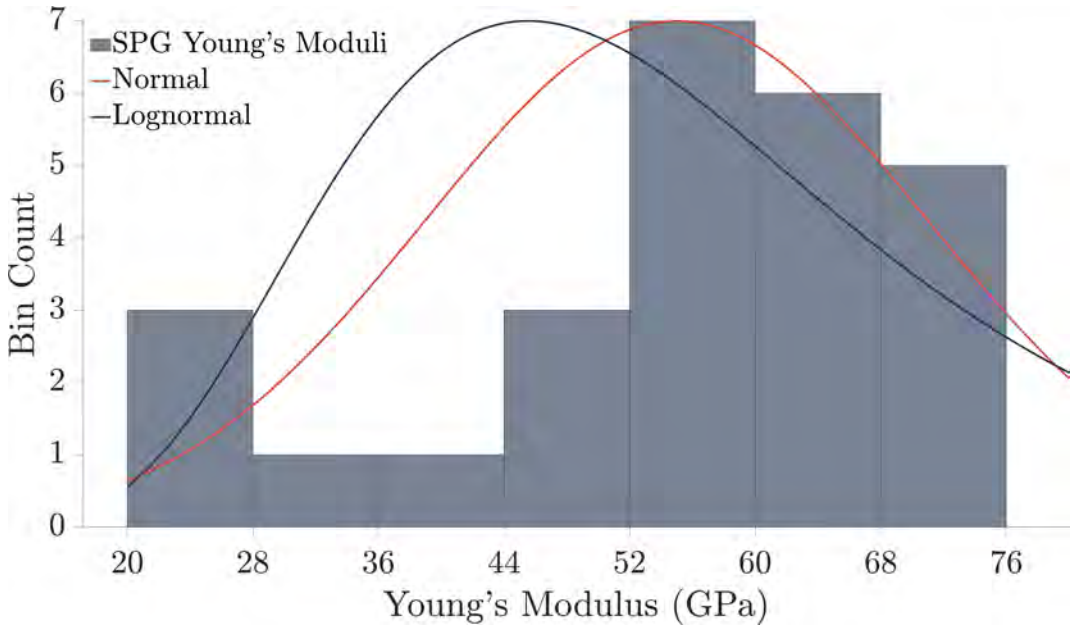

Figure 3.23: Histogram of SPG Young's modulus data based on current and historical laboratory testing with fitted distributions.

3.5.6.2 Unconfined Compressive Strength

There are seven available unconfined compressive strength tests on the SPG with a range of results from 100 to 230 MPa. The mean unconfined compressive strength of these samples is 175 MPa and the standard deviation of the seven samples is 42 MPa. A normal distribution was constructed for predicting uniaxial compressive strength of the SPG with a mean of 180 MPa and a standard deviation of 56 MPa, truncated at 100 and 230 MPa. The slightly wider and higher distribution was selected to better represent the prediction interval of the H-B failure envelope at zero confining stress. The distribution was also truncated to prevent predictions of UCS values not represented by test data in forward modeling.

3.5.6.3 Hoek-Brown Criterion

A H-B failure envelope was fit to the data from unfractured samples as shown in Figure 3.24. The mean UCS strength was used as a single data point in the regression per the recommendation of Hoek and Brown (2018). The tensile strength of this model was limited to the mean reported tensile strength of the material. The regressed model shown in Figure 3.24 has H-B intact material parameters of $m_i = 22.6$, $\sigma_{ci} = 179.6$ MPa, and tensile strength of 7.1 MPa. The r^2–value of this regression is 0.66, indicating a relatively good fit with some scatter in the data. The 68% prediction interval for the envelope with confining stress greater than zero has a width that varies about the regression in a range of ±50 to 56.5 MPa.

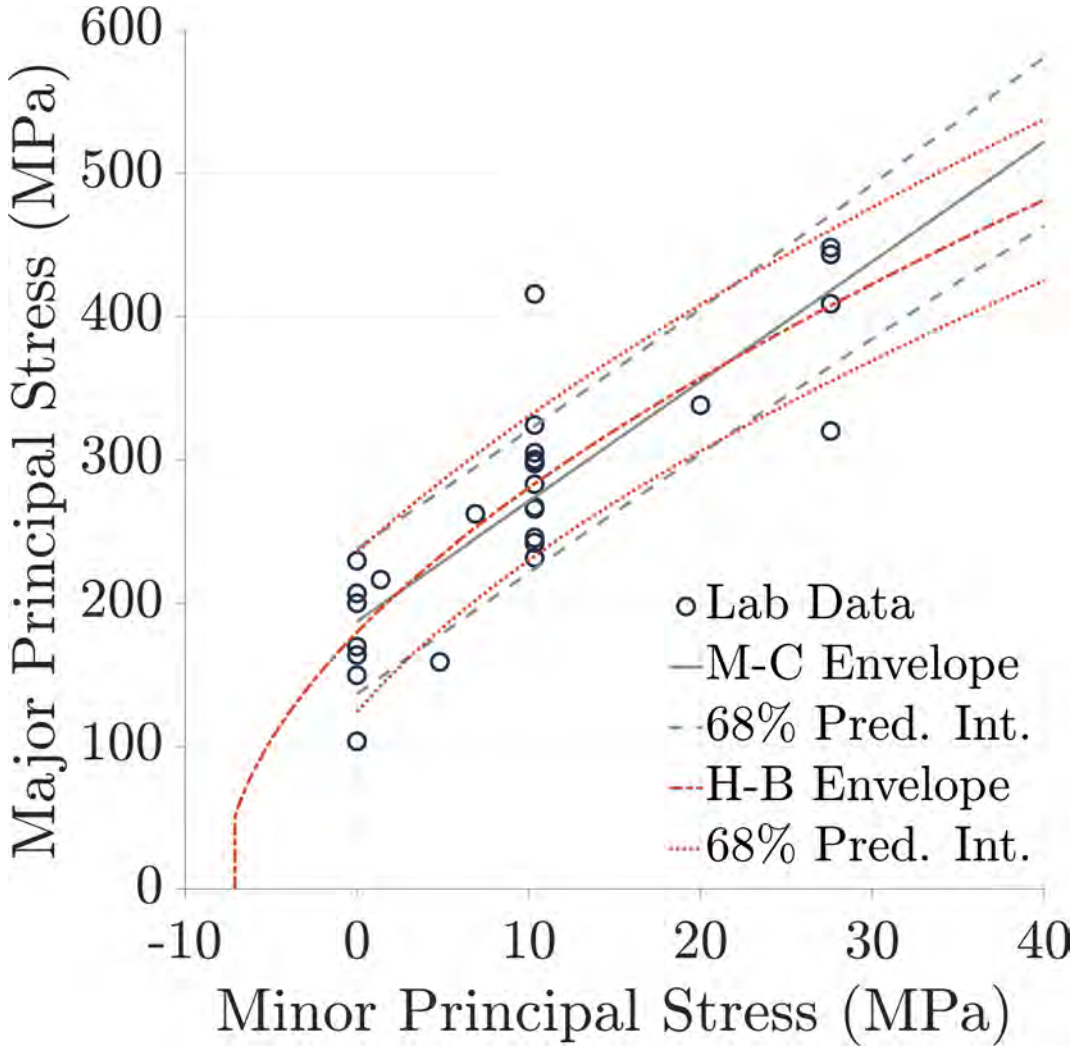

Figure 3.24: Silver Plume Granite yield envelopes (Mohr–Coulomb and Hoek–Brown) with 68% prediction intervals based on current and historical laboratory testing.

Hoek and Brown (2018) recommend using a tension cutoff on the strength envelope. The suggested empirical model for this tension cutoff is Equation 3.3, which in this case gives a maximum tensile strength of 7.1 MPa. This agrees well with laboratory test data for tensile strength reported by USGS which had a mean tensile strength of 8.9 MPa.

$$\sigma_t = \frac{\sigma_{ci}}{0.81m_i + 7} \tag{3.3}$$

where σ_t is tensile strength, σ_{ci} is uniaxial compressive strength, and m_i is the intact H-B material parameter.

3.5.7 Groundwater Conditions

Pilot bore groundwater data were digitized from the hard copy graph included in the report by Robinson et al. (1974). Groundwater flow values were then linearly interpolated from this data set at the points of interest along the pilot bore. Figure 3.25 shows groundwater flow data plotted versus depth, joint frequency, joint condition, month excavated, lithology, and distance to a mapped fault, all of which might reasonably be expected to have some correlation to groundwater flow. Note some apparent correlation to month, depth, joint frequency, and distance to a mapped fault but less apparent correlation to joint condition or lithology. The correlations do not have a clear distribution. Almost all correlations have a lower bound near zero and a variable upper bound.

Each of the variables which appeared to have some correlation to groundwater flow (depth, joint frequency, excavation date, and distance to nearest fault) was evaluated by linear least–squares regression for its actual correlation to groundwater flow. Each independent variable was binned appropriately. Depth was binned in 1 m increments from 0 to 460 m. Joint frequency has a small number of discrete unique values and so is not binned. The excavation month data are already categorical. The fault distance data were binned in 1 m increments from 0 to 100 m. The minimum, mean, median, and maximum face flow values (in L/min) for each bin of each independent variable were calculated. Face flows were then predicted for each station as the mean and median bin values applicable to that station for each independent variable. The r^2–value of each face flow prediction is calculated per Equation 2.69. r^2–value based on a mean and median prediction are tabulated in Table 3.5.

Note that the face flow as predicted by the depth and month appear to have the best correlation to the recorded face flow data, with the mean estimate being significantly better than the median estimate. A least–squares regression to a multi-linear function was used to develop a weighted average prediction of face flow based on the depth, joint

Table 3.5: Coefficients of determination, r^2, for face flow predictions based on correlation to depth, joint frequency, excavation month, and distance to the nearest mapped fault.

Correlation Parameter	r^2_{median}	r^2_{mean}
Depth	0.41	0.53
Joint Frequency	-0.10	0.04
Month	0.03	0.22
Fault Distance	-0.11	0.02

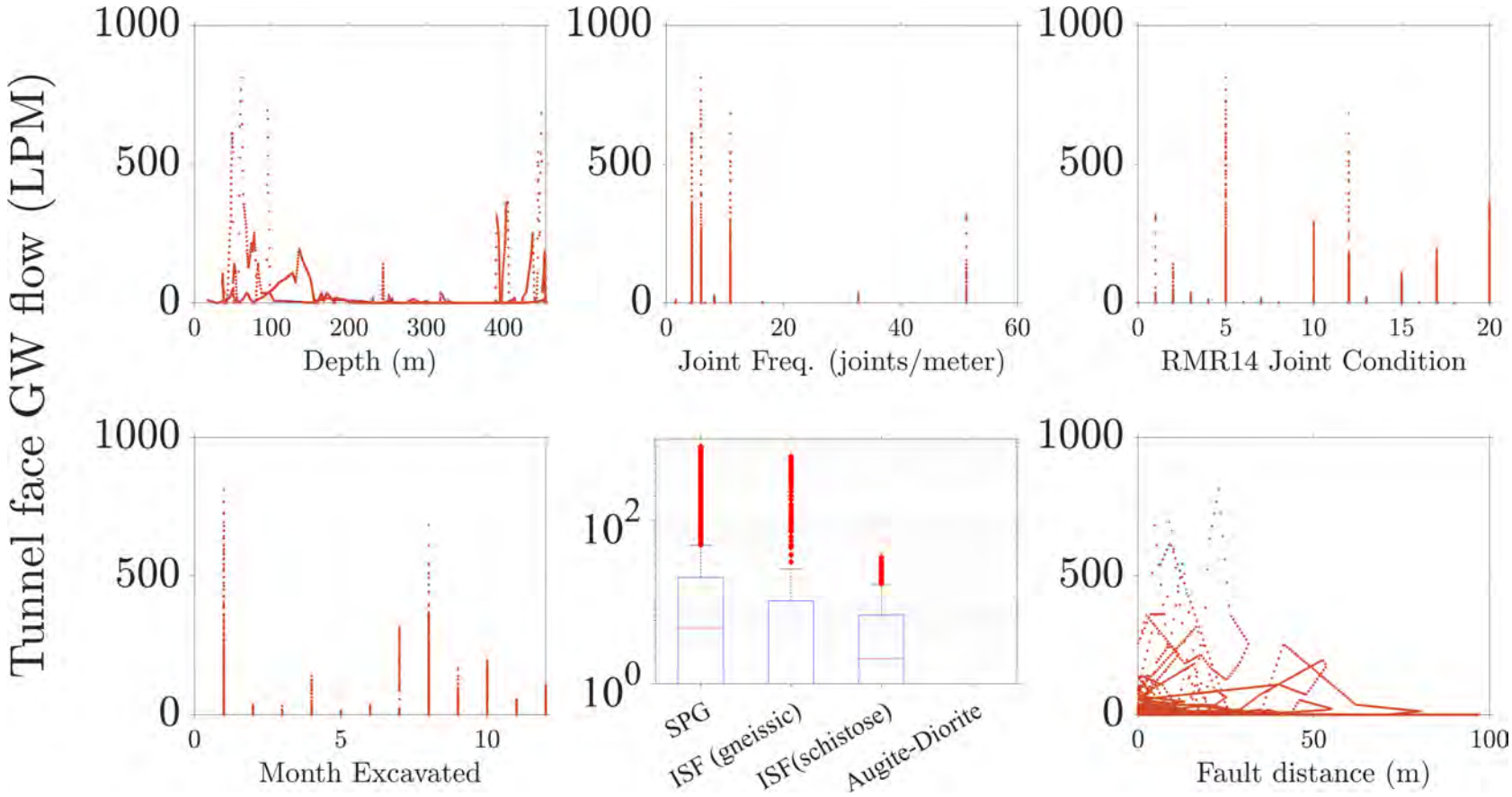

Figure 3.25: Face flow data recorded in the pilot bore vs. various other data recorded in the pilot bore.

frequency, month, and fault distance. Joint frequency and fault distance were found to negligibly increase the accuracy of the regression and were therefore excluded. The selected multi-linear regression model for predicting face flow is presented in Equation 3.4. This equation has a r^2–value of 0.55 suggesting that it reasonably predicts groundwater flow but has significant uncertainty.

$$FaceFlow(LPM) = 0.8 \cdot F(depth) + 0.2 \cdot F(month) \tag{3.4}$$

where $F(depth)$ is the mean face flow measured in the pilot bore binned by depth and $F(month)$ is the mean face flow measured in the pilot bore binned by month. A MatLab function for calculating these parameters was coded to vectorize this process for forward modeling. The prediction model is shown in Figure 3.26 along with the actual measured face flow in the pilot bore (Robinson et al. 1974). The correlation is also shown compared to the qualitative groundwater descriptions of Post and Eastwood (1973) in Figure 3.27.

The cross-sectional area of the pilot bore face was approximately 11.1 m^2 (120 ft^2). Scaling of the anticipated face flow to the actual cross-sectional area of a different tunnel cross-section may be required for forward modeling.

This correlation is fundamentally based on groundwater flows from the excavation of the pilot bore between October 1963 and December 1964. There is significant uncertainty in this face flow estimate arising from many sources. Seasonal variability and climate change may drastically alter the actual face flow in any given bore. The installation of the pilot bore, the subsequent installation of the Eisenhower and Johnson bores, and the continued drainage through the existing tunnels may have permanently altered the groundwater table. Anecdotal evidence such as historical accounts of swampy or marshy areas on the surface in the vicinity of the pilot bore east portal which are no longer present suggest a decline in local groundwater table. The drainage data recorded in the pilot bore suggest a declining groundwater table, even with the seasonal recharge. The operations of the Loveland Ski Area may also have an impact on both snow accumulation and snowmelt. This single point of reference for calibrating anticipated groundwater face flows should be considered a rough estimate, at best. A lower bound of zero face flow and an upper bound two to ten times higher than the estimates produced by this function would not be unreasonable estimates of the possible range of groundwater face flows in an advancing tunnel heading. Further study of the local groundwater table and its seasonable variability are likely warranted. In particular, the installation of multiple groundwater monitoring wells with long-term monitoring backed up by a rigorous hydrogeological modeling effort is strongly recommended.

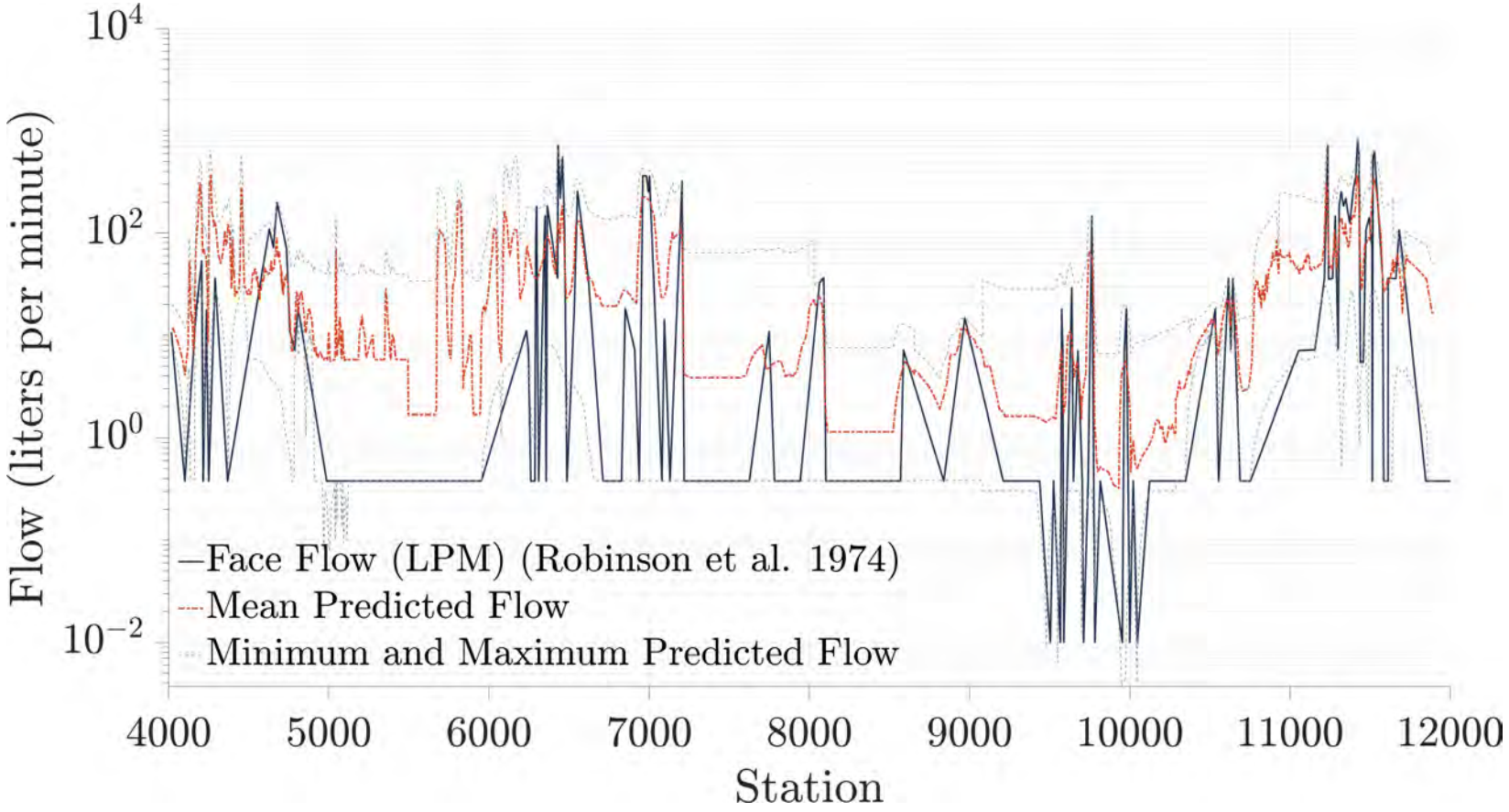

Figure 3.26: Face flow predicted by the developed correlation (Equation 3.4) compared to recorded face flow measured in the pilot bore. Face flow presented in log scale. Note that the zero flow data have been plotted as 10^{-2} in log space.

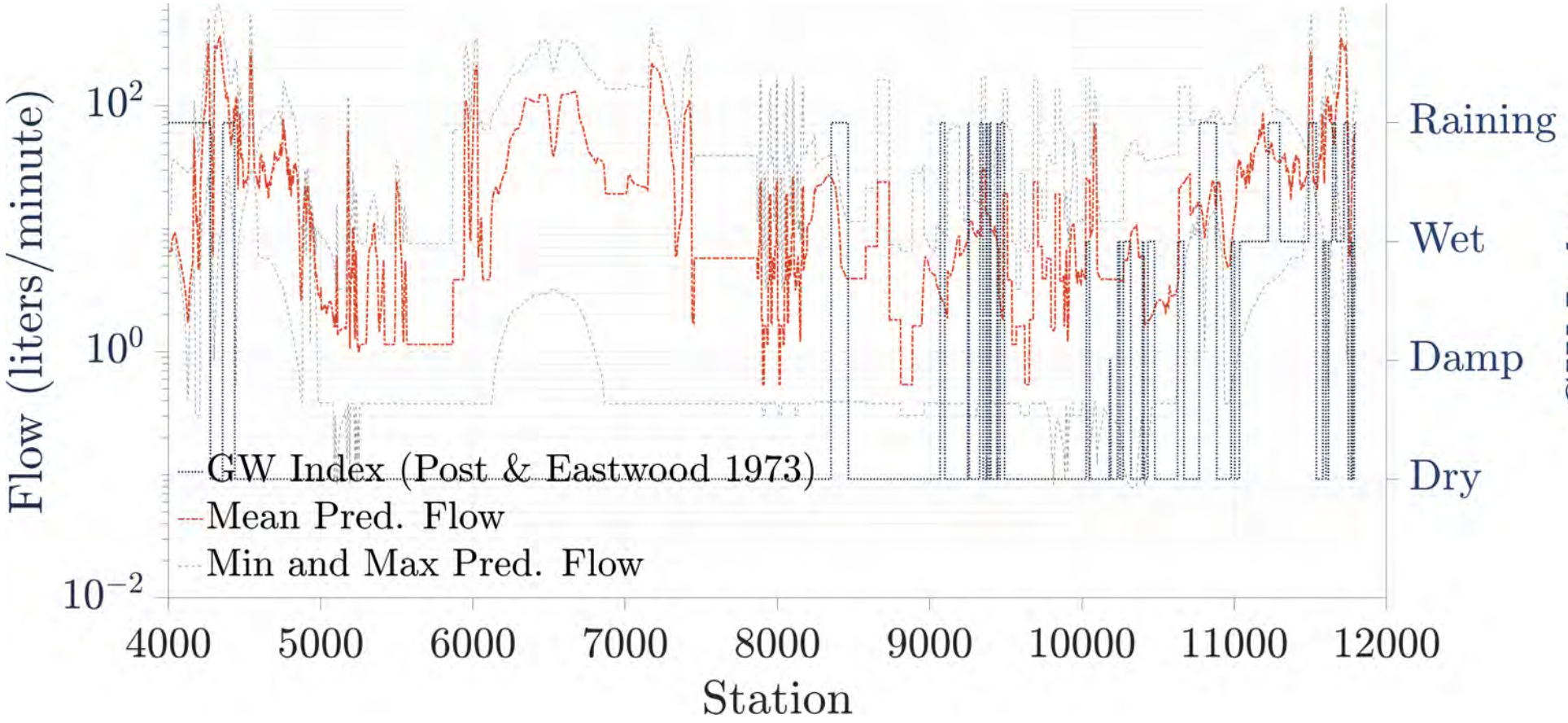

Figure 3.27: Face flow predicted by the developed correlation (Equation 3.4) in the Eisenhower bore compared to recorded groundwater descriptions.

3.5.8 Joint Spacings

Along the pilot bore, Robinson et al. (1974) recorded fracture spacing in four categories. Each category has an assigned range of fracture densities. Although they share similar trends, the data from Robinson et al. (1974) do not fully agree with the data recorded by Mattei (1965) and Miles and Mattei (1965) which appear to have a finer granularity to their descriptions. Mattei (1965) and Miles and Mattei (1965) also report discontinuity densities as discrete average values rather than a range for most cases. In this case, the additional data granularity is preferred over the range of values, so the deterministic data from Mattei (1965) and Miles and Mattei (1965) are used for this evaluation. To evaluate these joint spacing data probabilistically, an uncertainty on the joint spacing value is used. In general, it appears that joint spacing data reported by Mattei (1965) and Miles and Mattei (1965) can be considered accurate within approximately ±50%. Therefore, the upper and lower bounds of joint spacings have been estimated as ±50% from the discrete value reported by Mattei (1965) and Miles and Mattei (1965).

Along the Eisenhower bore, the joint spacings were recorded in three categories: less than 1/2 ft, 1/2 ft to 1 ft, and greater than 1 ft. No further joint frequency data are available, and the upper bound on joint spacing is unclear. For the purposes of this study, the upper bound of joint spacing was set at 3 ft (0.91 m) based on the best judgment of the author and the approximate upper bound of joint spacings reported in the pilot bore. Monte Carlo sampling of joint spacing was accomplished by triangular distributions within each category per Equation 2.70. The peak of the triangular distribution was calculated as the mean of the base 10 logarithm of each bound on the assumption that joint spacings are approximately logarithmically rather than arithmetically distributed.

3.5.9 Rock Mass Rating

The histogram of MC-generated rock mass rating (RMR_{14}) values for the full pilot and Eisenhower bores is shown in Figure 3.28. Note that the most likely value of the probabilistic histogram is lower than the most likely value from the deterministic histogram. Note also that the probabilistic histogram provides a much clearer impression of the distribution of values to be expected along the bore which can be binned into useful ground classes for forward design.

A heatmap of the RMR_{14} distributions at each station for the full alignment is shown in Figure 3.29. The colors of the heatmap indicate the frequency of occurrence of a given RMR_{14} value at a given station, i.e. they represent a histogram of the RMR_{14} values for a slice of the bore. Note, again, that the deterministic estimates consistently disagree with

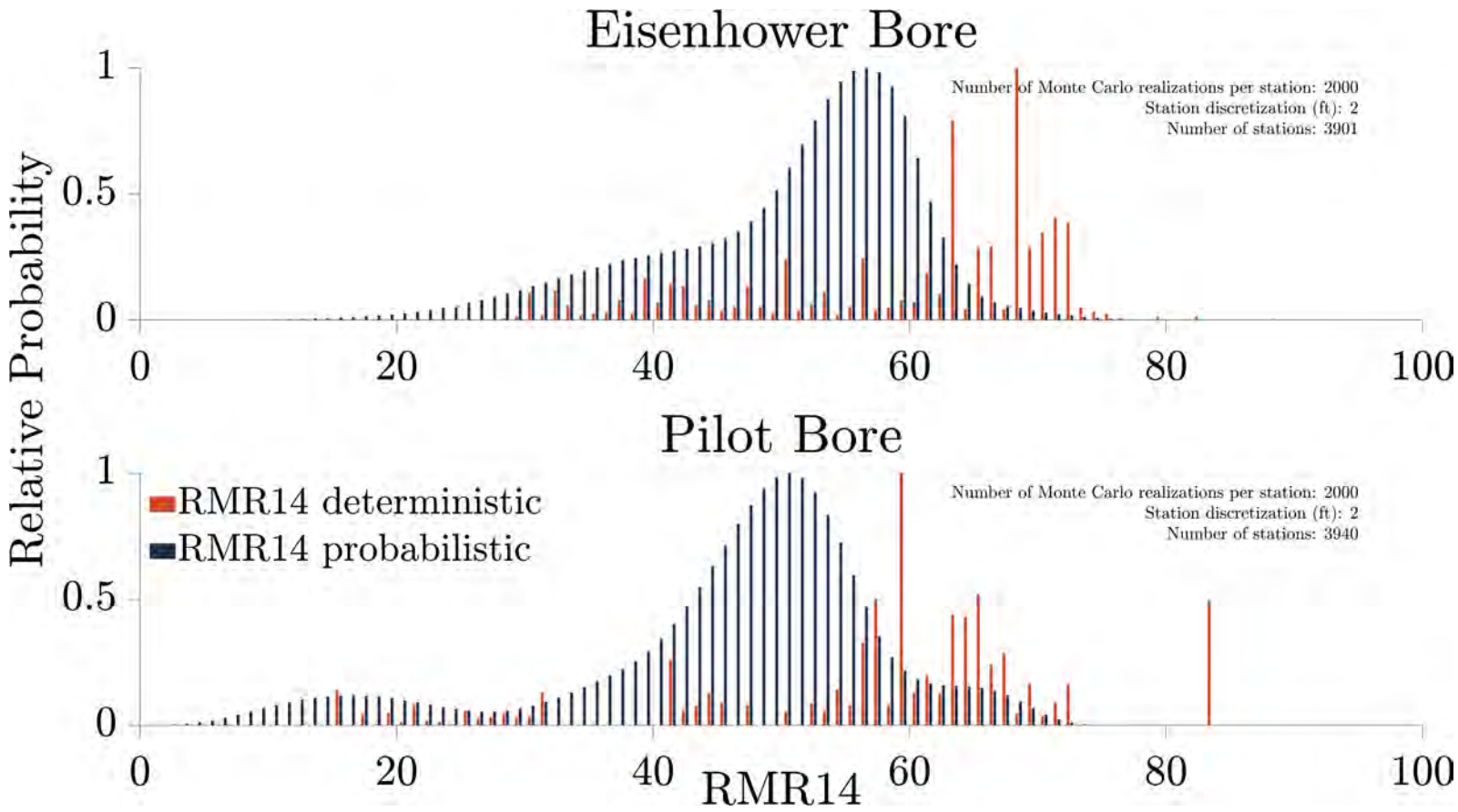

Figure 3.28: Histograms of RMR_{14} probabilistic and deterministic estimates for the entire Eisenhower and pilot bores of the EJMT. All 2000 Monte Carlo realizations at each station along each bore have been aggregated for the probabilistic histogram of the entire bore. The deterministic estimates from each station are aggregated together for the entire bore , as well, to provide a histogram of deterministic estimates for the entire bore. Note that the probabilistic estimates are significantly smoother and lower than the deterministic estimates.

the most likely probabilistic estimates.

$$RMR_{14b} = RMR_{14UCS} + RMR_{14\lambda} + RMR_{14JCond} + RMR_{14GW} + RMR_{14Alt} \quad \text{(restatement of 2.2)}$$

$$RMR_{14} = (RMR_{14b} + F_O) \cdot F_e \cdot F_s \quad \text{(restatement of 2.3)}$$

where RMR_{14b} is the base RMR score before application of the F_0, F_e, and F_s factors, RMR_{14} is RMR as published by Celada et al. (2014), RMR_{UCS} is the UCS component of the RMR score, RMR_{JSpac} is the joint spacing component of the RMR score, RMR_{JCond} is the joint condition component of the RMR score, RMR_{GW} is the groundwater component of the RMR score, RMR_{λ} is the joint frequency component of the RMR score, RMR_{Alt} is the rock mass alterability component of the RMR score, F_0 is the discontinuity orientation factor, F_e is the excavation method factor, and F_s is the in-situ stress state factor.

3.5.9.1 Unconfined Compressive Strength

After converting the UCS values to unconfined compressive strength component of RMR_{14} (RMR_{14UCS}) scores, the values less than 0 or greater than 15 are truncated to 0 or 15, respectively. Note that for the Lowson and Bieniawski (2013) relationship between UCS and RMR_{14UCS}, a UCS value greater than 247 MPa is required to achieve an RMR_{14UCS} score greater than 15. This means that any normally distributed UCS that has a mean other than $247/2 = 124$ will have an uneven truncation of the distribution. Normal UCS distributions with means below 124 MPa will tend to bias the UCS values high by truncating more scores less than 0 (as with the ISF), while UCS distributions with means above 124 MPa will tend to bias the RMR_{14UCS} values low by truncating more scores greater than 15 (as with the SPG). The normal distribution of the SPG truncates approximately 0.07% of the values on the low end and 11.3% of the values on the high end; the ISF distribution truncates approximately 3.0% of the values on the low end and 0.7% of the values on the high end. The non-normal mixture distribution of ISF and SPG truncates approximately 1.5% of the values on the low end but 5.7% of the values on the high end. Because of the prevalence of the SPG lithology in the EJMT, the end result is that approximately 9% to 10% of MC simulations have results truncated on the high end, while less than 1% have results truncated on the low end. This tends to bias the resulting probabilistic RMR scores slightly lower than the deterministic RMR scores.

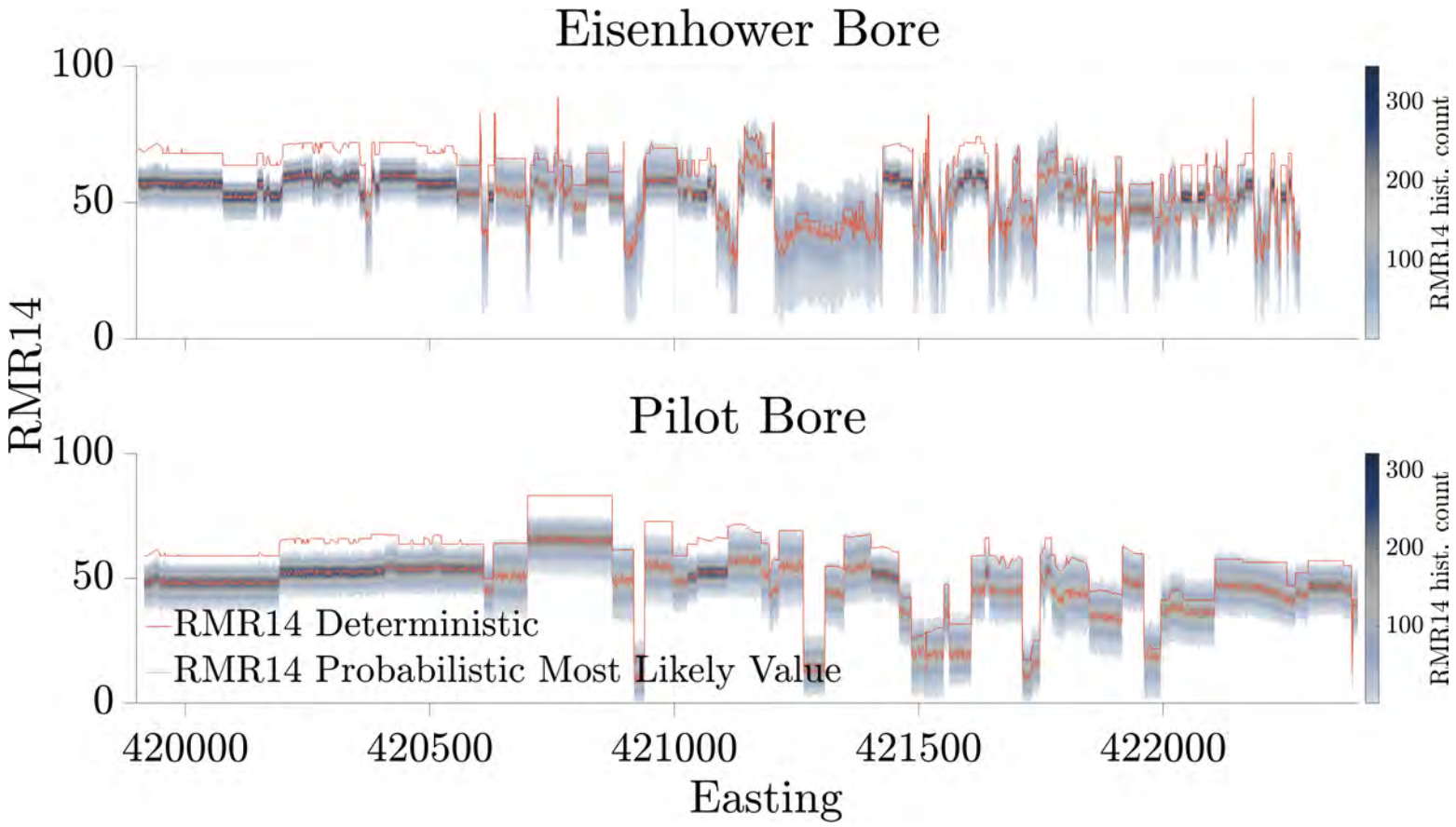

Figure 3.29: Histograms of RMR_{14} at each station presented as a heatmap slice at each station along the EJMT and compared to deterministic estimates (dotted line) at each station.

This property of the probabilistic modeling is considered a feature not a bug. In this case, probabilistic modeling has revealed an inherent bias to the RMR system when using only most likely values rather than the full range of plausible values. This also offers some mathematical support to the impression that tunnel projects tend to be biased towards results worse than initially expected. A peak probabilistic estimate is a more realistic portrayal of the ground conditions than a deterministic estimate.

UCS is picked from the distribution of UCS values determined from laboratory data. For both the SPG and ISF the UCS values are represented by truncated normal distributions. For transitional or mixed face zones where the rock encountered could be either SPG or ISF (mapped as such only in the Eisenhower bore), a mixture distribution consisting of the individual UCS probability density functions for the SPG and ISF was constructed (Figure 3.30).

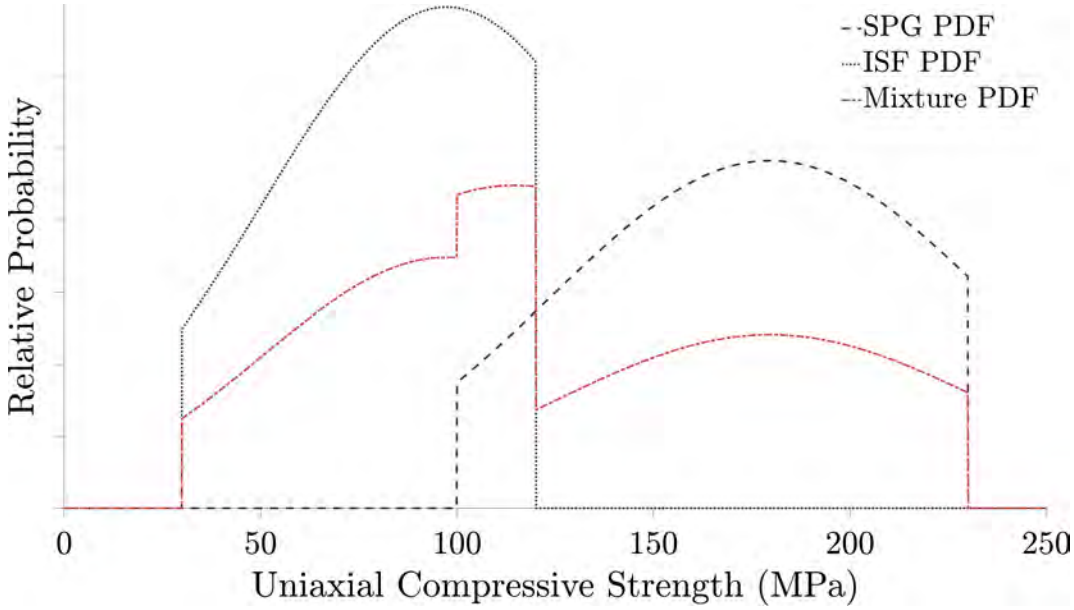

Figure 3.30: Mixture distribution of SPG and ISF unconfined compressive strength probability density functions (PDFs).

3.5.9.2 Joint Frequency (Joints per Meter)

The joint frequency component of RMR_{14} ($RMR_{14\lambda}$) was calculated based on the joint frequency, λ, as discussed in Section 3.5.8. Joint frequency is related to $RMR_{14\lambda}$ via the correlation of Lowson and Bieniawski (2013) as shown in Equation 2.6.

$$RMR_{14\lambda} = 40 \geq -6.36\lambda^{0.467} \geq 0 \qquad \text{(restatement of 2.6)}$$

where λ is the discontinuity density of the rock mass in joints/m. Note that the range of scores is limited to between 0 and 40.

3.5.9.3 Groundwater Conditions

The RMR_{14} component score for groundwater is intended to reflect excavation and support difficulties associated with groundwater inflow conditions including worker safety, outwash of joint fillings, hydraulic jacking of joints, hydraulic pressure on supports, and face collapse. The RMR_{14} score for groundwater ranges from 0 to 15 and is based on correlation to five qualitative descriptions: dry, slightly humid, humid, dripping, and water flow. Any continuous water inflow into the excavation immediately moves this score to the last category, water flow, and sets the score to zero. For this reason, the RMR_{14} groundwater score has significantly lower granularity at the upper end than the Q system joint water reduction factor (J_w) score which includes six categories of qualitative groundwater flow, four of which describe conditions of water flow. On the other hand, the Q system has less granularity on the lower end, where the two lowest J_w descriptions roughly correlate to the four lower RMR_{14} groundwater score descriptions. Neither of these systems provide any quantitative correlation to the range of groundwater inflow which would correlate to any given score. Also, as noted by Palmstrom and Broch (2006), the Q system $\frac{J_r}{J_a}$ parameter should be positively correlated to groundwater flow, a somewhat counterintuitive consequence of its formulation. For the purposes of this report ranges of groundwater flows have been correlated to groundwater component of RMR_{14} (RMR_{14GW}) groundwater and J_w scores in order to estimate these scores based on estimated ranges of anticipated groundwater inflows; see Table 3.6. The estimated correlations between flow ranges, RMR_{14}, and J_w are based purely upon the engineering judgment of the author and a careful reading of the historical data available for this particular case study and should not be considered a generic engineering recommendation. The groundwater flow is estimated via the correlation established in Equation 3.4.

3.5.9.4 Alterability

No slake durability test data are available for samples from the EJMT. In the absence of such data, the range of scores for slake durability was estimated based upon the best judgment of the author. For MC realizations random values were selected from a symmetric triangular distribution of the given range.

In general, granite is not subject to slaking; sections of the pilot bore through the SPG were given alterability component of RMR_{14} (RMR_{14Alt}) scores of 9 to 10. Sections of the

Table 3.6: Correlations assumed for this report between flow rate, RMR14(groundwater), Jw, and historical descriptions.

Groundwater Flow (LPM)	RMR Description	$RMR_{14}(GW)$	NGI Description	J_w	Historical Description
0	dry	15	Dry excavations or minor inflow (humid or a few drips)	1.0	dry
10^{-1}	slightly humid	10	*as above*		damp
$10^{-0.5}$	humid	7	*as above*		wet
10^{0}	dripping	4	Medium inflow, occasional outwash of joint fillings (many drips/raining)	0.66	raining
10^{1}	water flow	0	Jet inflow or high pressure in competent rock with unfilled joints	0.5	*none*
$10^{1.5}$	*as above*		Large inflow or high pressure, considerable outwash of joint fillings	0.33	*none*
10^{2}	*as above*		Exceptionally high inflow with decaying water pressure; causes outwash of material and perhaps cave in	$0.2 - 0.1$	*none*
$10^{2.5}$	*as above*		Exceptionally high inflow with no decay of water pressure; causes outwash of material and perhaps cave in	$0.1 - 0.05$	*none*

pilot bore through the augite-diorite dike were treated as SPG.

The ISF is composed of primarily metasedimentary gneiss that grades down towards a schist in some locations. The gneissic members of this formation are unlikely to experience significant slaking, but some of the more schistose members of the formation may be subject to slaking. Based on the geologic descriptions of the rocks along the pilot bore, the ISF members were separated into more gneissic and more schistose members. Sections of the pilot bore through the gneissic ISF members were assigned $\text{RMR}_{\text{14Alt}}$ scores of 7 to 9. Sections of the pilot bore through the schistose ISF members were assigned $\text{RMR}_{\text{14Alt}}$ of 4 to 6. For cases where it was unclear if the lithology was more schistose or more gneissic, a range of $\text{RMR}_{\text{14Alt}}$ from 4 to 9 was used. For mixed-face or SPG-ISF transition zones, a range of $\text{RMR}_{\text{14Alt}}$ from 4 to 10 was used.

3.5.9.5 Joint Conditions

The joint condition sub-component scores along the pilot bore were assigned deterministically for intervals along the pilot bore based on a careful reading of the pilot bore geologic report of Miles and Mattei (1965) and the construction report by Mattei (1965). Significant professional judgment went into this characterization. The true range of the joint conditions in the pilot bore represents one of the largest unknown-unknowns in the development of the RMR scores. The reports of Mattei (1965) and Miles and Mattei (1965) contain detailed descriptions of the conditions encountered at each unique interval along the tunnel. Although the methodology of joint characterization used in systems such as RMR and Q was not fully developed at this time, Mattei (1965) and Miles and Mattei (1965) did take detailed notes describing the jointing and the joint conditions. Most joint condition descriptions focused on the water flow from the joints, the amount of clay present in the joints, or observations of slickensides on the sides of the joint. Note that in soil mechanics and near-surface geotechnical characterization, "slickensides" often indicate a sheared clay surface. However, in this context, slickensides should be understood as a smoothly polished rock surface with striations in the direction of fault or joint movement rather than explicitly indicating the presence of clay minerals.

The joint condition component of RMR_{14} ($\text{RMR}_{\text{14JCond}}$) scores for the Eisenhower bore were estimated as a weighted sum of the reported blockiness & seaminess indices and decomposition & alteration indices as shown in Equation 3.5.

$$RMR_{14JCond} = \frac{20}{3}\left(0.36 \cdot BS + 0.64 \cdot DA\right) \tag{3.5}$$

where BS is the blockiness and seaminess index reported by Post and Eastwood (1973) and DA is the decomposition and alteration index reported by Post and Eastwood (1973). The BS and DA indices range from 0 to 3. The factor of 20/3 scales the weighted average of these scores to the range of $RMR_{14JCond}$ which ranges from 0 to 20.

To account for the uncertainty in the $RMR_{14JCond}$ estimates, the estimated values were perturbed by a factor of ±8. MC realizations were sampled from a triangular distribution with its peak at the estimated value and edges up to 8 points above or below this estimate. Scores were truncated at 0 and 20 in keeping with the overall format of the RMR_{14} system.

The most likely $RMR_{14JCond}$ scores for the pilot bore were estimated manually from a careful reading of the historical descriptions of Miles and Mattei (1965) and Mattei (1965). These estimates were again perturbed by the same ±8 factor as used for the Eisenhower bore and MC sampling proceeded in the same fashion.

3.5.9.6 Tunnel Orientation Relative to Discontinuities

Robinson et al. (1974) created stereonets of the joints mapped in the walls and faces of the pilot bore and sought to identify trends in the jointing. They noted that concentrations of joints visible on the stereonets are "probably not very significant, inasmuch as the largest one represents the attitudes of only 35 joints out of a total of 1,179 plotted." They concluded that "the joints in the pilot bore strike in all directions." They also noted that the average dip for the joints was approximately 45°.

For the purposes of back-analysis of the pilot bore, with joints dipping approximately 45° against the direction of the tunnel drive and striking in a wide range of directions but predominantly sub-perpendicular to the tunnel, an F_O factor of -7.5 is selected as reasonably representative of conditions.

For the purposes of early-stage probabilistic feasibility studies of potential future bores adjacent to the existing bores, it may be advisable to omit the tunnel orientation factor completely. Discontinuities, faults, joints, and fractures appear to be chaotically distributed. Further, the usefulness of this factor is somewhat dependent on the excavation and support method proposed.

3.5.9.7 ICE and Stress Factor

For this study Equation 2.9 was applied by estimating σ_c from the H-B envelope developed for the rock mass and estimating σ_{max} from tabulated boundary element stress coefficients by Eissa (1980) per Equation 2.9 and Equation 2.8. In the current study

the estimated *indice de comportamiento elastico* (ICE) values by the new method are consistently higher than the ICE values estimated by the Celada et al. (2014) method with the difference ranging from 1/2 a point to over 3400 points. The resulting differences in the F_s factor are as great as -0.3, i.e. in some cases the new method gives $F_s = 1.0$ where Equation 2.7 gives $F_s = 1.3$. Note that F_s only ranges from 1.0 to 1.3. In no case does the new method predict a higher F_s than the old method. F_s is a denominator factor in RMR_{14} for adjusting base rock mass rating (RMR_{14b}) from surface estimated values to approximate tunnel face values. Because Equation 2.9 and Equation 2.8 are consistently estimating F_s lower than Equation 2.7, the new method is more optimistic than the previous method.

The ICE formulation was further refined by checking for tensile stresses and comparing these to tensile strengths. Approximately 11% of the MC runs indicate that some tensile stress will occur around the excavation perimeter. In most of these cases, the tensile stress is still much less than the tensile strength of the intact rock (as estimated by Hoek and Brown (2018) strength parameters). Approximately 0.1% of all MC iterations show that tensile failure through intact rock would control the boundary of elastic-plastic behavior. However, for almost all cases the ICE is greater than 130 (often significantly greater), i.e. applicability of ICE has already saturated. This is true for this particular tunnel case study but may be relevant for other geologic strength and stress conditions.

Note that this continuum elastic assumption still neglects the possibility of tensile failure across a joint. This is considered an acceptable error for large-scale early stage probabilistic feasibility studies where the exact locations and orientations are not known.

3.5.10 Q Rock Mass Classification System

The six components of Q were estimated based on the available data in the pilot and Eisenhower bores. These components are rock quality designation (RQD), joint set number (J_n), joint roughness (J_r), joint alteration (J_a), J_w, and stress reduction factor (SRF). These parameters are related through Equation 2.10 to calculate Q.

$$Q = \frac{RQD}{J_n} \cdot \frac{J_r}{J_a} \cdot \frac{J_w}{SRF} \qquad \text{(restatement of 2.10)}$$

Figure 3.31 shows a heatmap of the Q values calculated along the EJMT pilot and Eisenhower bores. The colors of the heatmap indicate the frequency of occurrence of a given Q value at a given station, i.e., they represent a histogram of the Q values for a slice of the bore. Note, again, that the deterministic estimates consistently disagree with

the most likely probabilistic estimates. A histogram of all estimated Q values along the EJMT pilot and Eisenhower bores is shown in Figure 3.32. A heatmap (Figure 3.33) and histogram (Figure 3.34) of the rock mass quality index without stress factors (Q') values are also provided.

3.5.10.1 RQD

For the purposes of this study, rock quality designation (RQD) was estimated based on the reported joint frequency based on the method of Priest and Hudson (1976) as shown in Equation 3.6.

$$RQD = 100\,(0.1\lambda + 1)\,e^{-0.1\lambda} \tag{3.6}$$

where λ is the joint frequency in units of joints/m, i.e. the inverse of joint spacing. RQD was calculated directly from λ by Equation 3.6. The RQD values along the pilot and Eisenhower bores are shown in Figure 3.35.

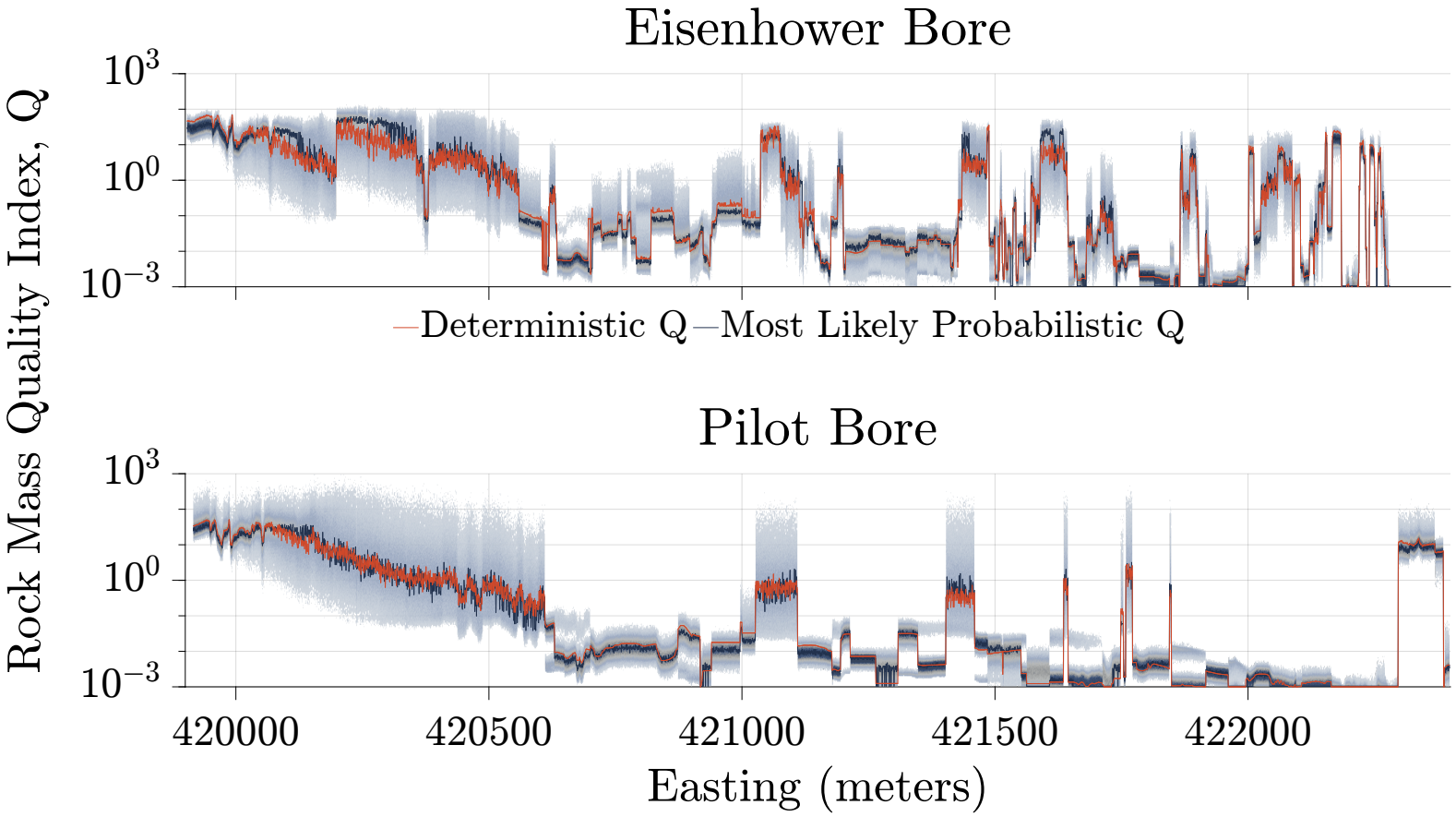

Figure 3.31: Heatmap of Q along the pilot and Eisenhower bores.

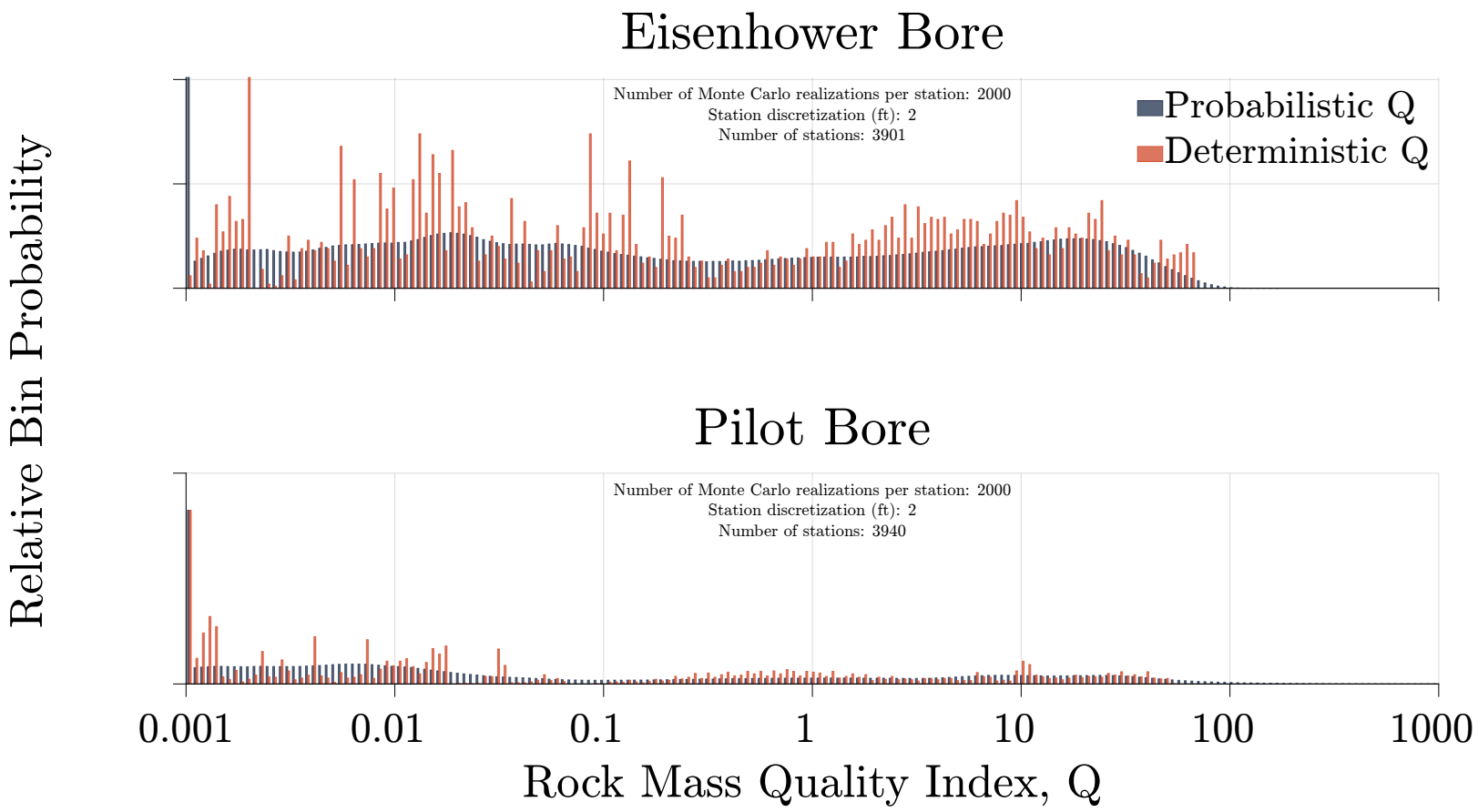

Figure 3.32: Histogram of Q along the pilot and Eisenhower bores.

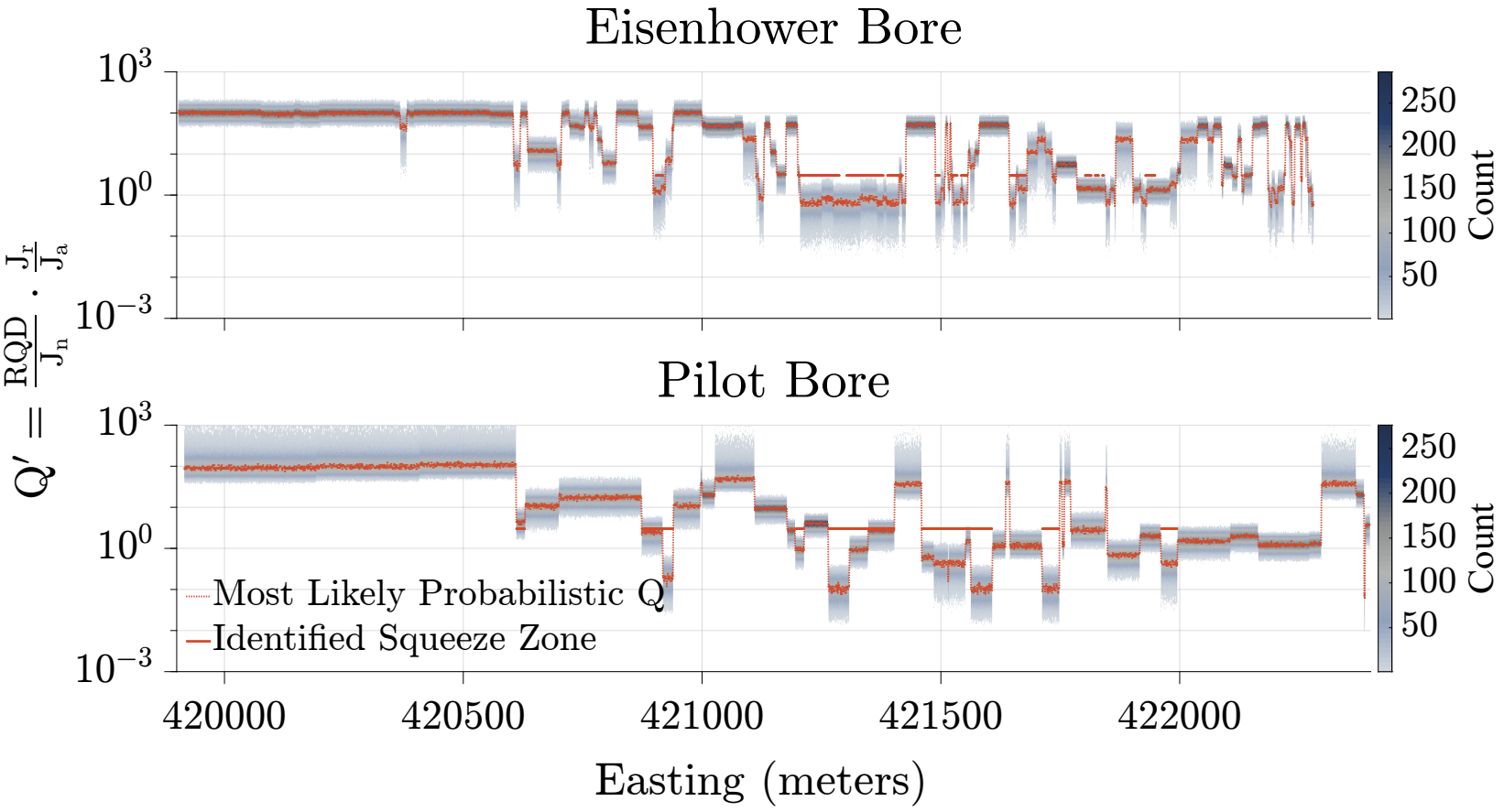

Figure 3.33: Heatmap of Q' along the pilot and Eisenhower bores.

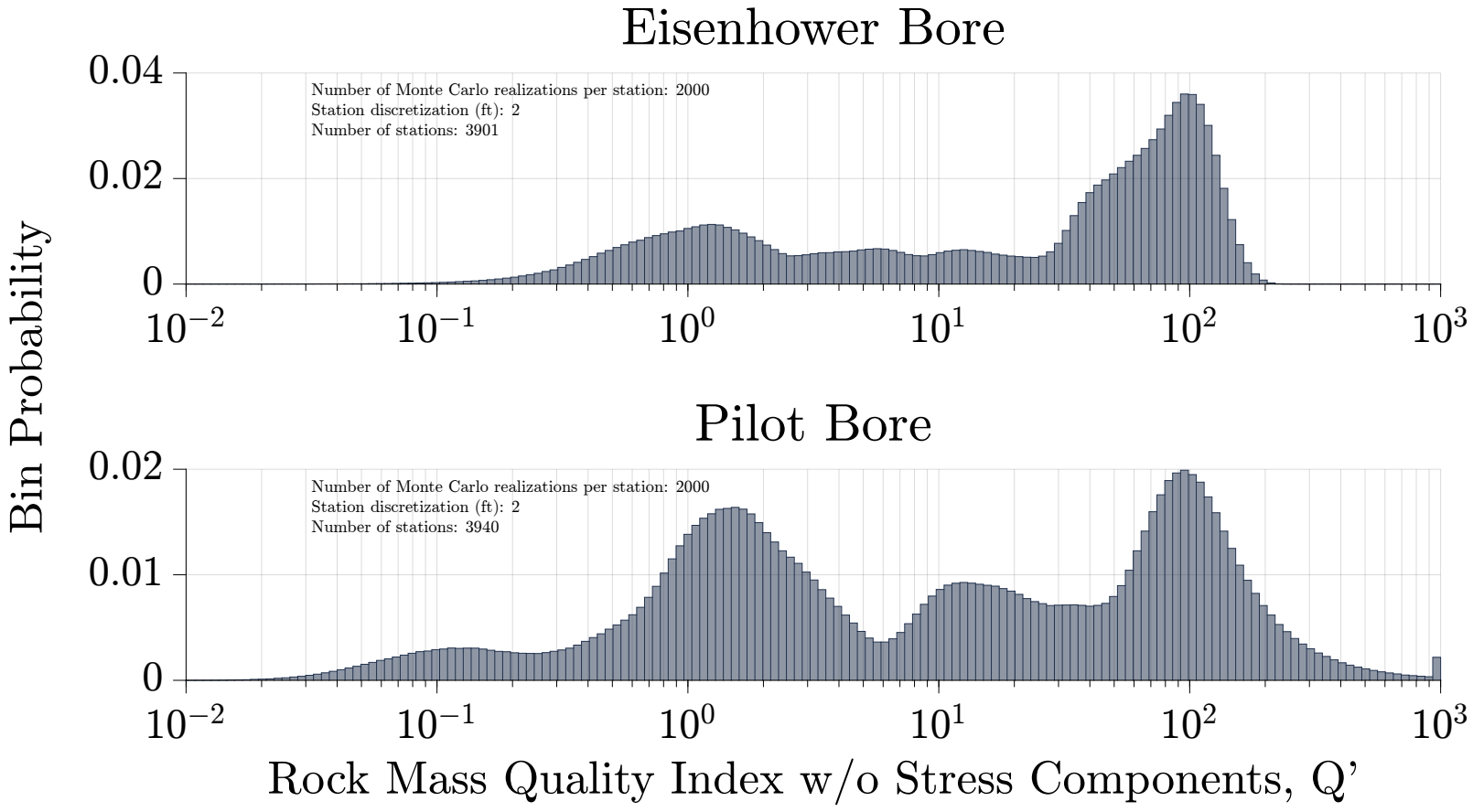

Figure 3.34: Histogram of Q' for the pilot and Eisenhower bores.

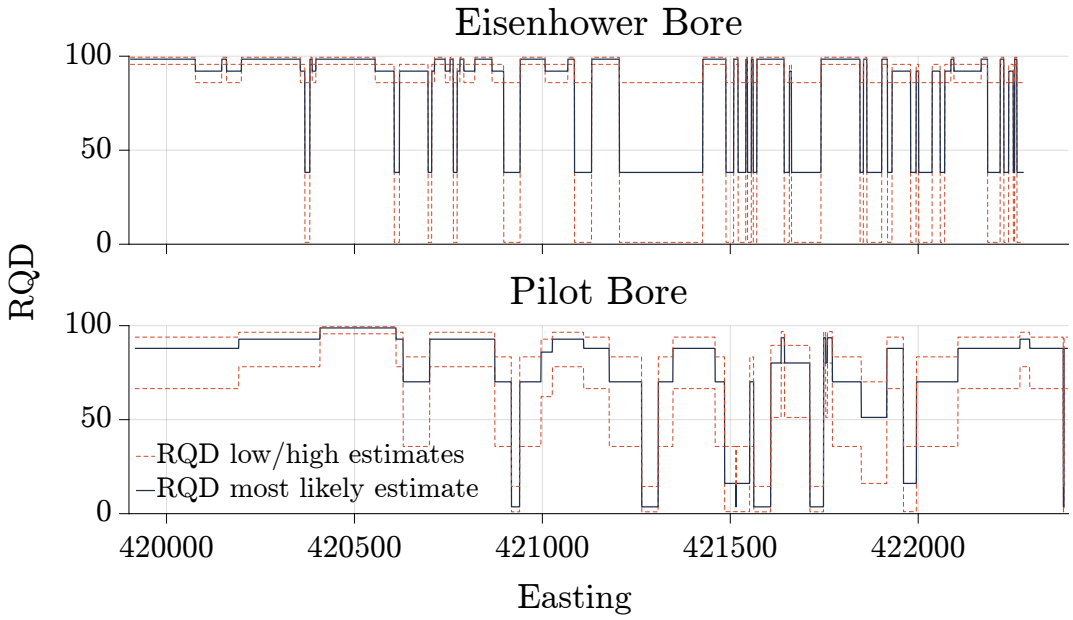

Figure 3.35: Most likely RQD and range along the pilot and Eisenhower bores.

3.5.10.2 Joint Set Number

The number of joint sets in a tunnel, not the frequency or quality of jointing, is represented by the joint set number (J_n). This component of Q is highly dependent on the ability to observe the excavation face and the judgment of the engineering geologist making the determination. It is intended to capture the risk of block fall due to intersecting joint sets. Developing the J_n value for the pilot and Eisenhower bores of the EJMT based on the available historical data is extremely problematic. The J_n portion of this rock mass classification represents one of the greatest unknown-unknowns in this research and should be considered an educated guess, at best.

Robinson et al. (1974) created stereonets of the joints mapped in the walls and faces of the pilot bore and sought to identify trends in the jointing. They created stereonets of all joints mapped along the pilot bore in the face and the wall and identified four concentrations on the stereonet which could be considered joints sets, with the greatest concentration of joints approximately parallel to the major direction of faulting in the area. However, the greatest concentration of joints accounted for "only 35 joints out of a total of 1,179 plotted" and further concluded that "the joints in the pilot bore strike in all directions", i.e. they are essentially random. In the most conservative estimation, the four joint sets along the pilot bore could be used to assign a J_n of 15 to the entire pilot bore. However, NGI (2015) notes that "When calculating the Jn value, it is very important to consider only the joints occurring at the same location and forming definite

blocks. In situations where the Jn-value is determined from joint observations in a longer section of an underground excavation, summing up all the joint sets results in a Jn-value that is too high." Therefore, considering the four joint sets mapped along the entire pilot bore and assigning a J_n of 15 is probably overly conservative. On the other hand, the heavily faulted portions of the pilot bore where the rock has been turned largely to fault gouge probably satisfy the Q system description of "crushed rock, earth like" and could be assigned a J_n of 20.

Despite the significant uncertainty associated with J_n for this project, it was necessary to assign a J_n value to each interval along the pilot bore and Eisenhower bore. In the Eisenhower bore, detailed geologic maps by Post and Eastwood (1973) were available showing most or all of the joints mapped along portions of the Eisenhower bore. However, these maps only cover approximately 20% of the total length of the Eisenhower bore. For that portion of the project, Lu (2020) was able to digitize joint orientations to a stereonet and determine J_n values. However, significant engineering judgment goes into determining the appropriate length window in which to evaluate the joint and in interpreting the resulting stereonet to determine a J_n value. In addition, the assignment of joint set numbers to areas described as fault gouge or shear zones that have no discrete mapped joints but are described as faulted, sheared, and fractured practically to the level of soil is problematic. There are no mapped joint sets in these areas, but the material is clearly not massive or intact.

In keeping with the structural domaining discussed in Section 3.3 a J_n value of 3 ± 1 was assigned to all points west of 421,000 m easting and a J_n value of 6 ± 1 was assigned to all points east of that plane. This is considered a reasonable estimate of the reliability and precision in the underlying data based on the randomness of the joints in the EJMT; the definition of J_n as the number of joint sets, not degree of jointing; and the stereonets plotted for the East and West structural domains. NGI (2015) describes a J_n value of 3 as "one joint set plus random joints" while a J_n value of 6 corresponds to "two joint sets plus random joints". For MC simulation, the J_n values were sampled from a triangular distribution with a peak at 3 or 6 and bounds ±1 unit from those values. The J_n values estimated for the pilot and Eisenhower bores are shown in Figure 3.36.

3.5.10.3 Joint Roughness and Alteration Numbers

The joint roughness (J_r) and joint alteration (J_a) scores along the Eisenhower bore were assigned based on the qualitative descriptions by Post and Eastwood (1973) as compared to the geologic descriptions of NGI (2015). The decomposition & alteration and

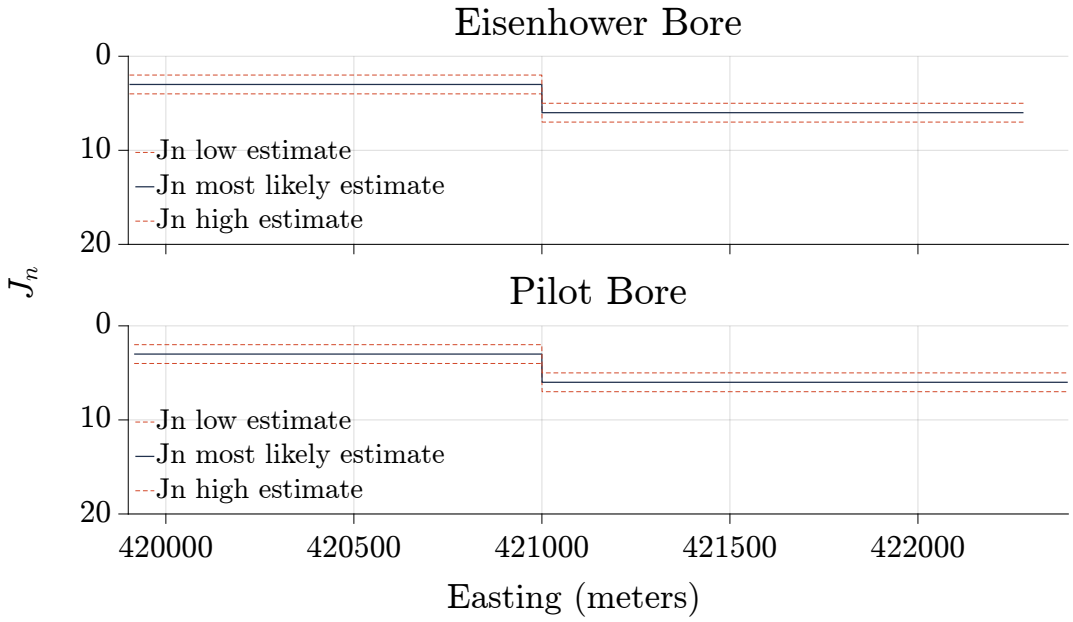

Figure 3.36: Most likely J_n and range along the pilot and Eisenhower bores.

blockiness & seaminess descriptions were correlated to J_r and J_a as shown in Table 3.7 and Table 3.8 based on the best judgment of the author.

The J_r and J_a scores along the pilot bore were assigned for intervals along the pilot bore based on a careful reading of the pilot bore geologic report of Miles and Mattei (1965) and the construction report by Mattei (1965). Significant professional judgment went into this characterization, and the quantitative data for the joint conditions represents one of the largest unknown-unknowns in the development of the Q scores for the pilot bore. The reports by Miles and Mattei (1965) and Mattei (1965) contain detailed descriptions of the conditions encountered at each unique interval along the tunnel. Although the methodology of joint characterization used in systems such as RMR and Q was not fully developed when the EJMT was constructed, Miles and Mattei (1965) did take detailed notes describing the jointing and the joint conditions. Most joint condition descriptions focused on the water flow from the joints, the amount of clay present in the joints, or observations of slickensides on the sides of the joint. Note that in soil mechanics and near-surface geotechnical characterization, "slickensides" often indicate a sheared clay surface. However, in this context, slickensides should be understood as a smoothly polished rock surface with striations in the direction of fault or joint movement rather than explicitly indicating the presence of clay minerals.

The most likely J_r and J_a scores for the pilot and Eisenhower bores were perturbed by ± 1 for the development of triangular distributions representing the uncertainty of these parameters. The J_r and J_a scores along the pilot and Eisenhower bores are shown in

Table 3.7: Correlations adopted for this study between historical blockiness and seaminess index; historical decomposition and alteration index; and Q system joint roughness number.

J_r values		Historical Blockiness and Seaminess Description			
		very blocky and seamy	*moderately blocky and seamy*	*blocky*	*not blocky or seamy*
Historical Decomposition and Alteration Description	Highly Decomposed	1	1	1.5	1.5
	Moderately Decomposed	1	2	2	2
	Slightly Altered	1	2	3	3
	Unaltered	1.5	2	3	4

Table 3.8: Correlations adopted for this study between historical blockiness and seaminess index; historical decomposition and alteration index; and Q system joint alteration number.

J_a values		Historical Blockiness and Seaminess Description			
		very blocky and seamy	*moderately blocky and seamy*	*blocky*	*not blocky or seamy*
Historical Decomposition and Alteration Description	Highly Decomposed	13	10	8	8
	Moderately Decomposed	10	8	4	3
	Slightly Altered	6	6	2	2
	Unaltered	4	4	1	1

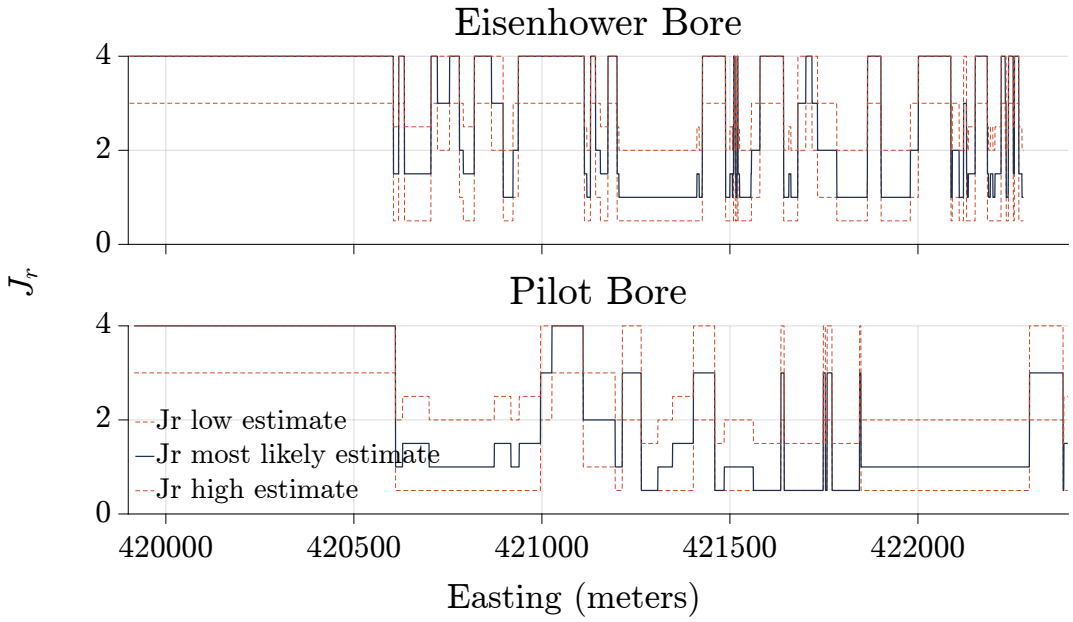

Figure 3.37: Most likely J_r and range along the pilot and Eisenhower bores.

Figure 3.37 and Figure 3.38, respectively.

3.5.10.4 Joint Water Reduction Factor

The joint water reduction factor (J_w), is intended to reflect excavation and support difficulties associated with groundwater inflow conditions including worker safety, outwash of joint fillings, hydraulic jacking of joints, hydraulic pressure on supports, and face collapse. The joint water reduction factor ranges from 0.05 to 1 and is based on correlation to six qualitative descriptions of water conditions. As noted in Section 3.5.9.3 the RMR_{14GW} has significantly lower granularity at the upper end than the Q system J_w score which includes six categories of qualitative groundwater flow, four of which describe conditions of water flow. On the other hand, the Q system has less granularity on the lower end, where the two lowest J_w descriptions roughly correlate to the four lower RMR_{14} groundwater score descriptions. Neither of these systems provide any quantitative correlation to the range of groundwater inflow which would correlate to any given score. For the purposes of this report ranges of groundwater flows have been correlated to RMR_{14} groundwater and J_w scores in order to estimate these scores based on estimated ranges of anticipated groundwater inflows. These assumed correlations are given in Table 3.6 in Section 3.5.9.3. The estimated correlations between flow ranges, RMR_{14GW}, and J_w are based purely upon the engineering judgment of the author and a careful reading of the historical data available for this particular case study and should not be considered a generic engineering

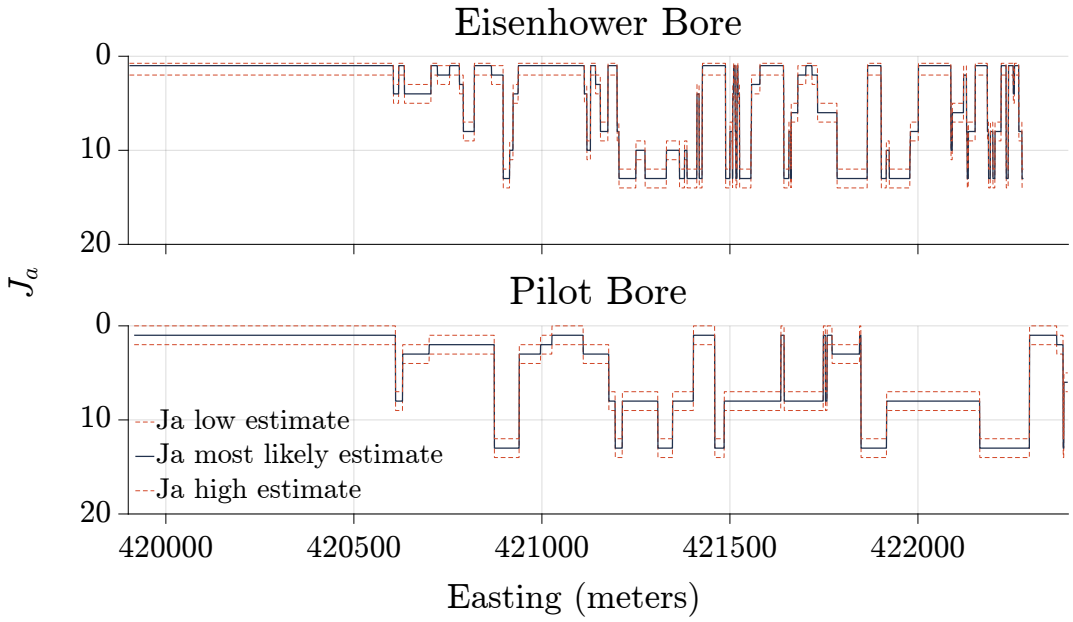

Figure 3.38: Most likely J_a and range along the pilot and Eisenhower bores.

recommendation. The groundwater flow is estimated via the correlation established in Equation 3.4. The J_w scores assigned along the pilot and Eisenhower bores are shown in Figure 3.39.

3.5.10.5 Stress Reduction Factor (SRF)

The Q-system's stress reduction factor is dependent on the stress condition and four broad geologic categories. Portions of the EJMT fall into category A or C for weak zones and squeezing zones respectively, while other portions fall into category B for competent, mainly massive rock.

The NGI (2015) handbook also requires estimating the maximum tangential stress based on elastic theory. In this case, for the least favorable stress ratio ($H/V = 0.18$) the maximum tangential stress from Kirsch (1898) is approximately 22.5 MPa. This is two orders of magnitude above the fault gouge strength, which suggests an SRF of approximately 20 through these zones.

SRF was estimated based upon calculated stress conditions and recorded geologic conditions along the alignment. The primary reference for this was the NGI (2015) handbook Table 6 as described and adapted in Section 2.3.3.1. To apply this table, it is necessary to determine whether a given point is expected to squeeze or not. NGI (2015) suggests applying the squeezing criterion of Singh et al. (1992) (Equation 2.14). Evaluation of this criterion against the identified squeeze zones in the EJMT pilot and

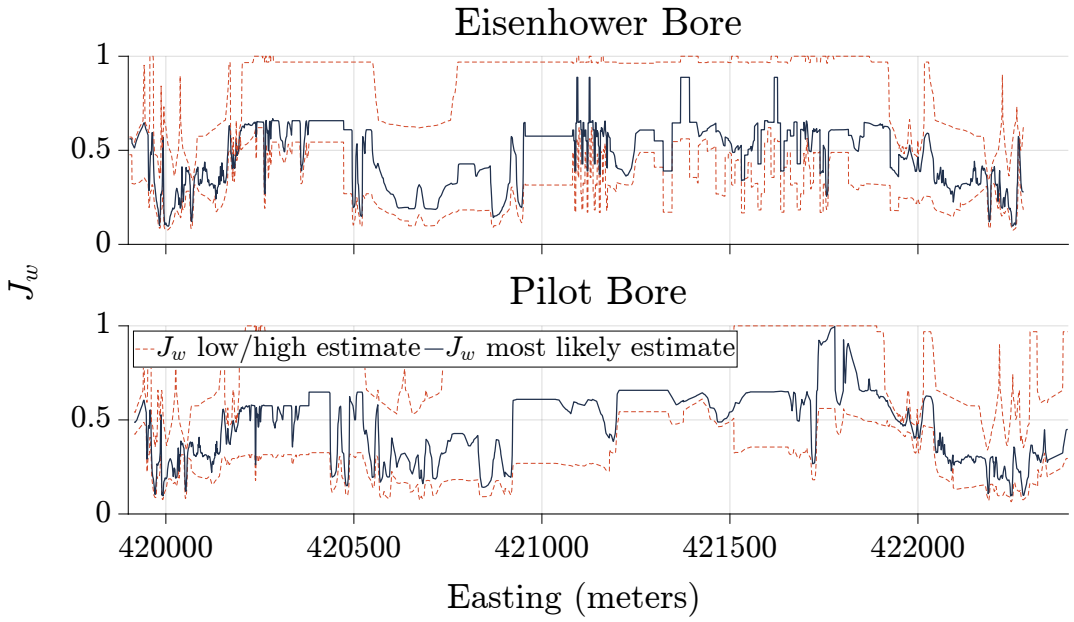

Figure 3.39: Most likely J_w and range along the pilot and Eisenhower bores.

Eisenhower bores gives an accuracy rate (correctly predicting squeezing and non-squeezing zones) of 90.2%. To improve this, the coefficients of Equation 2.14 were recalibrated against the identified squeezing zones in the pilot and Eisenhower bores.

Figure 3.40 shows the depth of each point along the pilot and Eisenhower bores plotted against their Q' values. Points were binned and the percent of points identified as squeezing in each bin is represented by the color of the bin. A prediction of squeezing was made when more than 50% of the Monte Carlo simulations for a given station result in a prediction of squeezing.

The recalibrated line has parameters $A = 277$ and $B = 0.285$ (Equation 3.7). There is a relatively minor change in the position of the line distinguishing between squeezing and non-squeezing conditions. This minor improvement in the Singh et al. (1992) squeezing criterion by calibration to the EJMT data lends credence to the general accuracy of this criterion. Although false positives and false negatives still exist, the recalibrated accuracy of 93.5% at predicting squeezing vs. non-squeezing conditions specific to the EJMT is acceptably accurate.

$$H_{squeeze} = 350 \cdot Q^{1/3} \qquad \text{(restatement of 2.14)}$$

$$H_{squeeze} = 277 \cdot Q'^{0.285} \qquad (3.7)$$

While squeezing is typically associated with clay-based sedimentary rocks, it is

theoretically possible in any rock mass exhibiting ductile creep failure. Squeezing has been observed in metasedimentary gneisses deriving from clay-rich rocks (Barla 2002) and is plausible in rocks which are fractured and altered with significant clay decomposition products. Based upon these facts and the observed historical behavior in the EJMT which was contemporaneously described as squeezing, it is assumed that squeezing is possible in the ISF portions of the EJMT.

The SRF value for the vicinity of the EJMT was estimated based on the correlation presented in Figure 3.40 and Equation 3.7. Figure 3.42 shows the SRF values assigned along the pilot and Eisenhower bores.

3.5.11 Geological Strength Index

Based on the Post and Eastwood (1973) historical rock mass classification system in the Eisenhower bore, which included detailed descriptions of eight categories of rock, GSI was estimated along the Eisenhower bore. Each of the eight historical classifications was correlated to a box of the Hoek and Marinos GSI chart (Hoek and Marinos 2000a,b; Hoek et al. 1998; Marinos and Hoek 2001; Marinos and Hoek 2000; Marinos et al. 2005). The GSI is assumed to be triangularly distributed within each box.

In the pilot bore there is no similarly detailed contemporaneous classification system. GSI values were estimated based on correlation to other available data. Hoek et al. (2013) offered Equation 2.21 and Equation 2.22 for correlating GSI to RMR and Q. Based on the available data in the Eisenhower bore, these equations were recalibrated for this particular case study, giving Equation 3.8 and Equation 3.9. The functional form of Hoek et al. (2013) has been intentionally preserved.

$$GSI = 1.5 \cdot RMR_{89JCond} + \frac{RQD}{2} \qquad \text{(restatement of 2.21)}$$

$$GSI = 2.49 \cdot RMR_{14JCond} + 8.03 \log_{10}(JS) + 29.7 \qquad (3.8)$$

$$GSI = 52 \frac{\frac{J_r}{J_a}}{1 + \frac{J_r}{J_a}} + \frac{RQD}{2} \qquad \text{(restatement of 2.22)}$$

$$GSI = 55.1 \frac{\frac{J_r}{J_a}}{1 + \frac{J_r}{J_a}} + 0.113 \cdot RQD + 19.59 \qquad (3.9)$$

(3.10)

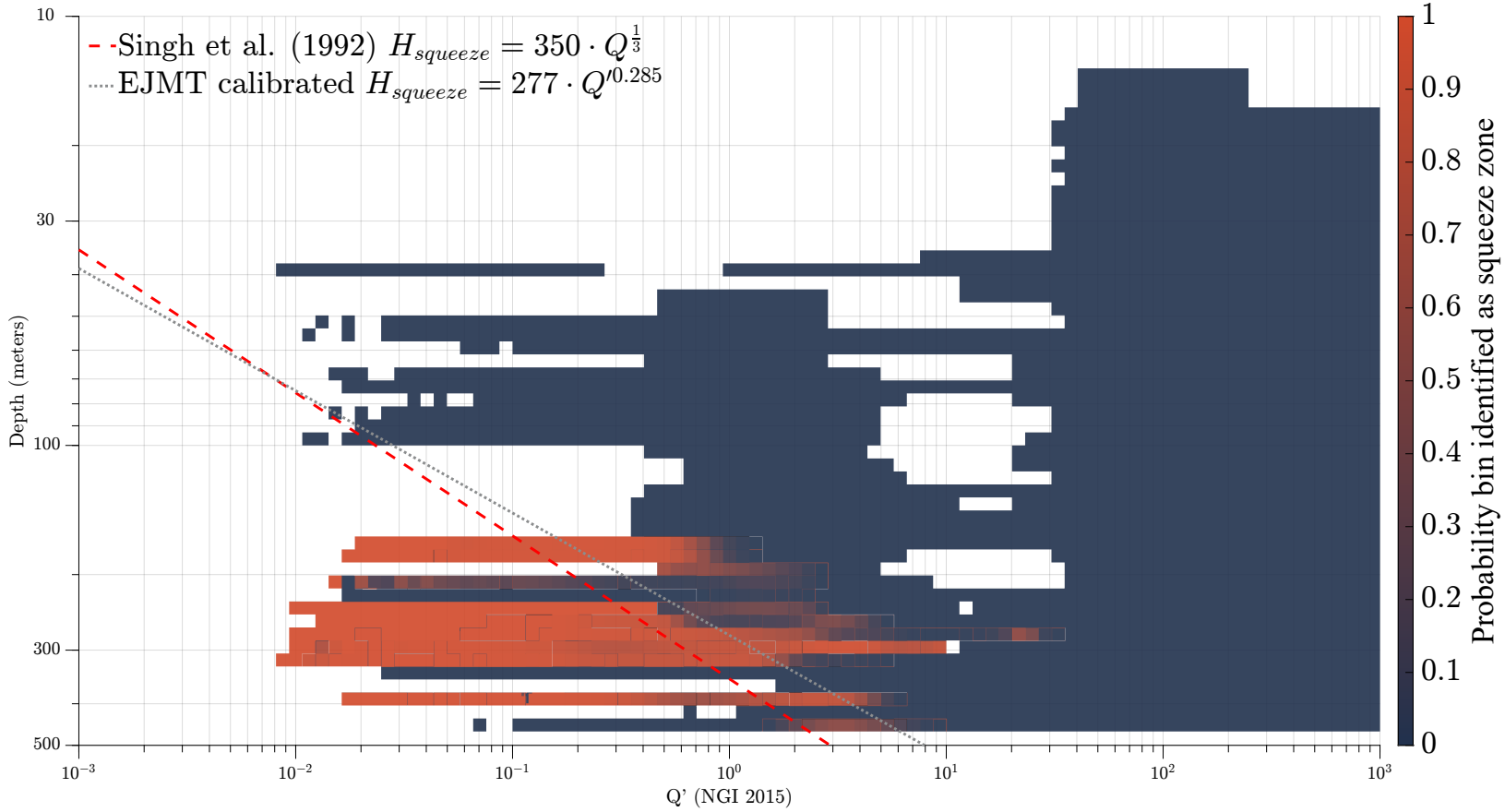

Figure 3.40: Depth vs. Q' for data points along the EJMT pilot and Eisenhower bores with percent squeeze zones binned and color coded. The squeeze prediction correlation by Singh et al. (1992) has a 90.2% accuracy at predicting squeezing and non-squeezing conditions in the EJMT dataset. The recalibrated criterion has a 93.5% accuracy at the same prediction.

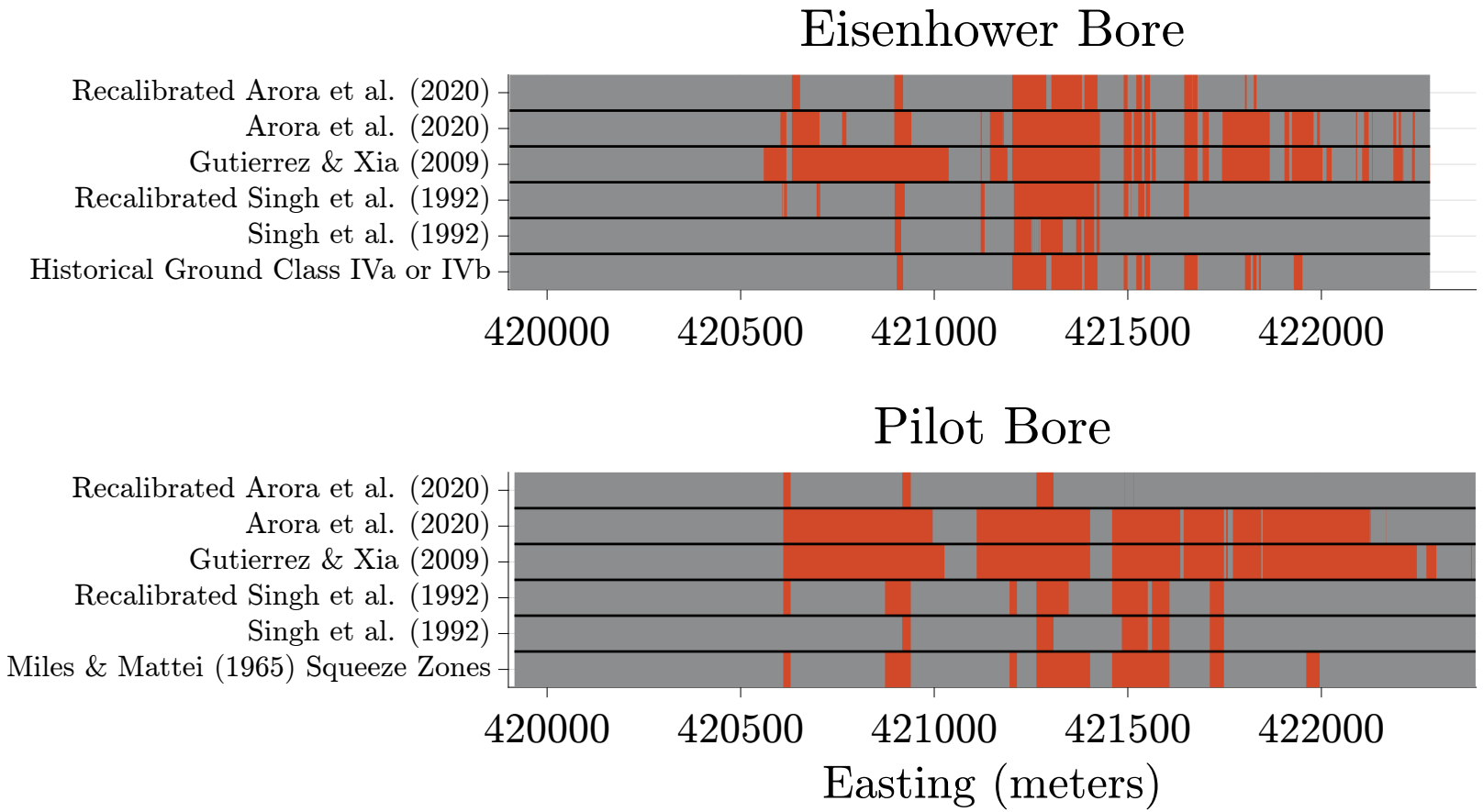

Figure 3.41: Identified squeeze zones, squeeze predictions by Equation 2.14, and squeeze predictions by Equation 3.7.

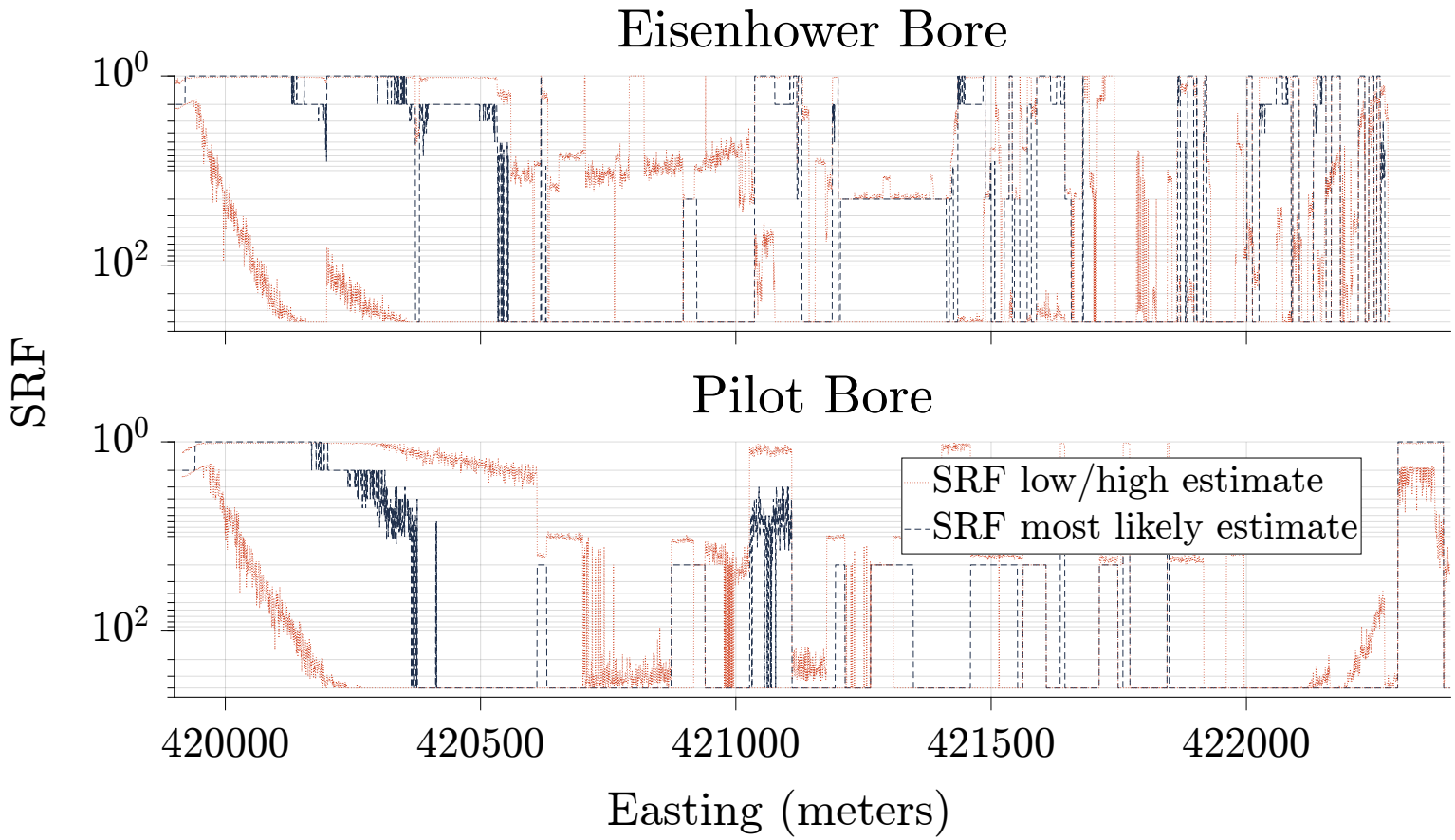

Figure 3.42: Most likely SRF and range along the pilot and Eisenhower bores.

where GSI is geological strength index, $RMR_{89JCond}$ is the rock mass rating (RMR_{89}) joint condition parameter, RQD is rock quality designation, $RMR_{14JCond}$ is the RMR_{14} joint condition parameter, JS is the joint spacing (m), J_r is the Q-system joint roughness parameter, and J_a is the Q-system joint alteration parameter.

The new correlation of Equation 3.8 is required because of changes to the underlying RMR parameters by Celada et al. (2014). Celada et al. (2014) have replaced the original joint condition parameter by Bieniawski (1989) with $RMR_{14JCond}$ and RMR_{14Alt}. Further, the RQD parameter has been deprecated entirely in favor of a joint spacing function after Lowson and Bieniawski (2013). The RMR_{89} joint condition score ranges from 0 to 30 while the $RMR_{14JCond}$ score ranges from 0 to 20. This implies that the joint condition coefficient would need to increase by a factor of 50% from the Hoek et al. (2013) factor of 1.5 to a factor of 2.25. The fitted factor of 2.49 is close, but not identical to, 2.25. The replacement of RQD with joint spacing leads to a dramatically different coefficient in the second term. In this case, the available data are for joint spacing, not RQD, and correlation of GSI to actual available data is preferred over correlation to an interpreted value of RQD. Additionally, this function includes a constant intercept component (29.7) not present in the original Hoek et al. (2013) equation. However, other work has found that RMR-GSI correlations tend to be inaccurate below some threshold of GSI, which has been previously found to be approximately 25 (Hoek 1994; Hoek and Brown 1997; Hoek et al. 1995). This work is in general agreement with these previous findings. The new adaptation of the Hoek et al. (2013) Equation 2.21 was created for this research project based on the available data in the Eisenhower bore. A multi-linear regression representing a plane surface in $RMR_{14JCond}$-JS space was fit relating the joint condition, joint spacing, and GSI based on the historical rock mass classifications. This three–parameter multi-linear regression model was tested with joint spacing, joint frequency, and RQD as possible inputs for the second term of the equation, and the base 10 log of each of those parameters, as well. The best fit model was found to be the one based on the joint condition and the base 10 logarithm of joint spacing. In addition, the logarithm of joint spacing is preferred because the joint spacing data cross several orders of magnitude. The equation of this surface is shown in Equation 3.8 and has a r^2–value of 0.61.

The new correlation of Equation 3.9 did not require reformulation as the Q-system J_r, J_a, and RQD parameters have not changed. However, recalibration of the constants was desired for this case study. The new Equation 3.9 has a r^2–value of 0.63, slightly better than the RMR based correlation but not dramatically so.

Although the r^2–value of Equation 3.8 and Equation 3.9 are somewhat low (0.61 to 0.63), they are better than the correlation of the original functions to this case.

Additionally, it indicates that there is some correlation of these properties to GSI, and Equation 3.8 and Equation 3.9 are considered acceptable for the current work. While Equation 3.8 and Equation 3.9 have some relevance to the evaluation of the EJMT, they are likely not generically applicable equations for evaluation of GSI. In fact, the most important conclusion to be drawn from the comparison of Equation 3.8 to Equation 2.21 and Equation 3.9 to Equation 2.22 may be that GSI is not uniquely correlated to any component of RMR or Q and should be carefully estimated by a trained engineering geologist for each unique case.

Hoek (2006) has made the same assertion that GSI should be estimated by trained and experienced personnel who can personally view the rock mass. Therefore, these GSI values are not recommended for forward modeling of new adjacent bores. They are used here only out of necessity. For the purposes of 3D extrapolation of GSI, only the values from the Eisenhower bore were used, which are based on in-situ observations by geologists at the time (Post and Eastwood 1973).

3.5.12 Hoek-Brown Damage Parameter

Post and Eastwood (1973) noted areas in the Eisenhower bore of the EJMT where overbreak exceeded 3 ft. Based on these data, the H-B damage parameter was estimated to range between 0.2 and 0.5 for areas with overbreak less than 3 ft and estimated to range between 0.4 and 0.7 for areas with overbreak greater than 3 ft. For the pilot bore, no data are available on the quality of the blasting, therefore the range of the damage parameter is estimated as 0.2 to 0.7. MC estimates of the damage parameter were made within the defined ranges assuming a symmetric triangular distribution.

Based on the laboratory data for the intact H-B parameters, the estimated damage parameter, and the estimated GSI (see Section 3.5.11) the parameters of the reduced H-B envelope were estimated based on the equations of Hoek and Brown (2018), i.e. Equation 3.11, Equation 3.12, Equation 3.13, and Equation 3.14.

$$\sigma_1 = \sigma_3 + \sigma_{ci}\left(m_b\frac{\sigma_3}{\sigma_{ci}} + s\right)^a \tag{3.11}$$

$$m_b = m_i e^{\frac{GSI-100}{28-14D}} \tag{3.12}$$

$$s = e^{\frac{GSI-100}{9-3D}} \tag{3.13}$$

$$a = \frac{1}{2} + \frac{1}{6}\left[e^{\frac{-GSI}{15}} - e^{\frac{-20}{3}}\right] \tag{3.14}$$

where σ_1 is major principal stress, σ_3 is minor principal stress, σ_{ci} is intact uniaxial compressive strength, m_i is the intact rock strength parameter, m_b is the rock mass strength parameter, s and a are Hoek-Brown empirical rock mass strength parameters, GSI is geological strength index, and D is the Hoek-Brown blast damage (disturbance) parameter.

3.5.13 Number of Monte Carlo Realizations Used

Histograms of RMR_{14} and Q scores at each station show multi-modal distributions in some cases. To evaluate the required number of Monte Carlo realizations, trial values from $N = 10$ to $N = 10,000$ were run and the change in the distribution of RMR_{14} and Q scores was observed. Some of the multi-modality goes away (i.e., the distributions smooth out) with higher number of MC runs, indicating that local deviations and extreme values are being overwhelmed by the majority of values. At $N = 10$ there are as many as 4 local maxima in the RMR_{14} histograms at each station. By $N = 500$ there is typically only a single local maximum, though some stations have a truly bimodal distribution, i.e. the bimodality is not smoothed out by additional Monte Carlo realizations. This dominant uni-modality with some bimodality holds true through $N = 10,000$ MC runs. $N = 2000$ was selected as a conservative number of MC realizations for each station along each bore based on this observation.

3.6 Implications

The previous section presented a methodology for the probabilistic evaluation of historical construction, geologic, and laboratory analytical data into a single model. The intent is to:

1. Demonstrate the effectiveness of probabilistic data reduction techniques for analyzing complex project data;
2. Demonstrate the effectiveness of probabilistic evaluations of the interaction of geologic and engineering parameters; and,
3. Provide a rich case study database for further studies.

In the following sections are evaluations of:

1. The correlation between the estimated rock mass classification parameters;
2. The correlation between the rock mass classification parameters and measured

advance rates; and,

3. The process of extrapolating from these data into a 3D geologic model.

3.6.1 Cross-Correlations of Q, RMR, and GSI

For this study, regressions comparing the results of RMR_{14}, RMR_{14b}, rock condition rating (RCR), Q, rock mass number (N), and Q' were performed for comparison to previous studies. Results of these regressions are presented in Figure 3.43 for the Eisenhower bore and Figure 3.44 for the pilot bore. Note that there is only an approximate correlation between RMR and Q for this study, as other researchers have noted elsewhere (Rehman et al. 2018; Singh and Goel 2011). In the Eisenhower bore the best correlation between the two systems is between RMR_{14b} and N, with RMR_{14b} versus Q' a close second. The A and B parameters of the RMR_{14b}-N fit line for the Eisenhower bore are 11.4 and 43.0, respectively, with $r^2 = 0.72$. In the pilot bore the best correlation between the two systems is between RMR_{14b} and Q', with RMR_{14} versus Q a close second and RMR_{14b} versus N a reasonable comparison. The A and B parameters of the RMR_{14b}-Q' fit line for the pilot bore are 10.9 and 35.5, respectively, with $r^2 = 0.73$. The N value does not include the SRF and the Q' value does not include either the SRF or J_w parameters. The RMR_{14b} value does not include the ICE or stress adjustment factor for RMR (F_s) parameters. This lends credence to the suggestion by Goel (Goel et al. 1996; Singh and Goel 2011) that the stress-based parameters of RMR and Q do not correlate well, but the other parameters do. However, the relatively weak correlation of RCR and N, the two specific parameters suggested by Goel et al. (1996), does not strongly support their case for the use of these parameters.

Additional comparisons between RMR and GSI as well as Q and GSI are shown in Figure 3.45 for the Eisenhower bore and Figure 3.46 for the pilot bore. The correlations show very wide scatter and relatively poor correlations compared to the RMR-Q correlations. The correlation between Q' and GSI in the Eisenhower bore was used as the basis for a multi-linear regression model for estimating GSI in the pilot bore, where data for estimating GSI are very limited. This leads to the exceptional correlation between GSI and Q in the pilot bore, which should not be taken as scientifically meaningful in this case.

3.6.2 Correlations to Advance Rate

Mattei (1965) described the drill-and-blast excavation cycle used during the construction of the pilot bore as follows:

- 90 minutes: drilling shot holes

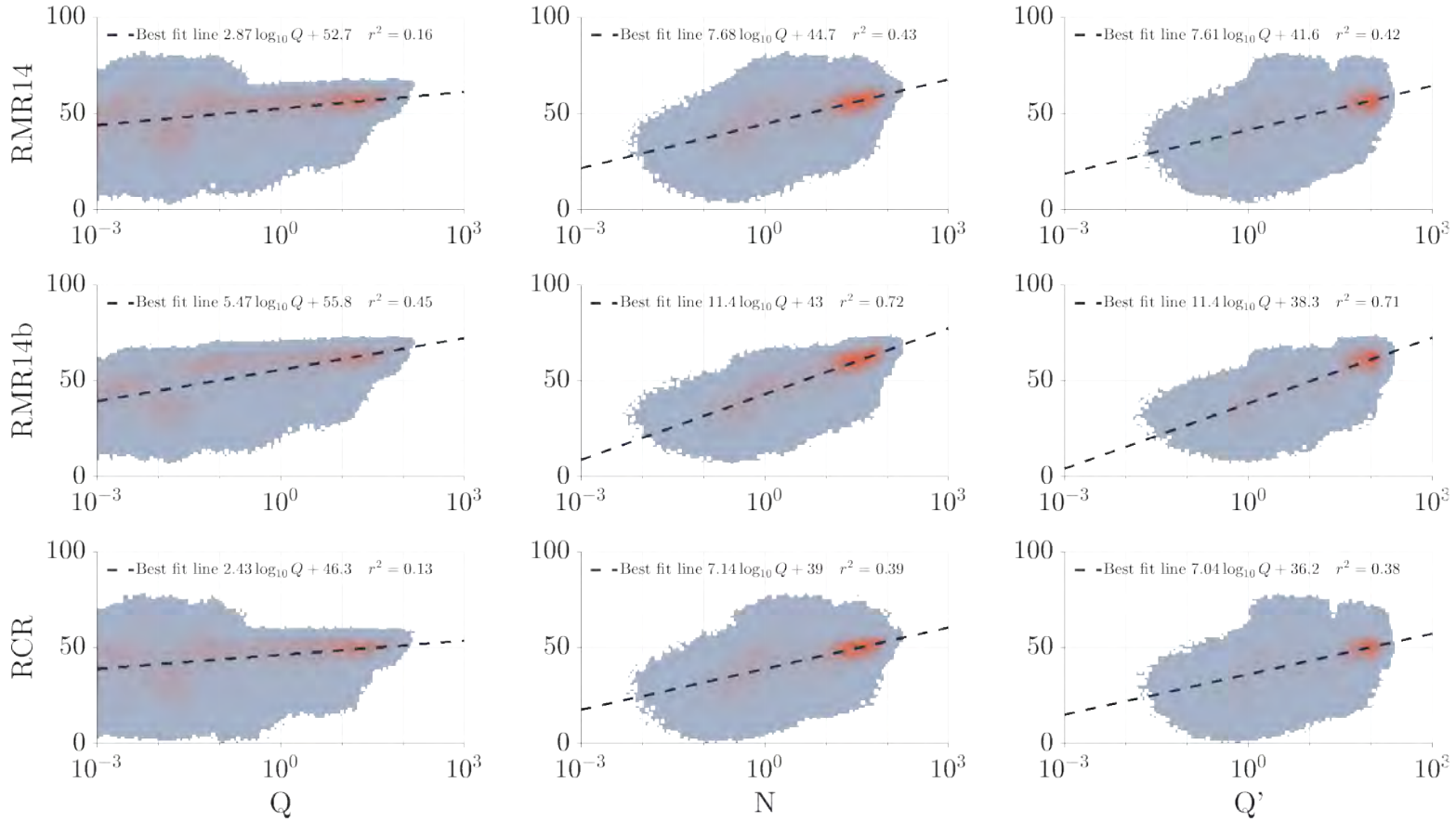

Figure 3.43: Heatmaps of various versions of RMR (RMR_{14}, RMR_{14b}, and RCR) versus various versions of Q (Q, N, and Q') in the Eisenhower bore. Warmer colors indicate more correlations in a given bin. Note that the best correlation between the two systems in this case appears to be between RMR_{14b} and N, with RMR_{14b} versus Q' a close second. The A and B parameters of the RMR_{14b}-N fit line are 11.4 and 43.0, respectively, with $r^2 = 0.72$.

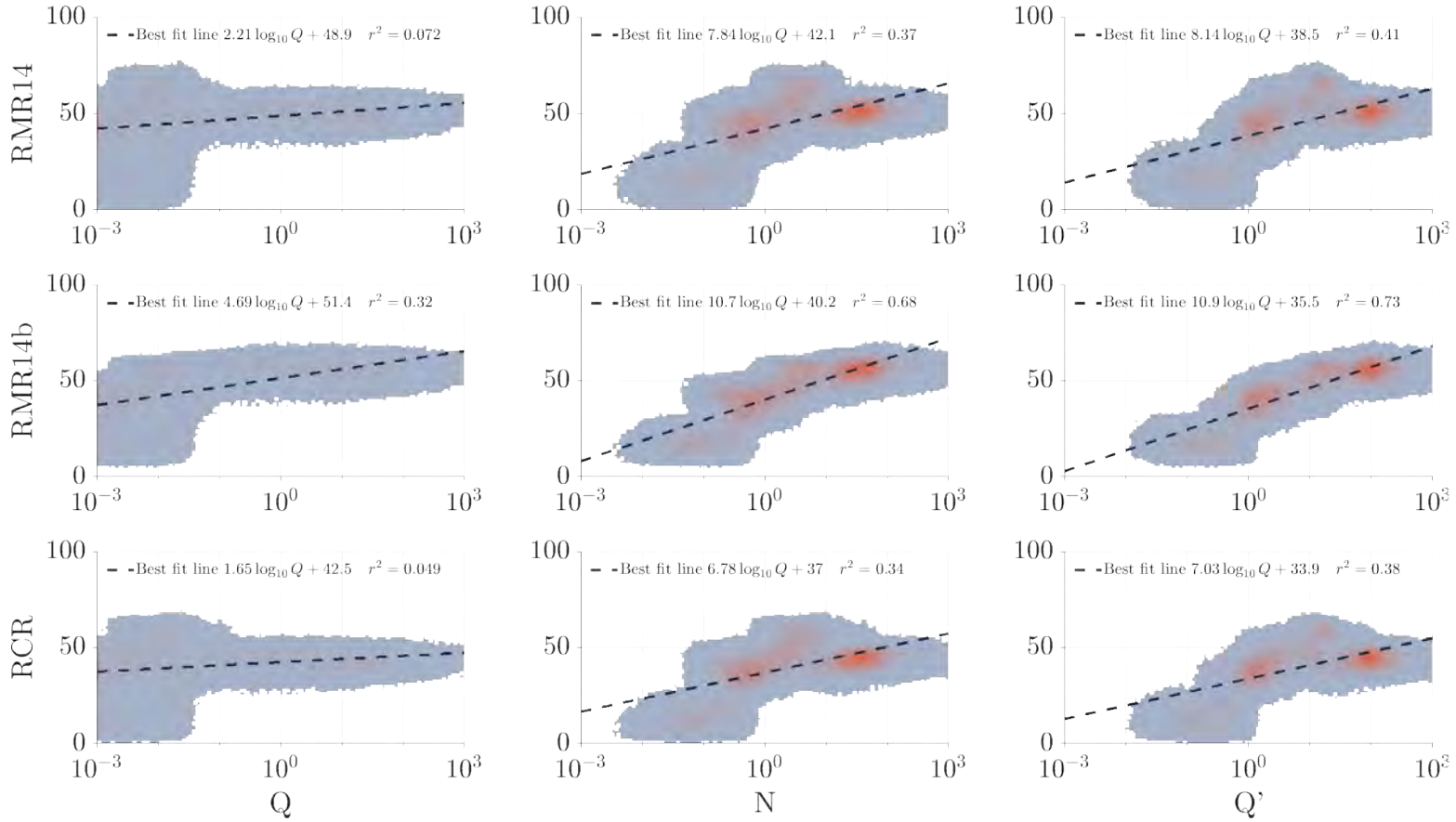

Figure 3.44: Heatmaps of various versions of RMR (RMR_{14}, RMR_{14b}, and RCR) versus various versions of Q (Q, N, and Q') in the pilot bore. Warmer colors indicate more correlations in a given bin. Note that the best correlation between the two systems in this case appears to be between RMR_{14b} and Q', with RMR_{14} versus Q a close second and RMR_{14b} versus N a reasonable comparison. The A and B parameters of the RMR_{14b}-Q' fit line are 10.9 and 35.5, respectively, with $r^2 = 0.73$.

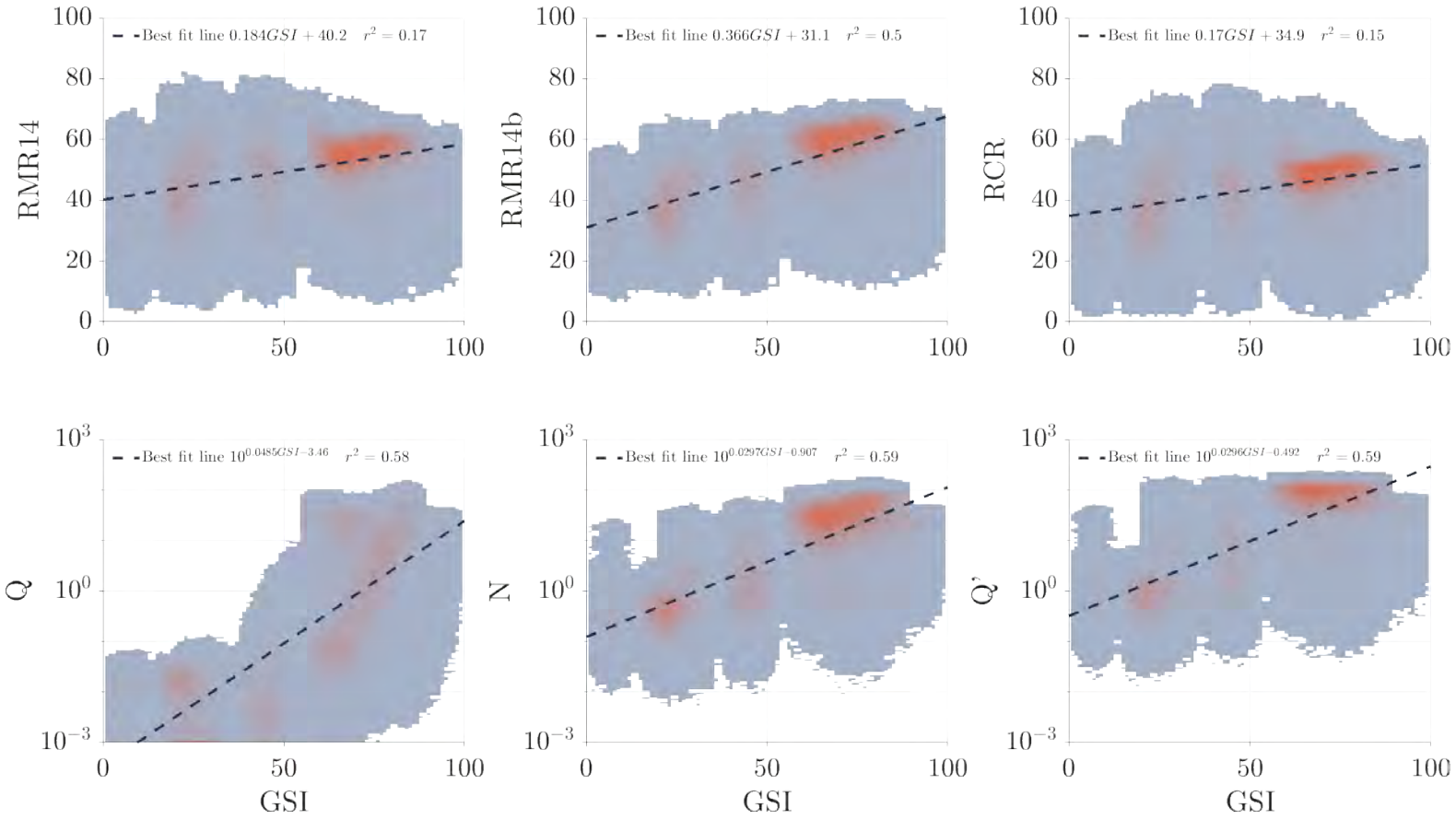

Figure 3.45: Heatmaps of RMR_{14}, RMR_{14b}, RCR, Q, N, and Q' versus GSI in the Eisenhower bore. Warmer colors indicate more correlations in a given bin. Note that the best correlation appears to be between N and GSI. However, this correlation is somewhat weak with $r^2 = 0.59$ and very wide scatter in the data.

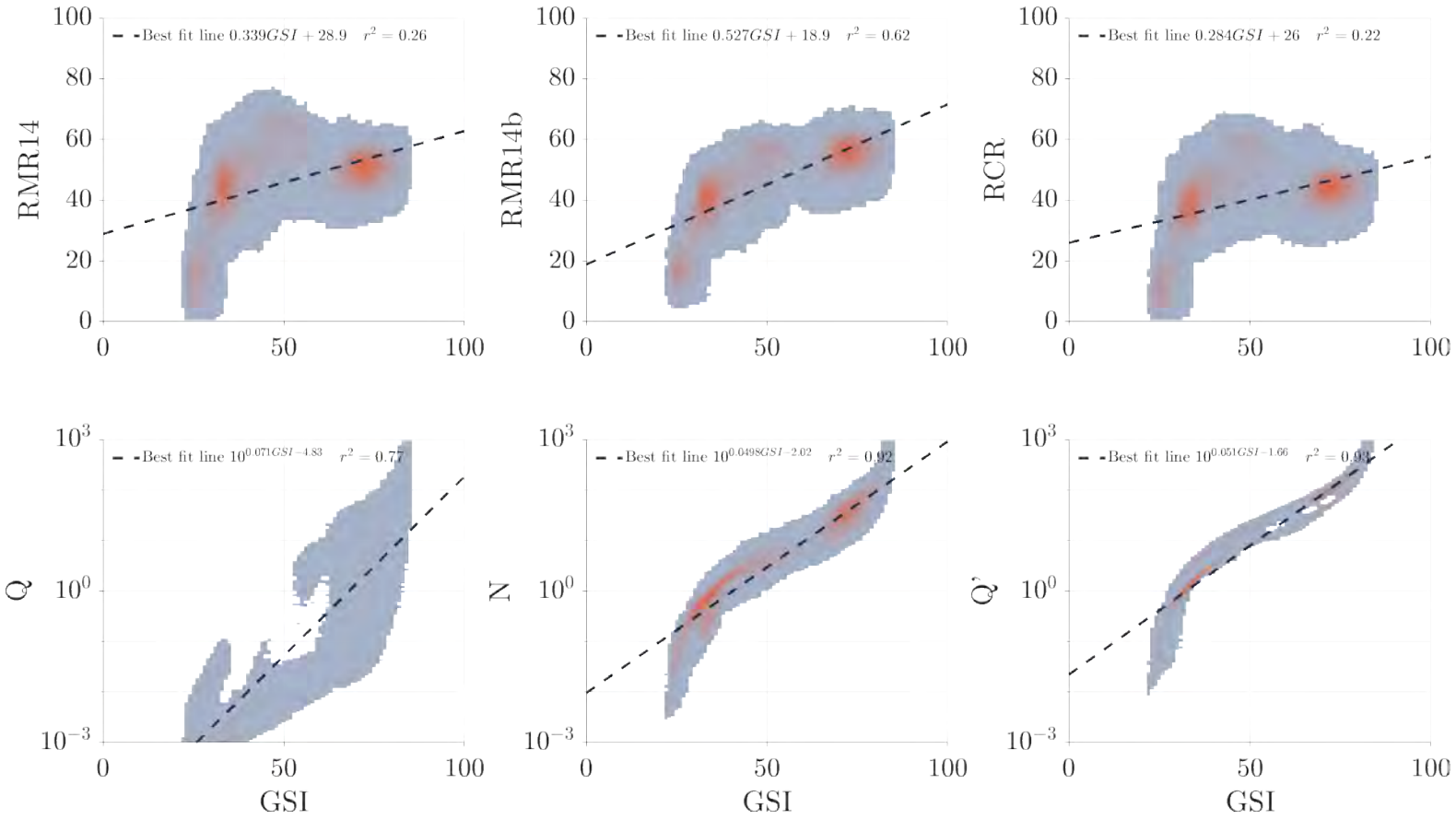

Figure 3.46: Heatmaps of RMR_{14}, RMR_{14b}, RCR, Q, N, and Q' versus GSI in the pilot bore. Warmer colors indicate more correlations in a given bin. Note that GSI was estimated from Q parameters for the pilot bore by multi-linear regression, leading to the relatively good correlation here.

- 15 minutes: wait for dust/gas to clear
- 60 minutes: mucking
- 45 minutes: mucking machine removed, track laid to face, geologic mapping conducted
- 30 minutes: setting steel

Thus, the total time for a typical construction cycle was four hours. Mattei (1965) states that the average round length was five ft, and the crew was working three 8-hour shifts, for a total rate of advance of 30 ft per day. The construction proceeded either six or seven days per week (144 or 168 hours per week). He goes on to note that in poor ground, the heading was advanced by shorter rounds or spading (or a combination of the two). The rate of advance declined to approximately 10.5 ft per day in poor ground conditions. Note that the cycle given by Mattei (1965) implies that the time from blasting to the installation of steel support was approximately 2.5 hours.

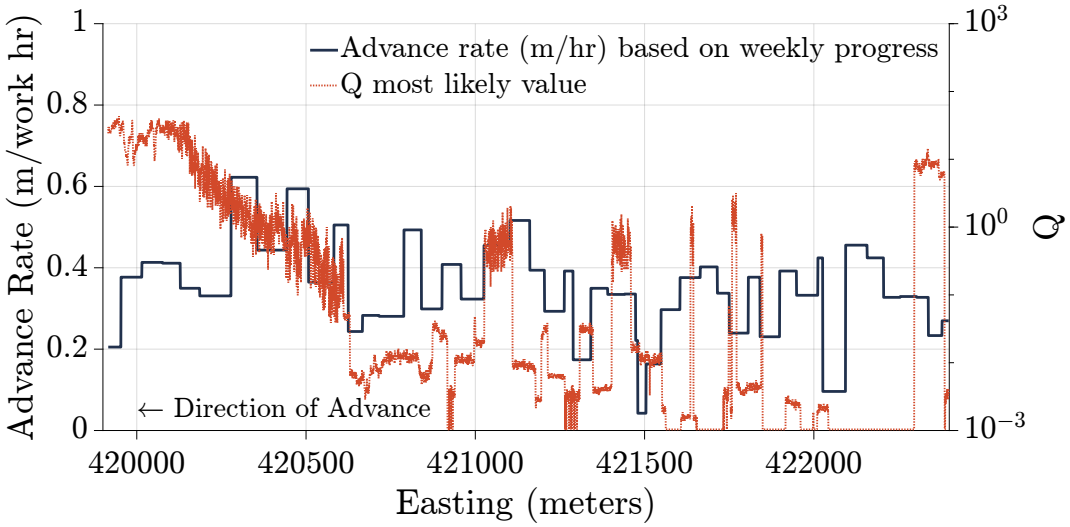

Figure 3.47: EJMT pilot bore weekly average advance rate data (m/working hour) after Mattei (1965) compared to most likely estimated Q-value from Monte Carlo simulation.

Actual recorded advance rates in the pilot bore, calculated as meters per hour averaged over one working week, varied from 0.014 to 0.62 m/hr (Mattei 1965; Miles and Mattei 1965; Robinson et al. 1974).

Reports by Hopper et al. (1972), Post (1973), and Post and Eastwood (1973) all provide some information on the rate of progress in the Eisenhower bore. In particular, the geologic maps by Post and Eastwood (1973) include annotations at several points indicating the date that position was excavated. These data were digitized along with the rest of the geologic map. Some data in the geologic map were not legible and some data may have been incomplete as well, leading to gaps in the data set, both temporally and

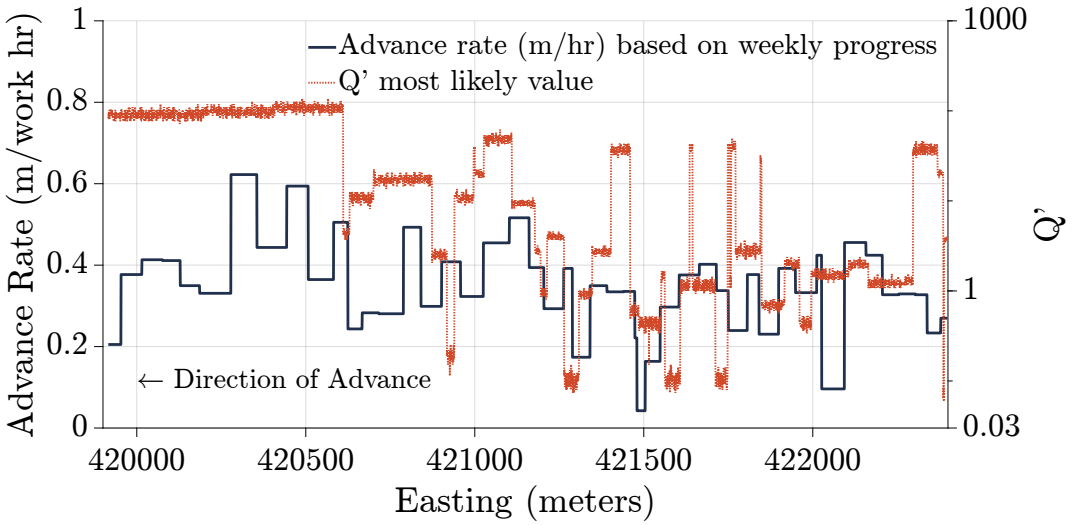

Figure 3.48: EJMT pilot bore weekly average advance rate data (m/working hour) after Mattei (1965) compared to most likely estimated Q'-value from Monte Carlo simulation.

physically. In addition, one section from 81+00 to 81+57 was excavated full face with a digger shield beginning on 31 May 1969 before the shield became stuck on 29 August 1969. The shield was subsequently abandoned in place and a top heading and bench system was re-adopted. Crown drift excavation re-started on 14 December 1970. The excavation in this section is likely unrepresentative of the overall tunnel progress. The amount of downtime which was spent constructing and abandoning the shield is unclear, and some downtime may have been due to a work stand-down while the contractor and CDOT discussed how to proceed. Also, it is unclear what work schedule was being employed in the Eisenhower bore construction. To convert the Eisenhower bore advance rate data to units of m/hour, a 20–hour workday is assumed. This would correspond to three 8-hour shifts, six days per week. This schedule was commonly employed in the pilot bore and is fairly typical for the era.

The cross-sectional area of the pilot bore varies from approximately 10.6 m^2 (114 ft^2) to 11.6 m^2 (125 ft^2). The cross-sectional area of the Eisenhower bore varies from approximately 126 m^2 (1360 ft^2) to 170 m^2 (1830 ft^2). The top heading cross-section varies from approximately 60.8 m^2 to 70.3 m^2. The bench cross-section varies from approximately 63.6 m^2 to 99.7 m^2.

There is very little correlation between the rock mass parameters evaluated for this project (RMR_{89}, RMR_{14b}, RMR_{14}, RCR, rock mass excavatability (RME), Q, Q', and N) and the recorded advance rate data for the EJMT pilot bore. Several regression models between the rock mass classifications estimated in the pilot and Eisenhower bores were evaluated, separately and together, against the recorded linear and volumetric

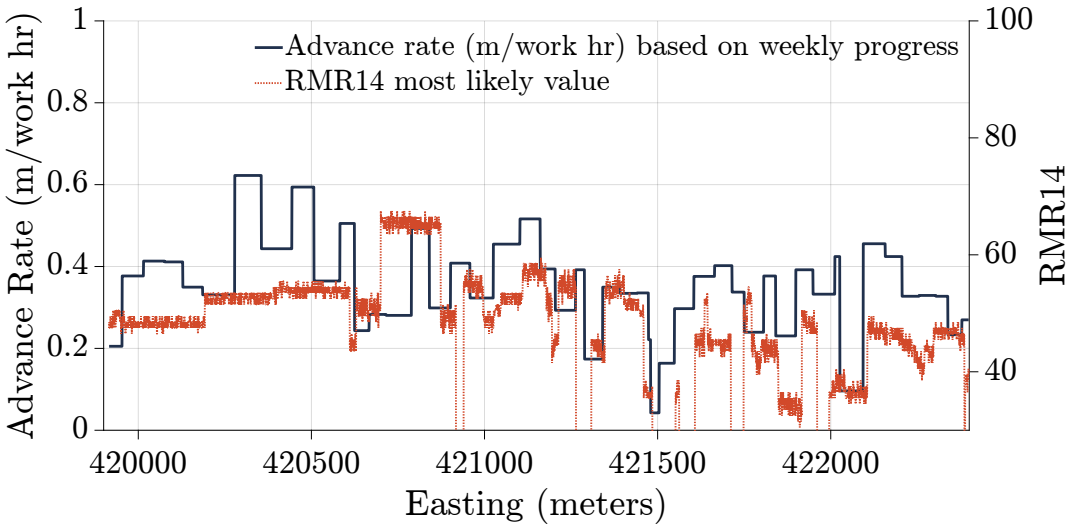

Figure 3.49: EJMT pilot bore weekly average advance rate data (m/working hour) after Mattei (1965) compared to most likely estimated RMR_{14}-value from Monte Carlo simulation.

advance rates in each bore. The best linear correlation was between the deterministically estimated RMR_{89} and the linear work progress data from the pilot bore (see Figure 3.50). However, this correlation had an r^2–value of 0.23, indicating little correlation between the parameters. Using a quadratic function as the correlation only marginally improve the fitting (r^2–value = 0.24). Barton (2000) proposed that a sigmoid curve defines the relationship between $\log_{10} Q$ and advance rate for drill-and-blast tunnels, so a regression to a two-term exponential function was attempted as well. Again, the best r^2–value was only 0.24. Table 3.9 summarizes the correlations between linear advance rates (m per working hour) and various rock mass classifications by linear, quadratic, and two-term exponential functions.

Given the low quality of the drill-and-blast advance rate correlations and changes in the tunneling industry since the construction of the EJMT, forward modeling of plausible advance rates for future bores in the vicinity of the EJMT by generic correlations such as those of Barton (2000) (Table 2.2) are likely as satisfactory as historical data. For forward modeling of plausible tunnel boring machine (TBM) advance rates, there are no historical data, so generic correlations such as those discussed in Section 2.4.5 are the only available solution.

Table 3.9: Pilot bore advance rate data correlations.

Rock Mass Classification	r^2 of linear function regression	r^2 of quadratic function regression	r^2 of two-term exponential function regression
RME	0.014	0.016	0.016
RMR_{89b}	0.231	0.242	0.244
RMR_{89}	0.231	0.242	0.244
RMR_{14b}	0.191	0.230	0.251
RMR_{14}	0.122	0.125	0.123
RCR	0.122	0.125	0.123
$\log_{10} Q'$	0.161	0.176	0.191
$\log_{10} N$	0.143	0.163	0.164
$\log_{10} Q$	0.053	0.082	0.071

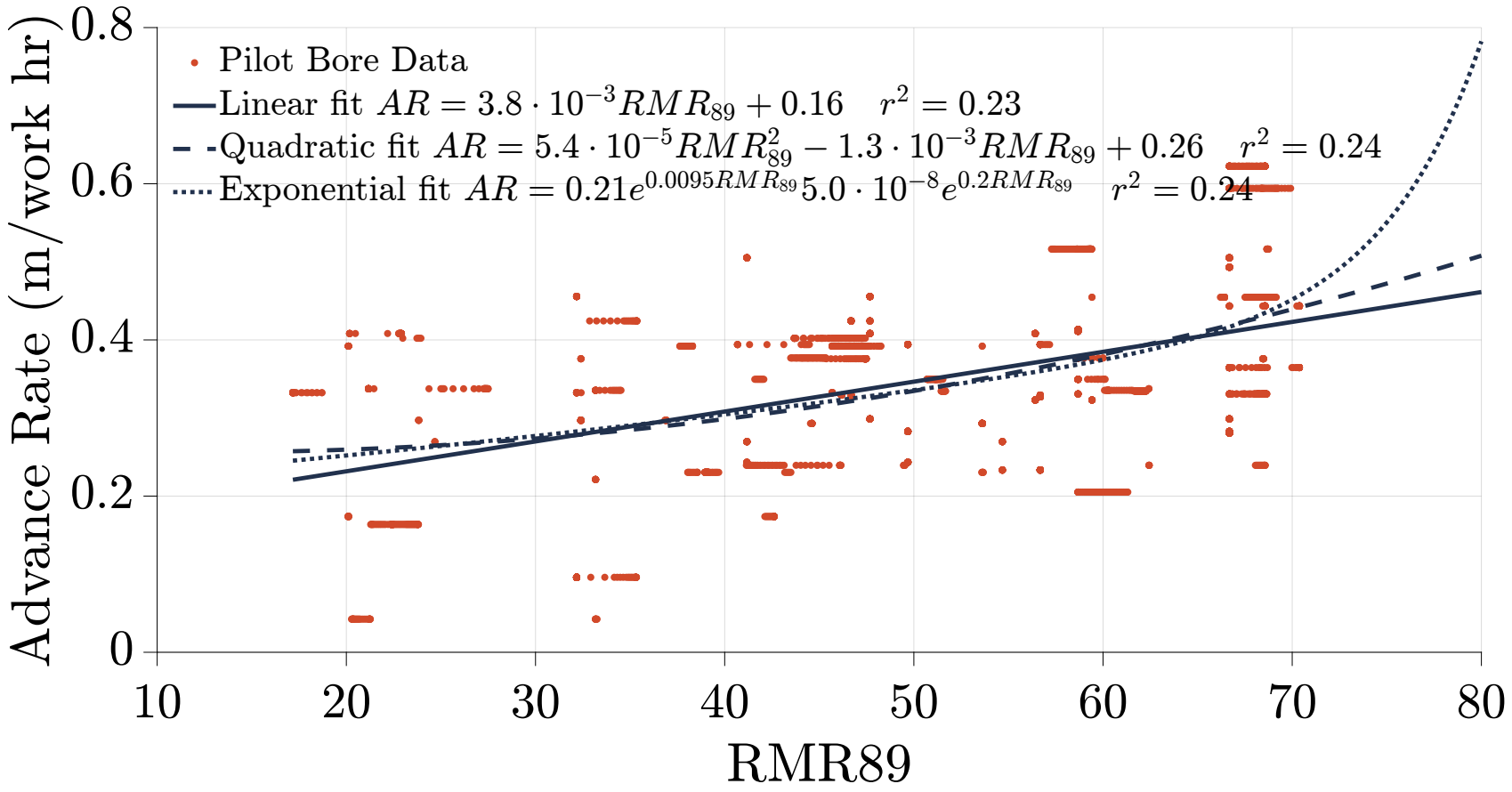

Figure 3.50: Correlations between recorded advance rates in the EJMT pilot bore and estimated RMR_{89}. Note low r^2 values indicating little correlation (or very high scatter) between RMR_{89} and advance rate. Correlations between advance rate and other rock mass classifications were also poor.

3.6.3 3D Modeling of Geologic Data

The research team also sought to enhance the usefulness of the case study data for future studies and to demonstrate the effectiveness of modern 3D modeling tools in the visualization, analysis, and use of the above probabilistic data. To that end, a 3D geologic model was developed and the probabilistic engineering data were extrapolated across this model.

3D geologic models were created in Leapfrog Geo (Seequent 2020) to characterize key aspects of subsurface geology focusing on the fault zone network and underlying lithology. Leapfrog Geo provides a suite of tools for implicit modeling of geologic surfaces including depositional and erosional surfaces, intrusions, faults and more. The implicit modeling method is widely popular in the 3D geologic modeling community for its flexibility and speed (Caumon 2010; Wellmann and Caumon 2018). The method uses the interpolation of a 3D scalar field to implicitly define surfaces, avoiding the comparatively rigid requirements of surface-based interpolation (Cowan et al. 2003). Geologic modeling in this study focused on data from the high-quality geologic maps acquired in the pilot bore, while surficial mapping of major lithological contacts and fault zones provided supplementary information. The surficial mapping products lacked key information such as structural orientations, and were thus of limited usefulness. Three distinct geologic models were generated for this study (Figure 3.51) The models can be combined freely by evaluating onto a common block model and using filters to superimpose various models.

The first model focuses on the subsurface lithology in the vicinity of the pilot bore (Figure 3.51(a)), highlighting the SPG, various ISF inclusions and the augite-diorite dike. Lithological contacts were modeled from polyline traces and structural orientation data, and in some cases the interpolants were adjusted manually to generate geologically realistic bodies. The complex shapes and heterogeneous occurrence of ISF inclusions limit the ability for this model to be extrapolated away from the pilot bore resulting in a limited extent of $\pm$100 m in each direction.

The second geologic model focuses on the fault zone network intersected by the pilot bore (Figure 3.51(b)). The fault zone model covers the same extent as the lithology model, providing an acceptable range of extrapolation for the fault zones encountered in the pilot bore ($\sim$100 m). Fault zones were modeled as 3D slabs centering around the fault trace with thickness defined from the available data by Miles and Mattei (1965), Post and Eastwood (1973), and Robinson et al. (1974). The formulated fault zone network model has been simultaneously developed in a probabilistic geologic modeling framework to investigate uncertainties about the 3D fault zone volumes in light of uncertainties present

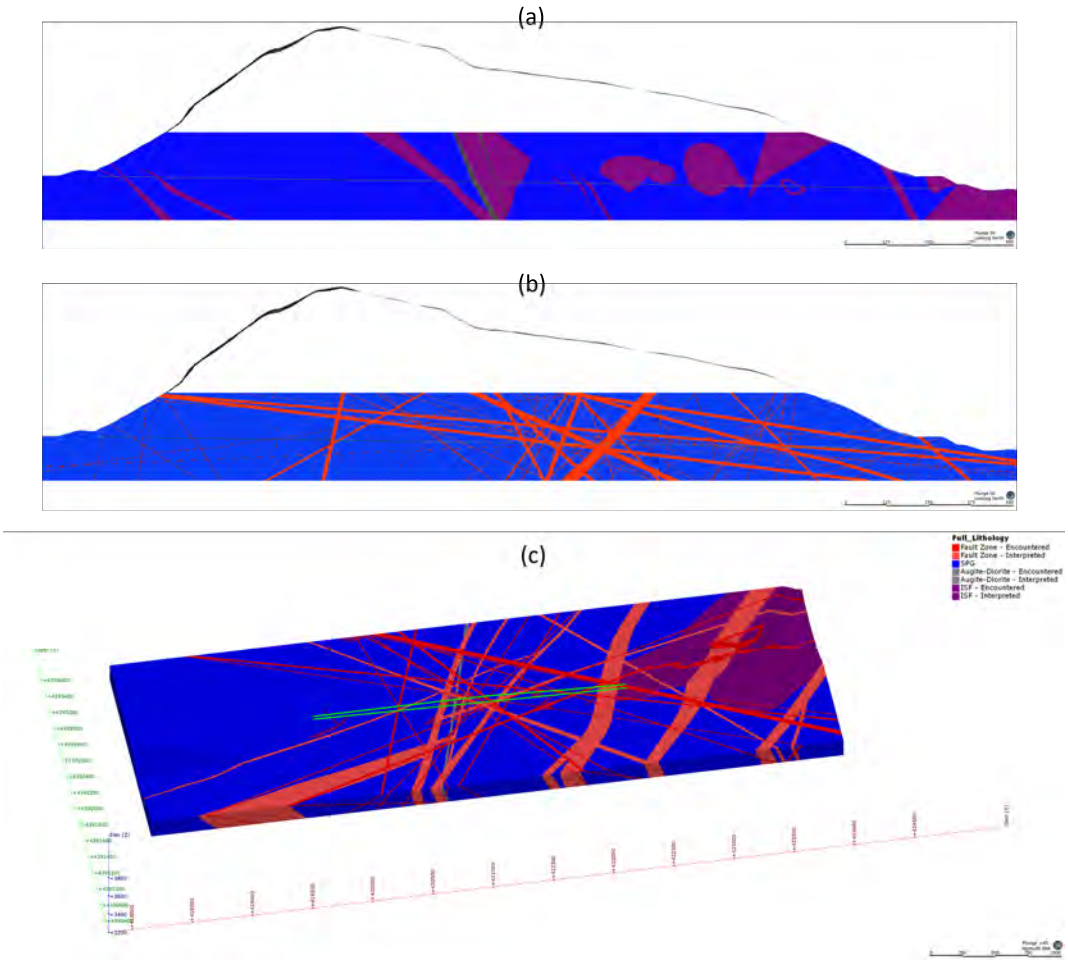

Figure 3.51: Suite of geologic models created to characterize the subsurface geology around the EJMT. (a) shows the lithological model based on pilot bore mapping, (b) shows the fault zone network model based on pilot bore mapping, and (c) shows a regional scale composite model combining the detailed information from (a) and (b) with interpreted structures from surficial mapping.

in the input data and modeling method (Krajnovich et al. 2020).

The third geologic model (Figure 3.51(c)) is a composite model which supplements the detailed lithology and fault zone network models with additional regional scale structures and lithological contacts derived from the surficial geologic map. This model covers a wide extent surrounding the EJMT, superimposing the detailed pilot bore geologic models with lower certainty extrapolations of regional structures. The mean orientation of mapped faults (as assessed by a Bingham distribution) was assigned to surficial fault zones lacking full structural information.

3.6.4 Numerical Interpolation of 3D Geologic Data

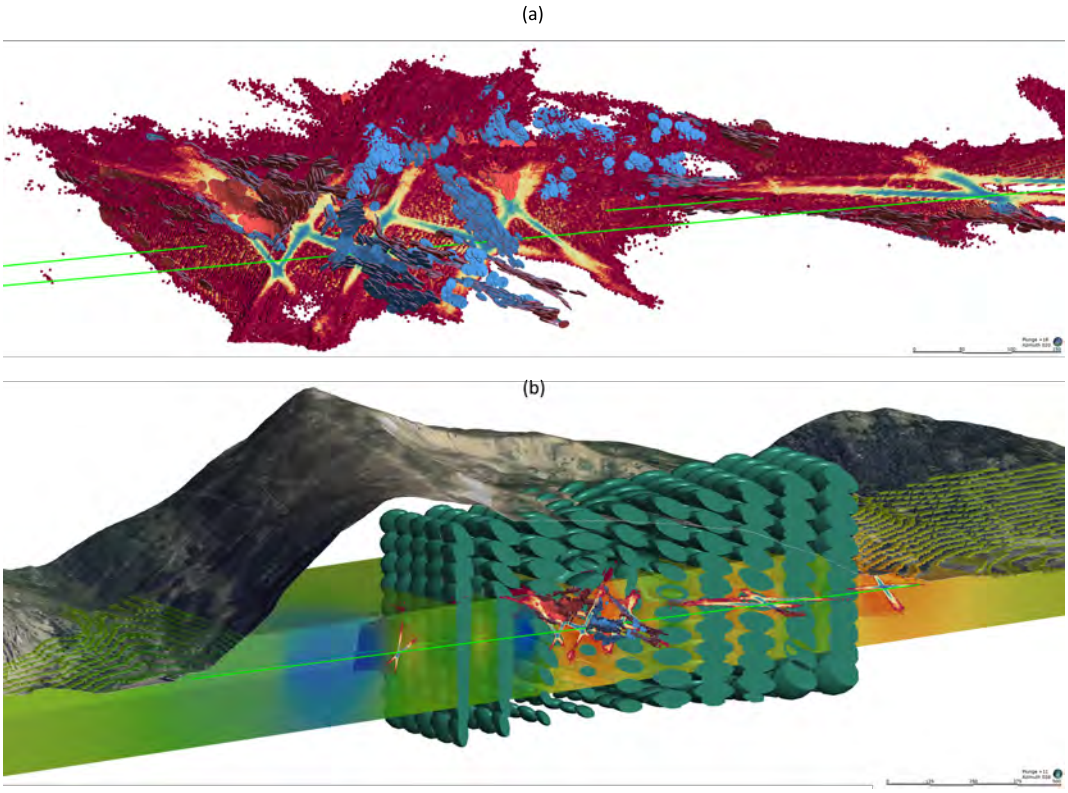

Figure 3.52: Generation of an RBF interpolant structural trend from a fault zone geologic model. (a) structural orientation data are extracted from the geologic model based on vertices of key geologic surfaces. (b) Initialization of a structural trend in Leapfrog, with parameter options including the strength of the trend and whether the trend is non-decaying.

Quantitative rock mass classification and geotechnical parameter data were extrapolated in 3D using the numerical radial basis function (RBF) interpolant functionality in Leapfrog (Leapfrog 2014). RBFs are tools for interpolating data in a three-dimensional

field, and have been leveraged in implicit geologic modeling for several years (Cowan et al. 2003; Hillier et al. 2017; Hillier et al. 2014). The wealth of quantitative geologic data assembled for this study were imported into Leapfrog and used to inform 3D RBF interpolants. The goal of this numerical interpolation is to populate the subsurface volume with predictions of the expected rock quality based on the variety of parameters introduced in this study. Like geologic models, the numerical RBF interpolants are evaluated onto a common block model for subsequent visualization and analysis.

RBF interpolants perform similarly to the commonly used kriging method, but differ in that they do not rely on the covariance function or a variogram, circumventing the assumption of data stationarity (Cowan et al. 2003). Instead, the RBF is initialized using a basic function chosen from a standard set; in Leapfrog, several customization options are available ranging from the type of basic function (linear or spheroidal) to its parameters (e.g., sill, nugget, range). The RBF interpolant can be further modified using structural orientation data in the form of structural trends. This functionality allows the numerical interpolant models to be guided by the underlying geologic models. Three structural trends were defined to characterize key aspects of the geologic model: the subsurface fault zone network, the lithological contacts of SPG intrusions into the ISF, and the major surficial fault zones. The appropriate trend type to apply to each numerical parameter for 3D interpolation was interpreted based on the believed primary factor influencing the distribution of that parameter. For example, some of the assumptions made were that RMR_{14Alt} is influenced primarily by the dense, subsurface fault zone network, RMR_{14UCS} by the distribution of the underlying lithology and RMR_{14GW} by potential infiltration from the major surficial fault zones. Because the selection of structural data to create an informative trend is potentially subjective, an additional method leveraging the probabilistic geologic modeling tool developed by Krajnovich et al. (2020) was demonstrated to account for structural uncertainties. A probabilistic fault zone model generated from 300 geologic model realizations was evaluated at its 50% likelihood confidence interval and the resulting surface was used to characterize a structural trend describing the fault zone network. Figure 3.52 illustrates the process for estimating a structural trend from a geologic model using this methodology.

While applying structural trends to the numerical interpolants enhances the detail and complexity of these models, the resulting interpolant has a limited extent governed by the size of the input structural trend. To overcome this, each numerical interpolant was cloned using a non-informative (isotropic) trend and extrapolated to the full extent of the composite 3D geologic model. The isotropic interpolant represents a baseline guess at the expected rock quality in areas that are not well informed by the underlying structural

geologic model. Figure 3.53 shows a comparison of the isotropic and fault zone derived structural trend interpolant for example rock mass classification parameter, GSI.

The rock mass classification systems RMR_{14} and Q, are synthesized from a collection of component parameters. In these cases, each parameter was modeled and interpolated in 3D independently using the most appropriate structural trend. The final rock mass classification score was then computed from the independent numerical interpolants at every cell of the model. This method preserves more information on the variability of each parameter than simply interpolating the RMR_{14} or Q scores directly.

The EJMT pilot bore provided a rich dataset for 3D geologic modeling, suggesting that greater emphasis should be placed on the value of pilot bore investigations for tunnel excavation. While the EJMT pilot bore involved a 12–ft diameter bore for geologists to enter and map, modern investigation tools such as photogrammetry, Light Detection and Ranging (LiDAR), directional drilling, and borehole televiewers could be used in future projects to reduce cost and improve data quality. In conventionally excavated tunnels, mapping can also be performed in the final tunnel excavation itself before support is installed. As evidenced by the present case study of the EJMT, such a dataset could prove valuable when considering the maintenance and future expansion of underground transportation infrastructure.

The 3D geologic models developed of the EJMT study area leverage state-of-the-art implicit geologic modeling software to characterize the subsurface in terms of lithology, geologic structures and quantitative engineering geologic descriptions. Though they are modeled separately, structural geologic models and engineering geologic numerical interpolant models are naturally interrelated. By informing numerical interpolant models with structural trends derived from relevant features of the structural geologic model, the resulting interpolants provide valuable insight into the complex distribution of engineering geologic properties. Future work will explore the inverse relationship, investigating how the distribution of engineering geologic properties may be used to refine the structural 3D geologic model itself. In addition to the flexibility and control afforded by implicit modeling algorithms, implicit geologic models can be conveniently evaluated onto discretized block models, providing a powerful format for analyzing the different members of a structural geologic model. Composite block models also provide an efficient format for combining 3D datasets of varying quality and coverage.

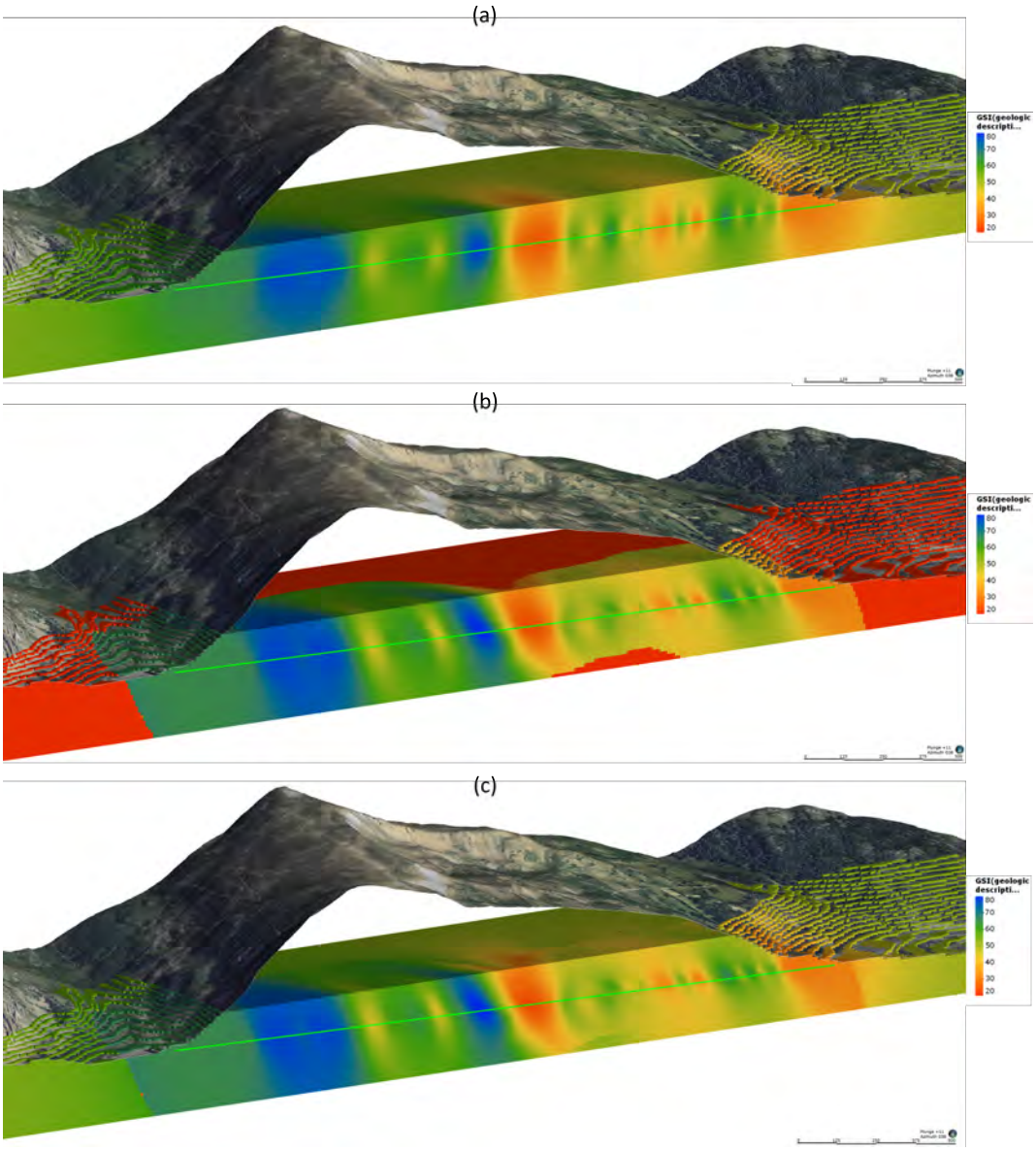

Figure 3.53: Comparison of RBF interpolants for an example rock mass classification parameter (GSI) using (a) an isotropic interpolant and (b) the fault zone derived structural trend. Areas where the interpolant returns erroneous values are colored bright red. (c) and (d) show the composite model combining both interpolants in section and plan view, respectively.

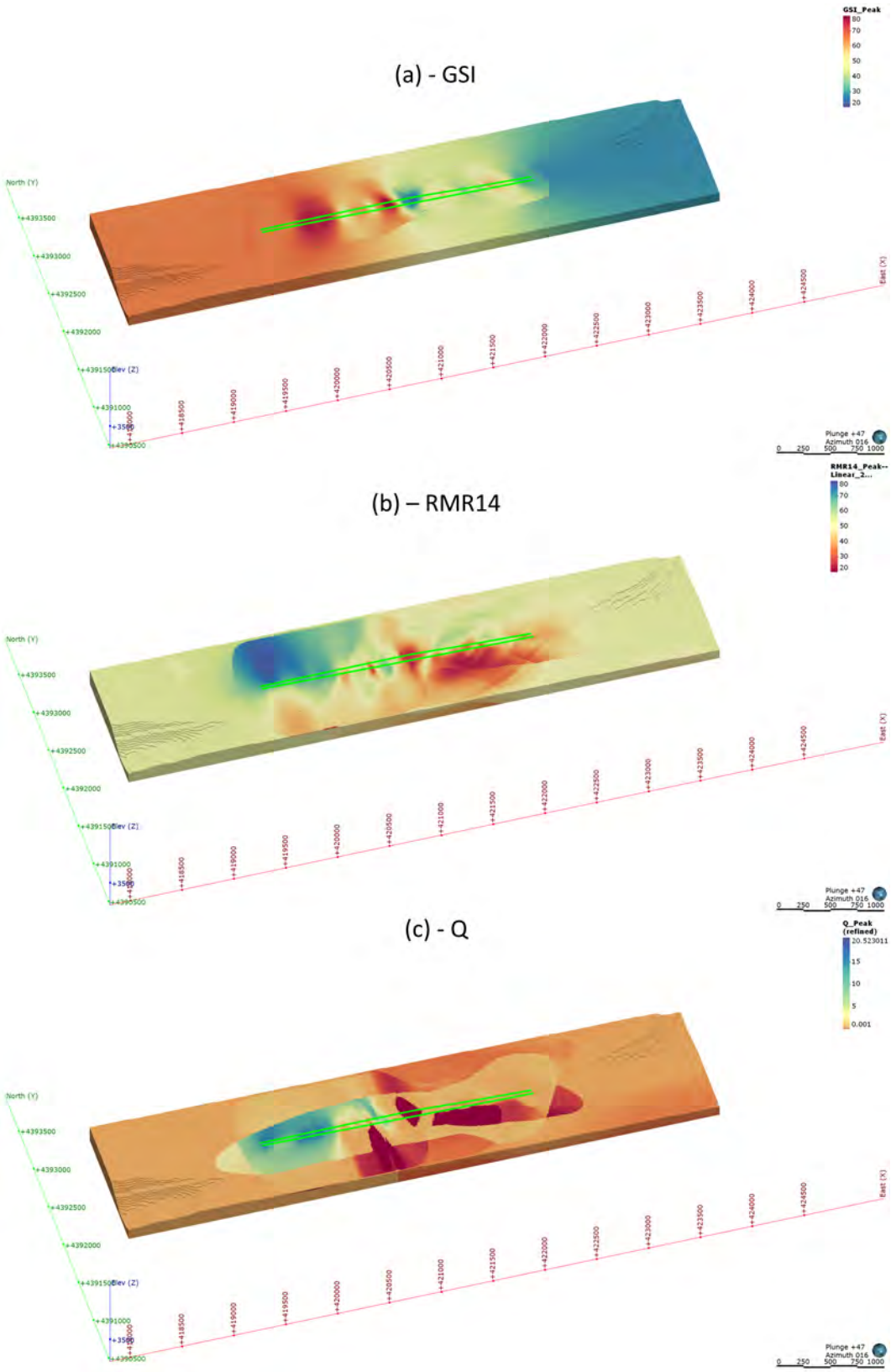

Figure 3.54: Final composite interpolants for GSI, RMR_{14} and Q.

3.6.5 Data Extrapolation in Three Dimensions

The rock mass classification parameters were extrapolated in 3D using RBFs and various interpolants including isotropic, lithologic, structural, and fault zone domaining. The interpolant used for each rock mass class parameter was selected based on the judgment of the authors. Where no better interpolant was available (e.g., outside the bounds of the fault zone domain modeling) the isotropic interpolant was the default. The RBFs and interpolants applied to each parameter are summarize in Table 3.10.

Table 3.10: Interpolant basis applied to each rock mass classification component.

Rock Mass Classification Component	Interpolant Used
$RMR_{alterability}$	lithology
$RMR_{stresscondition}$	lithology
RMR_{λ}	faulting
$RMR_{jointCondition}$	faulting
F_O	set globablly
RMR_{GW}	depth
SRF	lithology
RQD	faulting
J_n	structural domain
J_r	faulting
J_a	faulting
J_w	depth
GSI	structural geology

3.6.6 Block Model Validation

To validate the Leapfrog Geo block model developed by implicit geologic modeling and estimate whether this modeling technique is introducing additional uncertainty to the alignment optimization, the RMR values of the block model were compared to the RMR

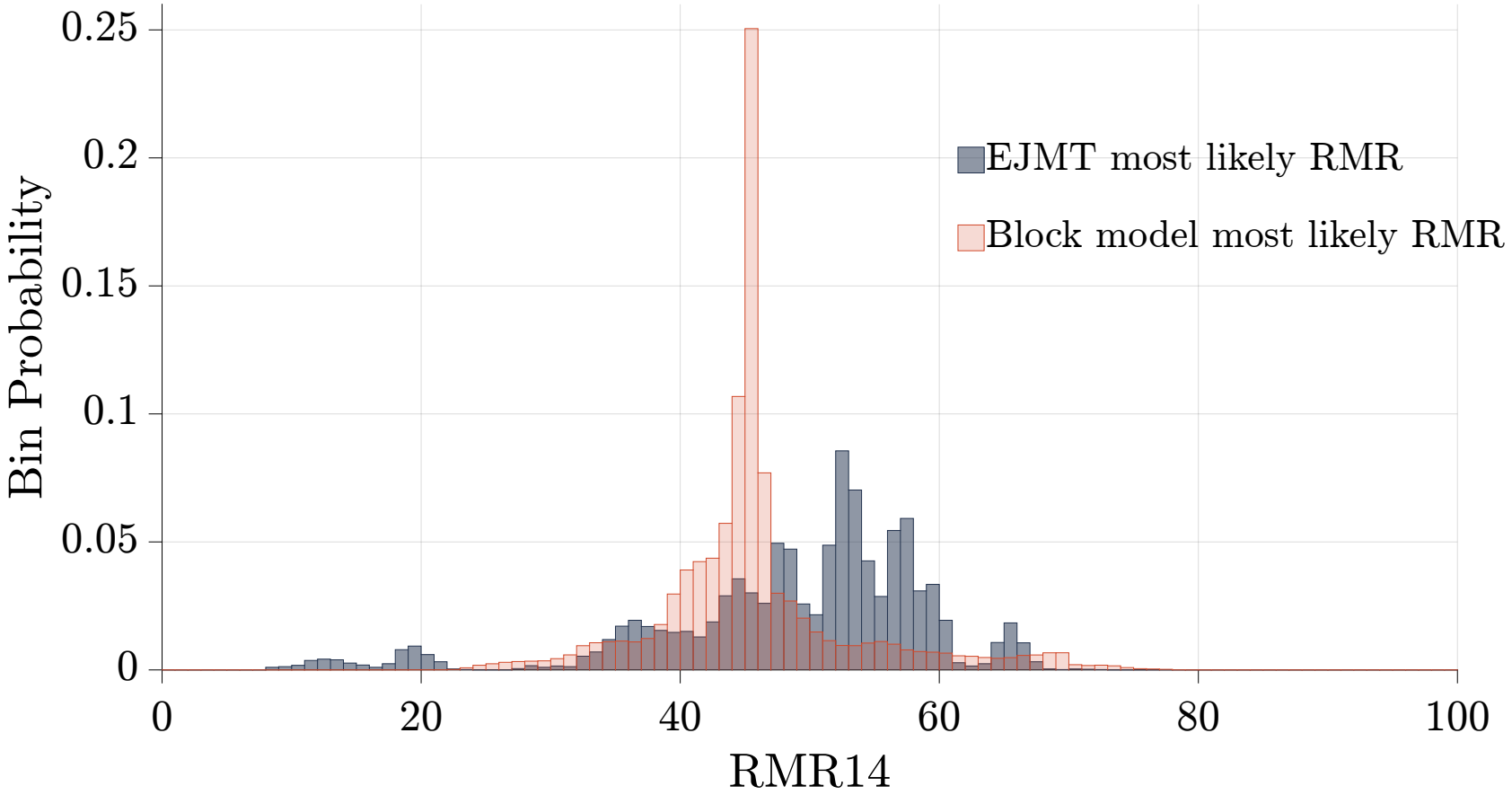

Figure 3.55: Histogram of most likely RMR values from the pilot and Eisenhower bores compared to the same metric calculated at each block of the implicit geologic model.

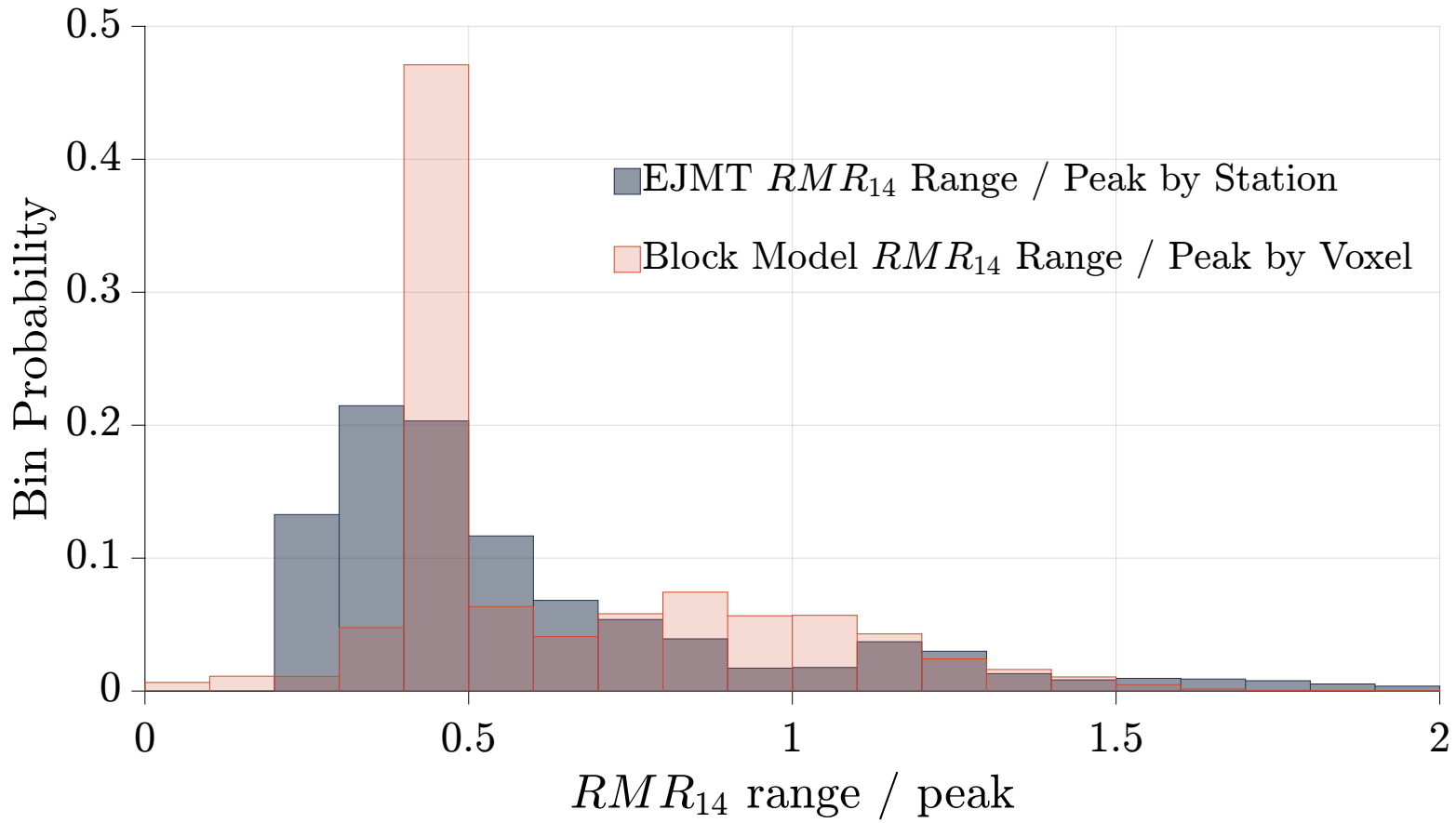

Figure 3.56: Histogram of the range of most likely RMR values normalized by most likely RMR from the pilot and Eisenhower bores compared to the same metric calculated at each block of the implicit geologic model.

values calculated for the pilot and Eisenhower bores. Figure 3.55 shows the histogram of the most likely RMR values at each point of the block model compared to the most likely RMR values at each point along the pilot and Eisenhower bores. Note that these two histograms do not line up well, indicating that the rock mass penetrated by the pilot and Eisenhower bores is slightly better on average than the rest of the modeled rock mass. Rather than taking the poor fit of the histograms to mean that the implicit geologic model is not matching the underlying data, the authors interpret this to mean that the rock mass in the area of the original bores is slightly better on average than the majority of the local rock mass.

Figure 3.56 shows the range of the RMR value at a given point normalized by the most likely RMR value at that point. The range divided by the most likely value is a metric of data dispersion, similar in concept to a standard deviation. The histogram from the pilot and Eisenhower bores matches well with the histogram from the block model, indicating that the implicit geologic modeling technique is not introducing significant additional uncertainty to the analysis which did not already exist in the underlying data. Actually, the block model appears to have slightly lower kurtosis compared to the underlying data, suggesting that the block model is reducing the uncertainty. It is likely that this reduction in uncertainty is not a feature of this modeling technique but an artifact of the technique showing some information entropy between the measured and extrapolated data.

3.6.7 Probabilistic-Deterministic Disagreement

The consistent disagreement between the deterministic and most likely probabilistic estimate of rock mass classification is a feature of the interaction of the underlying asymmetric probability distributions for each parameter of each rock mass classification. A deterministic estimate of rock mass classification would generally match the peak of a symmetric (e.g., normal/Gaussian) distribution. However, this is not true for asymmetric distributions or even for mixtures of symmetric distributions with different modes.

The RMR and Q values for a given point along the pilot bore and for the whole pilot bore are continuous random variables. Both RMR and Q are composed of several underlying variables (Equation 2.3 and Equation 2.10). Further, each component variable is a function of some underlying data. For example, RMR_{14UCS} is a function of the unconfined compressive strength of the intact rock.

In general, algebraic operations on random variables, both functional transformations, and compositions of multiple variables, do not produce distributions with closed-form definitions (Hogg et al. 2019; Springer 1979). It is often necessary to resort to non-closed-

form representations of the distribution to adequately represent such distributions. For this study, the Monte-Carlo method was adopted. Many random samples ($N = 2000$) were taken from each underlying data distribution. They carried each sample through the analysis by estimating the components of RMR and Q and combining these sub-components into the total score. This produces a distribution of possible RMR and Q values at each station and for the pilot bore, as shown in Figure 3.29 and Figure 3.31.

Simply taking the best estimate of each underlying data distribution and performing a deterministic calculation neglects the interaction of peak and non-peak parameters. Such a deterministic estimate does not necessarily return the peak value from the probabilistic histogram. Thus, a deterministic estimate is not equivalent to a peak probabilistic estimate. This behavior is demonstrated in Figure 3.29 and Figure 3.31, which show deterministic and probabilistic RMR_{14} and Q scores along the EJMT pilot bore. Note in Figure 3.29 that the deterministic assessment consistently overpredicts the probabilistic RMR_{14} value along the pilot bore alignment. This would lead to an unconservative design. The deterministic Q estimate does not have such a clear bias, but nevertheless fails to agree with the probabilistic Q value in most cases.

3.7 Summary and Conclusions

This chapter presents the development of a 3D geologic model of the EJMT vicinity incorporating uncertainty in the lithology, geologic structure, fault zones, and engineering parameters of the rock mass based on current and historical data. In the process of probabilistically evaluating this case study, we have found several interesting implications for current geotechnical engineering practice.

3.7.1 Strength Model Reduction

Section 3.5.5.4 suggests that reduction of a transversely isotropic model to an isotropic model is possible. Where the foliation-parallel and foliation-perpendicular material properties are substantially similar, especially where their uncertainty envelopes have significant overlap, a single set of material properties with uncertainty developed using both foliation-parallel and foliation-perpendicular data may adequately represent the bulk material properties of a transversely isotropic material. Where 3D geologic structural modeling has high uncertainty in the foliation orientation, incorporating the uncertainty in the transversely isotropic properties directly into a single isotropic model may be a more appropriate way of handling material property uncertainty than attempting to parse foliation orientation uncertainty in 3D and then apply transversely isotropic

material properties. This reduced model also has a significant advantage in reducing model complexity and thus model calculation time.

One shortcoming of the reduced-model Monte Carlo simulation is the loss of more complex mechanical behavior. For example, the model discussed here fails to capture discontinuum and creep deformation of the EJMT pilot bore. A more complex creep deformation model may be capable of capturing this behavior. However, for this research project, i.e., the probabilistic estimation of likely excavation and support conditions in new tunnels adjacent to the existing tunnels to support early-stage project feasibility studies, the simplistic model presented here may be a sufficient and efficient path forward.

3.7.2 Groundwater Conditions at the EJMT

The groundwater correlation presented above is fundamentally based on groundwater flows from the excavation of the pilot bore between October 1963 and December 1964. There is significant uncertainty in this face flow estimate arising from many sources. Seasonal variability and climate change may drastically alter the actual face flow in any given bore. The installation of the pilot bore, the subsequent installation of the Eisenhower and Johnson bores, and the continued drainage through the existing tunnels may have permanently altered the groundwater table. Anecdotal evidence such as historical accounts of swampy or marshy areas on the surface in the vicinity of the pilot bore east portal which are no longer present suggest a decline in local groundwater table. The drainage data recorded in the pilot bore suggest a declining groundwater table, even with the seasonal recharge. The operations of the Loveland Ski Area may also have an impact on both snow accumulation and snowmelt. This single point of reference for calibrating anticipated groundwater face flows should be considered a rough estimate, at best. A lower bound of zero face flow and an upper bound two to ten times higher than the estimates produced by this function would not be unreasonable estimates of the possible range of groundwater face flows in an advancing tunnel heading. Further study of the local groundwater table and its seasonable variability are likely warranted. In particular, the installation of multiple groundwater monitoring wells with long-term monitoring backed up by a rigorous hydrogeological modeling effort is strongly recommended.

3.7.3 Advance Rate Correlation

Although the EJMT advance rate data are old, the techniques employed in the excavation of the tunnel are fundamentally similar to modern drill-and-blast (D&B)

tunneling. The technology has improved, but the general process remains the same. Thus, modern estimates of advance rate estimation could be expected to correlate to these data, possibly including a reduction factor to account for improvements in technology since the EJMT construction. However, none of the evaluated rock mass classification parameters provided a good correlation to recorded advance rates in the EJMT pilot bore. This supports a broad uncertainty in the tunneling industry around project time scales. The accurate estimation of likely project time is an area which requires additional research in order to provide reasonable cost-estimating tools to project owners, engineers, and contractors. It may also be that project advance rate is simply not well-correlated to geologic conditions. Tunneling can be viewed as an industrial process, involving repeated cycles of excavation and support installation. A closer focus on the concerns of optimizing the excavation cycle may be more effective at estimating tunnel advance rates. This is an active area of research, for example, at the Colorado School of Mines Operations Research with Engineering group.

3.7.4 3D Implicit Geologic and Geotechnical Data Modeling

3D extrapolation of the probabilistic data provides valuable insights into the local geology and serves as a useful tool for ongoing work by CDOT in this area. The geologic model is similar in concept to the digital twin models used in many new construction projects for buildings and civil infrastructure. However, while a deterministic model of well-defined infrastructure is appropriate, the probabilistic model of engineering geologic conditions demonstrated here is a more appropriate representation of conditions in the vicinity of tunnel projects while providing necessary information on local engineering geologic conditions.

3.7.5 Deterministic–Probabilistic Disagreement

The probabilistic rock mass classifications presented here demonstrate a fundamental shortcoming of deterministic rock mass classifications: a deterministic estimate is not necessarily equivalent to a peak probabilistic estimate. A deterministic estimate may be biased away from the most likely probabilistic assessment. The deterministic-probabilistic disagreement of the rock mass classifications shown here is a feature of the interaction of the underlying asymmetric probability distributions for each parameter of each rock mass classification. In this case, probabilistic modeling has revealed an apparent bias the RMR_{14} and Q–systems are applied deterministically. The direction of the bias can be positive or negative depending on the nature of the underlying data and the probability

distributions used. For the EJMT, the bias was typically positive, overestimating rock mass quality. This bias means that a tunnel design based on a deterministic estimate of rock mass classification is likely to be unreliable. A tunnel design based on the most likely probabilistic assessment is a more realistic portrayal of the ground conditions than a deterministic estimate. This inherent deterministic bias may significantly contribute to the relatively frequent failure of tunnel construction cost estimates to match actual project costs. A probabilistic modeling approach using MC simulation of data carried through intermediate interpretations and numerical modeling may improve the reliability of preliminary tunnel designs.

CHAPTER 4

TUNNEL ALIGNMENT OPTIMIZATION THROUGH A THREE-DIMENSIONAL GEOLOGIC MODEL WITH UNCERTAINTY

This chapter presents the development of an algorithm which evaluates many plausible alignments through the three-dimensional (3D) geologic model developed in Chapter 3. First, a 100 m grid of locations where portals could plausibly be placed was developed, excluding some areas such as mapped landslides and stream channels. Second, all possible alignments connecting these portal locations were generated and filtered for several fatal flaws (e.g., grade requirements). Third, the rock mass classifications along the remaining alignments were evaluated and the plausibility of constructing a tunnel along each alignment was evaluated by empirical metrics based on rock mass classifications. Finally, the alignments were ranked in order of constructability. Valuable insights are offered into the feasibility of constructing a new tunnel adjacent to the existing Eisenhower-Johnson Memorial Tunnel (EJMT). Several candidate alignments are advanced for further consideration in Chapter 6.

4.1 Introduction

The selection of a new alignment adjacent to the existing EJMT is constrained by several practical considerations, e.g., grade requirements, proximity to the existing road alignment, and environmental considerations. Within these constraints there still exist a wide number of plausible portal locations on either side of the Continental Divide. This chapter demonstrates the creation and automation of a process for evaluating many possible alignments in order to identify the most feasible alignment or alignments for further design studies.

4.2 Methodology

In order to find the best plausible new alignment adjacent to the existing EJMT, discretization followed by successive evaluation and elimination of options was applied.

The remaining alignments after the filtering stage were then scored and ranked based on a number of empirical constructability metrics.

The problem is one of multi-objective optimization (Pareto optimization). Engineering feasibility is often reduced to a cost function, allowing for single-objective optimization. However, for this research project, the most technically optimal solution rather than the least expensive is sought. It is likely, but not certain, that the most technically optimal solution is close to the most cost-effective solution because the technically optimal solution minimizes excavation and support quantities which tend to drive project costs. Moreover, the author sought to avoid introducing additional uncertainty by avoiding estimating project costs. Precise unit cost estimates for tunnel projects vary widely, are changing rapidly, and include details which are extremely difficult to evaluate accurately at this early feasibility stage.

Classic optimization seeks paths to the optimum solution. This assumes that there is a single best solution to a given problem and that there exists some mathematical way of seeking this solution. The main constraints to the optimization are:

1. The multi-objective nature of this particular optimization problem;
2. The desire to explore multiple plausible solutions and thus evaluate the utility of the alignment optimization process developed here; and
3. A lack of clarity as to which optimization parameters evaluated here are truly most desirable;

A global optimization technique was used to evaluate the problem. In particular, the geographic problem domain was discretized into a grid of possible portal locations and a Monte Carlo (MC) simulation approach was implemented to randomly sample the other problem domain parameters (e.g., rock mass classifications).

Each sample point in the problem domain consists of an alignment connecting a pair of possible portals. Each sample point is evaluated probabilistically by many MC realizations ($N = 2000$) of the other problem parameters. Thus, each sample point can be evaluated probabilistically.

4.2.1 Portal Location Requirements

In the broadest sense, there exist an infinite number of geometrically possible portal locations on each side of a given ridge line through which a tunnel is desired. Any pair of portals can be combined, leading to a squared infinite number of geometrically possible number of alignments. Further, the portal locations are significantly constrained by practical considerations such as geometric design, environmental constraints, constructability

(e.g., trying to put a portal on a landslide), and proximity to the existing road alignment. The initial phase of portal selection constrains the plausible portal locations to finite areas based on such fatal flaw considerations. These finite areas were mapped in geographic information system (GIS) software. Figure 4.1 shows an overview of the general study area considered here.

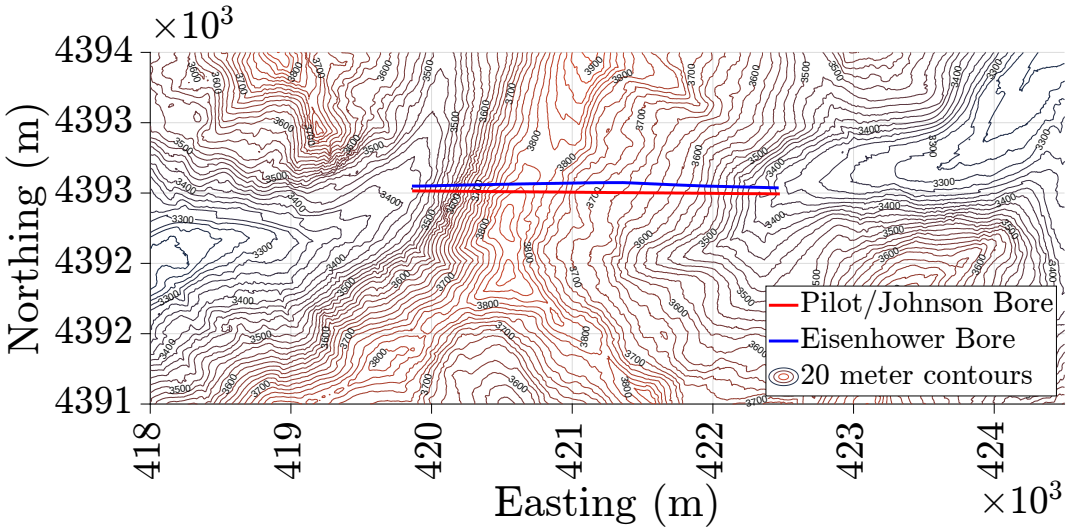

Figure 4.1: EJMT vicinity with elevation contours.

The finite plausible areas for portal locations were then discretized on a 100 m x 100 m grid overlain on the digital elevation model (DEM) which represents the centers of potential portal locations (Figure 4.2). A 100 m grid was selected based on the precision of the block model to be used in evaluating potential alignments, which is composed of 10 m blocks, and a reasonable compromise between precision and processing efficiency. The filtering, evaluation, and ranking process described herein was coded in MatLab and ran in approximately 20 min with a 100 m grid. Run times scale approximately linearly with the number of alignments and approximately quadratically with the number of portals.

Ranking the locations of the portals is a non-trivial problem with many and varied considerations. The factors used in defining areas where portals could plausibly be placed came primarily from considerations typically required in an environmental impact assessment by the National Environmental Policy Act (NEPA) as codified in 42 USC §4321 et seq. (Jackson 1970) and 40 CFR §1500-1599 (CEQ 1978).

The Colorado Department of Transportation (CDOT) has prepared a programmatic environmental impact statement (PEIS) for the broader Interstate 70 (I-70) corridor project in compliance with NEPA. The PEIS lists the requirements for comparing alterna-

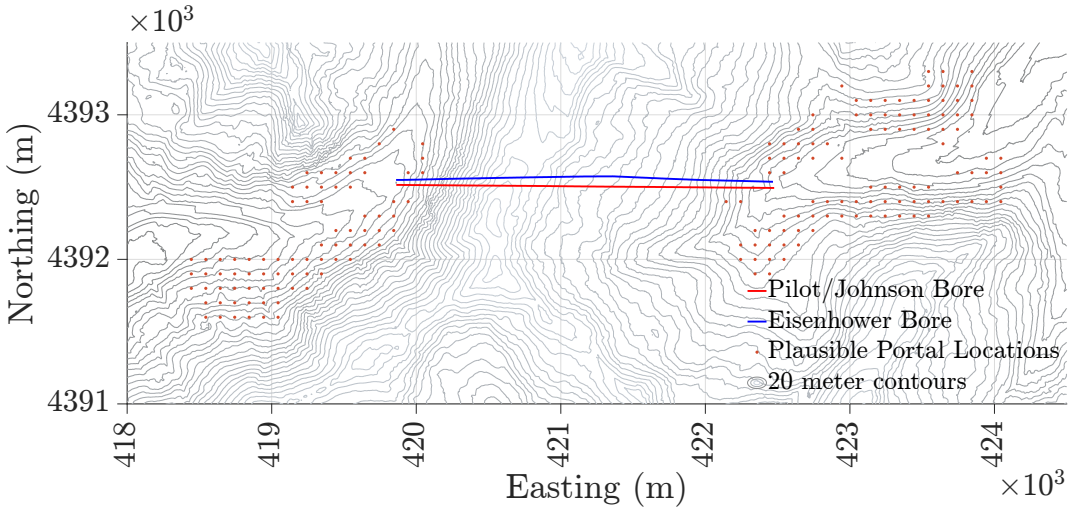

Figure 4.2: Locations of plausible portals (red dots) evaluated on a 100-m grid. There are 104 west portals and 79 east portals arranged on a 100 m grid with non-constructable areas (such as the alignment of Clear Creek) blocked out.

tives as "the ability to meet the purpose and need for the project...while also addressing environmental sensitivity, community values, transportation safety, and ability to implement [the project]" (CDOT 2011).

The CDOT PEIS includes two subsidiary technical reports on Alternatives Development and Screening and Section 4(f) considerations which offer additional detail on the evaluation criteria (CDOT 2011). The Alternatives Development and Screening report lists several important factors including:

1. Capacity
2. Accessibility
3. Mobility
4. Congestion
5. Safety
6. Environmental Sensitivity
   (a) Water quality
   (b) Fishery resources
   (c) Wetlands
   (d) Wildlife
   (e) Waters of the United States
   (f) Geologic hazards
   (g) Threatened, endangered and special status species
7. Community Values

(a) Land use
(b) Noise
(c) Recreation
(d) Historic and archeological resources
(e) Federal management
(f) Scenic features/views

8. Roadway geometry requirements
9. Operational requirements
10. Historic resources and Section 4(f) properties at Loveland Ski Area

The alternatives development and screening report states that "to avoid destabilizing rock around the existing bore which continues to carry traffic during construction new bores would have to be located at least 120 to 250 feet from the existing tunnel" (CDOT 2011b). It is unclear where this clear distance estimate comes from, but it is likely a professional opinion rather than a calculated value.

Discussions with CDOT helped to clarify some of the concerns CDOT has about a new portal location including having sufficient lay-down area, constructability on a complex slope, and geohazards such as rockfall and landslides.

Some of the listed considerations are not part of this research. For example, capacity is governed by the number of lanes or rails through the tunnel. The PEIS has already investigated the required number of lanes or rails and settled on several options. This research uses the double-lane and double-track options identified as acceptable. In addition, CDOT has requested that a single-track option be considered, even though the majority of the rail line will be double-track. Accessibility, mobility, congestion, and operational requirements are also considerations which are not being considered by this research, as they have no direct relation to the feasibility of constructing a bore. Safety considerations impact the required tunnel grade, as well as minimum cross-section sizes. Construction safety is not directly considered in this research, though standup time does impact construction safety.

Under environmental resources, the PEIS has eliminated concerns related to all sub-considerations except geologic hazards (landslides, rockfalls, etc.) and waters of the United States. It is assumed for the purposes of this research that construction within the ordinary banks of either Clear Creek (on the east side of the EJMT) or Straight Creek (on the west side of the EJMT) would not be permitted under Section 404 of the Clean Water Act (Muskie 1972) (33 USC 1151, 1251 et seq.). Geologic hazards in the vicinity of the EJMT are primarily landslides, avalanches, and rockfall. Landslide and rockfall hazards were evaluated by reference to the Colorado Landslide Inventory (CGS n.d.). The

landslide outlines were downloaded as shape files and incorporated directly into the map of plausible portal locations. Avalanche hazards in the vicinity of the EJMT are significant, but CDOT and the Loveland Ski Area already expend significant resources on avalanche mitigation in this area. It is assumed for the purposes of this study that an additional portal location near the existing portals would not significantly change this avalanche mitigation program.

Roadway geometry requirements are codified in the CDOT Roadway Design Guide (CDOT 2018a). This research did not focus on a detailed geometric design of the approach to each portal, but limited the distance from the existing portals to any new portal to less than 1 mile (1.6 km). The difference in elevation between the existing portals and the any new portal was limited to less than 100 m.

The remaining listed considerations can be summarized as impacts to historic and recreational resources as identified in the Section 4(f) Evaluation report (CDOT 2011). The 1966 Department of Transportation Act, Section 4(f), provided very strong protections for "parks, recreation areas, wildlife and waterfowl refuges, and historic sites" (Johnson 1966). More recent reorganization of US law has placed the text of the law in 49 USC 303 and 23 USC 138, with the associated detailed regulations under 23 CFR 774. However, the environmental impact assessments related to such areas are still commonly referred to as Section 4(f) investigations.

The CDOT (2011) Section 4(f) Evaluation report evaluated properties which meet or potentially meet the protection standards of 23 CFR 774. Notably, the EJMT itself is eligible for listing on the National Register of Historic Places, though it is not yet so listed. Two other Section 4(f) protected areas exist near the east portal of the existing EJMT, the Loveland Ski Area and the Herman Gulch Trailhead. No other Section 4(f) protected areas were identified in the vicinity of the west portal of the EJMT.

Shape files delineating the Loveland Ski Area, the Herman Gulch Trailhead, and the connected Continental Divide Trail were created manually in ArcGIS (ESRI 2019). The shape files of the local landslide and rockfall hazards were downloaded from the Colorado Geological Survey's Colorado Landslide Inventory (CGS n.d.). In between these items, a regular grid of portal locations was created on 100 m intervals.

4.2.2 Initial Alignment Development and Filtering

Assuming N portal locations are selected on one side of the divide and M portal locations are selected on the other side of the divide, there are $N \cdot M$ plausible alignments. The portal locations identified above were imported to MatLab (MathWorks 2019)

where they were convolved to create a matrix of plausible alignments defined as straight line segments. For a 100 m net of portal locations there are 79 portal locations on the western slope and 104 portal locations on the eastern slope. This generates 8,216 plausible alignments.

Several initial filtering parameters were employed to remove unsuitable alignments including:

1. Alignment grade (Figure 4.3);
2. Ground surface conflict (i.e., tunnel alignments which are bridges instead of tunnels, shown in Figure 4.4); and,
3. Intersection conflicts with the existing bores (Figure 4.5).
4. Alignments which cross from the existing bores (in plan view) and would thus create a complicated roadway traffic pattern (Figure 4.6 and Figure 4.7).

Table 4.1 shows the progress of the alignment filtering for grade requirements, surface conflicts, and intersection with the existing EJMT bores. Note that the order of filtering was selected for computational efficiency. It is much more computationally efficient to calculate grade for an alignment than evaluate polyline-surface intersections or the intersection of piecewise–defined lines. Therefore, at each filtering stage the next filter is applied only to those alignments which passed the previous filter.

4.2.3 Grade Requirements

CDOT stated that a new tunnel should have a minimum grade of 0.5% and a maximum grade of 2%. The minimum grade is required to promote drainage of water from the tunnel while the maximum grade is a defined by a combination of ventilation and traffic safety requirements. In addition, due to water rights issues, the tunnel should drain to the

Table 4.1: Initial alignment filtering by grade requirements, surface conflicts, and intersection with existing bores based on a 100 m net of portal locations on each side of the Continental Divide with 104 east portals and 79 west portals.

Filtering Stage	Number of Alignments	% of Unfiltered Alignments
Unfiltered	8216	100%
Grade Requirements	2065	25%
Surface Conflicts	438	5.3%
Intersections with Existing EJMT	438	5.3%
Crossing N–S Across Existing EJMT	89	1.1%

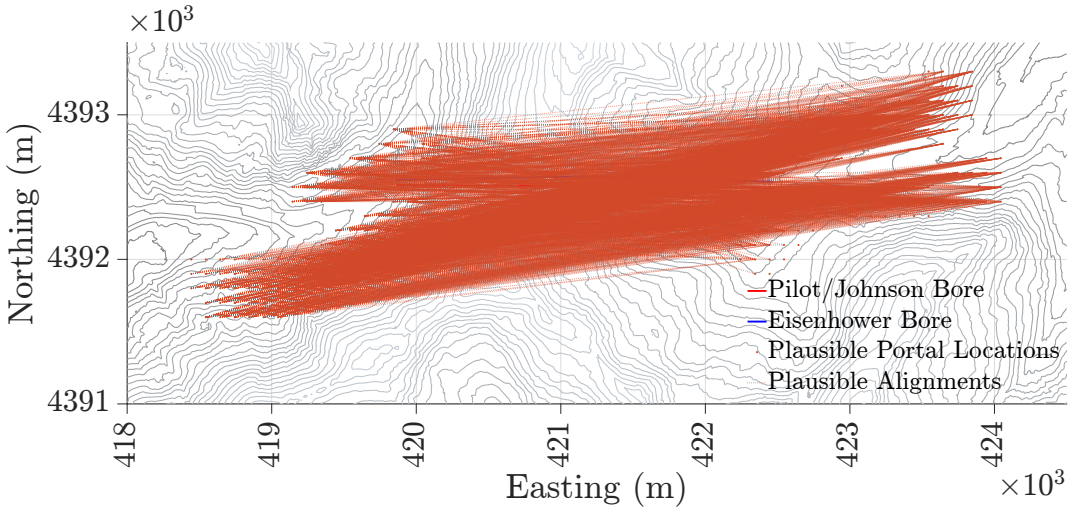

Figure 4.3: 2065 remaining plausible alignments after filtering for grade requirements.

east.

The grade of each alignment was calculated from the DEM according to Equation 4.1. Note that if ΔZ is consistently calculated as elevation of the west portal minus elevation of the east portal, the calculated grade also identifies the direction of drainage via its sign, and all negative grades can be excluded per CDOT's drainage direction requirement. For the 100 m net of portal locations, approximately 75% of alignments were eliminated due to grade considerations. The remaining alignments are shown in Figure 4.3.

$$G = \frac{\Delta Z}{L} \tag{4.1}$$

4.2.4 Surface Conflicts

The distance from each alignment to the ground surface DEM (USGS 2016a,b) was then calculated at 5 m intervals. Any alignment with more than 10 points above the DEM was excluded as having excessive surface conflicts. This primarily excludes alignments connected to portal locations which are on a hill side facing the Continental Divide, e.g., the slope facing the west portal. This calculation also provides a vector of depths below ground surface along the alignment, useful data for later analyses. Approximately 78% of the remaining alignments were eliminated due to surface conflicts, reducing the solution space to approximately 5.3% of the initial matrix of 8,216 plausible alignments. The remaining alignments are shown in Figure 4.4.

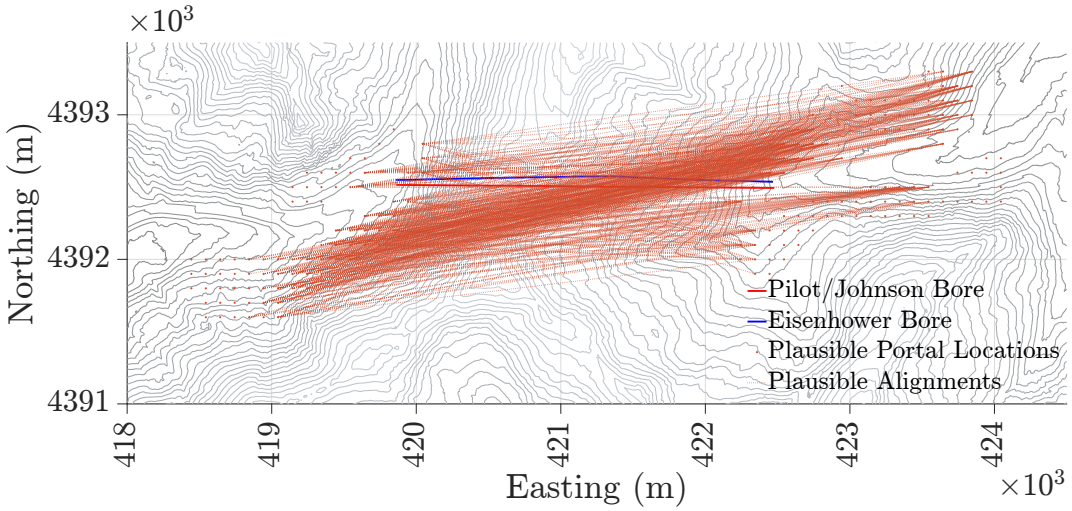

Figure 4.4: 438 remaining plausible alignments after filtering for ground surface conflicts.

4.2.5 Intersection Conflicts

The next filter was focused on intersections between plausible alignments and the existing EJMT bores. The plausible alignments are defined as line segments while the existing bores are defined as piecewise lines in three dimensions. In order to evaluate the possibility of the intersection of an existing bore with a proposed alignment it was necessary to write a function to calculate the minimum distance between line segments. The function loops through all segments of two piecewise–defined lines which are passed to it as vectors of segment endpoints and calculates the shortest distance between each pair of segments. The shortest distance between two intersecting lines is zero (the trivial case). The shortest distance between two parallel lines is constant and the segment joining the lines does not have a unique position. The shortest distance between two skew (non-intersecting, non-parallel) lines is a segment that is simultaneously perpendicular to both lines. In other words, the dot product of the vector defining the shortest segment between the two lines is zero. This is a unique property of that segment and a useful property for identifying both the position and length of the shortest segment between the skew lines.

The shortest distance between two line segments is only slightly more complicated; a constraint is required that the solution be within the range of the line segment. Two lines extending infinitely may intersect while two segments of those same lines may not. In this case, the solution for the shortest distance between the segments may not be perpendicular to both segments and may start or end at one end of either segment. An algorithm working through these possible solutions and calculating distances between the segments by vector algebra was implemented in MatLab by the author based on the work

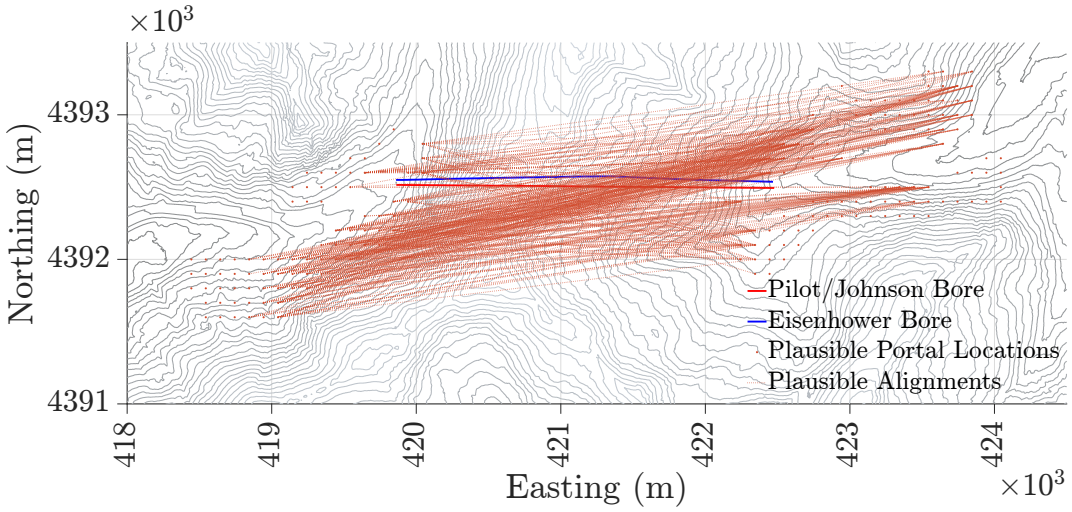

Figure 4.5: 320 remaining plausible alignments after filtering for intersections with the existing bores.

of Eberly (2006), Eberly (2020), and Sunday (2012).

The remaining alignments were filtered by their minimum distance to the existing Eisenhower and Johnson bores and are shown in Figure 4.5. An intersection between the existing and proposed alignment was defined as a distance between the two alignments less than the sum of each alignment's radius. The existing EJMT bores are approximately 17 m in diameter and the initial alignment optimization was conducted assuming a 10 m diameter new bore. Therefore, a distance less than 13.5 m between a proposed alignment and the existing bore was considered an intersection and the proposed alignment was excluded. No alignments were filtered out by this criterion as any intersecting alignments had already been removed due to other criteria. Note that by this point in the alignment filtering process some proposed portal locations had no remaining alignments connected to them. Approximately 75% of west portals and 69% of east portals were removed from consideration.

4.2.6 Rock Mass Classifications

Rock mass classifications along each alignment were sampled from the block models output from Leapfrog Geo (Seequent 2020) as described in Chapter 3. Three block models were output from Leapfrog Geo (lower bound, most likely, and upper bound estimates) for each rock mass classification parameter. The rock mass classification parameters sampled from the block models were:

1. rock mass rating (RMR_{14})
2. rock mass quality index (Q)

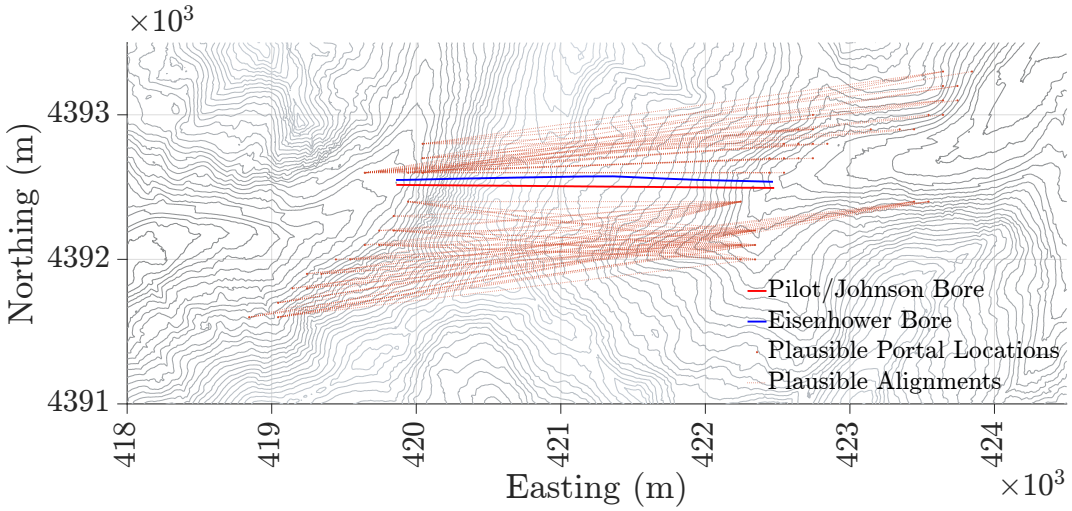

Figure 4.6: 89 remaining possible alignments after filtering out alignments which cross the existing alignments in plan view. For a new roadway tunnel crossing would complicate the traffic pattern. For a rail tunnel, crossing the existing alignment may not be a problem.

3. lithology
4. intact unconfined compressive strength or uniaxial compressive strength (UCS)
5. drilling rate index (DRI)
6. estimated groundwater flow in liters per minute (LPM)
7. estimated joint frequency in joints per meter

Note that RMR_{14} and Q were estimated directly at this stage, but their subcomponent scores were estimated probabilistically in 3D and then recombined into an aggregate score within Leapfrog Geo. See Chapter 3 for further details of this process. Rock mass excavatability (RME) was estimated from the intact UCS, DRI, estimated groundwater flow, joint frequency, and stand-up time (based on RMR_{14}).

Monte Carlo sampling ($N = 2000$) of the rock mass classification parameters was conducted assuming that the lower bound, most likely, and upper bound estimates of each parameter represented a triangular distribution of each parameter. 2000 Monte Carlo samples were taken from each distribution at 5 m intervals along each alignment evaluated. A 5 m spacing for sampline was selected based on the size of the lithologic block model, which had a 5 m discretization. The other rock mass classification parameter block models had a 10 m discretization, deemed to be the smallest reasonable discretization of the properties being evaluated. Thus, there is likely no additional information to be garnered from using a sampling interval less than 10 m for these parameters. However, it is assumed that a finer discretization does not adversely affect the results, other than to increase computer processing time.

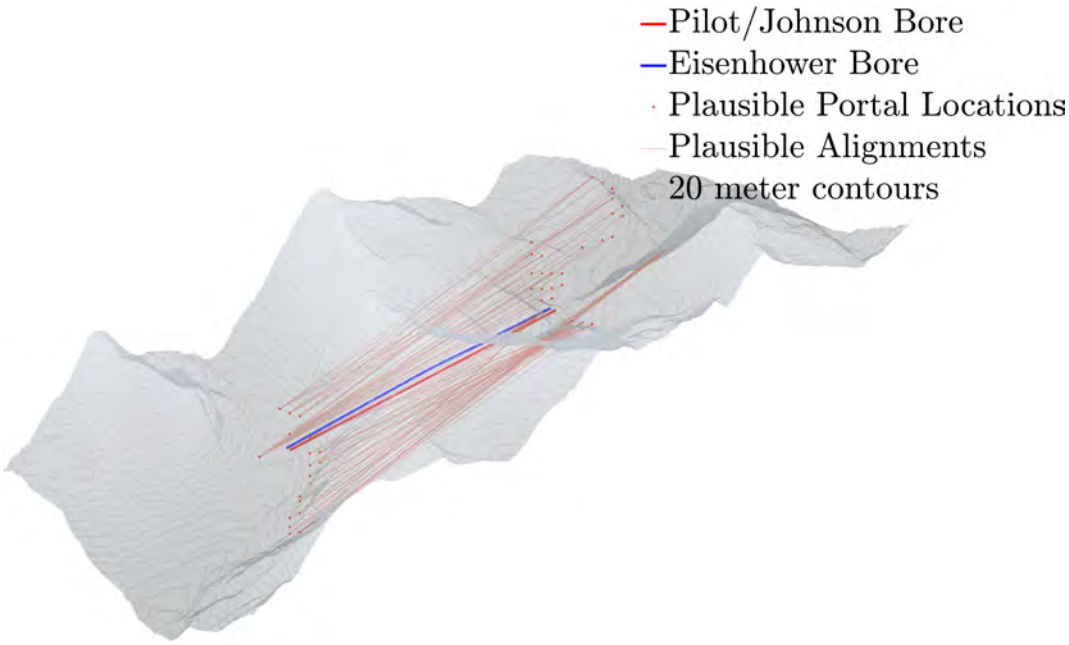

Figure 4.7: 89 remaining possible alignments after the various initial filtering criteria have been applied (grade requirements, ground surface conflicts, intersections with the existing bores, and excluding alignments which cross North-to-South or South-to-North across the existing bores) presented in three dimensions.

4.2.7 Estimation of Excavation Progress for Each Alignment

See Section 2.4.5 for a detailed overview of various empirical methods of estimating tunnel advance rates and Section 3.6.2 for correlations between rock mass classifications and advance rates recorded in the EJMT pilot bore. Advance rates in the pilot bore were not found to correlate well to any rock mass classification parameter. Lacking such a locally calibrated estimate of advance rate, drill-and-blast (D&B) advance rates were estimated based on Q per the recommendations of Barton (2000), Grimstad (1981), and Grimstad and Barton (1993). Tunnel boring machine (TBM) advance rates were estimated based on RME per the recommendations of Bieniawski et al. (2007, 2008), Bieniawski and Galera (2007), Bieniawski and Grandori (2007), and Bieniawski et al. (2006).

4.2.8 Preliminary Estimation of Support Requirements

Ground support requirements along each evaluated alignment were estimated based on the Q and RMR_{14} systems based on published empirical design correlations by NGI (2015) and Lowson and Bieniawski (2013).

A MatLab code was written to estimate required ground support based on the recommendations of Lowson and Bieniawski (2013) using the RMR_{14}–system. The routine

takes inputs of RMR_{14}, excavation span, and mean unit weight of overburden and returns recommended rock bolt length, rock bolt pattern spacing, and shotcrete thickness. The routine first calculates the estimated overburden pressure based on Equation 4.2 as suggested by Lowson and Bieniawski (2013) and then the required rock bolt spacing, rock bolt length, and shotcrete thickness to support that pressure when applied uniformly to a circular excavation.

$$p_v = \frac{100 - RMR}{100} \cdot 10\gamma\sqrt{\frac{B}{10}} \tag{4.2}$$

Note that the recommendations of Lowson and Bieniawski (2013) are based on the assumption that the shotcrete acts as an arch in compression, e.g., a circular tunnel with a uniform hydrostatic pressure. Note also that Lowson and Bieniawski (2013) make no allowance for a maximum rock bolt length. Most bolting recommendations suggest that bolts longer than half of the tunnel height or width are impractical to install. The required rock bolt length calculated according the Lowson and Bieniawski (2013) can easily exceed that recommendation. A lower bound on the effectiveness of rock bolts was applied at $RMR_{14} = 15$, i.e., in intermediate geomaterials or soil-like conditions. An upper bound on the use of rock bolts was implemented at $RMR_{14} = 85$, the point at which rock bolts would likely be applied in a spot bolting or wedge stabilizing fashion rather than as a consistent pattern.

The routine also assumed that a nominal shotcrete liner of 20 mm would be applied everywhere, even if the ground is likely self-supporting. This is a fairly common practice in the tunnel industry to help stabilize any small, loose blocks and bond the surface of the tunnel together. It is especially helpful for dealing with minor overbreak. Also, most publicly accessible tunnels, including road tunnels, incorporate at least a minimum lining even in self-supporting conditions.

No attempt was made to set an upper bound on shotcrete thickness. For very poor ground with high overburden, the recommendations of Lowson and Bieniawski (2013) may return an unrealistically thick shotcrete liner. For most tunneling cases, the practical limit of shotcrete thickness is about 300 mm. If the required shotcrete thickness is greater than this, a different liner system should be considered. A common solution is to add steel reinforcing bars or lattice girders to the shotcrete. For extremely poor ground conditions, cast concrete liners may be required. Other options include pre-cast or pre-stressed concrete liners or steel ribs. Steel ribs are sometimes used for squeezing ground conditions where it may be desired to install the support early but then allow it to yield significantly before eventually stiffening. This is accomplished by installing a yield element in the steel support such as a sliding gap or a weaker portion that is specifically intended to crush to

its final condition.

In general, although the recommendations of Lowson and Bieniawski (2013) may provide impractically long rock bolts or unrealistically thick shotcrete liners, the recommendations may be considered a reasonable estimate of the magnitude of ground support required for a given ground condition. A final design should be more rigorously evaluated than simple application of an empirical criterion and will likely deviate significantly from these recommendations. However, for the purposes of this study in estimating the relative feasibility of constructing one alignment versus another through locally variable geologic conditions these recommendations provide a reasonable metric of feasibility.

See Section 2.4.6 for a more complete discussion of the support recommendations by Lowson and Bieniawski (2013).

An additional MatLab code was written to estimate required ground support based on the recommendations of NGI (2015) using the Q–system. The routine calculates the required rock bolt and shotcrete supports for a tunnel at a given Q for a given excavation span. This routine is based on points read manually from the NGI (2015) rock support chart, linear interpolation between those points, and in some cases a least–squares regression of a function to those selected points. This allows for a continuous interpolation of required shotcrete thickness, bolt pattern spacing, bolt length, and reinforced rib spacing along the tunnel. While the functions selected for regression have been carefully selected and generally have a very good correlation to the points defined by NGI (2015), they are only good approximations and not exact fits, i.e., $r^2 < 1$. See Section 2.4.7 for a more complete discussion of the support recommendations by NGI (2015).

Note that the RMR_{14}-based estimates of shotcrete thickness are about 25-45% of Q-based estimates of shotcrete thickness, not counting the additional reinforced rib recommendations from the Q-system.

4.3 Results

The alignment optimization algorithm estimated many design metrics for each alignment. Figure 4.8, Figure 4.9, Figure 4.10, and Figure 4.11 show some of these estimated metrics. Interesting trends can be observed in these figures.

4.3.1 Alignment Scoring Methodology

Each parameter evaluated (e.g., median RMR, range of RMR, number of bolts required) was converted to a score from 0 to 1 indicating the position of that parameter within the range of that parameter for all alignments. For example, if alignment X had

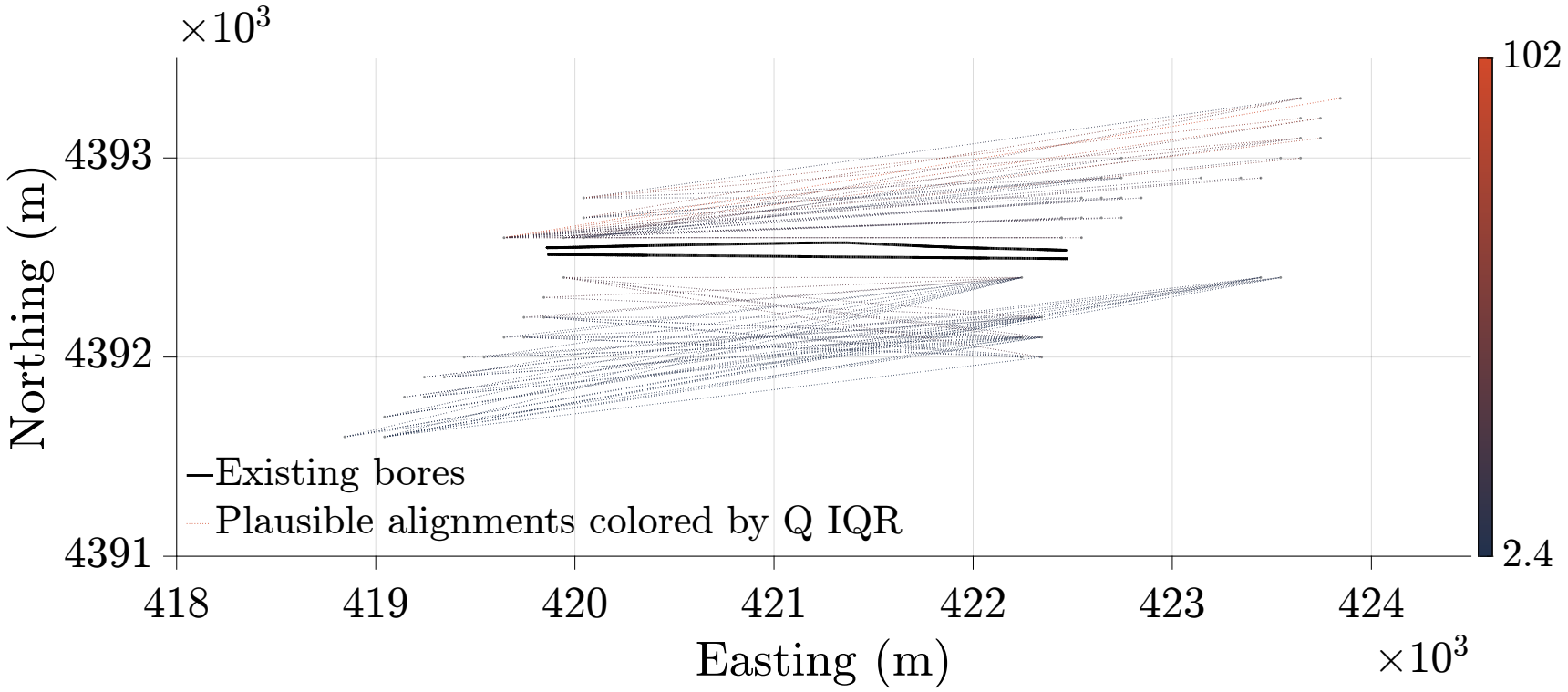

Figure 4.8: Interquartile range of Q.

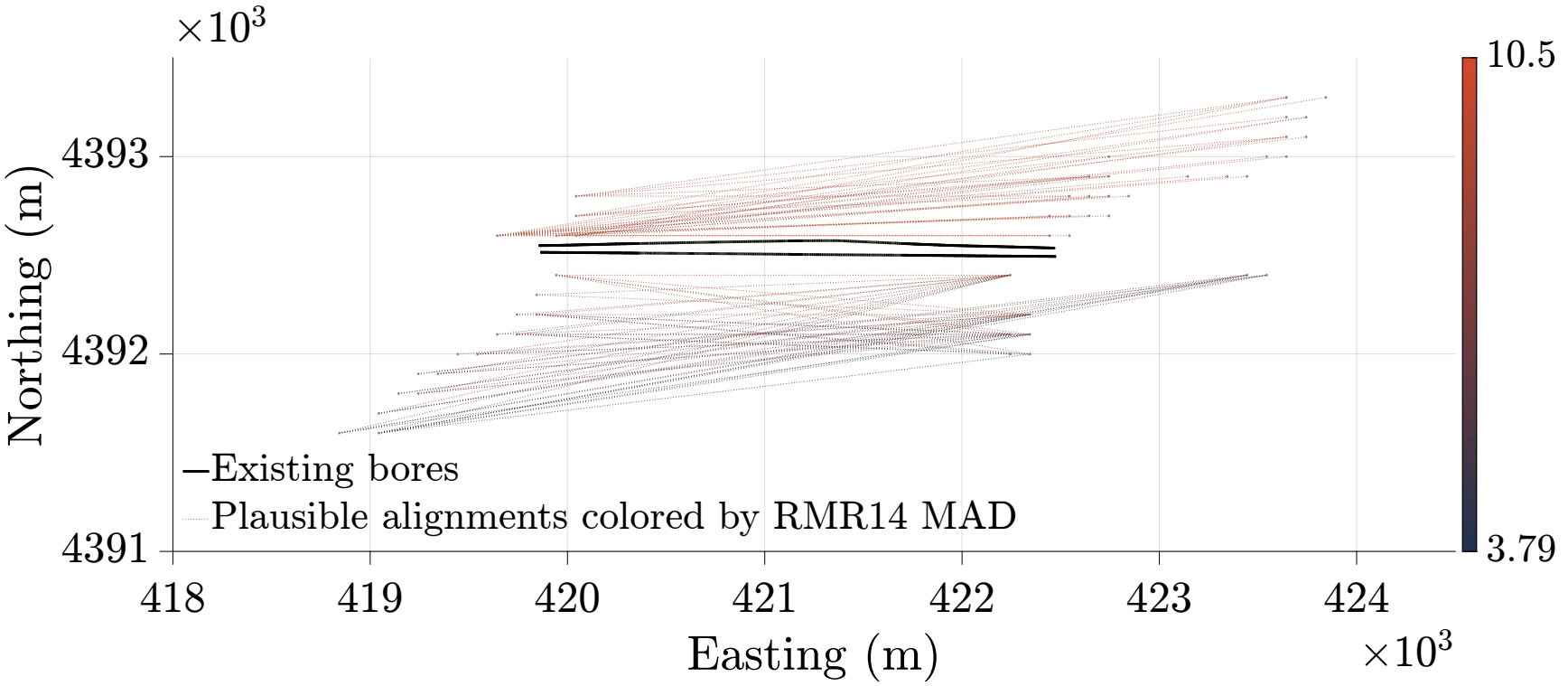

Figure 4.9: Median absolute deviation of RMR_{14}.

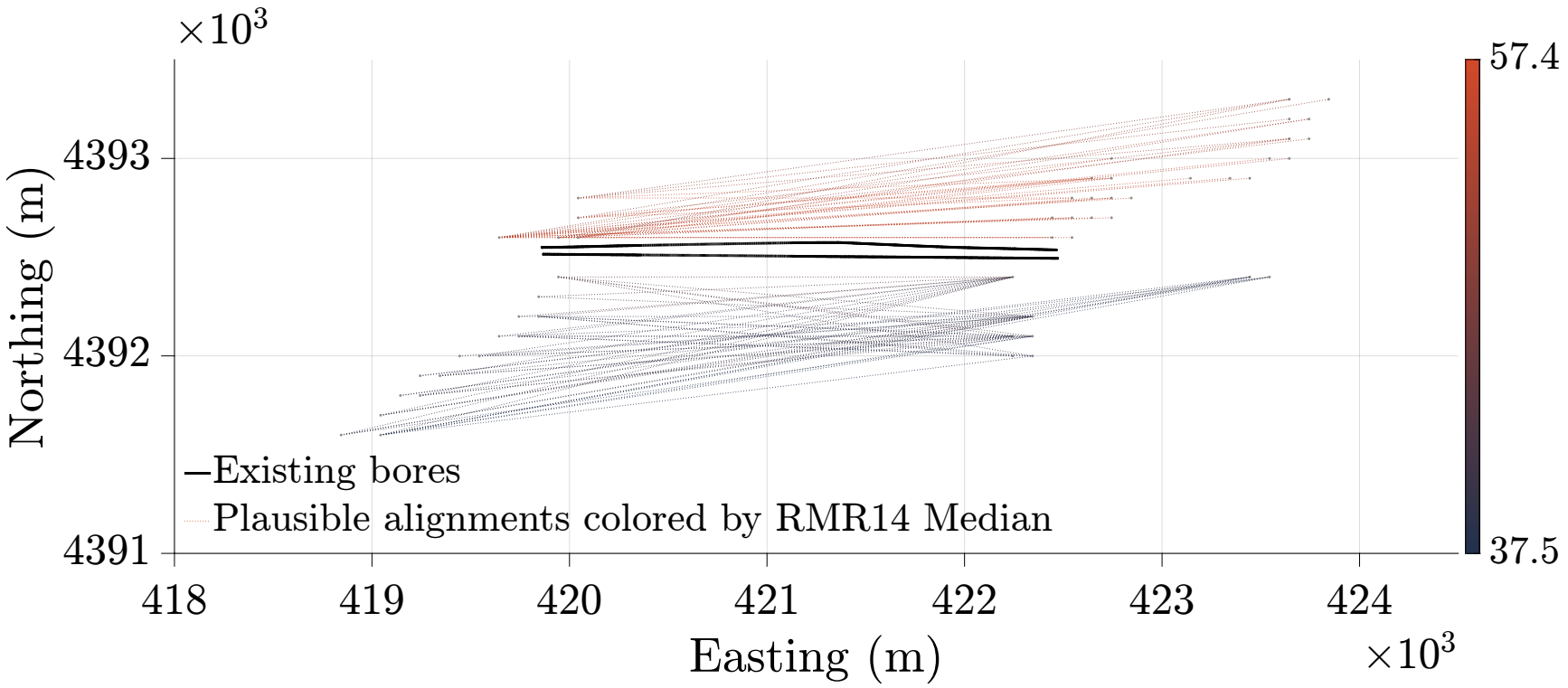

Figure 4.10: Median RMR_{14}.

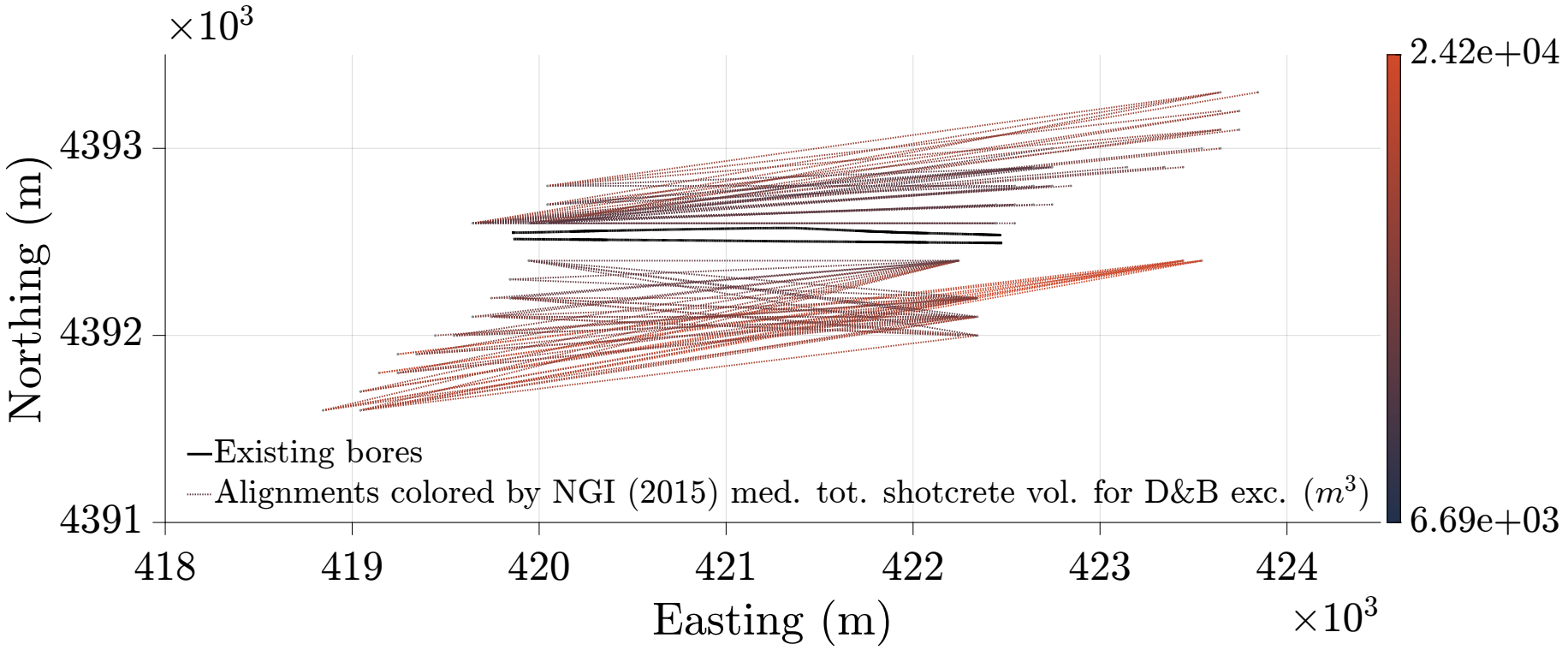

Figure 4.11: Estimated required volume of shotcrete based on Q.

a median estimated RMR_{14} value of 45 and the range of median RMR_{14} values for all alignments evaluated was 30 to 60, alignment X would be assigned a score of 0.5 for the property of median RMR_{14}. This process was repeated for a wide variety of metrics including:

1. Summary statistics of RMR_{14} and Q
    (a) Mean, median, and mode
    (b) 5th and 95th percentiles
    (c) Range
    (d) 5% and 10% trimmed range
    (e) Interquartile range (IQR)
    (f) Median absolute deviation (MAD)
    (g) Skewness
    (h) Kurtosis
2. Other metrics
    (a) Length
    (b) Mean depth
    (c) Maximum depth
    (d) % fault zone
    (e) Squeezing prediction based on Singh et al. (1992) recalibrated to EJMT data
3. Support design metrics
    (a) Total estimated length of bolts by RMR_{14} and Q (assuming 250 kN / 55 kip bolts)
    (b) Total estimated shotcrete volume by RMR_{14} and Q (assuming 30 MPa / 4000 psi shotcrete)
    (c) Estimated stand-up time from RMR_{14} 5th, 50th, and 95th percentiles
    (d) RME
    (e) Estimated TBM advance rate by RME
    (f) Estimated D&B advance rate by Q

The normalized scores were then added together to produce an aggregate score for each alignment considering each of the above metrics. No additional weighting was conducted. The alignments were then simply sorted by their scores. Although this aggregated score does have some value, some additional granularity is valuable. In particular, the above metrics include both TBM– and D&B–based metrics. Therefore, groups of metrics were combined to provide combined scores based on a family of related metrics. Each alignment then had ten scores based on some simple and grouped metrics including:

1. Max depth

2. Average depth
3. Length
4. Aggregated scores
5. Measures of central tendency of rock mass classifications
6. Measures of dispersion and consistency of rock mass classifications
7. TBM-specific metrics
8. D&B-specific metrics
9. RMR-based metrics
10. Q-based metrics

Taking the best alignment based on each of these metrics gave seven alignments that were ranked highest in one or more of these categories.

4.3.2 Highest and Lowest Scoring Alignments

Figure 4.12 and Figure 4.13 show the highest and lowest scoring alignments considered here.

4.4 Discussion

Table 4.3 shows the seven best alignments which scored highest in one or more of the scoring groups. Note that alignment 5448 is the highest scoring in four categories (gross score, D&B–focused metrics, Q–based metrics, and rock mass rating (RMR)–based metrics). It is noteworthy that the shortest and shallowest alignments do not score the highest when metrics of excavation and support are considered. It is common to assume that the shortest or shallowest tunnel will be the cheapest or easiest option to implement. However, this analysis demonstrates that there is some efficiency to be gained by seeking more favorable rock mass quality over simply choosing the shortest or shallowest tunnel.

This alignment optimization methodology by itself does not clearly indicate which of the alignments is best, although the repeated presence of alignment 5448 within the highest scoring group suggests that this alignment may be most favorable. Chapter 6 advances these seven alignments for further comparison by numerical modeling.

The highest scoring alignments are generally nearer the existing bores. There is a cluster of high-scoring alignments just north of the Eisenhower bore, suggesting that a new bore in this vicinity may be the most advantageous choice for CDOT.

This evaluation did not consider the stability of the landslide north of the east portal of the EJMT. This landslide was activated during the pilot bore construction and stabilized with a large toe berm which is now incorporated into the north side of the

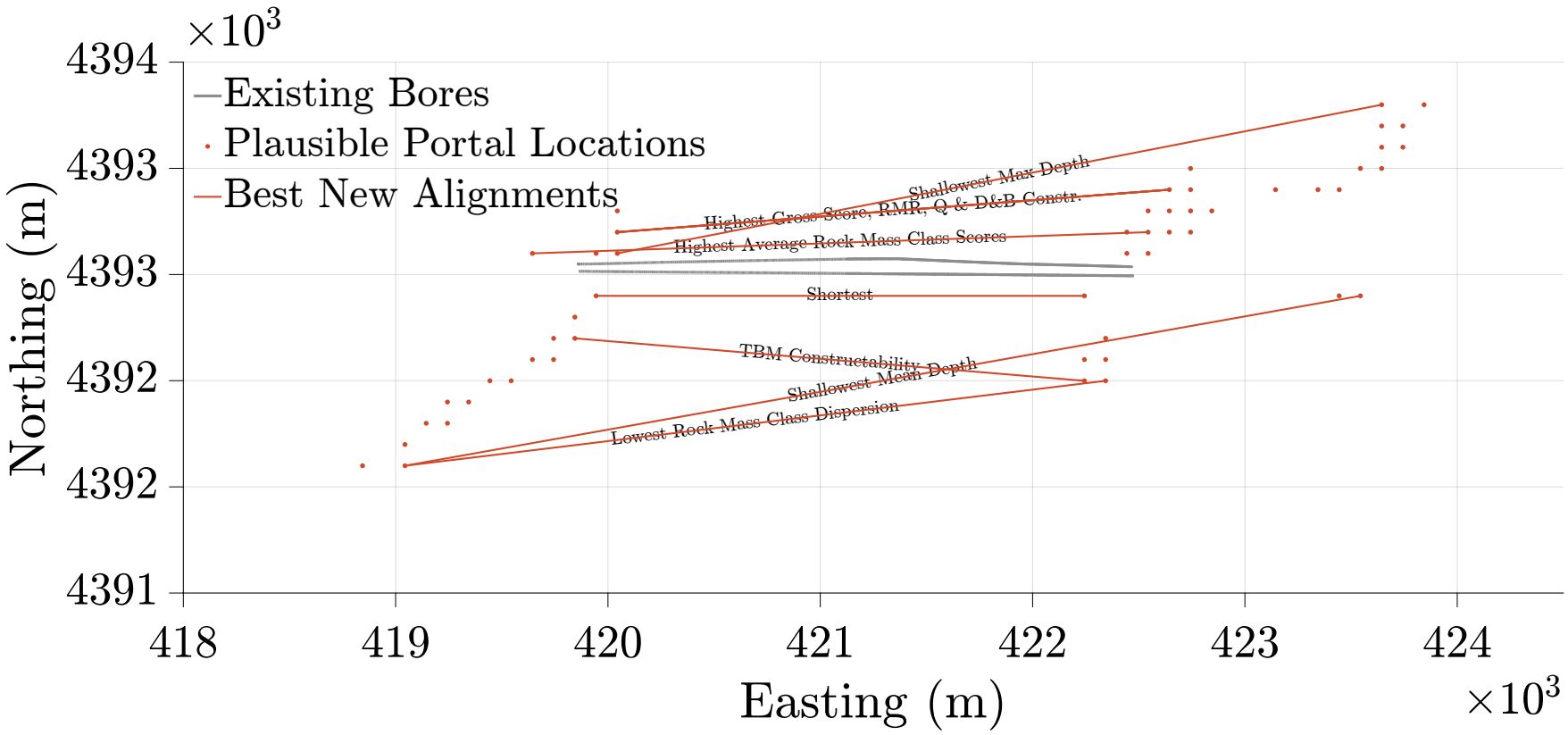

Figure 4.12: Highest scoring alignments by various metrics.

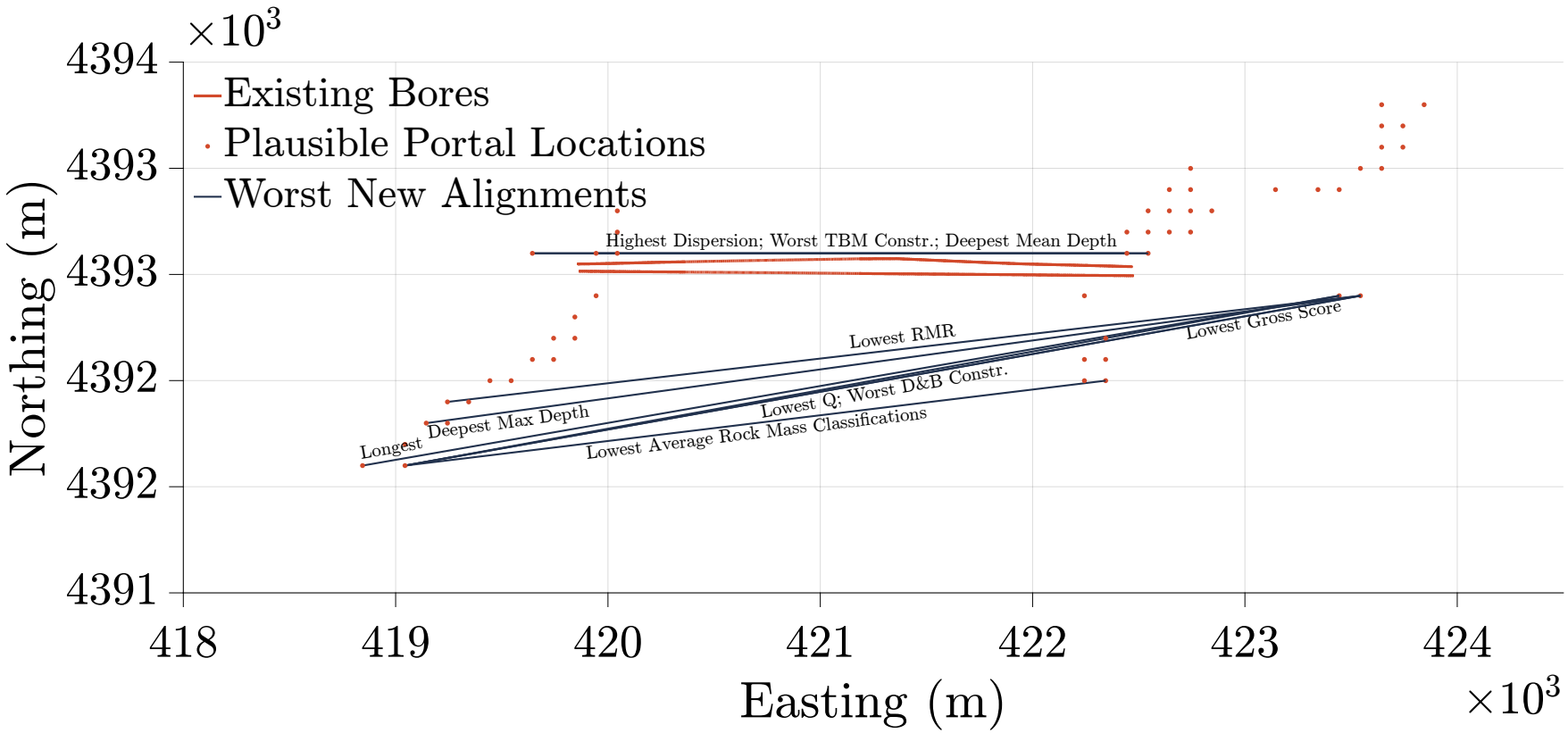

Figure 4.13: Lowest scoring alignments by various metrics.

portal structure. Additional study of this landslide and its potential intersection and impact upon any new bore is highly recommended.

4.4.1 Correlation of Parameter Consistency with TBM Constructability

Note that ground consistency (i.e., low parameter dispersion) is not a metric intentionally built into the TBM–constructability metrics such as RME. However, this alignment optimization found that higher empirical TBM–constructability metrics were encountered on alignments with the greatest consistency of rock mass classification parameters. The empirical metrics appear to be unintentionally capturing a preference for consistent ground conditions in TBM excavation. This suggests that further study on TBM–constructability metrics focused on TBM success correlated with parameter dispersion may be warranted.

4.4.2 Alignment Optimization Sensitivity to Tunnel Diameter

This study initially investigated a tunnel with a 10 m diameter (including liner thickness). A simple sensitivity analysis was also conducted with tunnels ranging from 9 to 14 m in diameter. The results, in terms of the highest and lowest scoring alignments, did not change significantly between the diameters. Some parameters are sensitive to diameter, such as the amount of ground support required, but for purposes of comparing different alignments with the same diameter, there is no significant dependence on diameter.

4.4.3 Excavation Cross-Section

This alignment optimization was limited to a single cross-sectional shape (circular). An additional useful step may be cross-section optimization. A poly-arc cross-section can contain the required rectangular infrastructure with a lower total cross-sectional area, thus limiting excavation costs. However, circular cross-sections are very efficient under a wide range of loading conditions, and are the only cross-sections that can currently be excavated by a hard rock TBM. Additionally, over-optimization leading to frequent changes in the excavation cross-section can create additional construction difficulties and thus costs. A further study focused on cross-section optimization (likely based in cost estimates) would be a valuable contribution to the tunneling industry.

4.5 Summary and Conclusions

This chapter demonstrated a technique for probabilistically optimizing an alignment through an uncertain geologic model. Several optimization parameters have been considered. The suitability of these optimization parameters will be further explored in Chapter 6 by applying numerical modeling to the seven best alignments.

Alignment 5448 ranked the highest by several metrics, including all optimization parameters aggregated. If alignment 5448 continues to be the most favorable alignment following numerical modeling, this suggests that the aggregation of various metrics into a single tunnel alignment feasibility score may be possible. This would be a useful tool for project owners early in the evaluation of potential tunnel feasibility.

4.5.1 Squeezing and Rock Burst

The above analysis considered the possibility of squeezing within the clay-rich gneisses of the Idaho Springs Formation (ISF). Squeezing is fundamentally a ductile failure mode and would not occur if a brittle failure mode controlled the rock mass. The analogous problem for a rock mass failing in a brittle mode would be rockburst. Rockburst is still a somewhat poorly understood phenomenon but even in the 1960s miners were aware of "popping rock" that could be deadly. There is no mention of this ground failure mode in any of the documentation reviewed, so it seems likely that no catastrophic brittle failures occurred in the EJMT. However, a deeper tunnel in the same vicinity might encounter such a ground condition. No attempt has been made in this alignment optimization to predict the possibility of rockburst because the alignments considered were at approximately the same depth below ground surface or shallower.

4.5.2 Future Work

Alignment optimization is relatively insensitive to tunnel diameter for circular cross-section tunnels. Future studies could consider the comparative optimization of alternative cross-sectional area and geometry. Additional evaluation of constructability via sequential excavation could be included in the evaluation of alternative cross-sections.

This study did not evaluate curved alignments. Future research could address the possibility of optimizing the tunnel alignment using curvature.

The constructability of TBM tunnels appears to be linked to the consistency of the rock mass classification parameters. The relevance and utility of this observation requires further study and consideration.

Table 4.2: Calculated Optimization Parameters of Best Seven Alignments

		Alignment ID						
Description	**Units**	**211**	**243**	**2273**	**2929**	**4495**	**5448**	**8131**
West Portal Easting	m	419,840	419,040	419,940	419,040	419,640	420,040	420,040
West Portal Northing	m	4,392,200	4,391,600	4,392,400	4,391,600	4,392,600	4,392,700	4,392,600
West Portal Elevation	m	3,469	3,471	3,460	3,471	3,405	3,464	3,474
East Portal Easting	m	422,240	422,340	422,240	423,540	422,540	422,640	423,640
East Portal Northing	m	4,392,000	4,392,000	4,392,400	4,392,400	4,392,700	4,392,900	4,393,300
East Portal Elevation	m	3,456	3,446	3,425	3,394	3,382	3,450	3,434
Length	m	2,408	3,324	2,300	4,571	2,902	2,608	3,668
Max Depth	m	393	388	414	419	427	357	352
Mean Depth	m s	178	197	220	152	218	200	164
Fault Zone Fraction		29.9%	44.0%	30.9%	48.3%	25.0%	0.0%	26.9%
Median RMR14		39.1	37.7	44.7	37.7	56.1	57.4	50.7

Continued on next page

Table 4.2 – continued from previous page

Description	Units	Alignment ID 211	243	2273	2929	4495	5448	8131
Median Q		7.0E-2	5.5E-2	2.6E-1	6.3E-2	1.3E+0	1.2E+0	1.2E-1
Median Total Bolt Length Estimate by RMR for D&B Excavation	m	$8.4 \cdot 10^5$	$6.9 \cdot 10^5$	$7.7 \cdot 10^5$	$1.4 \cdot 10^6$	$4.4 \cdot 10^5$	$1.9 \cdot 10^5$	$4.1 \cdot 10^5$
Median Total Shotcrete Volume Estimate by RMR for D&B Excavation	m^3	$3.9 \cdot 10^3$	$4.7 \cdot 10^3$	$3.3 \cdot 10^3$	$7.1 \cdot 10^3$	$2.9 \cdot 10^3$	$2.3 \cdot 10^3$	$3.9 \cdot 10^3$
Median Total Bolt Length Estimate by RMR for TBM Excavation	m	$3.0 \cdot 10^5$	$2.5 \cdot 10^5$	$3.3 \cdot 10^5$	$5.3 \cdot 10^5$	$2.1 \cdot 10^5$	$8.9 \cdot 10^4$	$1.8 \cdot 10^5$
Median Total Shotcrete Volume Estimate by RMR for TBM Excavation	m^3	$2.7 \cdot 10^3$	$3.2 \cdot 10^3$	$2.4 \cdot 10^3$	$4.9 \cdot 10^3$	$2.3 \cdot 10^3$	$1.8 \cdot 10^3$	$2.8 \cdot 10^3$
Median Total Bolt Length Estimate by Q for D&B Excavation	m	$1.6 \cdot 10^5$	$2.4 \cdot 10^5$	$1.1 \cdot 10^5$	$3.2 \cdot 10^5$	$1.0 \cdot 10^5$	$8.6 \cdot 10^4$	$1.9 \cdot 10^5$
Median Total Shotcrete Volume Estimate by Q for D&B Excavation	m^3	$1.2 \cdot 10^4$	$1.8 \cdot 10^4$	$8.6 \cdot 10^3$	$2.4 \cdot 10^4$	$8.4 \cdot 10^3$	$6.9 \cdot 10^3$	$1.5 \cdot 10^4$

Continued on next page

Table 4.2 – continued from previous page

Description	Units	Alignment ID						
		211	**243**	**2273**	**2929**	**4495**	**5448**	**8131**
Median Total Number of Shotcrete Ribs by Q for D&B Excavation	# ribs	548	1013	392	1289	235	53	624
Squeeze Prediction Fraction		0.0%	0.0%	3.5%	0.0%	4.3%	0.0%	0.0%
Bieniawski (1989) Estimated Stand Up Time by RMR	hours	25	20	57	20	315	383	142
Bieniawski (2006) Estimated TBM Advance Rate by RME	m/day	14	13	10	13	12	12	14
Barton (2002) Estimated D&B Advance Rate by Q	m/hour	0.23	0.21	0.38	0.22	0.60	0.59	0.27

Table 4.3: Best Alignments By Various Optimization Metrics

Alignment ID	211	243	2273	2929	4495	5448	8131
Shortest			X				
Shallowest Mean Depth				X			
Shallowest Maximum Depth							X
All Metrics Aggregated						X	
Highest Average Rock Mass Class					X		
Most Consistent		X					
TBM-focused Metrics	X						
D&B-focused Metrics						X	
RMR-based Metrics						X	
Q-based Metrics						X	

CHAPTER 5

CALIBRATION OF FINITE DIFFERENCE MODEL BY BACK ANALYSIS OF THE EJMT PILOT BORE

This chapter focuses on the development, calibration, and reduction of a numerical model of the Eisenhower-Johnson Memorial Tunnel (EJMT) pilot bore. This case study was detailed in Chapter 3. The purpose of the ongoing research project is to develop a probabilistic methodology for evaluating the feasibility of alternative tunnel alignment options. The development and calibration of this numerical model is an initial step towards evaluating the feasibility of excavating and supporting any arbitrary new bore in the vicinity of the existing bores. This chapter focuses on modeling the pilot bore and thereby calibrating a numerical model via back analysis. Special attention was paid to the area where the pilot bore passed through the fault zone and experienced significant squeezing and overloading of the tunnel supports, and comparing these model results to available data on tunnel support loads and deformations.

5.1 Introduction

This chapter presents a back-analysis of the EJMT pilot bore. The numerical models were created to validate the probabilistic material parameters developed previously and to provide a tool for forward modeling of potential future alignments adjacent to the existing EJMT. Two types of numerical models are discussed here: an elastic-perfectly-plastic (EPP) finite-difference model and an elastic finite-difference model. Both models were evaluated for their ability to reproduce measured load and deflection data recorded during construction. Model reduction from plastic to elastic was pursued to improve model times and make large scale Monte Carlo (MC) simulation possible in the next step, forward modeling of adjacent bores. Ultimately, the EPP model produced better results for only a slight increase in processing time and was selected for forward modeling.

Back analysis is, as the name suggests, an inverse problem. Like most inverse problems, there are many possible solutions. Using simple yet robust statistical methods, this

chapter seeks to find the simplest model which gives reasonable results in a reasonable time span. For the calibrated model to be useful in the forward modeling Monte Carlo simulation the fastest possible model is required to apply the model thousands of times within a span of hours to days. As famous statistician George Box was fond of saying "all models are wrong, but some are useful" and the true test of a model's relevance is whether that model is illuminating and practically applicable (Box 1976, 1979). Thus, the aim of this chapter is not to seek the most detailed, accurate, or realistic possible model of the EJMT pilot bore but rather a simple and acceptably accurate surrogate model.

5.2 Project Description

There are no known complete and detailed as-built drawings of the pilot bore. However, a contemporaneous construction report by the Colorado Department of Transportation (CDOT) on-site project engineer contains extensive descriptions of the excavation methodology and progress as well as shop drawings of the steel sets used (Mattei 1965). In addition, a detailed geologic report was prepared by Miles and Mattei (1965) during construction and the United States Geological Survey (USGS) published an extensive professional paper on the project (Robinson et al. 1974). Of value are the shop drawings of the steel sets used provided in the report of Mattei (1965), which are reproduced in Figure 3.2.

5.2.1 Geologic Setting

The geologic materials along the pilot bore alignment consist of approximately 75% igneous Silver Plume Granite (SPG) and 25% meta-sedimentary Idaho Springs Formation (ISF) (gneiss and schist), with local dikes of augite-diorite (Richards 1963; Robinson et al. 1974). Both bores cross the Loveland Pass-Berthoud Pass fault zone, a "wide zone of Precambrian and Tertiary faulting" (Robinson et al. 1974). For a more complete description of the local and regional geology see Chapter 3.

5.2.2 Geomaterial Properties

Geomaterial properties for this modeling were developed based on field and laboratory testing conducted during the construction of the pilot bore. In addition, the authors took new samples in the vicinity of the EJMT east portal and performed testing for confirmation and the filling of a data gap pertaining to the ISF. Chapter 3 contains a detailed description of the geomaterial properties developed for this analysis. In particular, Sec-

tions 3.5.4, 3.5.5, and 3.5.6 contain detailed discussions of the development of the material models applied in this back analysis for the fault gouge, ISF, and SPG, respectively. Using current and historical laboratory- and field-testing data new elastic and plastic properties of the materials around the pilot bore were developed in Chapter 3. Statistical distributions of the elastic moduli and Mohr-Coulomb yield properties were developed by typical regression methods. Tables 3.2, 3.3, and 3.4 summarize the material properties developed from the available data.

5.2.3 Historical Design

The EJMT pilot bore's steel supports were originally designed using a version of the empirical method first described by Terzaghi (1946) and Proctor et al. (1946). This technique was slightly modified for this project as described by Hopper et al. (1972) and Robinson et al. (1974) and is characterized by Equation 5.1.

$$P = C\,(B_t + H_t)\,\gamma \tag{5.1}$$

where P is the uniform vertical rock load predicted on the tunnel arch, C is an empirical constant dependent on rock conditions, primarily fracture spacing and presence of fault gouge, B_t is tunnel width, H_t is tunnel height, and γ is the unit weight of overburden rock.

The EJMT pilot bore tunnel was approximately 3.7 m (12 ft) wide and high. The original design called for a trapezoidal cross-section with timber supports. However, at the contractor's request, the design was modified to a horseshoe cross-section with steel supports before the tunnel had advanced significantly. The majority of the pilot bore was constructed with a flat invert, though some zones included a curved invert. The overburden unit weight was approximately 26.0 kN/m3 (165 pcf). Robinson et al. (1974) estimated the value of C in Equation 5.1 to range from 0.35 to 1.6 based on the judgment of the design engineers. The C-value was primarily based on the anticipated fracturing and alteration of the rock at any given point, using an ad hoc system. Hopper et al. (1972) also attempted to apply an early ground reaction curve (GRC) concept to the design of the Eisenhower bore, those this method still failed to fully anticipate the difficulties encountered there.

The steel sets for the pilot bore were designed based on the pressures predicted by Equation 5.1 and the elastic design equations by Proctor et al. (1946). Robinson et al. (1974) used the steel set loads from the pilot bore to calibrate the Terzaghi (1946) rock load factors to predict the likely steel set loads in the main bores. Unfortunately, these calibrated rock loads ended up underpredicting the rock loads in the main bores, likely due

to a lack of linear scaling in rock loads with bore diameter. As Hopper et al. (1972) stated at the time of the Eisenhower bore's construction: "for large tunnels where very high squeeze loads are anticipated the ultimate load calculated by Terzaghi's method should be carefully appraised in the light of test results and in-situ measurements as well as other available analytical procedures."

5.2.4 Steel Sets Used in the Pilot Bore

According to the as-built drawings, all of the steel beams used in the Eisenhower bore were made of American Society for Testing and Materials (ASTM) grade A441 steel. A441 steel was a popular high–strength, low–alloy, manganese–vanadium steel suitable for welding which was introduced by ASTM in 1960 and added to the American Institute of Steel Construction (AISC) Specifications in 1961. In 1989, A441 steel was discontinued and replaced by A572 steel, and in 1994 this steel designation was removed from the AISC Specifications. A992 steel currently dominates modern steel construction for primary structural members. A441 steel has a yield point of 50 kips per square inch (ksi) and a tensile strength of 70 ksi.

The exact material and section properties of the steel used in the construction of the EJMT pilot bore are unclear. Contemporaneous reports by Robinson et al. (1974) and Mattei (1965) note that the cross-sections were 4–in I-sections with a weight of 7.7 pounds per linear foot (plf) and 6–in H-sections with a weight of 25 plf. This study assumes that these beams had a yield strength of 50 ksi (345 megapascals (MPa)), as was typical for structural steel of the era and matching the ASTM A441 steel used in the Eisenhower bore. Based on historical steel section data in Brockenbrough and Schuster (2018) the 4–in (Page 96) and 6–in (Page 220) steel sections would have cross-sectional areas of 2.21 in^2 (1426 mm^2) and 7.35 in^2 (4742 mm^2), respectively. This gives an axial thrust capacity for each section of 111 kips (492 kN) and 368 kips (1635 kN), respectively. The strong-axis moment of inertia of the 4–in and 6–in sections are 6.0 in^4 and 47 in^4, respectively. Historical photos of the pilot bore show the steel sets placed with their strong axis in bending, as would be expected for typical steel set installation.

5.3 Histogram Fit Methodology

The fit of the model results to the available data was evaluated via a discrete least-squares technique which compares the histogram of a given model output to the histogram of that same parameter as measured by instrumentation in the original pilot bore. In general, matching the recorded leg thrust was the primary objective of the fitting

technique. The coefficient of determination (r^2) calculated between the model data and the instrument data was the metric optimized.

The coefficient of determination between the model data histogram and the instrument data histogram was calculated by Equation 5.2.

$$r^2 = 1 - \frac{SSR}{SST} \tag{5.2}$$

$$SSR = \text{sum of squared residuals}$$

$$= \sum_{i=1}^{n} (y_i - f_i)^2 \tag{5.3}$$

$$SST = \text{total sum of squares}$$

$$= \sum_{i=1}^{n} (y_i - \bar{y})^2 \tag{5.4}$$

$$y_i = \text{instrument data histogram bin probability for bin } i$$

$$f_i = \text{model data histogram bin probability for bin } i$$

$$\bar{y} = \text{mean instrument data histogram bin probability} \tag{5.5}$$

Data falling outside of the bins defined for the instrument data were treated as errors, i.e., the y_i value for those values is zero.

5.4 Stress Field

All of the numerical modeling approaches considered here require some information on the stress field in which the tunnel sits. Hoskins et al. (1974) reported data from flat jack tests and borehole strain relief tests in the pilot bore and the cross-passages between the pilot and Eisenhower bores. Table 3.1 summarizes the results of these data which are the best available estimates of the H/V stress ratio in the vicinity of the EJMT. The data by Hoskins et al. (1974) are generally sufficient for the initialization of the Fast Lagrangian Analysis of Continua (FLAC) finite difference method (FDM) models.

Simpler analysis techniques, such as a convergence-confinement model, would require input of the vertical stress transferred to the supports by the broader stress field, not the stress field itself. Therefore, the author attempted to estimate the rock loads transferred to the supports by correlation to rock mass classifications.

Robinson et al. (1974) reported significant load and deflection data from the construction of the pilot bore. However, there were not enough detailed, coupled load-deflection

data to properly calibrate a GRC for the wide range of ground conditions in the EJMT. In particular, the current authors were unable to locate the original data by Terrametrics, the instrumentation contractor on the job, which describe the change in measured loads and deflections in the pilot bore. For most cases, only the ultimate equilibrated loads were reported and, in some cases, the total deflections were recorded.

Therefore, several empirical correlations were evaluated for their consistency with the available load data. Empirical correlations evaluated were:

1. Barton et al. (1974)
2. Unal (1983)
3. Goel and Jethwa (1991)
4. Singh et al. (1992)
5. Goel et al. (1995)
6. Bhasin and Grimstad (1996)
7. Lowson and Bieniawski (2013)

Goel and Jethwa (1991) most closely matched the observed rock loads in the pilot bore.

For the purposes of this back analysis, the available data detailing equilibrated rock loads were divided by the estimated total overburden at each instrumented station to develop a value between 0 and 1 which the author defined as the ground response factor (GRF). The GRF is essentially a single point on the GRC indicating the fraction of the total overburden that was borne by the EJMT pilot bore supports given the construction means and methods of the time. This value ranged from 0 to 18.2% for the 33 instrumented stations in the EJMT pilot bore with rock load data. When GRF is plotted against rock mass rating (RMR_{14}) and rock mass quality index (Q) there appears to be an upper bound for GRF as a function of RMR_{14} or Q (Figure 5.1). The author adopted an exponential decay function to approximate this relationship. Data from stations 4384 and 4389 do not fit with this pattern. These two stations are within a shallow, highly weathered and altered fault zone near the western portal of the tunnel that is not generally representative of the rest of the tunneling conditions observed. Stations 4384 and 4389 were therefore excluded from the rest of this analysis.

The best fit exponential curve for the GRF vs. RMR_{14} relationship is shown in Figure 5.2. The functional relationship is Equation 5.6 which has a coefficient of determination (r^2–value) of 0.513. The upper bound of the apparent GRF-RMR_{14} correlation is given by Equation 5.7.

$$GRF = 0.16799e^{-0.06227 \cdot RMR} \tag{5.6}$$

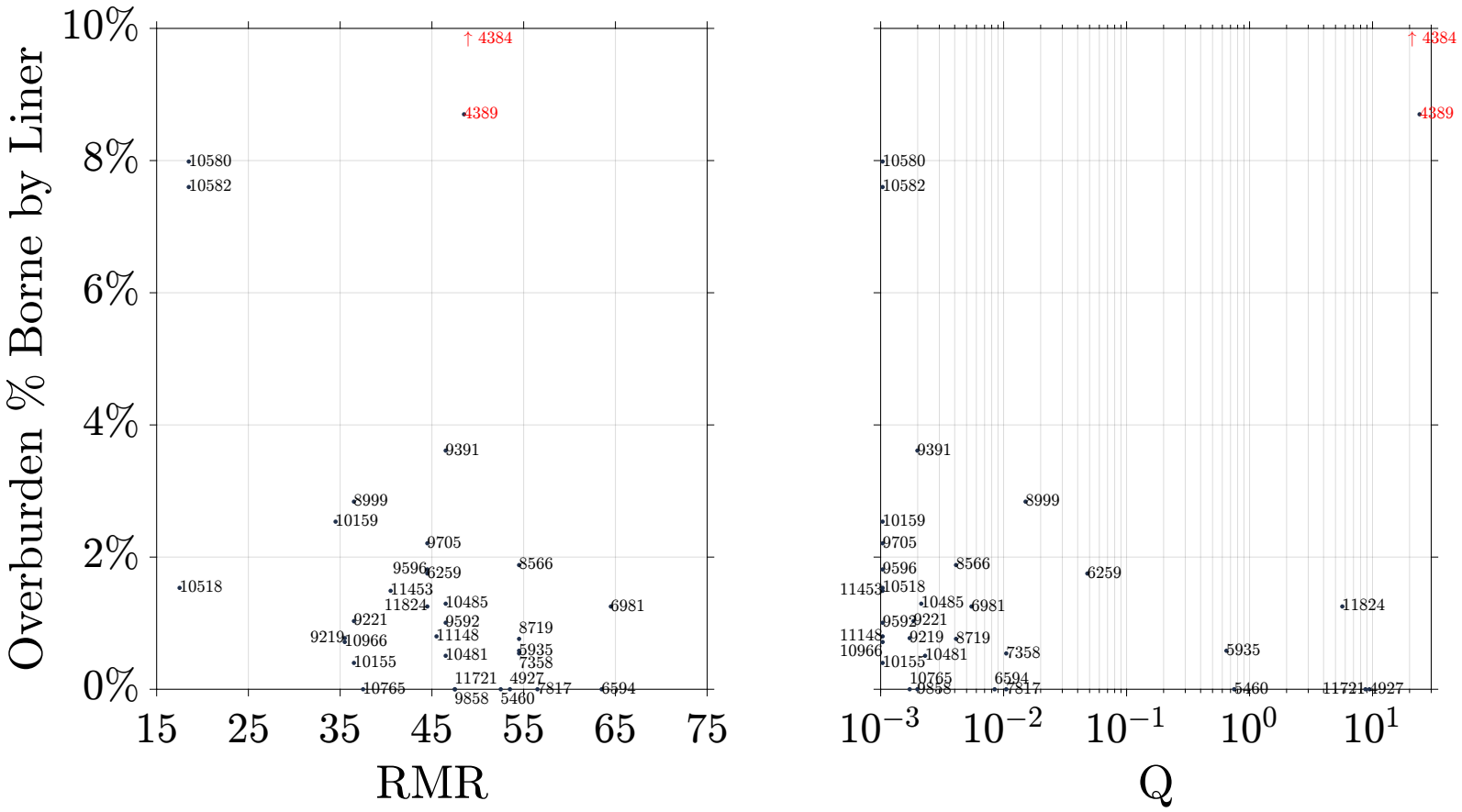

Figure 5.1: Ground response factor (GRF) versus RMR_{14} and Q for the instrumented stations in the EJMT pilot bore. Pilot bore data from data from Robinson et al. (1974). GRF is defined as load measured on the tunnel support at a given station divided by the total overburden on the tunnel at that station.

$$GRF = 0.2202e^{-0.04012 \cdot RMR} \tag{5.7}$$

A similar pattern of decaying ultimate load on the supports can be observed when the GRF is plotted against the Q-value (Figure 5.3). However, the trend is not as clear and the scatter is larger ($r^2 = 0.18$).

Alternatively, the overburden pressure experienced by the tunnel liner can be estimated not as a percentage of total overburden but as an implied active height (IAH). This method of estimating overburden pressure on tunnel supports harks back to the Terzaghi (1946) methodology for estimating tunnel pressure as an active zone above the tunnel. The assumption is that the act of tunneling loosens a portion of the rock mass above the tunnel, which must then redistribute its weight horizontally through shear to the surrounding rock mass or vertically to the tunnel support. Given a known average unit weight of overburden, the tunnel support load can be estimated as the height of this active mass resting on the tunnel liner. From the Robinson et al. (1974) pilot bore support load data, IAH was estimated above each support set and compared to the estimated rock mass classifications at each instrumentation point (Figure 5.4).

IAH also appears to be correlated with depth (Figure 5.5). There are some notable exceptions (e.g., stations 10580 and 10582) and the overall trend is weaker then the correlation between IAH and RMR_{14}.

Note that depth and rock mass classification are also positively cross-correlated as shown in Figure 5.4. At greater depths, there is generally more intact rock with less weathering, leading to higher RMR_{14} values.

A multi-linear regression model relating IAH to tunnel depth and the most likely estimated RMR_{14} for each station along the EJMT pilot bore with vertical rock load data was developed because the vertical pressure on the tunnel supports, represented by IAH, appears to be correlated to both RMR_{14} and tunnel depth. The regression surface shown in Figure 5.6 is described by Equation 5.8.

$$IAH = 9.66 + 0.0166d - 0.236RMR \tag{5.8}$$

where d is the depth of the tunnel and RMR is rock mass rating. Equation 5.8 has an r^2–value of 0.41 indicating that these parameters have some correlation but there is significant scatter and outliers.

Various more complex forms of this regression were attempted including polynomial functions of each term and interaction terms. However, none of the more complex models were significantly more accurate as measured by r^2–value. Therefore, in the interests of

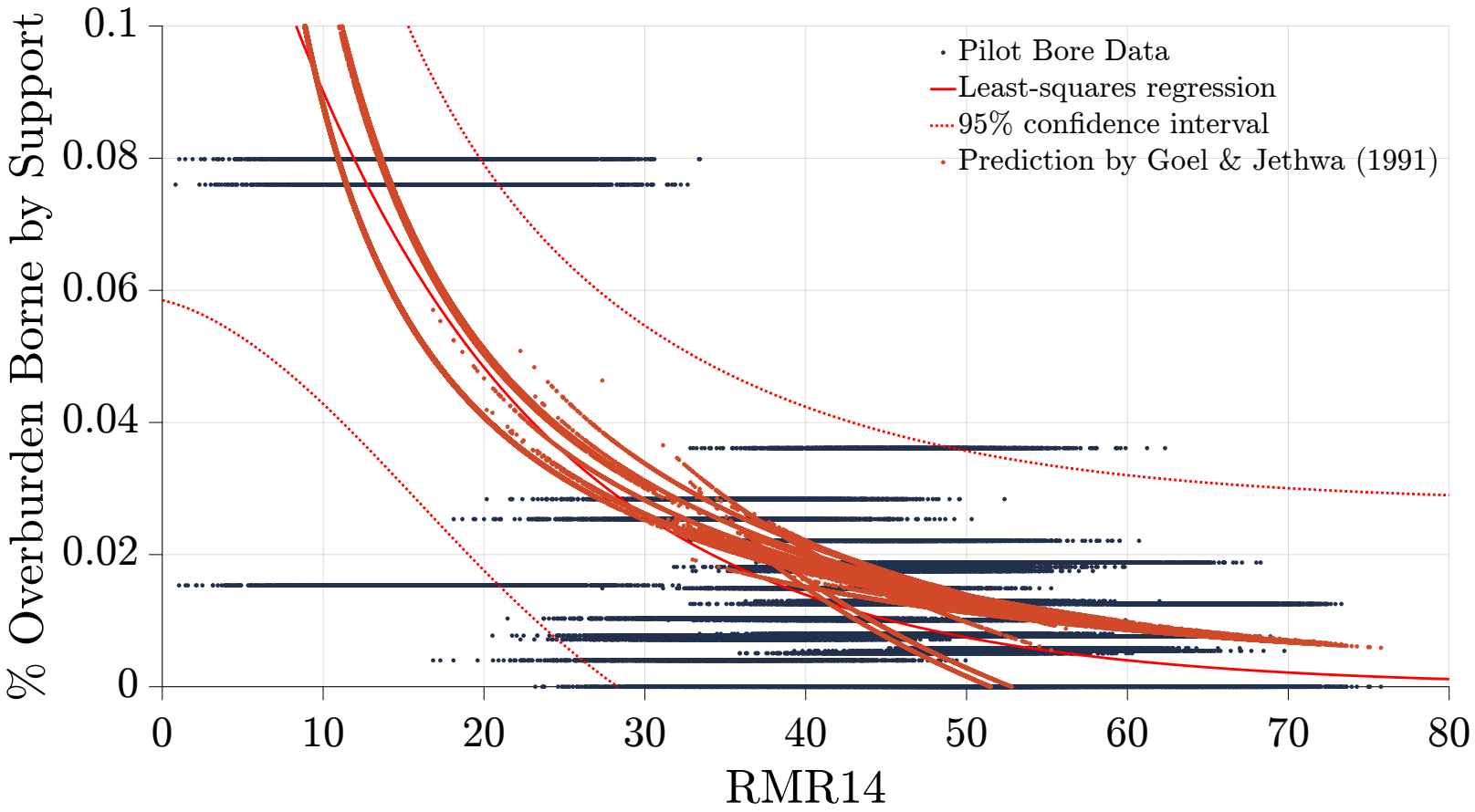

Figure 5.2: GRF versus RMR_{14} as recorded in the pilot bore by Robinson et al. (1974) along with a least-squares regression to an exponential function and the prediction model by Goel and Jethwa (1991).

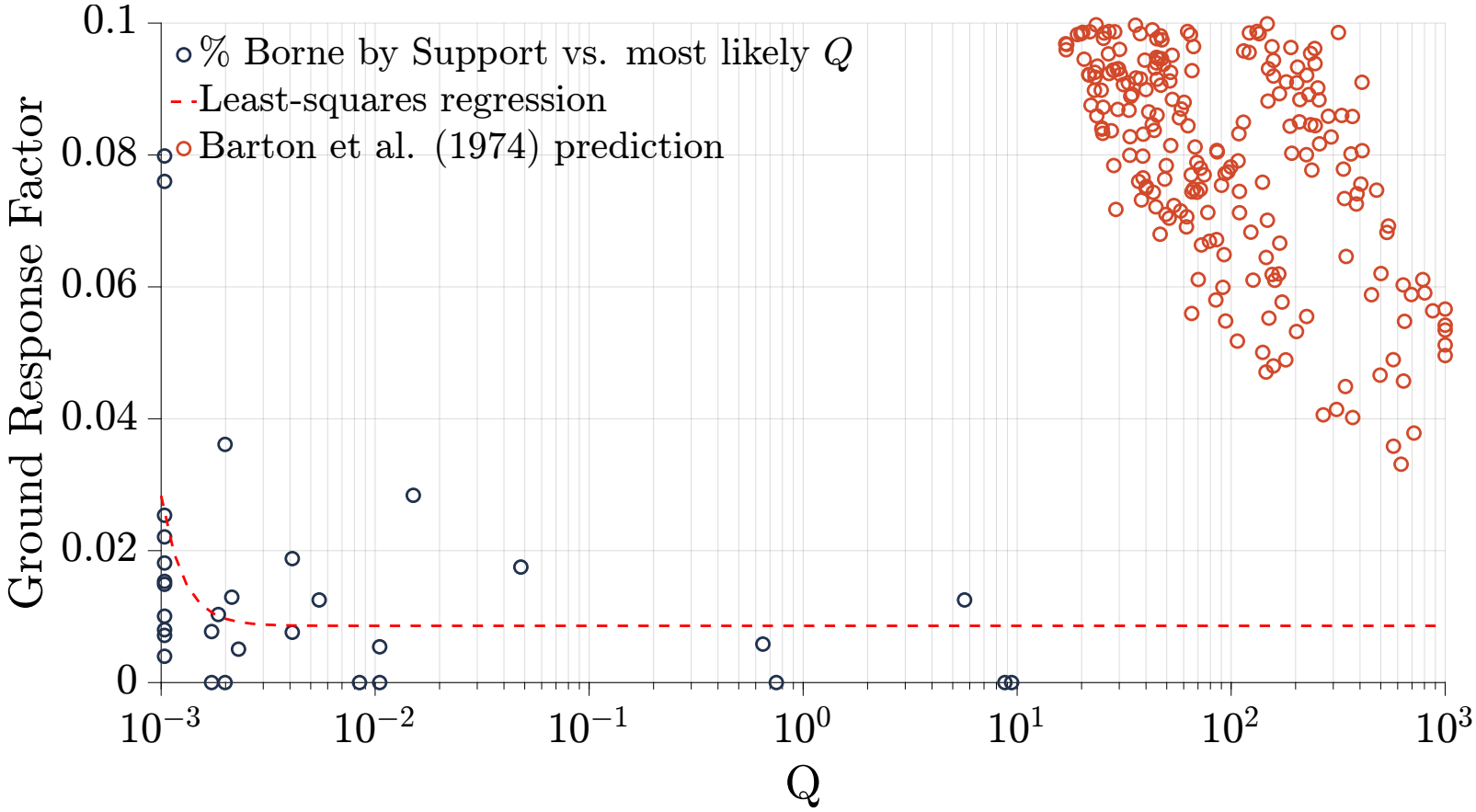

Figure 5.3: GRF versus Q as recorded in the pilot bore by Robinson et al. (1974) along with a least-squares regression to an exponential function and the prediction model by Barton et al. (1974). Note that the predictions by the Barton et al. (1974) model are much higher than the recorded ground loads in the pilot bore.

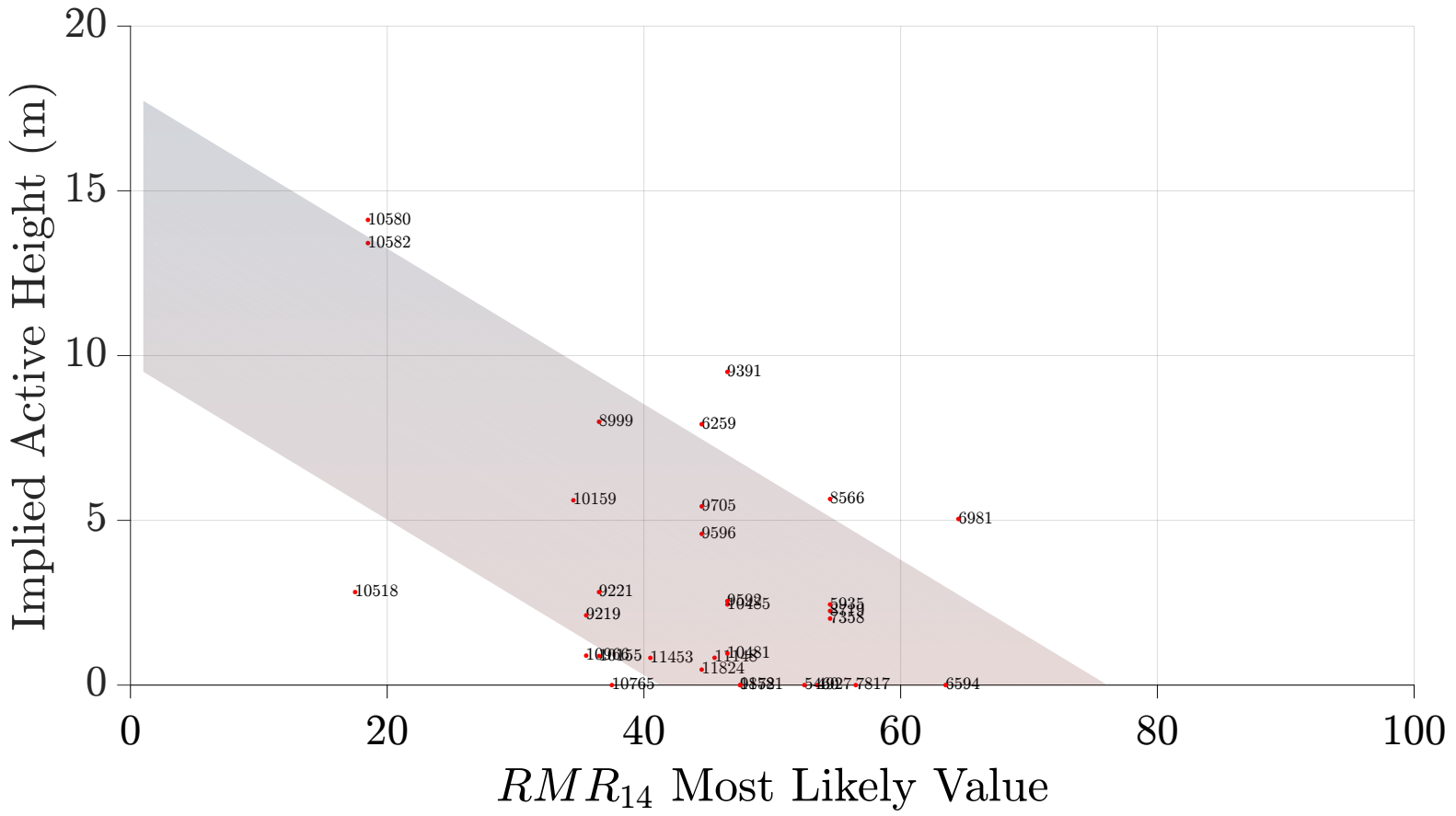

Figure 5.4: Implied active height (IAH) versus RMR_{14} with the multi-linear regression fit surface. Data from Robinson et al. (1974).

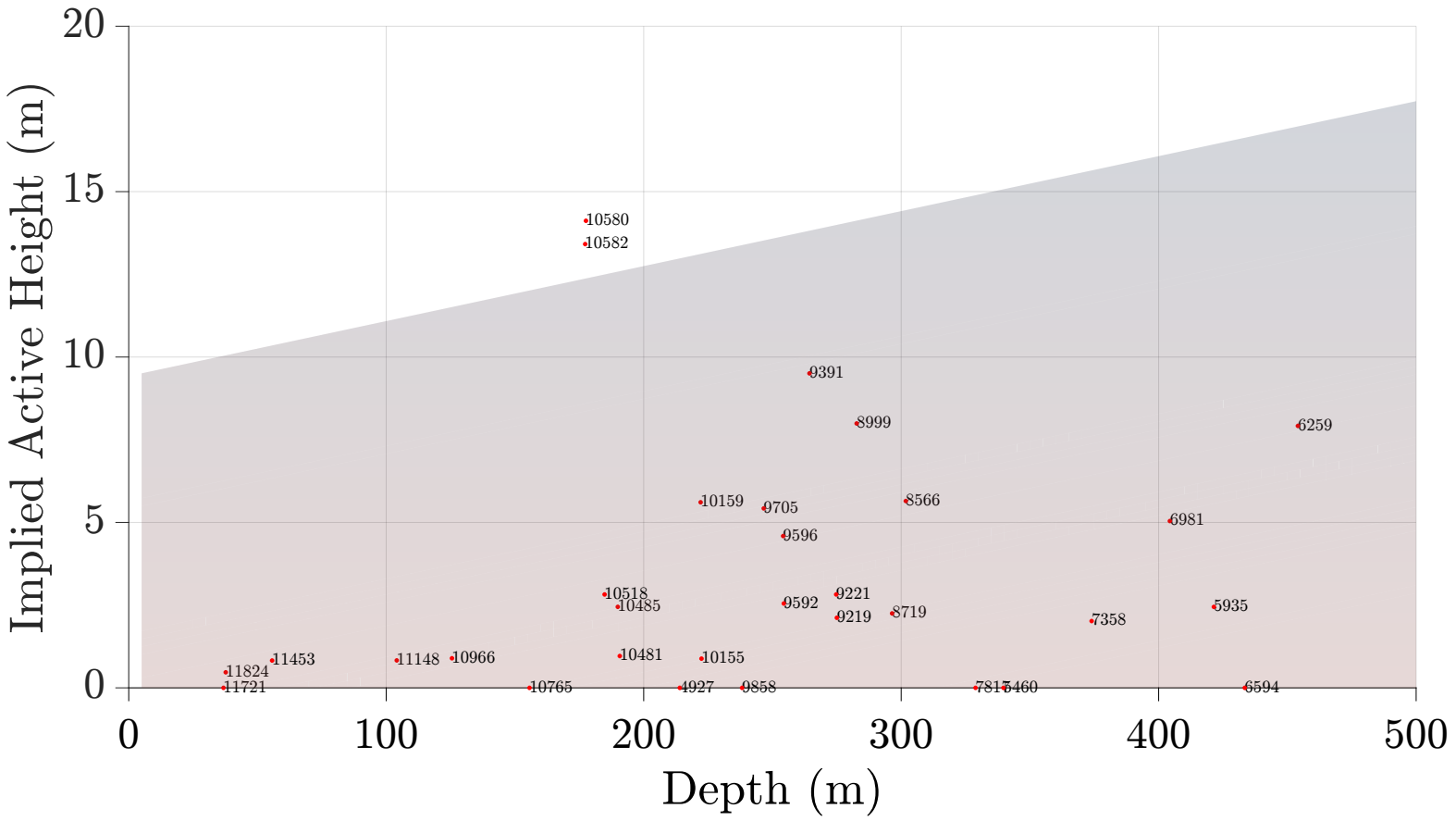

Figure 5.5: Implied active height (IAH) versus depth below ground surface with the multi-linear regression fit surface. Data from Robinson et al. (1974).

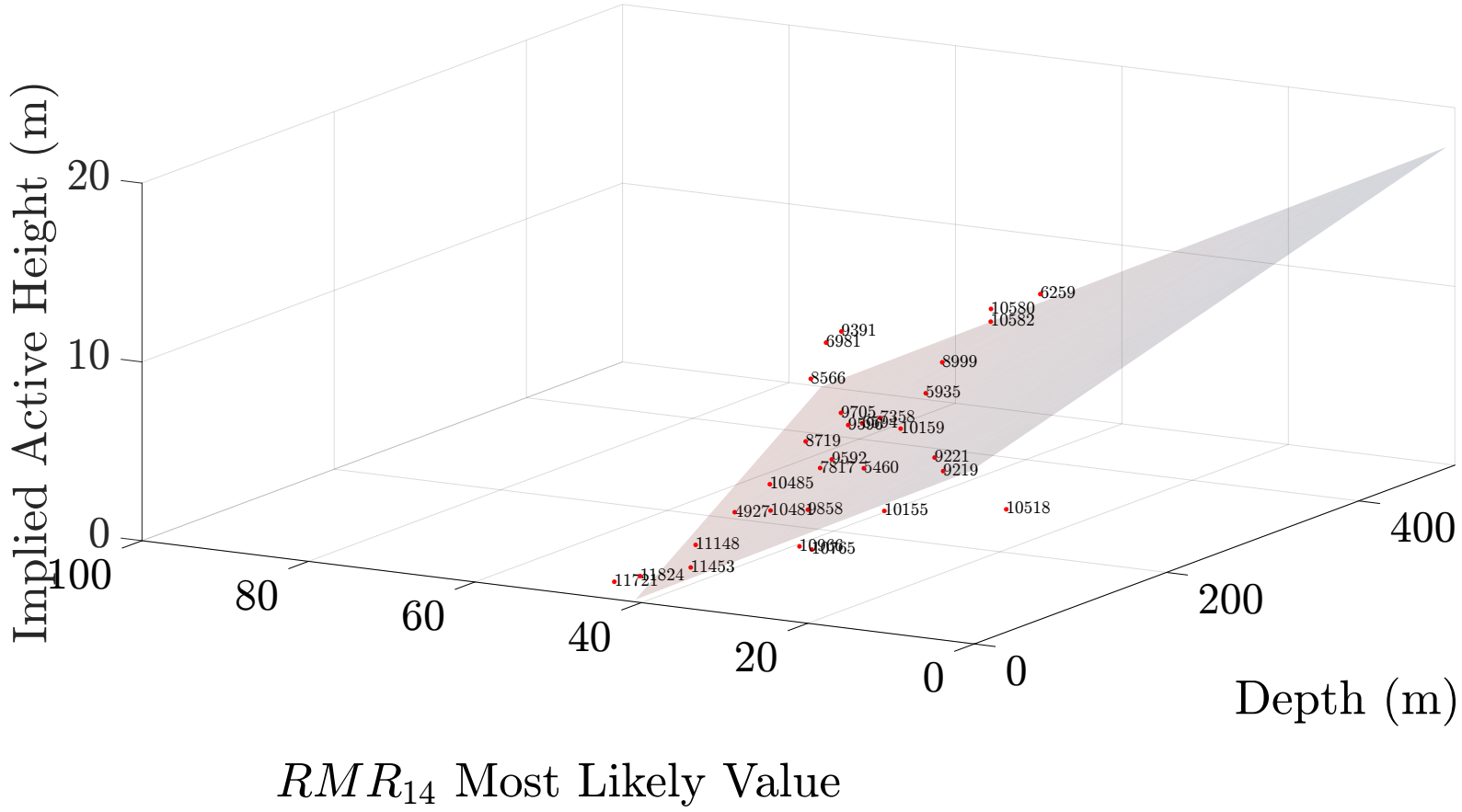

Figure 5.6: Implied active height (IAH) versus depth below ground surface and RMR_{14} with the multi-linear regression fit surface. Data from Robinson et al. (1974).

simplicity, Equation 5.8 is preferred for estimating the pressure on tunnel supports directly from rock mass rating (RMR).

5.5 FLAC Modeling

The modeling and reduction process began with an elastic-perfectly-plastic (EPP) finite difference method (FDM). Using the histogram fitting methodology described in Section 5.3 the author evaluated the accuracy of the model relative to recorded instrument data. From there, the author reduced to a fully elastic model and again compared the histogram of the model results to the histogram of instrument data. Going from an EPP model to an elastic model simplifies the mechanical behavior of the ground around the tunnel liner. In general, the mechanical behavior of the liner remains the same at each step. The FLAC FDM uses elastic beam theory to represent the stresses and strains in the liner.

Table 3.2 summarizes the fault gouge material properties, and the distribution of those properties, which were used in the initial FLAC squeeze zone modeling.

Table 3.4 and Table 3.3 summarize the SPG and ISF material properties, and the distribution of those properties, which were used in the FLAC modeling and beam-spring modeling.

5.5.1 Initial FLAC Model of Squeeze Zone

An initial FLAC model was developed of the pilot bore through the squeeze zone. This model used material parameters of the fault gouge as a baseline; the model was calibrated by escalating the material parameters until the histogram of model deflections approximated the histogram of measured deflections through the pilot bore squeeze zone.

The pilot bore construction report includes detailed horizontal and vertical profiles of the pilot bore through the Loveland Fault squeeze zone. These profiles have been reproduced in Figure 5.7 and Figure 5.8. The data from these figures were digitized at each steel set location through the pilot bore squeeze zone. The measured crown, invert, and wall displacement data show an approximately normal distribution.

The modeling of the pilot bore squeeze zone was conducted using FLAC (Itasca 2020). The initial model was a continuous, homogeneous, isotropic, and linear elastic (CHILE) model. Zero-displacement model boundaries were placed at 16 m from the centerline of the tunnel, the grid was discretized in uniform 0.25-m increments, and the tunnel profile was excavated in a single step. The squeeze zone material around the tunnel was modeled as a single fault gouge material with the elastic constants discussed above. Several parameters

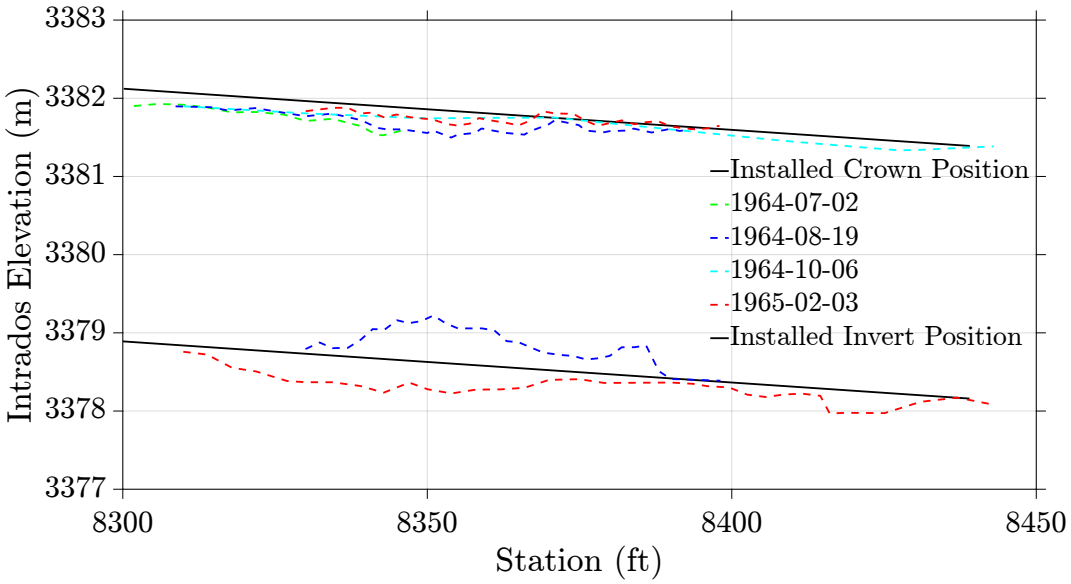

Figure 5.7: Vertical deflections of the pilot bore through the squeeze zone (Mattei 1965).

were iterated to observe their effects on the model. The iterated parameters were:

1. Standup time before support installation (0, 100, and 1000 steps);
2. The liner system used (4-in steel set, 6-in steel sets, and 6-in steel sets with invert struts);
3. Support spacing (0.23, 0.30, 0.38, 0.46, 0.61, 0.76 m);
4. Horizontal / vertical stress ratio (0.18, 0.35, 0.52, 0.69, and 0.86); and
5. Young's modulus escalation factor (1, 3, and 5).

Note that sections with invert struts have a curved invert while the other two sections have a flat invert.

For each combination of parameters, 40 Monte Carlo realizations with material properties selected randomly from the associated material property distribution were developed. Multiplying the 810 combinations of discrete model parameters by 40 Monte Carlo realizations of material properties per set of model parameters give gives 32,400 total realizations of the model.

The random material properties were selected using a MatLab code which also wrote the associated FLACish (FISH) code to a text file. FISH is a programming language which can be used to control FLAC models. The FISH code was called in FLAC and ran through each realization successively.

The model can be calibrated by selecting those parameters which make the model displacement distributions most closely approximate the measured displacement distributions. In this case, those parameters are stress ratios of 0.18 and 0.35 with a median Young's

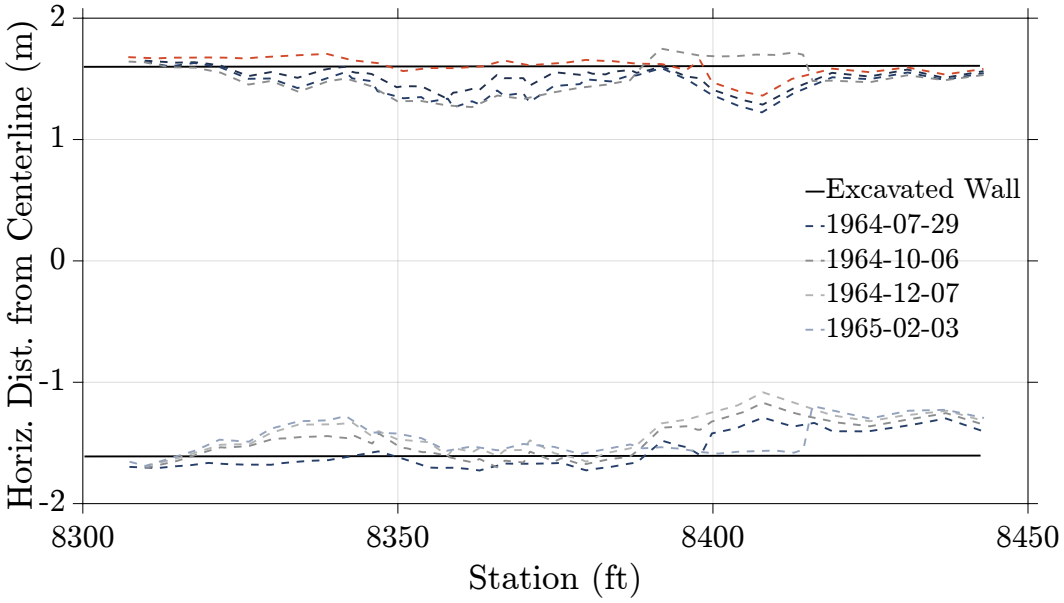

Figure 5.8: Horizontal deflections of the pilot bore through the squeeze zone (Mattei 1965).

modulus of 38 MPa (escalated by a factor of five from the fault gouge material model). This combination of parameters has N = 4320 Monte Carlo runs. Figure 5.9 shows the crown, invert, and wall deflections for these model runs compared to reported deflection data by Mattei (1965). The modeled crown deflections agree very well with measured crown deflections, with the model distribution being slightly wider than the measured distribution, i.e., having slightly greater kurtosis. The invert deflection distribution shows a bias towards lower deflections (less heave) and lower kurtosis than the measured data. The wall deflection distributions show a bias towards less convergence and significantly lower kurtosis.

The Young's modulus of this best fit squeeze zone model (fault gouge modulus escalated by a factor of five) is approximately 1/3 of the Young's modulus measured by the South Dakota School of Mines (SDSM) flat-jack testing, approximately 3 times the modulus measured by United States Bureau of Reclamation (USBR) plate-jack testing. It is also at the lower end of the rock mass moduli estimated by taking intact rock modulus and adjusting it via empirical correlations to rock mass classifications (Figure 5.10).

Low stress ratios (0.18 and 0.35) give the best agreement between the modeled distribution of wall squeezing and the measured distribution of wall squeezing. However, the modeled wall deformation in general does not match well with the observed wall deformation. These low horizontal stress models tend to predict more deflection of

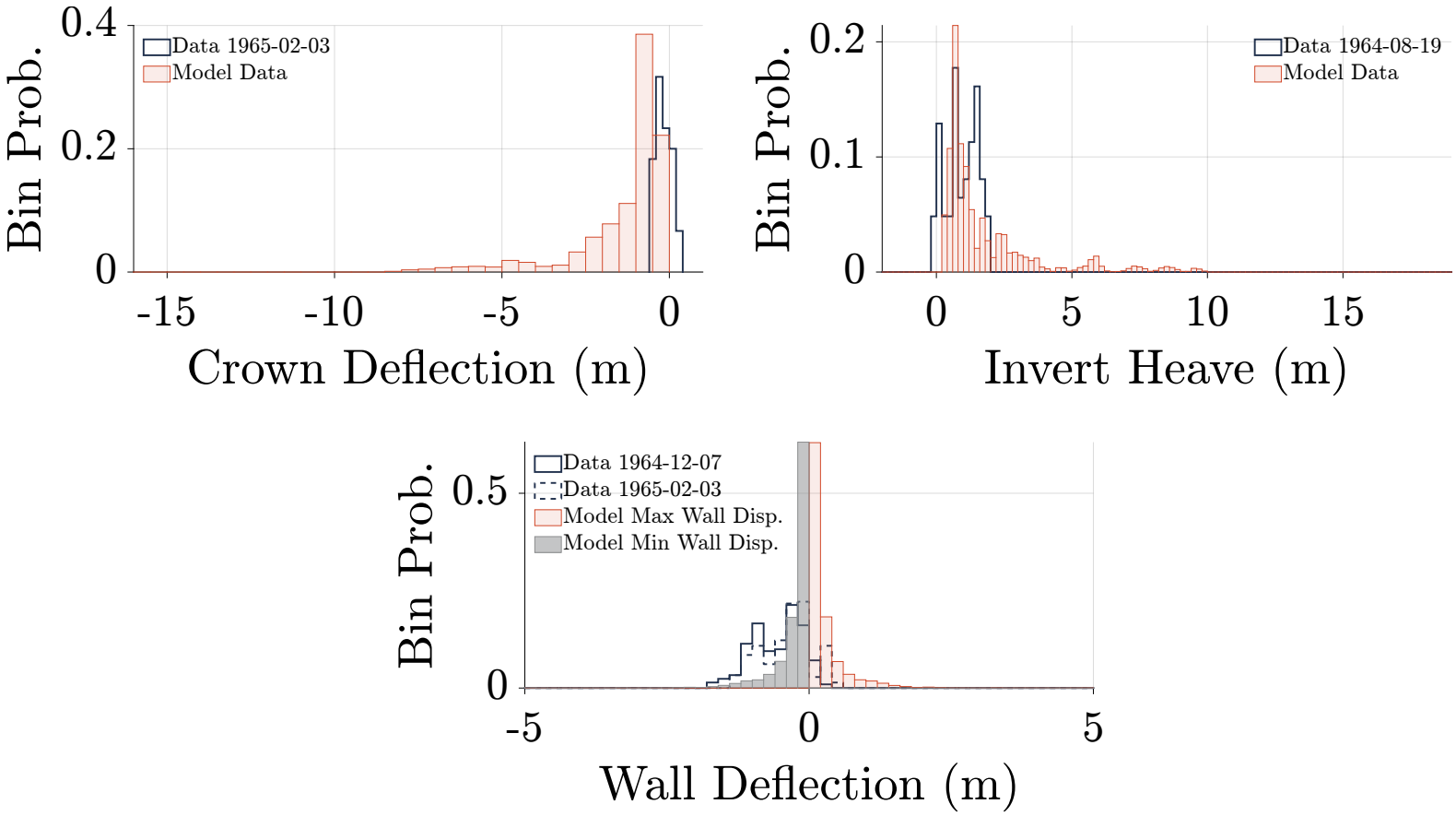

Figure 5.9: Histogram of crown, invert, maximum and minimum wall displacements from $N = 4320$ elastic Monte Carlo simulations in FLAC of the pilot bore squeeze zone with the calibrated parameters of $E = 38$ MPa and $H/V = 0.18$ to 0.35 compared to reported data by Mattei (1965).

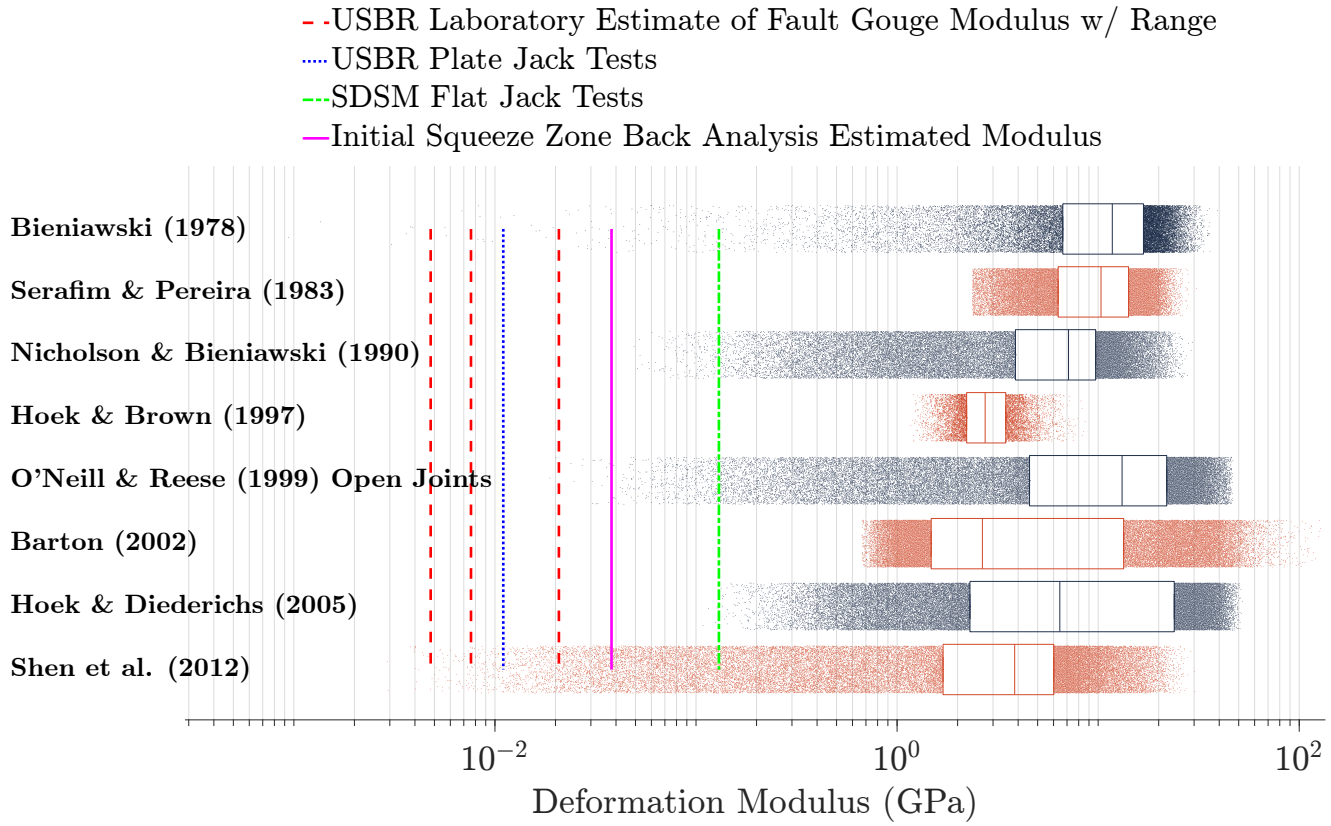

Figure 5.10: Empirical correlations between rock mass classifications and rock mass modulus evaluated for the pilot bore rock mass classification data.

the tunnel wall away from the centerline than is shown by the observed data. In other words, the modeled tunnel tends to "squat", while the observed tunnel behavior was wall convergence combined with vertical contraction of the tunnel.

Table 5.1: Lowest plausible estimated rock mass moduli by various empirical correlations.

Empirical Correlation	SPG	ISF
Serafim & Pereira (1983)	596 MPa	596 MPa
Nicholson & Bieniawski (1990)	189 MPa	28.3 MPa
Hoek & Brown (1997)	596 MPa	326 MPa
O'Neill & Reese (1999)	50 MPa	7.5 MPa
Barton (2002)	1000 MPa	669 MPa
Shen et al. (2012)	8.73 MPa	1.31 MPa
Notes: For comparison, see the below laboratory and in-situ estimates of the fault gouge Young's modulus, which likely represent a lower bound of plausible moduli for this area.		
Laboratory measurements of fault gouge samples	Median 7.6 MPa	Range 4.79 to 20.8 MPa
Four USBR in-situ plate jacking tests (Cohen 1970), legacy values	Mean 4.7 MPa	Std. Dev. 2.1 MPa
USBR in-situ plate jacking tests recalculated values using ISRM (2007) suggested methods	Mean 11 MPa	Std. Dev. 4.9 MPa
Hoskins et al. (1974) in-situ modulus by flat jack testing in the squeeze zone	Approx. 130 MPa	

5.5.2 Second Round of FLAC Modeling: Elastic ISF and SPG Models

Given the results of the inital squeeze zone modeling, the next modeling attempt focused on developing a FLAC FDM with elastic material properties. The author used 50 MC realizations at each of 33 stations along the EJMT pilot bore with recorded leg thrust data. The vertical reaction at the bottom of each support leg (for horseshoe supports) or the bottom corners of the support (for closed-invert supports) was recorded from the equilibrated FLAC model. This reaction most closely matches the leg thrust reported by Robinson et al. (1974), which was taken from load cells installed at those locations.

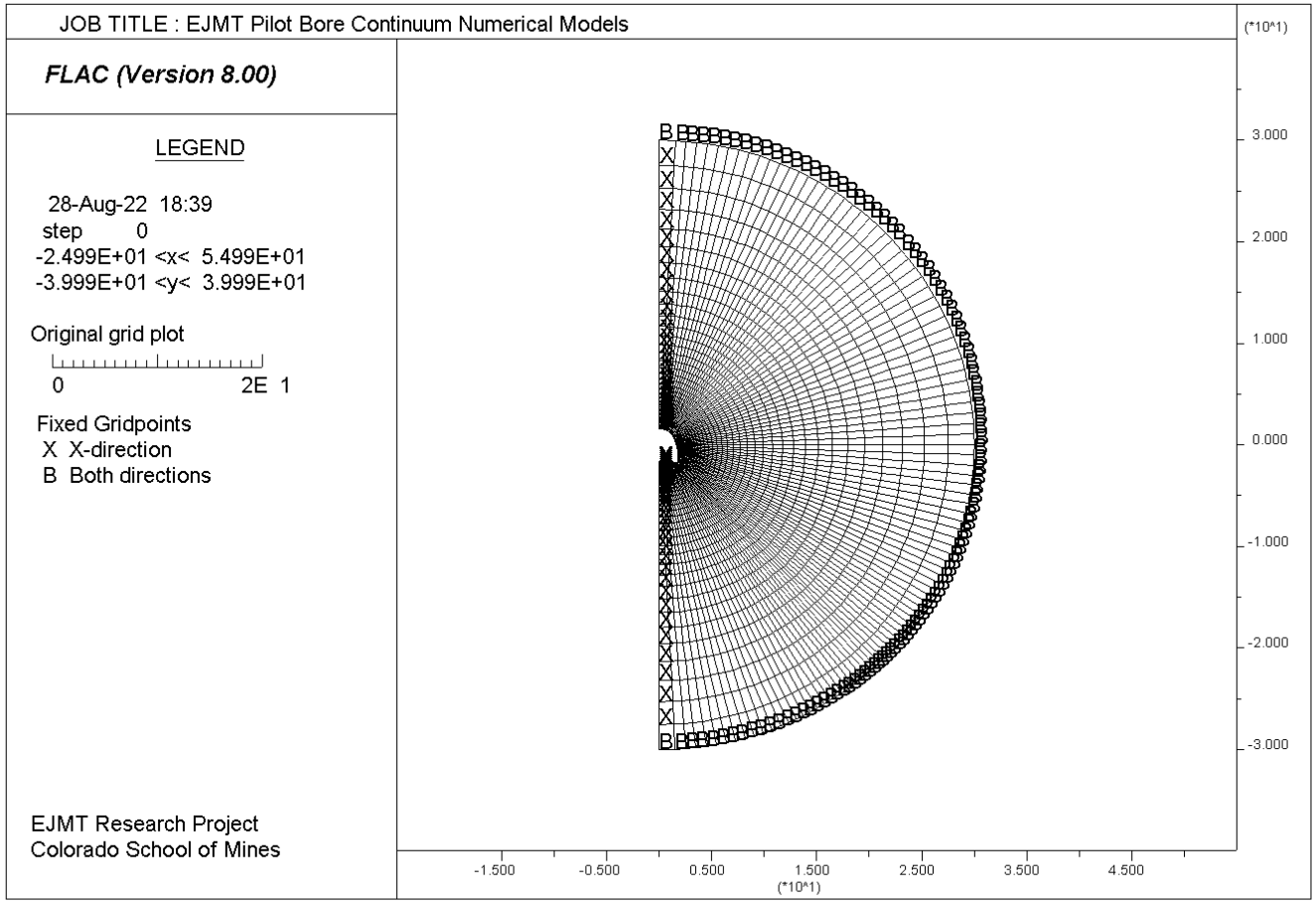

Figure 5.11: Radial meshing used in the elastic and elastic-perfectly-plastic FLAC models of the pilot bore. Axes are in units of meters.

The FLAC model was a radially–meshed model of the right half of the tunnel, taking advantage of the vertical line of symmetry, as shown in Figure 5.11. The mesh size was densest at the tunnel liner and gradually loosened to the model boundary. These boundary conditions, the distance of the model boundary from the tunnel, and the gradation of mesh density were selected by a trial-and-error process to achieve minimal influence of the boundary conditions on the model results.

Boundary conditions were fixed at the distal boundary, horizontally fixed at the line of symmetry, and left free at the tunnel liner. Figure 5.12 shows a typical FLAC output, in this case a plot of deviator stress in the model at the end of one run.

The FLAC model simulated standup time by initially equilibrating the model with an internal stress applied at the tunnel boundary. This internal stress was calculated as some fraction of the initial in-situ field stress. After initial equilibration, the internal stress was removed and the liner was installed. Then the model was run to final equilibrium and the stresses in the tunnel liner were recorded. An example of the plotted tunnel liner axial forces is shown in Figure 5.13.

The factor by which the initial in-situ field stress is multiplied to arrive at the initial internal stress applied to the tunnel boundary is called the standup stress factor. The standup stress factor is bounded between 0 and 1. A standup stress factor of 1 indicates that the liner bears the entire initial in-situ field stress, i.e. no ground relaxation is allowed and the liner is installed instantaneously after the excavation of the tunnel. A standup stress factor of 0 indicates that the liner carries none of the ground load, i.e. the tunnel wall deforms to an equilibrium state before the liner is installed. The actual standup stress factor is somewhere between these two extremes. Calibrating the model by selecting an appoprirate standup stress factor which simulates the actual ground relaxation which occurred during the construction of the pilot bore is one goal of this back analysis.

Figure 5.14 shows the calibration effort which was undertaken by the author. The standup stress factor was varied, a set of Monte Carlo realizations performed, and the agreement of those model results with the available data was evaluated. This process was iterated until the model-data agreement reached an optimum point with respect to the standup stress factor. Initial calibration was carried out using the elastic model for expediency. The plastic model iteration then proceeded from the optimum point of the elastic model, requiring far fewer iterations to achieve its optimum point. The calibrated standup stress factors for the elastic model is 0.22.

Figure 5.15 shows the histogram of leg thrusts from the elastic model as compared to instrument data. The elastic FLAC model has an approximately lognormal, long-tailed distribution that roughly approximates the histogram of the instrument data with an

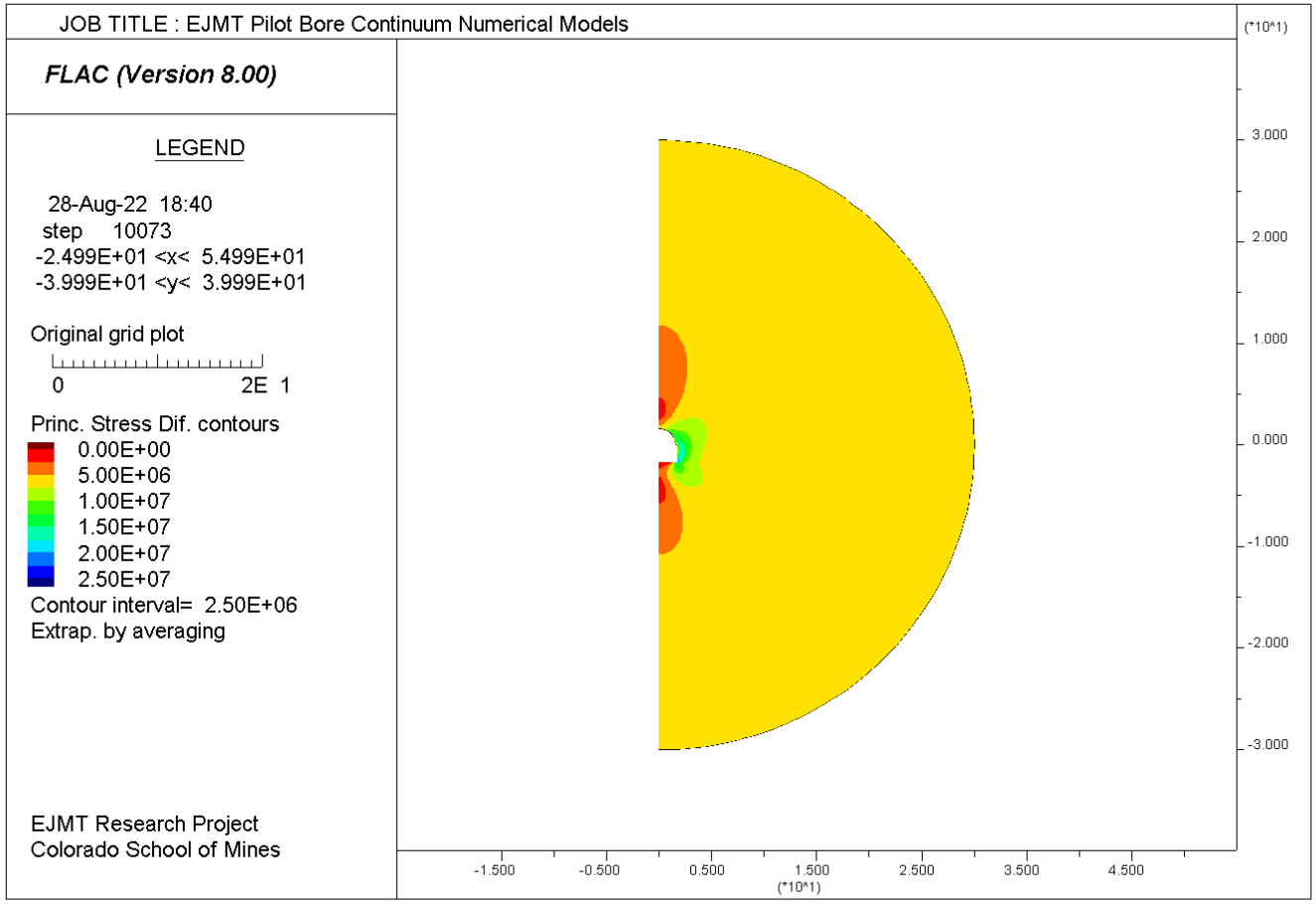

Figure 5.12: Typical FLAC result showing the deviator stress (principal stress difference, $\sigma_1 - \sigma_3$) around the tunnel. Axes are in units of meters. Contours of deviator stress are in units of pascals.

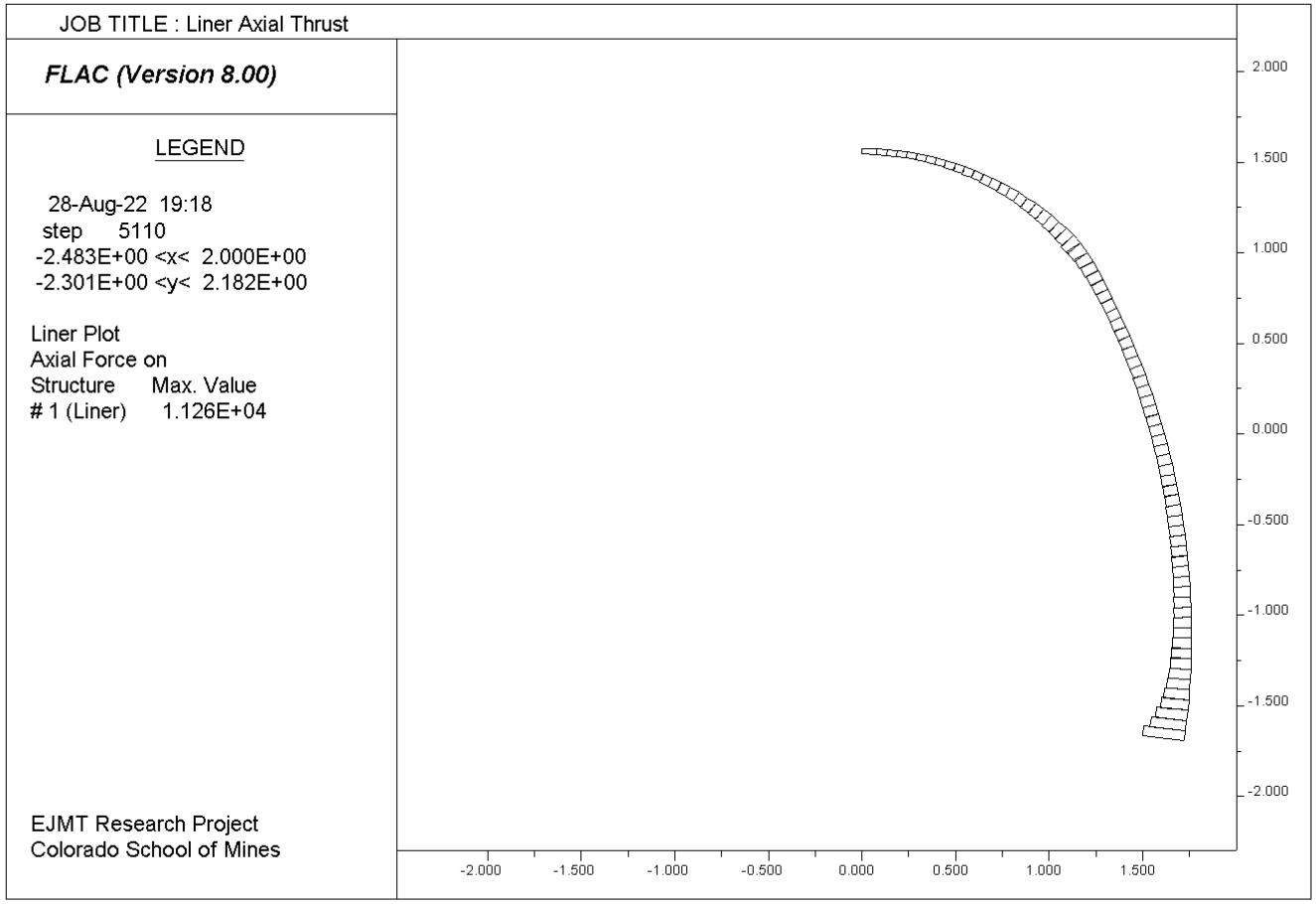

Figure 5.13: Typical FLAC result showing the axial thrust in the tunnel liner. Axes are in units of meters. Forces in units of newtons. Forces plotted on the deformed liner shape without deformation exaggeration.

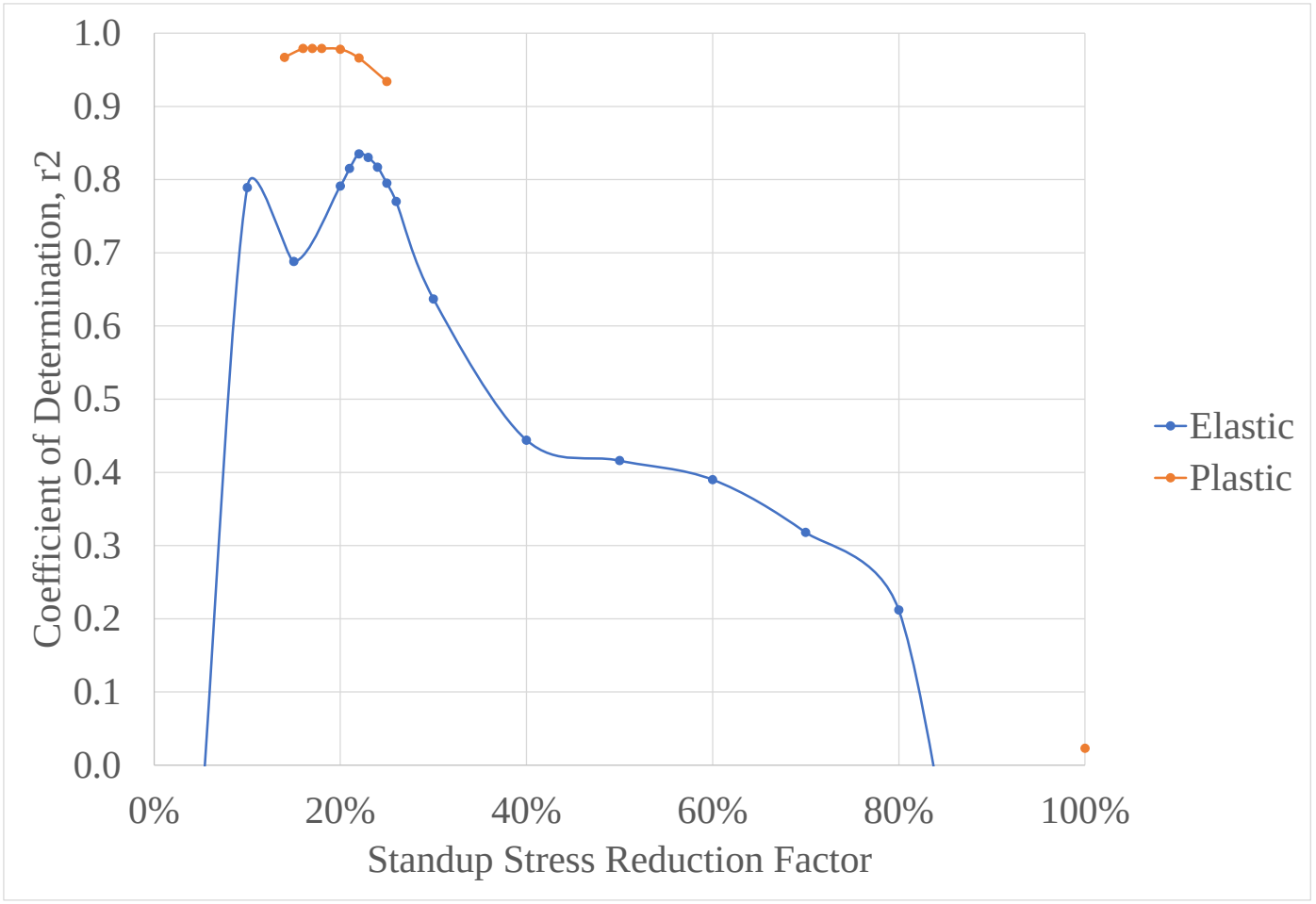

Figure 5.14: Calibration of the standup stress factor in the elastic and elastic-perfectly-plastic numerical models of the EJMT pilot bore.

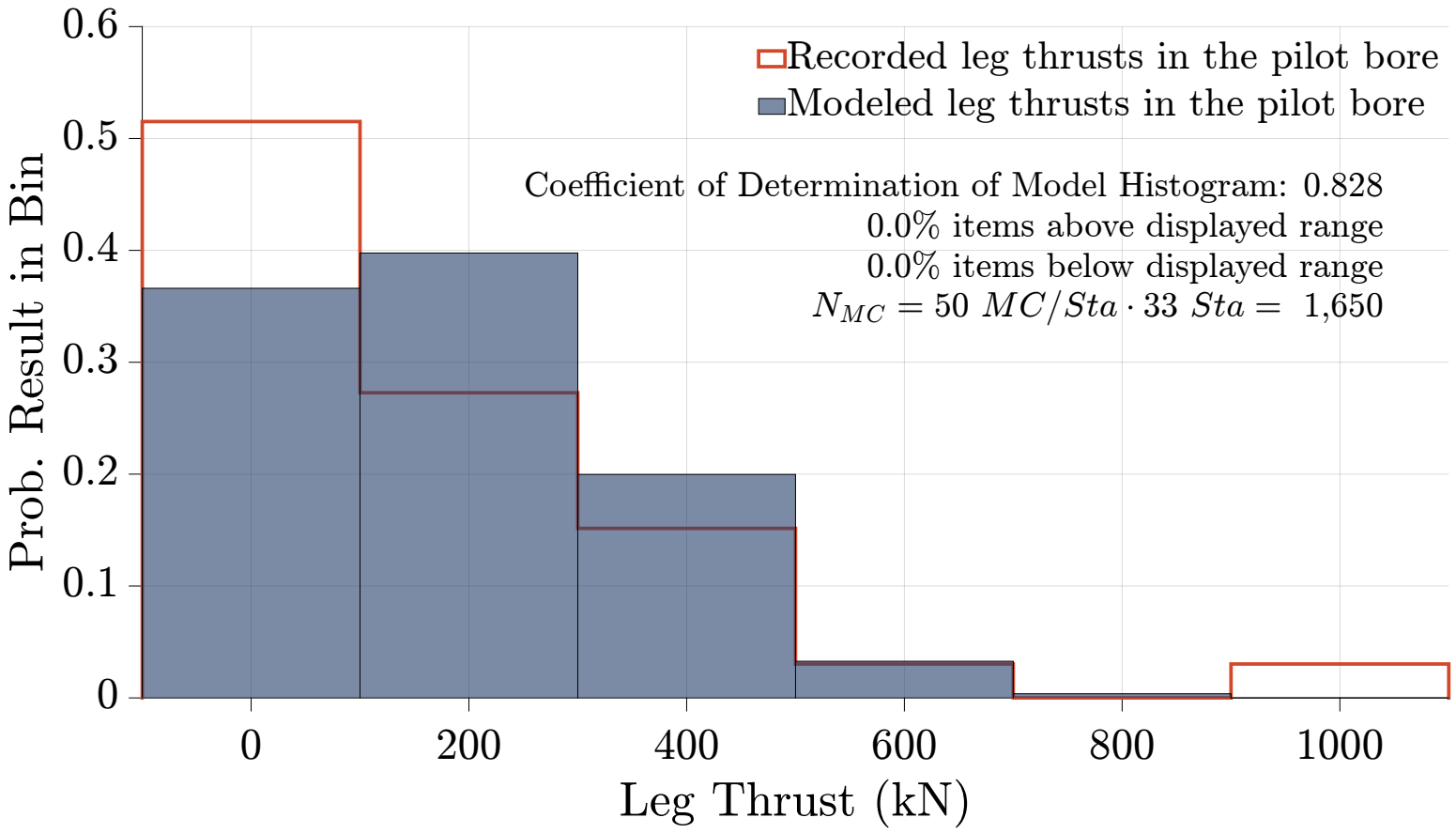

Figure 5.15: Histogram of recorded leg thrust data in the pilot bore (Robinson et al. 1974) vs. histogram of elastic FLAC model leg thrust results.

r^2–value of 0.828.

Figure 5.16 shows the r^2–value of the model histogram to the instrument data versus the number of MC realizations used. Interestingly, the model converges to its ultimate performance very quickly. Beyond approximately 25 MC realizations per station (1650 total MC realizations in the pilot bore) the model does not significantly improve its fit to the instrument data.

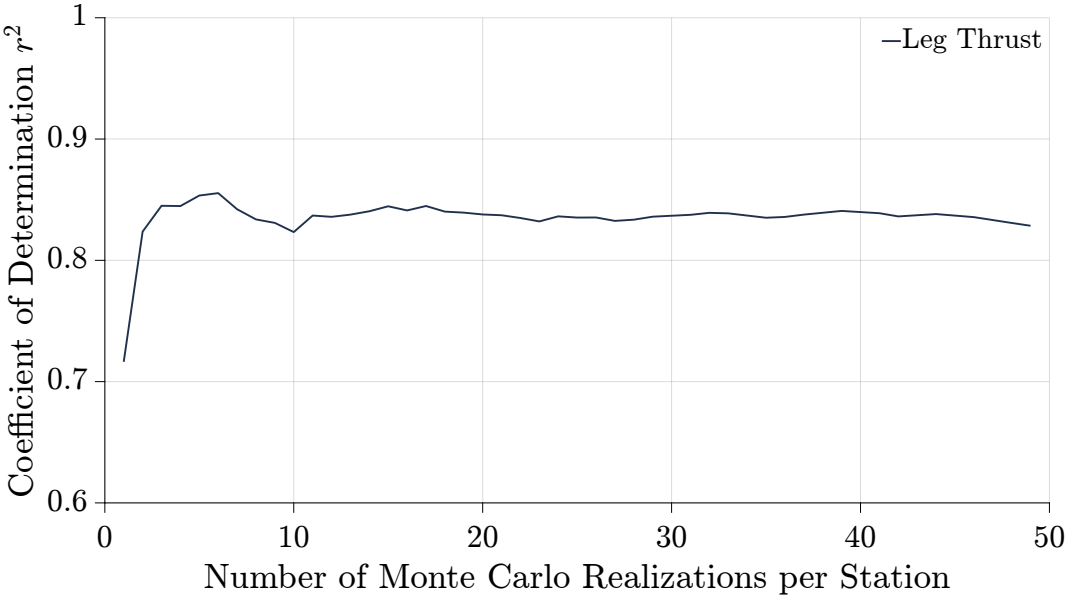

Figure 5.16: Coefficient of determination versus number of Monte Carlo realizations of the elastic FLAC model used. Note that above approximately 25 Monte Carlo realizations the coefficient of determination is essentially constant.

5.5.3 Third Round of FLAC Modeling: Plastic ISF and SPG Models

Following the elastic modeling, the model was refined by the use of elastic-perfectly-plastic properties using a Hoek-Brown strength criterion Hoek and Brown (2018). The Hoek-Brown strength criterion estimates the strength of the rock mass by degradation of intact rock properties. The author used 25 MC realizations at the same 33 stations along the EJMT pilot bore previously evaluated with the elastic model. The standup stress factor was calibrated in a similar fashion to the elastic model. However, the plastic model iteration proceeded from the optimum point of the elastic model, requiring far fewer iterations to achieve its optimum point, as shown in Figure 5.14. The calibrated standup stress factors for the elastic model is 0.17. Figure 5.17 shows the histogram of leg thrusts from the model as compared to instrument data. The FLAC model has an approximately lognormal, long-tailed distribution that approximates the histogram of

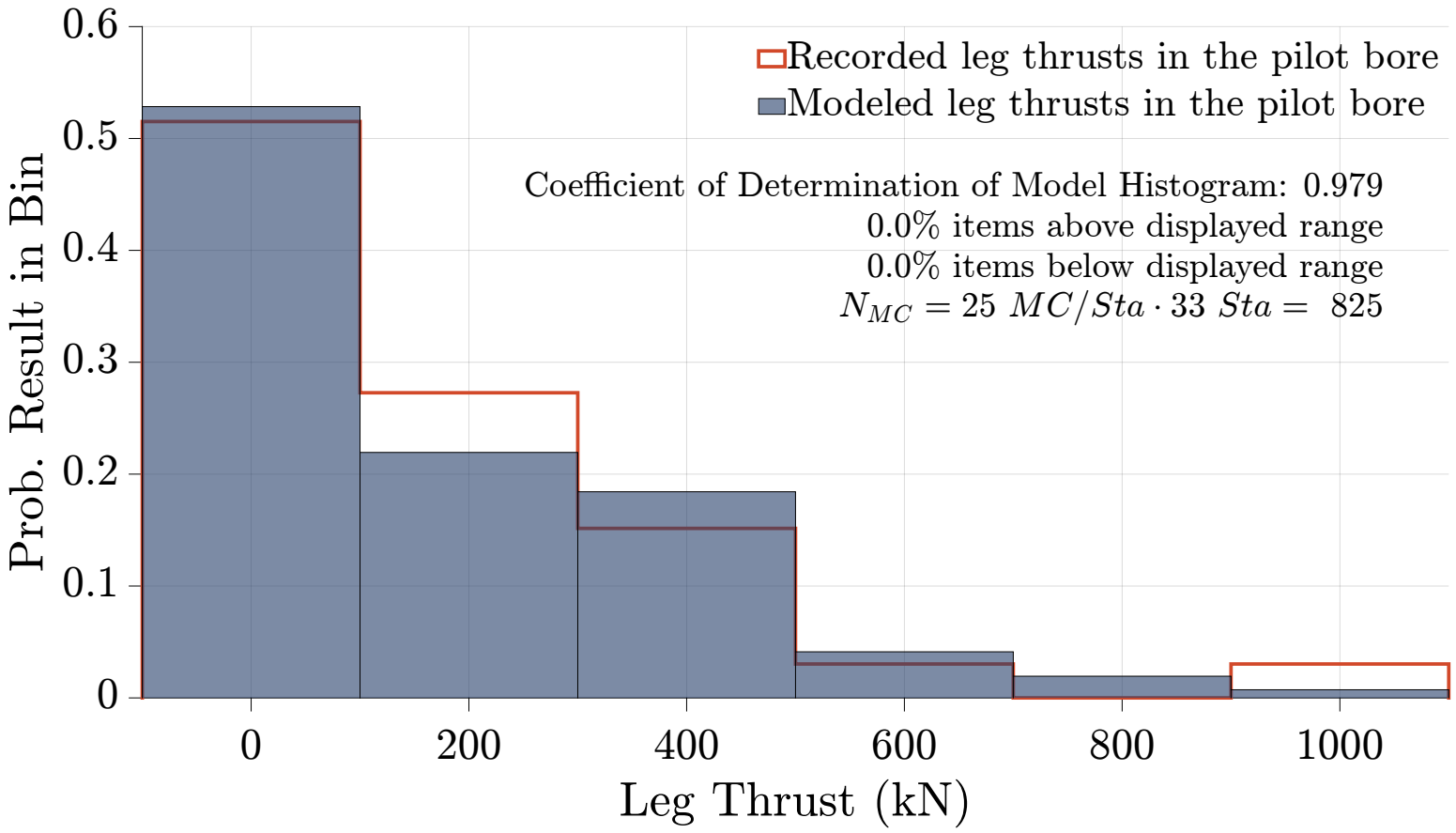

Figure 5.17: Histogram of recorded leg thrust data in the pilot bore (Robinson et al. 1974) vs. histogram of plastic FLAC model leg thrust results.

the instrument data. The fit of the plastic model to the data is better than the elastic model with an r^2–value of 0.979. The plastic FLAC model appears to be correlated to conditions recorded in the EJMT pilot bore and could present a reasonable starting point for estimating conditions likely to be encountered.

Figure 5.18 shows the r^2–value of the plastic model histogram to the instrument data versus the number of MC realizations used. Based on the results from the elastic modeling, 25 MC realizations per station were used for the plastic modeling. As with the elastic model, the plastic model converges rapidly to a fairly constant r^2–value value; 25 MC realizations per station appears to be an acceptable number of realizations.

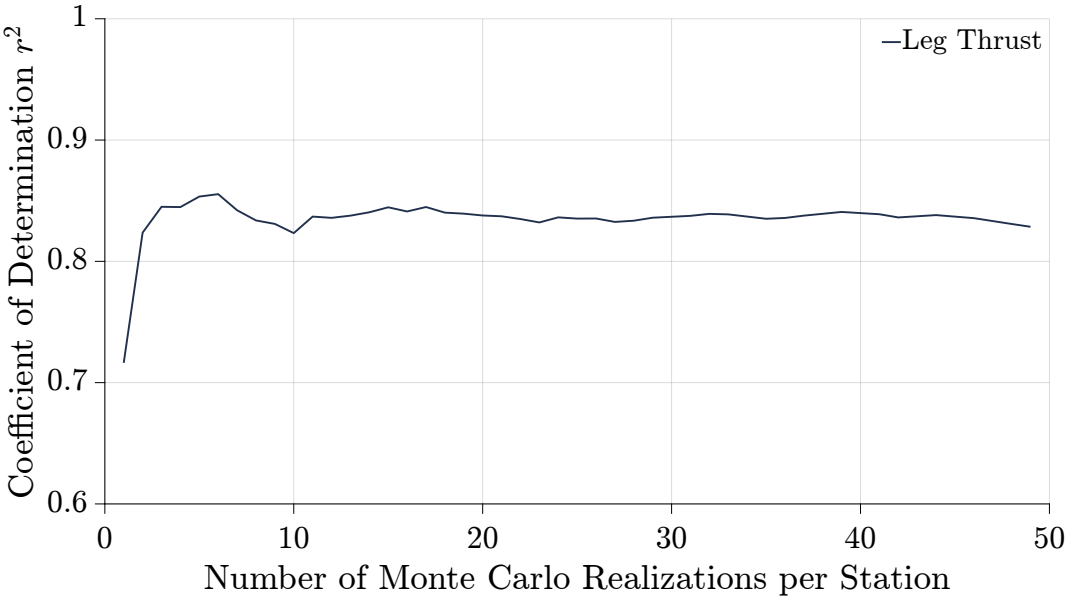

Figure 5.18: Coefficient of determination versus number of Monte Carlo realizations of the plastic FLAC model used.

5.5.4 Discussion of FLAC Model Results

Finite difference models in FLAC using the mechanical properties of the fault gouge show excessive loads and deformations of the tunnel compared to observed loads and deformations, even in the squeeze zones. After determining that modeling using the estimated fault gouge material properties does not reproduce squeeze zone deformation behavior reported in the pilot bore, the author increased the stiffness of the modeled material to determine what properties would replicate the available in-situ data. Material properties which most closely approximate the deformation behavior observed in the tunnel are more in line with typical methods of estimating rock mass strength and deformation parameters by degradation from intact properties using empirical correlations.

This suggests that the fault gouge is not a continuous material which controls the deformation behavior of the rock mass but a material which occurs in bands, pockets, and as joint infilling which contributes to but does not control the overall deformation behavior of the rock mass. The fault gouge represents a lower bound of material properties and is not sufficiently extensive to fully control the load and deformation behavior of the tunnel.

On the other hand, some empirical correlations to rock mass modulus are capable of predicting moduli which reproduce the squeeze zone deformation behavior. Table 5.1 shows the lowest plausible estimates of rock mass modulus by various empirical correlations for the SPG and ISF. Figure 5.10 shows the box-and-whisker plots of the empirical modulus estimates. Most of the empirical estimates in Table 5.1 and Figure 5.10 are well above the required Young's modulus for the elastic model to begin to approximate the deformation behavior of the squeeze zone (38 MPa). However, the worst plausible deformation modulus estimates by some empirical correlations are in this vicinity. The lower bound modulus estimates by Shen et al. (2012) and O'Neill and Reese (1999) match the rock mass modulus estimated by FLAC back analysis through the squeeze zone. The correlation of Nicholson and Bieniawski (1990) is also reasonable for the ISF, but not the SPG.

The FLAC models appear to be reasonably predicting thrust across the invert of the tunnel lining. The magnitude and range of the FLAC results roughly correlates with the available data. However, there are insufficient invert thrust data to make a full comparison between the results of the models and the recorded data. Figure 5.19 shows the available data compared to the model results. Note that the r^2–value is very low; it is this author's opinion that this r^2–value is inaccurate in this case because of a lack of instrumentation data to fill out the histogram.

The modeled crown deflections do not agree well with the available instrumentation data. The FLAC models predict approximately 0 to 50 mm of crown deflection into the tunnel. Actual crown deflections ranged from 27 mm into the tunnel to 14 mm out of the tunnel. None of the FLAC models show egging behavior, i.e., the crown moving up as the walls move in. Such behavior was recorded in some stations in the pilot bore squeeze zone. Figure 5.20 shows the available data compared to the model results.

The FLAC models are generally underpredicting horizontal convergence by approximately 1 order of magnitude. The FLAC models predict from approximately 55 mm of horizontal convergence to 23 mm of widening. Actual horizontal convergences ranged from approximately 550 mm into the tunnel to 180 mm out of the tunnel. Figure 5.21 shows the available data compared to the model results.

In general, it is expected that a continuum model will underpredict deformations when

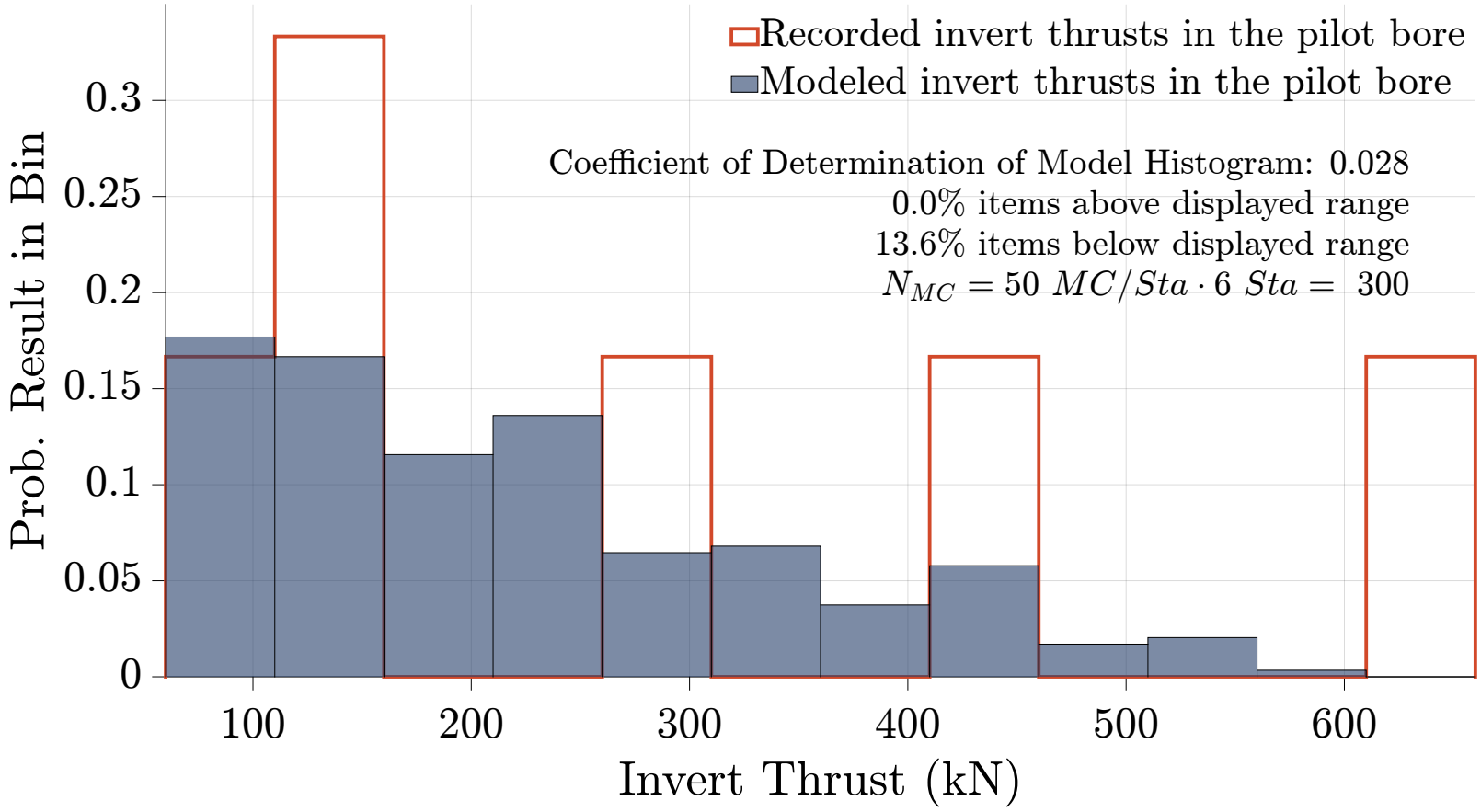

Figure 5.19: Histogram of recorded invert thrust data in the pilot bore (Robinson et al. 1974) vs. histogram of plastic FLAC model invert thrust results.

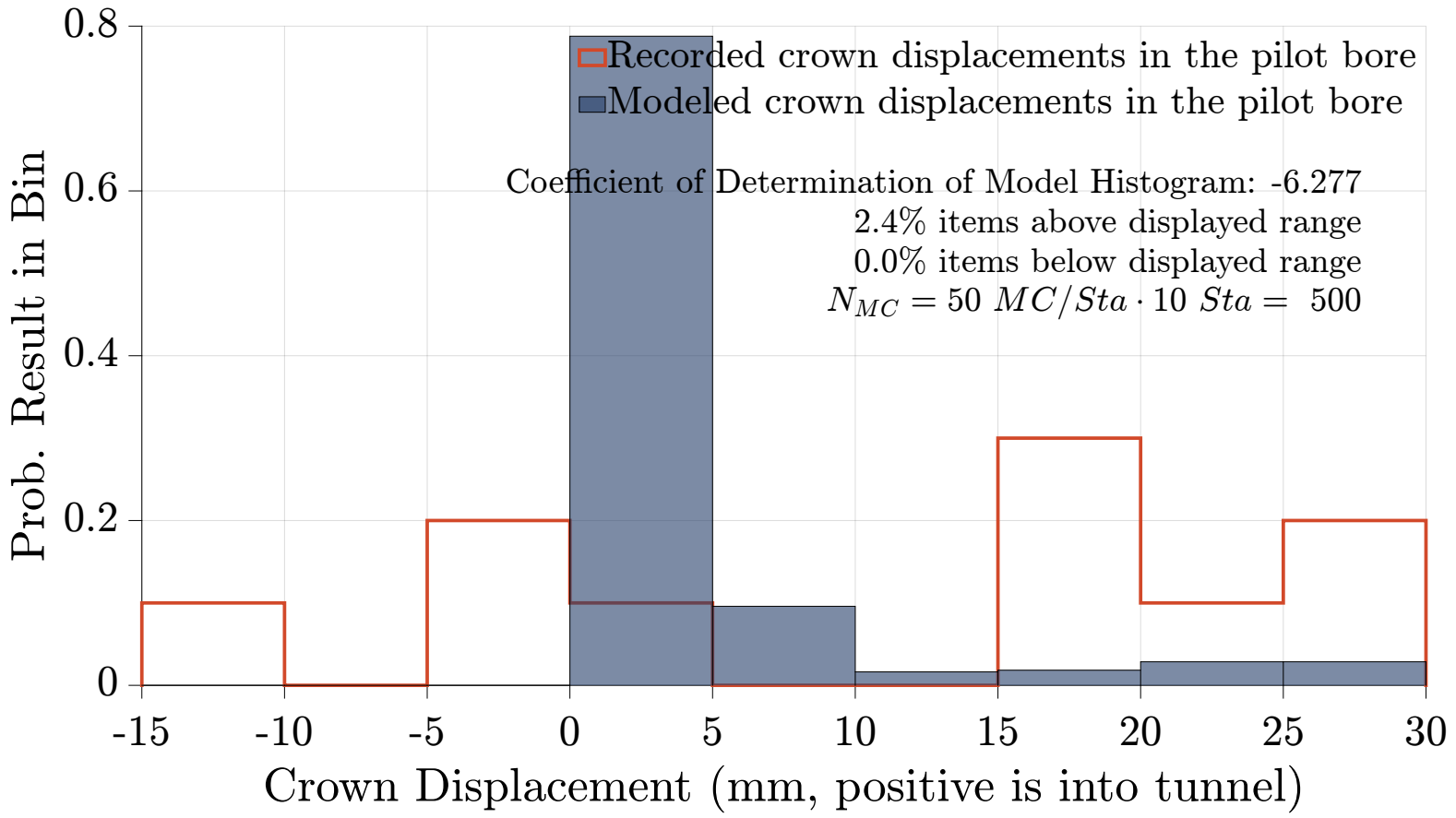

Figure 5.20: Histogram of recorded crown displacement data in the pilot bore (Robinson et al. 1974) vs. histogram of plastic FLAC model crown displacement results.

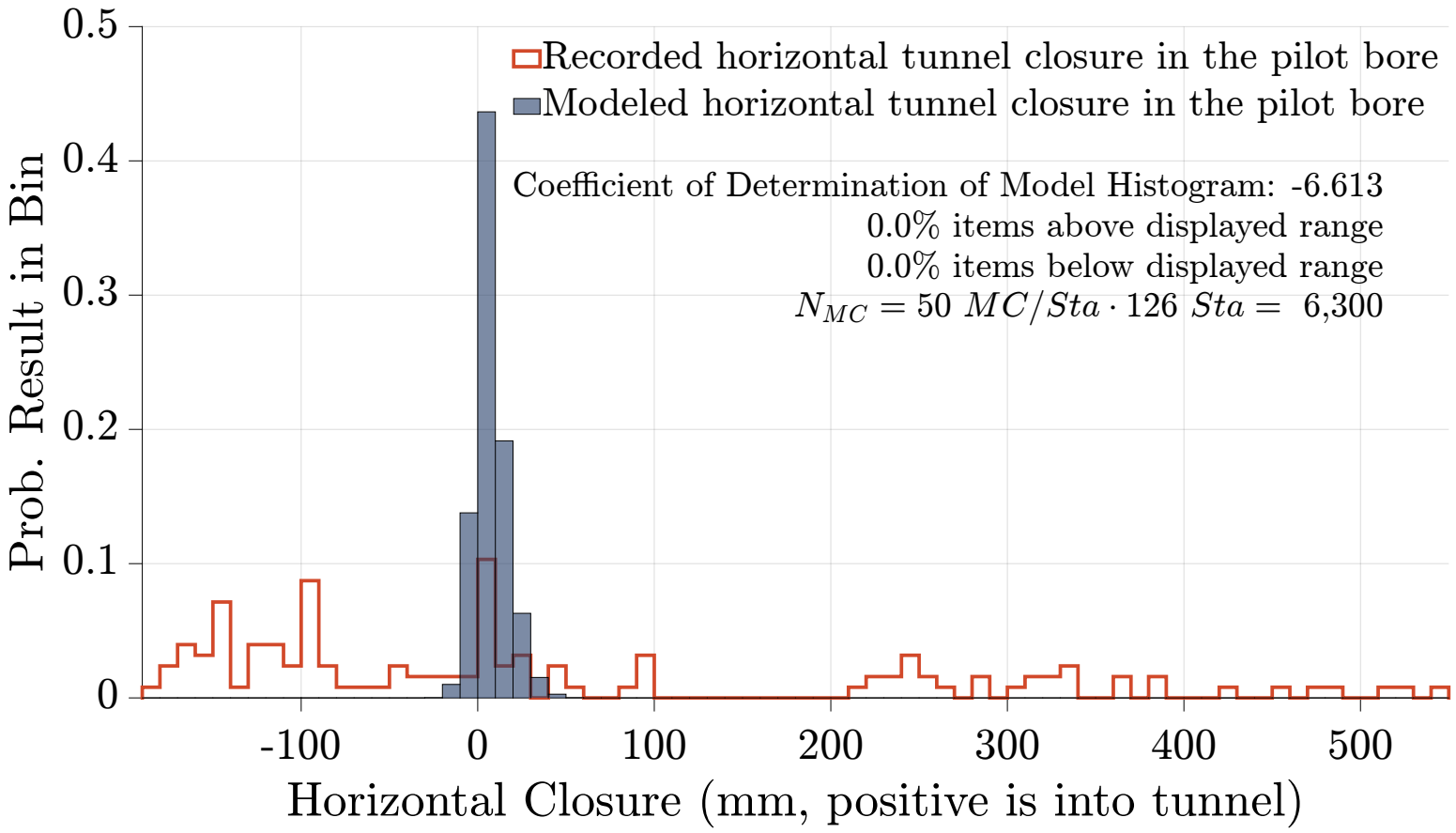

Figure 5.21: Histogram of recorded horizontal convergence data in the pilot bore (Robinson et al. 1974) vs. histogram of plastic FLAC model horizontal convergence results.

compared to an actual rock mass which may have significant deformation along discrete joints. This suggests that a calibrated GRC might significantly improve the FLAC model. Unfortunately, there are not sufficient coupled load-deformation data from the EJMT to calibrate such a curve.

The results of the elastic and plastic model results are substantially similar. However, there is a significant improvement in accuracy by using an elastic-perfectly-plastic model. In addition, the more complex model is only slightly more computationally expensive, and still fast enough to be useful for the purposes of this research project.

5.6 Summary and Conclusions

This chapter presents a back analysis of the EJMT pilot bore, constructed in the 1960's, to develop and calibrate a numerical model which approximates the load and deformation behavior of the original construction. This numerical model will be used for forward modeling of new potential bores adjacent to the existing bores. The outputs from the forward modeling (Chapter 6) will validate the alignment optimization effort (Chapter 4).

In the absence of sufficient data to define a ground reaction curve for the EJMT pilot bore, the author developed a function to estimate the active rock mass height above the instrumented EJMT pilot bore stations by correlation to RMR_{14}. This function is intended for use with various analytical solutions which estimate the stresses in the tunnel lining based on applied ground loads, e.g. the convergence-confinement method.

An initial FLAC FDM using the fault gouge material properties through the squeeze zone showed that the gross material properties of the rock mass in this zone are not controlled by the fault gouge. Properties of the intact SPG and ISF reduced via empirical correlations more closely approximate the behavior of the rock mass than properties of the fault gouge. This chapter presents elastic and elastic-perfectly-plastic FLAC finite-difference modeling of the EJMT pilot bore. The elastic FLAC model did an adequate job reproducing the available leg thrust data from the construction of the pilot bore, achieving an r^2–value of 0.828. The model was then refined to an elastic-perfectly-plastic model using a Hoek-Brown strength criterion. This plastic model did an excellent job reproducing the range and variability of the leg thrust data, achieving an r^2–value of 0.979. In addition, the modeled invert thrusts appear to reasonably approximate the limited available invert thrust data from the pilot bore. The elastic-perfectly-plastic model is not accurately reproducing the deformations recorded in the pilot bore, however, the model may still be satisfactory for the purposes of this research

project. By comparing the change in the r^2–value to the number of MC realizations used per station the author has demonstrated that 25 MC realizations per station adequately simulates the distribution of pilot bore leg thrust data. This model, combined with 25 MC realizations per station, also has an adequately efficient run time, completing a batch of runs in less than 1 day. This makes this modeling solution suitable for forward modeling and MC simulation of potential future bores adjacent to the existing EJMT.

CHAPTER 6

MONTE CARLO SIMULATION WITH A FINITE DIFFERENCE MODEL FOR RAPID COMPARISON OF TUNNEL ALIGNMENT ALTERNATIVES

Using the three-dimensional (3D) implicit geologic model from Chapter 3, candidate alignments identified in Chapter 4, and the calibrated finite difference model from Chapter 5, this chapter presents models of possible alignments adjacent to the existing Eisenhower-Johnson Memorial Tunnel (EJMT) and compares their performance. The authors made preliminary estimates of required tunnel supports via the rock mass rating (RMR) and rock mass quality index (Q) systems. Each tunnel support system is tested at intervals along each possible tunnel alignment using Monte Carlo (MC) simulation of ground properties based on the 3D probabilistic implicit geologic model developed in Chapter 3. Results of the numerical modeling effort demonstrate the feasibility and effectiveness of large-scale 3D implicit geologic modeling, validate the previously developed alignment optimization algorithm, and provide interesting insights into the Q and RMR systems when used as empirical design heuristics.

6.1 Introduction

In this chapter, the author evaluates seven plausible new alignments adjacent to the existing EJMT on Interstate 70 (I-70) in Colorado's Rocky Mountains. Colorado Department of Transportation (CDOT) is interested in potentially adding new bores adjacent to the existing bores to relieve traffic congestion, as well as possibly adding multi-modal transportation options along the I-70 corridor. Chapter 3 presented a 3D implicit geologic model which captures variable uncertainty via low, most likely, and high estimates of each engineering geologic parameter modeled. In Chapter 4 seven candidate alignments were selected through the geologic model using a multi-objective optimization (Pareto optimization) strategy. In Chapter 5 the author developed an efficient numerical model and calibrated it to the EJMT vicinity via data from the 1960's-era EJMT pilot bore. In this chapter, the calibrated numerical model is applied to each of the candidate alignments

using Monte Carlo-simulated parameters from the geologic model.

The objective of the forward modeling presented in this chapter is to evaluate a group of possible new tunnel alignments for the EJMT and to compare their effectiveness relative to each other. The modeling does not provide specific designs of the new tunnel bore but is conducted to determine if potential tunnel designs can influence new tunnel alignments. It is generally assumed that the epistemic uncertainty inherent in the model developed in Chapter 5 is uniformly distributed across all variables and conditions. Thus, even though further refinement to the model may be possible, and could improve the model's accuracy, the current model can serve as a benchmark for evaluating the relative value of each of the plausible alternatives modeled.

A secondary goal of this modeling effort is to compare the Q–based (NGI 2015) and RMR–based (Lowson and Bieniawski 2013) empirical tunnel support design systems via the finite difference method (FDM) model to validate their effectiveness. Using classic axial-moment interaction equations for reinforced concrete members, the performance of each empirical tunnel lining design method (RMR and Q) was evaluated at each station for 100 Monte Carlo realizations. The overall reliability of each system was found to be fairly high, though the Q system performed slightly better for all seven alignments evaluated.

6.2 Methodology

For a detailed description of the FDM model employed in the forward modeling, see Chapter 5. In short, the model uses the FDM as implemented in Fast Lagrangian Analysis of Continua (FLAC), a commercially available modeling software widely used in geotechnical engineering.

The elastic parameters of the rock mass at a given station, Young's modulus and Poisson's ratio, are based on values estimated from intact material parameters by correlation to rock mass classifications. Six empirical rock mass modulus correlations were averaged together for each Monte Carlo realization, including:

1. Serafim and Pereira (1983)
2. Nicholson and Bieniawski (1990)
3. Hoek and Brown (1997)
4. O'Neill and Reese (1999)
5. Barton (2002)
6. Shen et al. (2012)

The FLAC model is a radially–meshed model of the right half of the tunnel, taking

advantage of the vertical line of symmetry, as shown in Figure 5.11. The mesh size is densest at the tunnel liner and gradually loosens to the model boundary. Boundary conditions are fixed at the distal boundary, horizontally fixed at the line of symmetry, and left free at the tunnel liner. These boundary conditions, the distance of the model boundary from the tunnel, and the gradation of mesh density were selected by a trial-and-error process to achieve minimal influence of the boundary conditions on the model results.

The FLAC model simulates standup time by initially equilibrating the model with an internal stress applied at the tunnel boundary. This internal stress is calculated as some fraction of the initial in-situ field stress. The value by which initial in-situ stresses are multiplied to arrive at the internal stress used during the standup period is termed the standup stress factor. After initial equilibration, the internal stress is removed and the liner is installed. Then the model is run to final equilibrium and the stresses in the tunnel liner are recorded. The calibrated standup stress factor used for the plastic model in this chapter is 0.17. Figure 5.14 shows the calibration effort which was undertaken by the author. The calibration of the numerical model by back analysis is described in more detail in Chapter 5.

Post-yield, the behavior of the rock mass is governed by an elastic-perfectly-plastic model. The yield criterion used here is that defined by Hoek and Brown Hoek and Brown (2018). The Hoek-Brown strength criterion estimates the strength of the rock mass by degradation of intact rock properties.

The tunnel support elements are modeled in FLAC as liner elements. The elastic mechanical behavior of an individual element between two nodes is defined by the classical Euler-Bernoulli beam theory. The post-yield behavior of a liner element is handled by an elastic-perfectly-plastic model in FLAC.

Further assumptions used in the forward modeling:

1. The ground surrounding the tunnel is continuous, homogeneous, and isotropic. The ground behaves in a linear elastic fashion up to its yeild strength, as determined by the Hoek-Brown strength criterion. Post-plastic behavior is constant and unbounded, i.e an elastic-perfectly-plastic material.
2. Combined loading is calculated by superposition, assuming elastic member behavior. Axial forces, bending moments, and transverse shears do not affect each other.
3. Bolt tensile strength was assumed to be 250 kN. Note that bolt strength is an input to the RMR-based design but is not an input to the Q-based empirical design system. The Q-system is largely based on 20 mm bolts, which typically have a tensile strength in the 150-200 kN range. Bolts with a 250 kN tensile capacity are

more commonly 25 mm in diameter.

4. Shotcrete compressive strength was assumed to be 28 MPa (approximately 4000 psi). This value is an input to both the Q and RMR design systems.
5. 25 Monte Carlo realizations were run at each station along each alignment. Back analysis calibration showed that 25 MC realizations per station was generally sufficient to achieve maximum model accuracy.
6. A 10–m diameter circular tunnel was assumed for this analysis.
7. Steel was assumed to have Young's modulus of 200 GPa and a yield strength of 420 MPa (approximately 60 ksi).
8. The liner was discretized into 100 nodes around the full circumference of the circular liner.

Support requirements were estimated for each station and MC realization along each alignment of the forward models based on the recommendations of NGI (2015) and Lowson and Bieniawski (2013).

The effect of rock bolts on rock mass modulus was addressed via the homogenization approach. In this technique, an equivalent continuum material is modeled in place of a rock mass with explicit bolt elements. To date, the homogenization approach has typically focused on estimating equivalent strength, rather than stiffness, of the rock mass (Indraratna and Kaiser 1990; Osgoui and Oreste 2010). The equivalent reinforced rock mass deformation modulus has typically been modeled simply as equivalent to the unreinforced rock mass deformation modulus, but with increased yield strength.

However, Nguyen et al. (2018) derived an explicit equation for the increase in ground stiffness as a function of the rock bolt pattern based on an assumed elastic composite action of the bolt, grout, and ground. Although these simplifying assumptions certainly introduce some error to the solution, they are in keeping with the simplifying assumptions already made in generating the FDM. Note that the Nguyen et al. (2018) formulation models the increase in ground stiffness as a decreasing function from the excavation surface to the end of the bolt. For the purposes of application to the beam-spring model, the mean value along the bolt was used.

Bolt length, bolt pattern spacing, and shotcrete thickness for each MC simulation were adopted based on the recommendations of the Q and RMR systems. Ground stiffness was then estimated based on the recommended bolt parameters using the composite ground stiffness model of Nguyen et al. (2018).

The FDM model with parameters based on the Q and RMR systems was then run for each of the seven best alignments identified by the alignment optimization algorithm developed in Chapter 4. Alignments were discretized at 20 m intervals and 25 Monte Carlo

realizations were evaluated at each interval.

ACI (2016) gives the default strength of shotcrete as 28 MPa (4000 psi); this strength was assumed for the shotcrete strength in the liner, regardless of energy absorption rating. ACI (2016) states that "the modulus of elasticity, and the density of shotcrete are equivalent to that of conventional cast-in-place concrete". Therefore, it was assumed that Young's modulus of the shotcrete can be calculated based on ACI (2019) equation 19.2.2.1.b, restated here as Equation 6.1. For 4000 psi shotcrete, this gives Young's modulus of 3,600 ksi or 24.9 GPa.

$$E = 57000 \cdot \sqrt{f'_c} \quad \text{pounds per square inch (psi)} \tag{6.1}$$

where E is Young's modulus of the concrete and f'_c is compressive strength of the concrete.

The overburden pressure transmitted to the liner was not directly reduced because of the installation of rock bolts. In theory, rock bolts should create a reinforced ground arch and thus the effective active overburden height bearing on the liner would be less than without the rock bolts. Instead, the increased ground stiffness should allow additional load-shedding, or arch-forming action, to transfer load within the FDM model away from the tunnel. This arch-forming action is implicit in the FDM. The magnitude of the arch-forming action, and thus the reduction in active overburden height, has not been direclty investigated or quantified in this study.

The tensile strength of the plain shotcrete liner is a required input to the model. However, tensile strength of concrete is a topic of significant debate. ACI (2019) contains a rupture modulus, but not a direct tension strength. These are not fundamentally the same thing, as the modulus of rupture is specifically for strength of plain concrete beams in bending. The values in Table 6.1 are available in the literature for estimating concrete tensile strength. This study assumes the ACI (2019) modulus of rupture correlation as the tensile strength of concrete because tension in the liner is primarily developed due to bending.

The grout used for grouting the rock bolts was assumed to have a strength of 34 MPa (5000 psi) and Young's modulus of 28 GPa ($4{\cdot}10^6$ psi).

For the NGI (2015) reinforced rib design recommendations the reinforced ribs can be thought of as T-beams in flexure for the purposes of this analysis. In all of the NGI (2015) recommended configurations, the effective flange width per (ACI 2019) is less than the rib spacing.

Liner rupture was defined as 0.3% strain, a typical assumption for the failure strain

Table 6.1: Correlations between compressive and tensile strength of concrete from literature.

Equation	Tensile Strength of 28 MPa (4000 psi) Concrete	Source
$0.08 \cdot f'_c$	320	McCormac and Brown (2014)
$0.10 \cdot f'_c$	400	McCormac and Brown (2014)
$0.15 \cdot f'_c$	600	McCormac and Brown (2014)
$7.5 \cdot \sqrt{f'_c}$	474	ACI (2019) (note that this is $0.7 \cdot \sqrt{f_c}$ for f_c in MPa
$1.7 \cdot f_c^{'2/3}$	428	Raphael (1984) static tensile strength
$2.6 \cdot f_c^{'2/3}$ to $3.4 \cdot f_c^{'2/3}$	655 to 857	Raphael (1984) apparent seismic tensile strength
$2.3 \cdot f_c^{'2/3}$	580	Raphael (1984) apparent static tensile strength (recommended for finite element modeling)

of concrete or shotcrete. This strain level was used to define the ultimate strength of the liner. Note that fiber reinforced shotcrete commonly has a more ductile strain softening behavior post-failure than typical concrete. The 0.3% strain level would be indicative of cracking, but not necessarily collapse failure. Depending upon the desired definition of "failure" of the liner, some cracking may be acceptable and a strain of 0.3% may be overly conservative.

Seven alignments were selected for modeling adjacent to the existing EJMT. The alignments were selected based on an alignment optimization algorithm as discussed in Chapter 4. Several optimization parameters were considered. The seven alignments selected for modeling were the highest ranked options by one or more parameters.

6.3 Results

The factor of safety against failure of a given MC realization was calculated based on the interaction of modeled axial and moment loads as well as the interaction of modeled axial and shear loads. Axial-moment interaction reliability was calculated based on standard methods of calculating this failure mode for concrete beam-columns (e.g., ACI

(2019) or McCormac and Brown (2014)). Note that most of the nodes of a liner may be within the diagram, but if even a few (or one) are outside of the axial-moment interaction diagram, the liner may be considered to have failed (depending upon the definition of failure).

Loads were tracked in the liner at the crown and springline of each model. The axial-moment and axial-shear interaction diagrams plot as a quadrilateral in axial force-bending moment or axial force-shear force space. A given set of liner loads plots as a point on this diagram. Thus, there are 2 points on each interaction diagram representing the crown and springline liner loads for a given MC realization at a given station along a given alignment. For each of these points, the capacity can be calculated as the distance from the origin to the failure envelope which passes through the axial-moment point. The demand is the distance from the origin to the calculated axial and moment loads in the liner. Capacity divided by demand is the classical definition of a factor of safety. Thus, a factor of safety can be calculated for each alignment, station, and MC realization at both the crown and springline, which are typically the critical points in the design.

Figure 6.1 and Figure 6.2 show interaction diagrams for two example Monte Carlo realizations along alignment 5448. Note that the moment and shear loads in each case are very small as compared to the axial loads. This is typical of the design outputs in this case, and an expected result. In an ideal uniform biaxial stress field, the stresses around a circular opening become purely axial. Although this case is not ideal, the stresses in the liner do tend to be dominated by axial thrust and not bending moment or shear.

Figure 6.1 has been selected to show a case with a factor of safety near 1. The blue dot, indicating the loads at the springline, controls the minimum factor of safety. In general, loads at the springline are the critical case for liner design in this study.

Figure 6.2 has been selected to show a case with a factor of safety less than 1. In these cases, the modeled loads plot outside the interaction diagram polygon. This is also an unusual realization in which the modeled bending moment in the liner has a significant magnitude.

Once the factor of safety has been calculated for each MC realization the reliability of the design can be estimated from the cumulative distribution function (CDF) of the factor of safety. For a desired factor of safety, the reliability of the design is simply the value of the CDF at that factor of safety. This can also be thought of as the integral of the probability density function (PDF) from $FS = \infty$ to the desired factor of safety, or one minus the integral of the PDF from $FS = 0$ to the desired factor of safety. Figure 6.3 shows the calculated design reliability for each modeled alignment for designs as suggested by both the Q and RMR systems. Note that the RMR-based designs have reliabilities

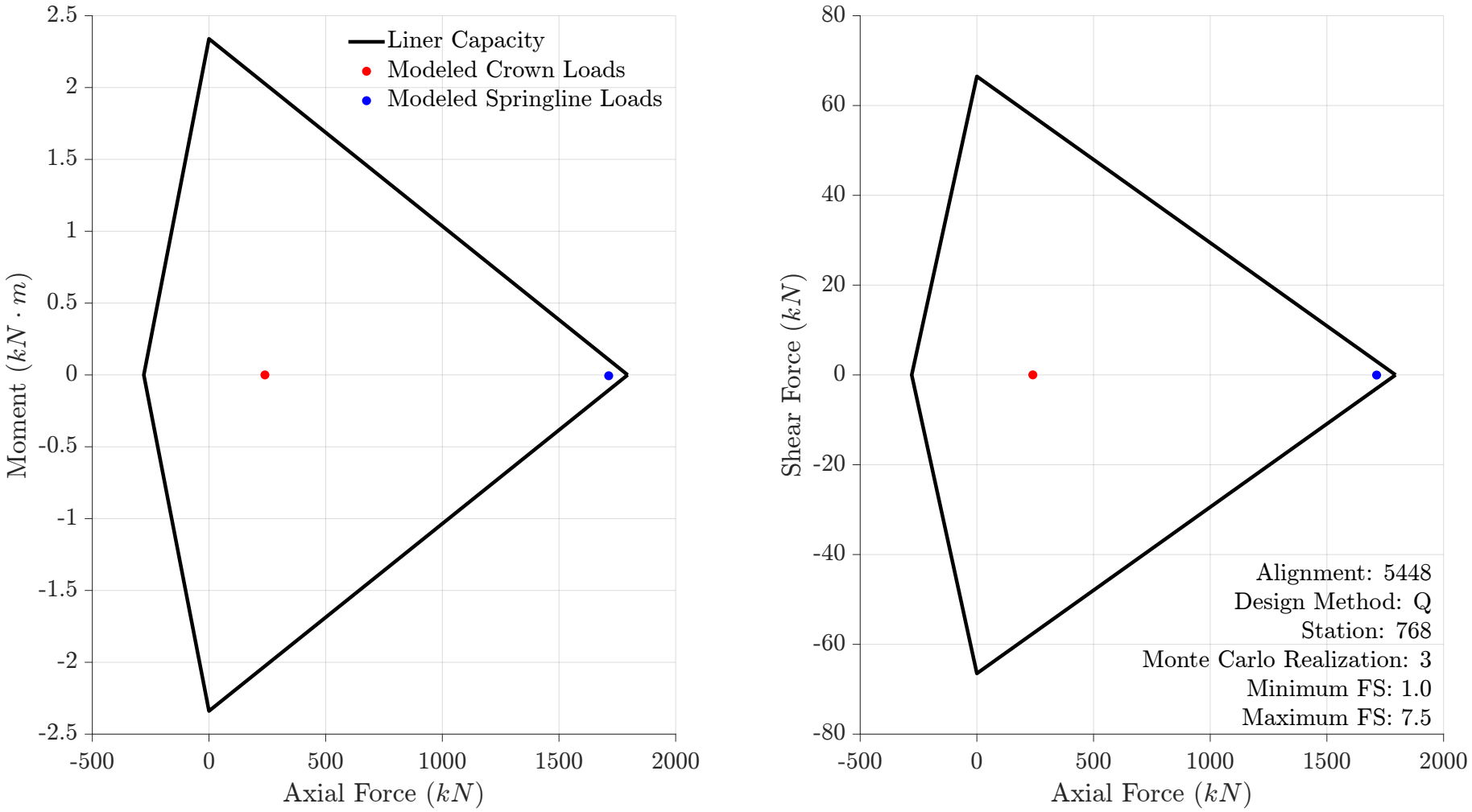

Figure 6.1: Calculated axial, moment and shear loads at the crown and springline plotted versus liner capacity for one Monte Carlo realizations of alignment 5448 at Station 7+68. Tunnel lining design for this model estimated using the Q-system. Left figure is axial-moment interaction. Right figure is axial-shear interaction.

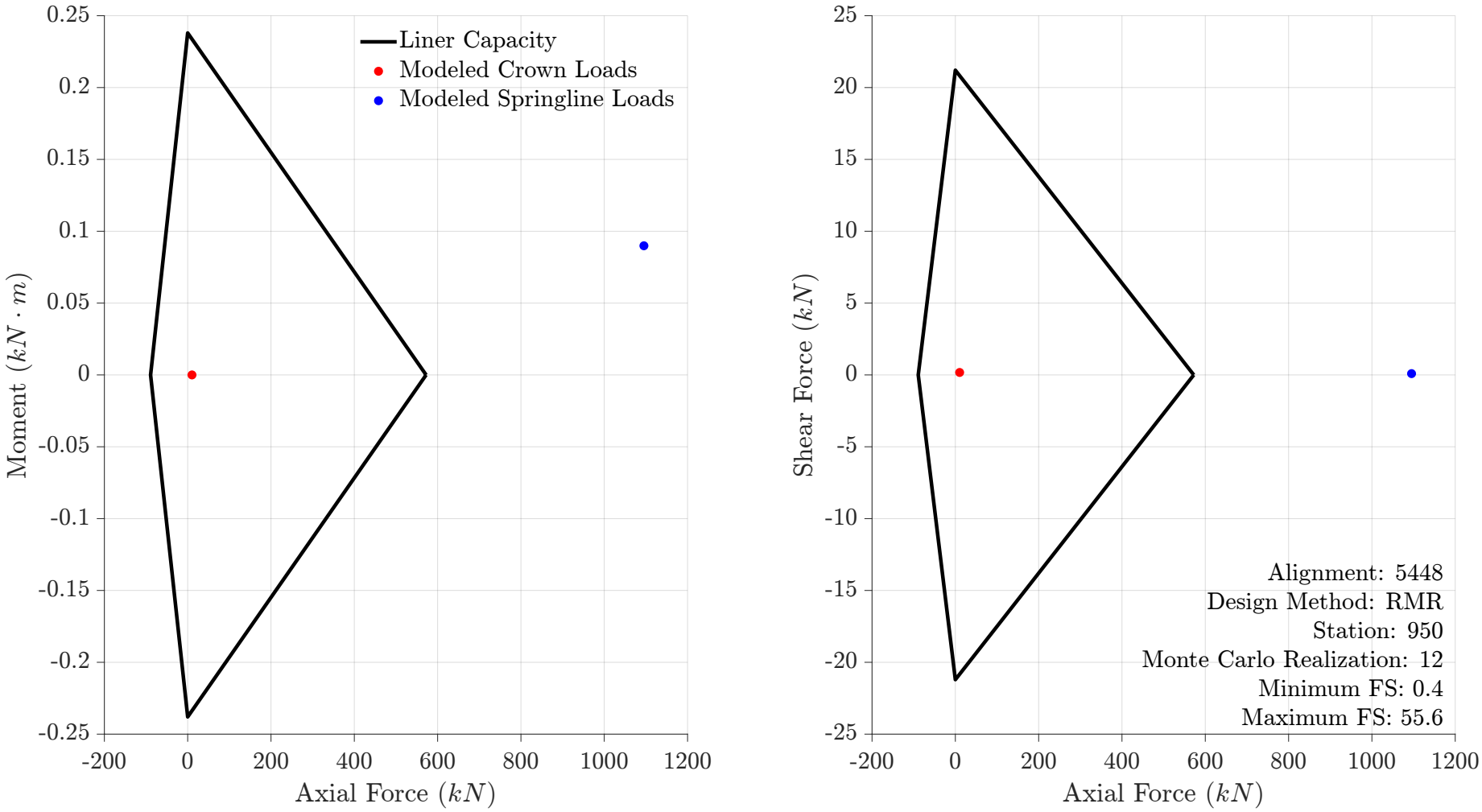

Figure 6.2: Calculated axial, moment and shear loads at the crown and springline plotted versus liner capacity for one Monte Carlo realizations of alignment 5448 at Station 9+50. Tunnel lining design for this model estimated using the RMR-system. Left figure is axial-moment interaction. Right figure is axial-shear interaction.

which being to drop off closer to a factor of safety of 1, and tend to decline more quickly at higher factors of safety. This suggests that the RMR-based designs have less inherent conservatism.

Table 6.2 and Table 6.3 summarize the results of the forward models for each alignment. Design reliability has been tabulated for factors of safety of 1, 1.5, and 2 as a metric of design suitability. A design method which provides unreliable safety factors is unsuitable because it is likely to experience excessive deformations, cracking, or failures. Design reliability has also been tabulated for a factor of safety of 10 as a metric of design cost-effectiveness. Designs which are overly conservative will have very high factors of safety, but will cost more as well.

Table 6.2 and Table 6.3 also tabulate the predominant location and failure mode suggested by the modeling. The column '% critical loads at model crown' shows what percentage of models resulted in the critical load combination occurring at the crown of the model. The highest results is 8.3%, and most alignments had far fewer (or no) cases where the critical load combination occurred at the model crown. This is an expected result when the principal stress is vertical, as the axial thrust tends to become maximum at the springline in these cases. This is broadly characteristic of more than 90% of modeled realizations for this study.

6.4 Discussion

Table 6.3 and Table 6.2 show aggregated model results for the seven alignments advanced for forward modeling. Note that results for Q and RMR based models show similar trends, though different outcomes in some cases.

Alignment 5448 was the highest-scoring alignment during the alignment optimization (Chapter 4) analysis in four categories: overall, drill-and-blast (D&B)–focused metrics, RMR–based metrics, and Q–based metrics (see Table 4.3). According to the numerical modeling, the design reliability of this alignment is not the absolute highest, but it is above 99% by both the Q- and RMR-based designs. In general, the modeling outcomes suggest that the Q- and RMR-based designs represent a reasonable starting point design, and a realistic first-order estimate of the likely required support systems. Thus, the alignment optimization metrics evaluated in Chapter 4 are a reasonable estimate of the most favorable alignment. Alignment 5448 is therefore suggested as a plausible starting point for future design studies.

In general, the proposed alignments with the empirically suggested (Q- and RMR-based) liner designs performed well in the sense of meeting a minimum design reliability.

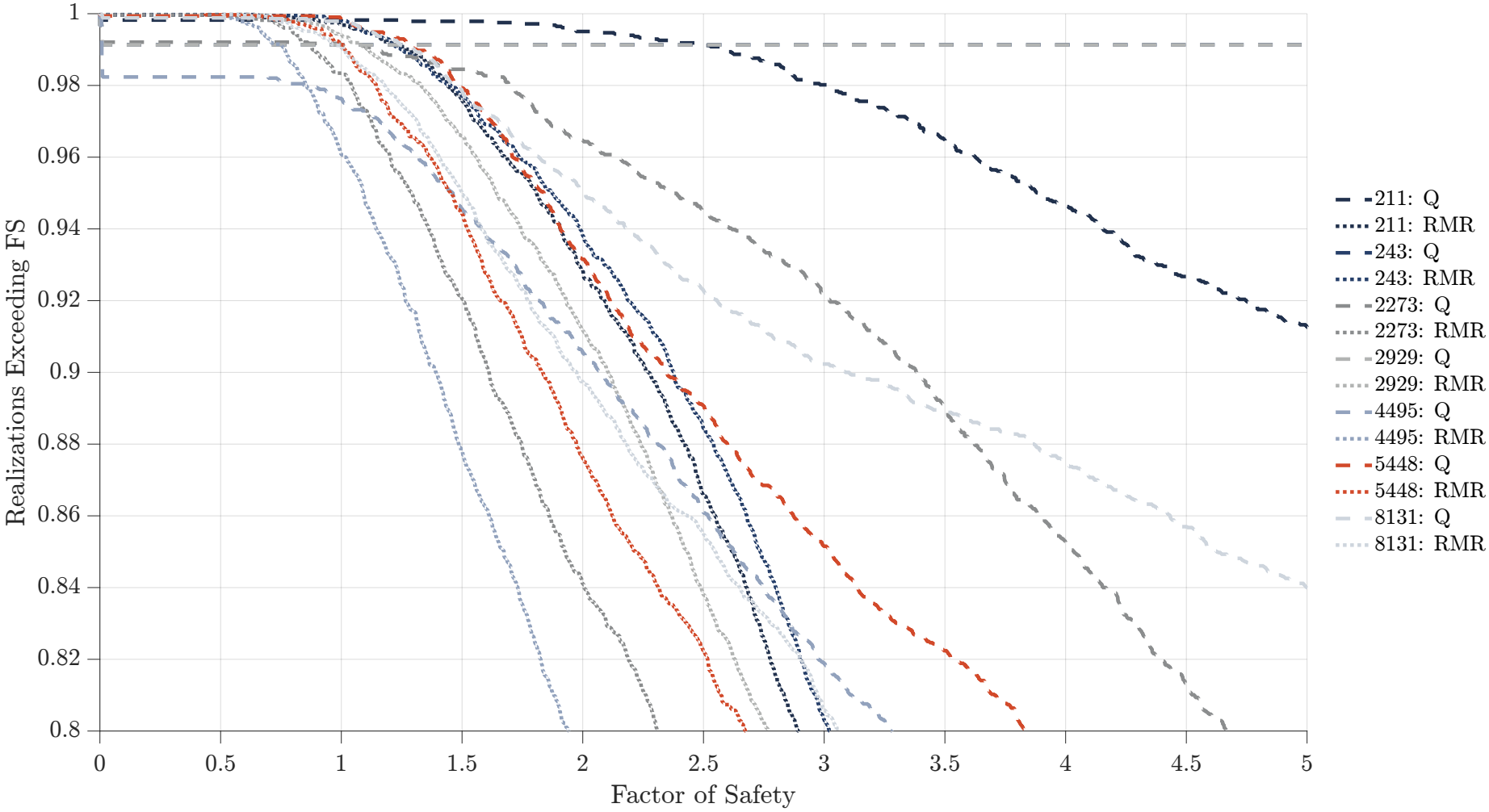

Figure 6.3: Design reliability for each alignment by the Q and RMR systems.

Table 6.2: Forward modeling results for RMR–system based liner models.

Alignment ID	Number of Stations	Design Reliability at $FS = 1.0$	Design Reliability at $FS = 1.5$	Design Reliability at $FS = 2.0$	Design Reliability at $FS = 10.0$	% Critical Loads at Model Crown	% Critical Load Combination Axial-Moment Interaction
211	113	99.7%	97.6%	92.8%	32.3%	0.88%	98.2%
243	157	99.8%	97.7%	93.8%	18.6%	0.64%	98.7%
2273	111	98.3%	92.1%	84.1%	15.2%	0.90%	96.4%
2929	207	99.4%	96.6%	91.2%	39.0%	0%	99.5%
4495	127	96.1%	87.8%	78.9%	17.6%	0%	100%
5448	125	99.1%	94.4%	87.6%	19.5%	0%	97.6%
8131	172	99.1%	95.0%	89.7%	30.4%	0%	99.4%

Table 6.3: Forward modeling results for Q–system based liner models.

Alignment ID	Number of Stations	Design Reliability at $FS = 1.0$	Design Reliability at $FS = 1.5$	Design Reliability at $FS = 2.0$	Design Reliability at $FS = 10.0$	% Critical Loads at Model Crown	% Critical Load Combination Axial-Moment Interaction
211	113	99.8%	99.8%	99.5%	85.2%	0.88%	86.7%
243	157	99.1%	99.1%	99.1%	99.1%	8.3%	79.6%
2273	111	99.1%	98.5%	96.5%	62.6%	7.2%	91.0%
2929	207	99.1%	99.1%	99.1%	99.0%	7.7%	83.6%
4495	127	97.6%	94.6%	90.6%	48.8%	3.9%	96.1%
5448	125	99.8%	97.9%	93.2%	54.5%	0.8%	96.0%
8131	172	99.8%	97.8%	95.0%	73.6%	1.2%	91.3%

In most cases, reliability of the empirical designs was quite high, exceeding 96% at a factor of safety of 1 in even the worst cases. The very high design reliabilities could be viewed positively, i.e. the Q and RMR systems work well. They could also be taken as indicating that the Q and RMR systems are overly conservative. In many cases, the calculated factor of safety is very high. By looking at the design reliability at a factor of safety of 10, we can get a sense of the excessive conservatism introduced by these empirical design methods. For the RMR-based designs the design reliability at a factor of safety of 10 exceeded 15% for all modeled alignments, and reached 39% for one alignment. For the Q-based designs the design reliability at a factor of safety of 10 exceeded 45% for all modeled alignments, and reached 99% for one alignment. This suggests that these empirical design tools introduce excess conservatism into the designs and should only be taken as an initial estimate, not a final design. Figure 6.3 shows this result graphically, with the Q-based designs having design reliabilities which fall off more gradually with increasing factor of safety.

Figure 6.4 shows the calculated factor of safety versus the input design Q value for each modeled realization. Note the abrupt change in typical results at a value of $Q = 0.4$. This coincides with the change in the Q-system between the use of reinforced ribs and the use of plain shotcrete linings. The plain shotcrete linings have less inherent conservatism, with most modeled factors of safety falling between 1 and 100. The modeled factors of safety for the reinforced rib systems are much higher, with typical factors of safety between 100 and 10,000. This suggests that the reinforced rib supports, as suggested by NGI (2015), may be overdesigned for most cases.

Figure 6.5 shows the calculated factor of safety versus the input design RMR value for each modeled realization. Note that the range of modeled safety factors is approximately 1 to 100. This is very similar to the results for the Q-based designs without reinforced ribs. This lends credence to the general suitability of each system, with the exception of the reinforced rib designs.

Another interesting observation from Figure 6.5 is an apparent downward trend in the mean factor of safety with respect to RMR. It appears that the RMR-based designs may have a non-uniform conservatism. They are more conservative in poor rock conditions and less conservative in good rock conditions. This heteroscedasticity may also represent greater uncertainty in the ground conditions to be encountered in overall poorer rock formations. In other words, this may be a reasonable engineering response to the higher likelihood of failure, and greater consequences of failure, in poor ground conditions.

The lack of uniform reliability and uniform conservatism across each system is concerning from the perspective of reliability-based design. The calibration of load and resistance

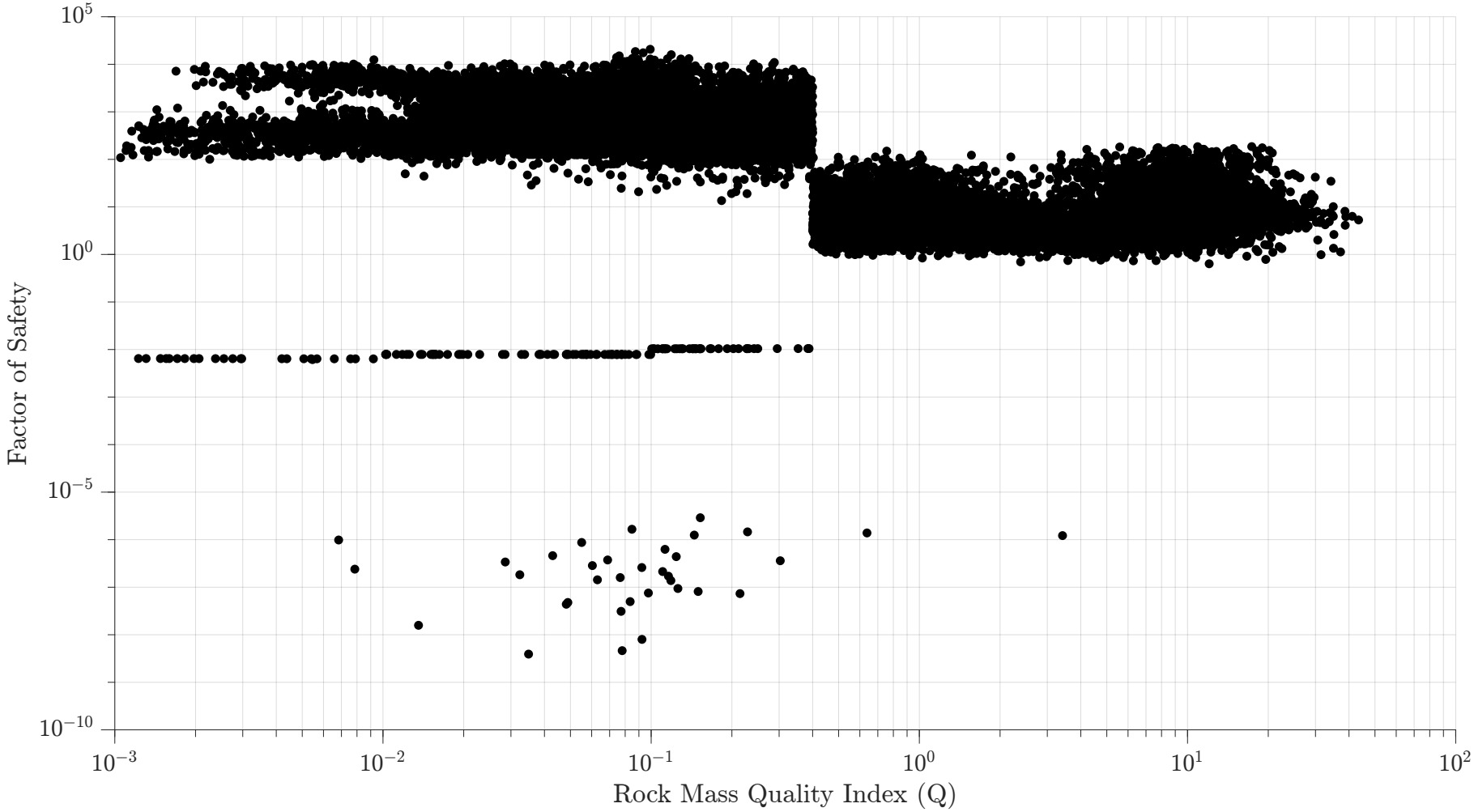

Figure 6.4: Calculated factor of safety versus estimated Q value for seven alignments modeled in FLAC.

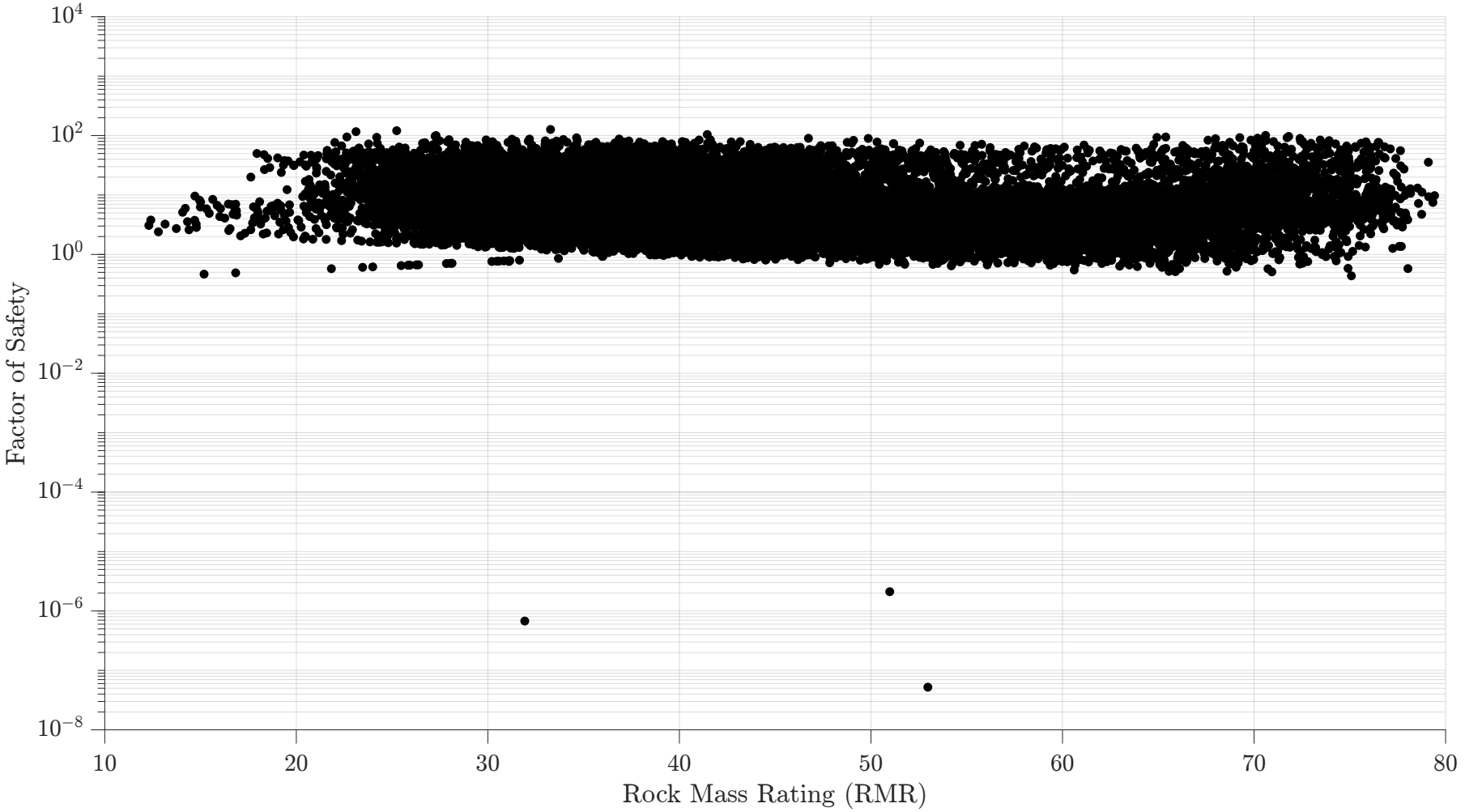

Figure 6.5: Calculated factor of safety versus estimated RMR value for seven alignments modeled in FLAC.

factors requires that uncertainty in the factors be fairly uniformly distributed. It also suggests that these systems may only be narrowly applicable at the middle of their ranges (cases of moderately good ground conditions). This may be because each system was calibrated to a dataset dominated by tunnels constructed in moderately good ground conditions. In general, if these systems are to remain relevant, these results suggest that additional calibration to a broader range of rock mass qualities is necessary. Also, refinement of the calibration to reduce excess conservatism is advisable to improve construction cost-effectiveness.

6.5 Summary and Conclusions

Results of the numerical modeling effort demonstrate the feasibility and effectiveness of large-scale 3D implicit geologic modeling, validate the previously developed alignment optimization algorithm, and provide interesting insights into the Q and RMR systems when used as empirical design heuristics.

For the seven alignments evaluated, the numerical models showed that the Q- and RMR-based designs are a reasonable starting point for the likely required support system. In addition, the systems appear to be fairly uniform in their outputs, with the exception of the Q-based reinforced rib designs. This suggests that an alignment optimization algorithm using these support systems will be capable of reasonably estimating the likely relative magnitude of required support for each tunnel alignment, and thus estimating the optimal tunnel alignment. This supports the author's assertion that the newly developed alignment optimization algorithm is a reasonable and useful tool for early-stage feasibility studies of alternative tunnel alignments.

The overall reliability of each empirical design system was found to be fairly high. Both systems suggested designs which achieved minimum acceptable factors of safety with high reliability. However, the systems may have excess conservatism built in, particularly in the case of the reinforced rib designs suggested by the Q system. Reevaluation and recalibration of the reinforced rib designs suggested by the Q system may be warranted.

The RMR system may have a non-uniform conservatism built in. Factors of safety appear to be systematically lower at high RMR values. This may be a desired feature of the system, representing wider uncertainty and more extreme consequences for failure in poor ground conditions. Alternatively, it may be a product of the dataset to which the system was calibrated. In either case, recalibration of the system to a wider dataset more representative of the full range of possible ground conditions may be warranted.

However, for the purposes of selecting an alignment that is optimal for further design

studies, the RMR and Q systems agree well in their relative ranking of alignments of the alignments. Both systems appear to be useful for deciding whether a given alignment is worth further consideration relative to other alignments, though the usefulness of each system as an empirical design heuristic is questionable.

The dominance of D&B excavation case studies in the empirical calibrations of the Q and RMR systems may be playing a significant role here. A recalibrated empirical design correlation focused on tunnel boring machine (TBM) construction case studies may be a valuable future research effort. This has been attempted before (e.g., rock mass quality index for TBM tunneling (Q_{tbm})) but no such metric has gained wide adoption so far. On the other hand, perhaps the usefulness of empirical design metrics has simply declined with the advent of widespread and efficient numerical modeling and design tools based more firmly in fundamental mechanics.

CHAPTER 7

SUMMARY, CONCLUSIONS, AND RECOMMENDATIONS

7.1 Summary

This report answers a practical engineering question: how to select a new tunnel alignment adjacent to existing infrastructure under significant uncertainty. The developed methodology:

1. Is probabilistic;
2. Incorporates a realistic evaluation of the uncertainty in the input parameters;
3. Efficiently evaluates an effectively infinite solution set using discretization and Monte Carlo simulation; and
4. Has been compared to a numerical simulation which itself has been validated by back analysis.

Along the way, interesting observations have been made about the usefulness and applicability of various empirical tunnel engineering criteria, particularly the use of the rock mass quality index (Q) and rock mass rating (RMR) systems as empirical design heuristics.

Chapter 3 thoroughly evaluates the Eisenhower-Johnson Memorial Tunnel (EJMT) case study, including probabilistic distributions of several input parameters. The EJMT research team developed a three-dimensional (3D) implicit geologic model of the existing tunnel vicinity to use as a test bed for the alignment optimization.

Chapter 4 discretized the solution space of possible alignments in the vicinity of the existing EJMT. A multi-factor optimization technique based on the 3D geologic model using Monte Carlo sampling of probabilistic parameters was applied along each alignment. Seven alignments scored highest by various optimization metrics and were advanced for further study.

Chapter 5 presents a back analysis of the EJMT pilot bore in order to calibrate a finite difference numerical model applicable to analyses of new bores adjacent to the existing bores. The model was calibrated using a discrete least-squares approach with the target being the accurate reproduction of recorded axial thrusts in the legs of the

EJMT pilot bore. The model was tested in both an elastic and elastic-perfectly-plastic case; the elastic-perfectly-plastic model was found to be significantly more successful at replicating the available in-situ data. The final calibrated model was acceptably accurate and time–efficient for rapid application to many Monte Carlo realizations of multiple plausible bores.

Chapter 6 applies the calibrated model through many Monte Carlo realizations of the previously identified most plausible seven alignments adjacent to the existing EJMT. The results of the forward modeling validate the results of the alignment optimization and provide interesting insights into the general applicability of the Q and RMR empirical design heuristics.

7.2 Conclusions

Many useful conclusions can be drawn from the work presented in this report. Some are more specific to the case study studied here while others are more general.

1. In cases where a material is transversely isotropic but there is significant uncertainty in the foliation orientations and the foliation–normal and foliation-parallel material properties, it may be more practical to reduce the material model from transversely isotropic to isotropic with uncertainty. This has the advantage of simplifying subsequent modeling while still capturing the probabilistic uncertainty in the rock mass.
2. The data and analysis presented in Chapter 3 demonstrate an important application of random variable algebra to rock mass classifications. Deterministic estimates may consistently under– or over–estimate the most likely probabilistic estimate. The functional transformations and convolutions of various symmetric and asymmetric probability density functions into a final estimate makes it difficult to predict whether a deterministic estimate will reasonably approximate the most likely outcome of a probabilistic estimate. In any case, the deterministic estimate lacks important information on outcome uncertainty. Tunnel designs based on deterministic estimates of rock mass classification are likely to be unreliable, possibly unconservatively so.
3. None of the evaluated rock mass classification parameters (Q, RMR, geological strength index (GSI), and rock quality designation (RQD)) provided a good correlation to recorded advance rates in the EJMT pilot bore. No satisfactory solution was found to this problem. This remains a significant unanswered question. Note that advance rate, in this context, refers to the rate of tunnel heading advance

per unit of working time. The term advance rate may mean different things in different tunneling contexts, especially when drill-and-blast (D&B) and tunnel boring machine (TBM) tunneling are contrasted.

4. The use of 3D implicit geological modeling incorporating probabilistic uncertainty has great promise in civil infrastructure projects. The case study presented here demonstrates the utility and feasibility of this technique, given modern computational tools. Although this technique has been applied previously in the mining industry, it remains relatively obscure in the civil infrastructure world. It seems likely that this technique will gain greater usage in the next few years due to its simplicity, effectiveness, and applicability.
5. The EJMT case study demonstrates the possibility for clay-rich gneissic rocks to plastically creep (squeeze). Further, previously developed empirical metrics for predicting squeezing, particularly those of Arora et al. (2020), Gutierrez and Xia (2009), and Singh et al. (1992), appear to be somewhat applicable to the squeezing of gneissic rocks, with some minor recalibration.
6. The fault gouge in the vicinity of the EJMT appears to contribute to, but not control, the overall material properties of the rock mass. Estimation of rock mass properties from intact rock properties using empirical correlations to Q, RMR, RQD, and GSI were satisfactory for predicting rock mass properties through the EJMT pilot bore squeeze zone.
7. For the seven alignments evaluated, the numerical modeling from Chapter 6 showed that the Q- and RMR-based designs are a reasonable starting point for the likely required support system. In addition, the systems appear to be fairly uniform in their outputs, with the exception of the Q-based reinforced rib designs. This suggests that an alignment optimization algorithm using these support systems will be capable of reasonably estimating the likely relative magnitude of required support for each alignment, and thus estimating the optimal tunnel alignment.
8. The overall reliability of each empirical design system was found to be fairly high. Both systems suggested designs which achieved minimum acceptable factors of safety with high reliability. However, the systems may have excess conservatism built in, particularly in the case of the reinforced rib designs suggested by the Q system. Reevaluation and recalibration of the reinforced rib designs suggested by the Q system may be warranted.
9. The RMR system may have a non-uniform conservatism built in. Factors of safety appear to be systematically lower at high RMR values. This may be a desired feature of the system, representing wider uncertainty and more extreme consequences

for failure in poor ground conditions. Alternatively, it may be a product of the dataset to which the system was calibrated. In either case, recalibration of the system to a wider dataset more representative of the full range of possible ground conditions may be warranted.

7.3 Recommendations to CDOT

The author has several broad recommendations pertaining to CDOT's fundamental question which inspired this report: Where should a new bore be placed adjacent to the existing EJMT?

1. Alignment 5448 from this analysis was the best. This exact alignment should not be taken as the best possible option, *per se*, but a useful starting point for additional analyses. All alignments evaluated were straight lines; a curved alignment may allow for some additional optimization. Further refinement of the analysis beyond the coarse 100 m portal grid used here is also advisable.
2. The selection of TBM versus D&B tunneling has an impact on the best plausible alignment. TBM tunneling works better through fairly consistent ground conditions while D&B tunneling is more adaptable to varied ground conditions. Consider involving contractors early in the design process to determine whether D&B or TBM tunneling will be preferred in this particular case. This selection has more to do with availability, Colorado Department of Transportation (CDOT)'s desired level of involvement in project execution, and unpredictable future economic conditions (e.g., skilled labor and machine availability) than with technical engineering concerns. However, TBM tunneling appears to be slightly more favorable south of the existing EJMT alignment while D&B tunneling appears to be slightly more favorable north of the existing EJMTalignment.
3. The geologic conditions trend better to the north of the existing tunnels.
4. The geologic conditions trend somewhat better slightly above the existing alignments. If carefully designed, a new alignment above the existing alignments may also provide the opportunity to intercept and divert some groundwater flows which currently present operational difficulties for the existing bores.
5. Install piezometers around the existing EJMT and monitor them over a period of several years to gain a more thorough understanding of the seasonal groundwater flows in this area. A thorough hydrogeological model calibrated by back analysis to these data would be helpful both in design of new bores and in operation of the existing bores.

6. Simple empirical correlations are useful for comparing between plausible options, when applied with an understanding of their limitations. Avoid using existing empirical design heuristics calibrated to the Q– and RMR–systems until these systems have been recalibrated for consistency across their full range.
7. Avoid deterministic analyses. Rock mechanics and tunnel design are inherently uncertain. The uncertainties associated with tunnel design are not generally symmetric or normal (Gaussian); a thorough understanding of the true behavior of a tunnel–rock mass interaction requires an understanding of the full distribution of possible properties and outcomes. Failure to understand the epistemic and aleatory uncertainty in tunnel design can bias results unconservatively.
8. This report models the tunnel liners based on rockbolt and shotcrete supports. This support system would like be effective in the vicinity of the EJMT. However, other support systems of comparable strength and stiffness would likely also be appropriate. Steel supports, if used, would likely require sliding-gap closures to be flexible enough to apply within squeezing ground conditions, as described by Hoek et al. (2008). Precast concrete supports may not have sufficient flexibility to accomodate squeezing ground conditions, may require a separate initial support system and delayed installation, or may require a unique solution to achieve sufficient flexibility to accomodate the squeezing while remaining ductile.

7.4 Future Work

This report leaves some unanswered or newly-raised questions which would provide an interesting point of departure for further study. Some of these are likely large enough to serve as the seed for an entire additional project while others may have more finite answers.

1. This evaluation did not consider the stability of the landslide north of the east portal of the EJMT. This landslide was activated during the pilot bore construction and stabilized with a large toe berm which is now incorporated into the north side of the portal structure. Additional study of this landslide and its potential intersection and impact upon any new bore is highly recommended.
2. Constructability of TBM tunnels appears to be negatively correlated with the dispersion of rock mass classification parameters. The relevance and utility of this observation bears further study and consideration.
3. Neither the Q, RMR, GSI, or RQD rock mass classification systems were able to accurately predict advance rates in the EJMT pilot bore. In general, accurate

estimation of tunnel project timelines is a significant challenge in the modern tunnel construction industry. No current system appears widely accepted, and poor estimation of project timelines often leads to cost overruns. This is an area requiring further research; the outcomes would be very valuable to all stakeholders in tunnel construction. Note that advance rate, in this context, refers to the rate of tunnel heading advance per unit of working time. The term advance rate may mean different things in different tunneling contexts, especially when D&B and TBM tunneling are contrasted.

4. This alignment optimization was limited to a single cross-sectional shape (circular). Evaluation of alternative cross-sections or the optimization of a poly-arc cross-section would be a valuable exercise and tool for the tunneling industry. Additionally, optimization of sequential excavation sequencing would be a useful contribution.
5. The current alignment optimization technique focused on technical feasibility rather than costs. Future work could extend the alignment optimization methodology to probabilistic consideration of tunnel costs.
6. This study did not evaluate curved alignments. Future research could address the possibility of optimizing the tunnel alignment using curvature.
7. Hydrogeologic modeling of the EJMT and calibration of a model by back analysis would be a very practically useful project to CDOT.
8. Additional numerical modeling, analysis, or design techniques could be evaluated as an input to the alignment optimization algorithm. For example, a convergence-confinement model may be a time-efficient way of estimating the likely support requirements along an alignment, as opposed to the current Q- and RMR-based techniques.

REFERENCES

AASHTO (2017). *LRFD Road Tunnel Design and Construction Guide Specifications*. Tech. rep. Washington, D.C.: American Association of State Highway and Transportation Officials.

Abad, J, B Celada, E Chacon, V Gutierrez, and E Hidalgo (Apr. 1983). "Application of geomechanical classification to predict the convergence of coal mine galleries and to design their supports". In: *Proceedings of the 5th Congress of the International Society of Rock Mechanics*. Vol. 2. Melbourne, Australia: International Society for Rock Mechanics and Rock Engineering, PE15–PE19.

Abel, John F (May 1966). "Tunnel Mechanics". doctoral dissertation. Golden, Colorado: Colorado School of Mines.

ACI (June 2016). *Guide to Shotcrete*. ACI Standard 506R-16. Detroit, Michigan: American Concrete Institute, p. 57.

— (2019). *ACI 318-19*. Farmington Hills, Michigan: American Concrete Institute.

Aleinikoff, J N, Jr. Reed J.C., and E Dewitt (1993). "The Mount Evans batholith in the Colorado Front Range - Revision of its age and reinterpretation of its structure". In: *Geological Society of America Bulletin* 105, pp. 791–806.

Alejano, Leandro R, Javier Arzúa, Nezam Bozorgzadeh, and John P Harrison (May 2017). "Triaxial strength and deformability of intact and increasingly jointed granite samples". In: *International Journal of Rock Mechanics and Mining Sciences* 95, pp. 87–103.

Alemdag, S, Z Gurocak, A Cevik, A F Cabalar, and C Gokceoglu (Mar. 2016). "Modeling deformation modulus of a stratified sedimentary rock mass using neural network, fuzzy inference and genetic programming". In: *Engineering Geology* 203, pp. 70–82.

Alemdag, Selcuk, Zulfu Gurocak, and Candan Gokceoglu (Oct. 2015). "A simple regression based approach to estimate deformation modulus of rock masses". In: *Journal of African Earth Sciences* 110, pp. 75–80.

Alvarez Grima, M, P A Bruines, and P N W Verhoef (July 2000). "Modeling tunnel boring machine performance by neuro-fuzzy methods". In: *Tunnelling and Underground Space Technology* 15.3, pp. 259–269.

Amadei, B (Feb. 1988). "Strength of a regularly jointed rock mass under biaxial and axisymmetric loading conditions". In: *International Journal of Rock Mechanics and Mining Sciences & Geomechanics Abstracts* 25.1, pp. 3–13.

— (Apr. 1996). "Importance of anisotropy when estimating and measuring in situ stresses in rock". In: *International Journal of Rock Mechanics and Mining Sciences & Geomechanics Abstracts* 33.3, pp. 293–325.

Amadei, Bernard and William Z Savage (1993). "Effect of joints on rock mass strength and deformability". In: *Comprehensive rock engineering: Principles, practice, and projects*. Ed. by Edwin T Brown. 1st ed. Vol. 1. Oxford ; Pergamon Press, pp. 313–329.

— (1989). "Anisotropic Nature of Jointed Rock Mass Strength". In: *Journal of Engineering Mechanics* 115.3, pp. 525–542.

Aristaran, Manuel et al. (June 2013). *Tabula*.

Arora, Ketan, Marte Gutierrez, Ahmadreza Hedayat, and Caichu Xia (July 2020). "Tunnels in squeezing clay-rich rocks". In: *Underground Space*.

ASTM (2008). *Standard Practices for Preparing Rock Core as Cylindrical Test Specimens and verifying Conformance to Dimensional and Shape Tolerances*. Tech. rep. West Conshohocken, Pennsylvania: ASTM International, Inc.

— (2011). *Standard Classification for Cost Estimate Classification System*. Tech. rep. West Conshohocken, Pennsylvania: ASTM International, Inc.

— (2014). *Standard test method for compressive strength and elastic moduli of intact rock core specimens under varying states of stress and temperatures*. Tech. rep. West Conshohocken, Pennsylvania: ASTM International, Inc.

Aydan, O, T Akagi, and T Kawamoto (1993). "The squeezing potential of rocks around tunnels; Theory and prediction". In: *Rock Mechanics and Rock Engineering* 26.2, pp. 137–163.

Aydan, Ö, R Ulusay, and T Kawamoto (Apr. 1997). "Assessment of rock mass strength for underground excavations". In: *International Journal of Rock Mechanics and Mining Sciences* 34.3, 18.e1–18.e17.

Aydan, Omer and Toshikazu Kawamoto (2000). "The Assessment of Mechanical Properties of Rock Masses Through RMR Rock Classification System". In: *GeoEng2000*. Melbourne, Australia: International Society for Rock Mechanics and Rock Engineering (ISRM).

Barla, Giovanni (Jan. 2002). "Tunnelling mechanics Tunnelling under squeezing rock conditions". In: *Eurosummer School*, pp. 169–268.

Barton, N (Feb. 2002). "Some new Q-value correlations to assist in site characterisation and tunnel design". In: *International Journal of Rock Mechanics and Mining Sciences* 39.2, pp. 185–216.

Barton, Nicholas R (1995). "The influence of joint properties in modelling jointed rock masses". In: vol. 3. 8th Congress of ISRM. Tokyo, Japan: International Society of Rock Mechanics.

Barton, Nicholas R, R Lien, and J Lunde (1974). "Engineering classification of rock masses for the design of tunnel support". In: *Rock Mechanics* 6.4, pp. 189–236.

Barton, Nicholas Ryland and Z.T. Bieniawski (Feb. 2008). "RMR and Q - Setting Records Straight". In: *Tunnels and Tunnelling International*, pp. 26–29.

Barton, Nicholas Ryland and Eystein Grimstad (2014). *Q-system - An Illustrated Guide Following Forty Years in Tunnelling*. Tech. rep., p. 45.

Barton, Nick R (2000). *TBM Tunnelling in Jointed and Faulted Rock*. Rotterdam, Netherlands: A.A. Balkema Publishers.

Beiki, Morteza, Ali Bashari, and Abbas Majdi (Oct. 2010). "Genetic programming approach for estimating the deformation modulus of rock mass using sensitivity analysis by neural network". In: *International Journal of Rock Mechanics and Mining Sciences* 47.7, pp. 1091–1103.

Belknap, E P, J B Gilmore, and Walt Mystkowski (Dec. 1988). *Landslide and Convergence Report*. Memorandum. Denver, Colorado: Colorado Department of Transportation (CDOT), p. 3.

Bhasin, R (1991). "Evaluation of soft rock conditions in tunnels through the Lower Himalayan regions; A Contribution for updating of the Q-system". PhD thesis. MSc Thesis, University of Oslo.

Bhasin, Rajinder and Eystein Grimstad (1996). "The use of stress-strength relationships in the assessment of tunnel stability". In: *Tunnelling and Underground Space Technology* 11.1, pp. 93–98.

Bieniawski, Z T (Nov. 1976). "Rock mass classifications in rock engineering". In: Proceedings of the Symposium on Exploration for Rock Engineering. Johannesburg, South Africa: South African Institution of Civil Engineering, Geotechnical Division; South African National Group on Rock Mechanics.

— (Oct. 1978). "Determining rock mass deformability: experience from case histories". In: *International Journal of Rock Mechanics and Mining Sciences & Geomechanics Abstracts* 15.5, pp. 237–247.

— (1984). *Rock Mechanics Design in Mining and Tunneling*. 9th Editio. Rotterdam, Netherlands: A.A. Balkema Publishers.

— (1989). *Engineering Rock Mass Classifications*. New York, NY: John Wiley & Sons.

— (1993). “Classification of rock masses for engineering: The RMR system and future trends”. In: *Rock testing and site characterization*. Ed. by John A Hudson. 1st Editio. Vol. 3. Comprehensive rock engineering. Oxford, UK: Pergamon Press, pp. 553–573.

Bieniawski, Z T, David Aguado, Benjamín Celada, and Alejandro Rodriguez (Aug. 2011). “Forecasting Tunnelling Behaviour”. In: *Tunnels and Tunnelling International*, pp. 39–42.

Bieniawski, Z T, B Celada, and J M Galera (2007). “TBM Excavatability: Prediction and Machine-Rock Interaction”. In: *Proceedings of the Rapid Excavation and Tunneling Conference*. Toronto, Ontario, pp. 1118–1130.

Bieniawski, Z T, B Celada, J M Galera, and I Tardaguila (2008). “New Applications of the Excavatability Index for Selection of TBM Types and Predicting their Performance”. In: *Proceedings of the ITA World Tunnel Congress 2008*. Agra, India: International Tunnelling and Underground Space Association.

Bieniawski, Z T and Jose Miguel Galera (Sept. 2007). “Predicting TBM Excavatability”. In: *Tunnels and Tunnelling International*, pp. 25–28.

Bieniawski, Z T and Remo Grandori (Dec. 2007). “Predicting TBM Excavatability - Part II”. In: *Tunnels and Tunnelling International*, pp. 15–18.

Bieniawski, Z. T. (1973). “Engineering classification of jointed rock masses”. In: *Transactions, South African Institution of Civil Engineers* 15.12, pp. 335–344.

Bieniawski, Z. T., B Celada Tamames, J M Galera Fernández, and M Álvarez Hernández (May 2006). “Rock Mass Excavatability (RME) index: A new way to selecting the optimum tunnel construction method”. In: *Safety in the Underground Space - Proceedings of the ITA-AITES 2006 World Tunnel Congress and 32nd ITA General Assembly*. Vol. 21. Seoul, South Korea: International Tunnelling and Underground Space Association, p. 237.

Blindheim, Olav T (June 2007). “A Critique of Qtbm”. In: *Tunnels and Tunnelling International*, pp. 32–35.

Bonnema, Janet (1972). *Straight Creek Tunnel Isometric Reinforcement Details*. Construction Drawings. Denver, Colorado: Colorado Department of Transportation (CDOT), p. 5.

Box, George E.P. (1976). “Science and Statistics”. In: *Journal of the American Statistical Association* 71.356, pp. 791–799.

— (1979). “Robustness in the Strategy of Scientific Model Building”. In: *Robustness in Statistics*. Academic Press, Inc., pp. 201–236.

Branch, M, T Coleman, and Y Li (Jan. 1999). “A Subspace, Interior, and Conjugate Gradient Method for Large-Scale Bound-Constrained Minimization Problems”. In: *SIAM Journal on Scientific Computing* 21.1, pp. 1–23.

Breitung, Karl (Mar. 1984). “Asymptotic Approximations for Multinormal Integrals”. In: *ASCE Journal of Engineering Mechanics* 110.3, pp. 357–366.

Brockenbrough, Roger L and Joseph Schuster (2018). *Design guide 15: Rehabilitation and retrofit*. Tech. rep.

Brown, Edwin T (2012). "Risk assessment and management in underground rock engineering—an overview". In: *Journal of Rock Mechanics and Geotechnical Engineering* 4.3, pp. 193–204.

Bruland, Amund (1998). "Hard Rock Tunnel Boring". doctoral dissertation. Trondheim, Norway: Norwegian University of Science and Technology (NTNU).

BTS and ICE (2004). *Tunnel Lining Design Guide*. Tech. rep. London, England: The British Tunnelling Society and The Institution of Civil Engineers.

Buchi, Ernst (1984). "Einfluss geologischer parameter auf die vortriebsleistung einer tunnelbohrmaschine". doctoral dissertation. Bern, Switzerland: University of Bern.

Byrd, Richard H, Robert B Schnabel, and Gerald A Shultz (Jan. 1988). "Approximate solution of the trust region problem by minimization over two-dimensional subspaces". In: *Mathematical Programming* 40.1, pp. 247–263.

Cai, M, Peter K Kaiser, H Uno, Y Tasaka, and M Minami (2004). "Estimation of rock mass deformation modulus and strength of jointed hard rock masses using the GSI system". In: *International Journal of Rock Mechanics and Mining Sciences* 41.1, pp. 3–19.

Cai, Ming and Peter Kaiser (2006). "Visualization of rock mass classification systems". In: *Geotechnical and Geological Engineering* 24.4, pp. 1089–1102.

Cameron-Clarke, I S and S Budavari (1981). "Correlation of rock mass classification parameters obtained from borecore and in-situ observations". In: *Engineering Geology* 17, pp. 19–53.

Carranza-Torres, Carlos and Maxwell Engen (2017). "The support characteristic curve for blocked steel sets in the convergence-confinement method of tunnel support design". In: *Tunnelling and Underground Space Technology* 69.March, pp. 233–244.

Carroll, Roderick D, James H Scott, and D R Cunningham (1966). "Elastic Moduli of Granitic Rock from In-Situ Measurements of Seismic Velocity". In: *Geological Survey Professional Paper* 550-C, pp. C25–C28.

Carter, J P and F H Kulhawy (Aug. 1988). *Analysis and Design of Drilled Shaft Foundations Socketed Into Rock*. Research Report EL-5918. Palo Alto, California: Electric Power Research Institute, p. 190.

Caumon, Guillaume (2010). "Towards stochastic time-varying geological modeling". In: *Mathematical Geosciences* 42.5, pp. 555–569.

CDOT (1953). *Continental Divide Tunnel Study*. Tech. rep. Denver, Colorado: Colorado Department of Transportation.

CDOT (1973). *Plan and Profile of Federal Aid Project No. I70-3(34)220 Straight Creek Tunnel*. Tech. rep. Denver, Colorado: Colorado Department of Transportation.

— (1979). *Plan and Profile of Federal Aid Project No. I-70-3(82)220*. Tech. rep. Denver, Colorado, United States: Colorado Department of Transportation.

— (Mar. 2011). *I-70 Mountain Corridor Final Programmatic Environmental Impact Statement*. Tech. rep. Colorado Department of Transportation (CDOT), p. 527.

— (2018a). *Roadway Design Guide*. Tech. rep. Denver, Colorado, United States: Colorado Department of Transportation.

— (2018b). *Eisenhower Tunnel Traffic Counts*.

— (n.d.). *Eisenhower-Johnson Memorial Tunnel*.

Cecil III, Owen Sinclair (1970). "Correlations of Rock Bolt-Shotcrete Support and Rock Quality Parameters in Scandinavian Tunnels". doctoral dissertation. Urbana, Illinois: University of Illinois at Urbana-Champaign.

Celada, B, I Tardáguila, P Varona, A Rodríguez, and Z T Bieniawski (2014). "Innovating tunnel design by an improved experience-based RMR system." In: Proceedings of the World Tunnel Congress 2014 - Tunnels for a Better Life. Foz do Iguacu, Brazil, p. 9.

Celada, Benjamín and Z.T. Bieniawski (2020). *Ground characterization and structural analyses for tunnel design*. Boca Raton, Florida: CRC Press, Taylor & Francis Group.

CEQ (Nov. 1978). *Protection of Environment*.

CGS (n.d.). *Colorado Landslide Inventory*. Tech. rep. Golden, Colorado: Colorado Geological Survey.

Chen, Fuyong, Lin Wang, and Wengang Zhang (June 2019). "Reliability assessment on stability of tunnelling perpendicularly beneath an existing tunnel considering spatial variabilities of rock mass properties". In: *Tunnelling and Underground Space Technology* 88, pp. 276–289.

Christensen, Peter, Larry Dysert, Peter R Bredehoeft, Todd Pickett, and John K Hollmann (Aug. 2020). *Recommended Practice 17R-97: Cost Estimate Classification System*. AACE International.

Christensen, Peter and Larry R Dysert (1997). *Recommended Practice No. 17R-97 Cost Estimate Classification System*. AACE International.

Christian, John T, Charles C Ladd, and Gregory B Baecher (1994). "Reliability Applied to Slope Stability Analysis". In: *ASCE Journal of Geotechnical Engineering* 120.12, pp. 2180–2207.

Chun, Byung-Sik, Yong-Jea Lee, Deok-Dong Seo, and Beyong-Seok Lim (May 2006). "Correlation deformation modulus by PMT with RMR and rock mass condition". In: *Tunnelling and Underground Space Technology* 21.3-4, pp. 231–232.

Cohen, Howard J (Nov. 1970). *In Situ Uniaxial Jacking Tests - Straight Creek Tunnel, Loveland Pass Colorado, Performed by the USBR for the Division of Highways, State of Colorado*. Tech. rep. Denver, Colorado: United States Bureau of Reclamation, p. 39.

— (Mar. 1971a). *Straight Creek Tunnel - Supplementary Test Results*. Tech. rep. Denver, Colorado: United States Bureau of Reclamation, p. 21.

— (Jan. 1971b). *Straight Creek Tunnel Triaxial Shear Results*. Laboratory Report. Denver, Colorado: United States Bureau of Reclamation, p. 31.

Coon, R F and A H Merritt (June 1970). "Predicting In-Situ Modulus of Deformation Using Rock Quality Indexes". In: *Determination of the In-situ Modulus of Deformation of Rock*. ASTM Special Technical Publication 477. Philadelphia, Pennsylvania: American Society for Testing and Materials, pp. 154–173.

Cowan, E J et al. (2003). "Practical implicit geological modeling". In: vol. 8. Bendigo, Victoria: The Australasian Institute of Mining and Metallurgy, pp. 89–99.

Dahl, Filip, Amund Bruland, Eivind Grav, and Bjorn Nilsen (June 2010). "Trademarking the NTNU/SINTEF drillability test indices". In: *Tunnels and Tunnelling International*, pp. 44–46.

Dahl, Filip, Amund Bruland, Pål Drevland Jakobsen, Bjørn Nilsen, and Eivind Grøv (Mar. 2012). "Classifications of properties influencing the drillability of rocks, based on the NTNU/SINTEF test method". In: *Tunnelling and Underground Space Technology* 28, pp. 150–158.

Daniel, C G, L S Pfeifer, J V Jones III, and C M McFarlane (2013). "Detrital zircon evidence for non-Laurentian provenance, Mesoproterozoic (ca. 1490-1450 Ma) deposition and orogenesis in a reconstructed orogenic belt, northern New Mexico, USA: Defining the Picuris orogeny". In: *Geological Society of America Bulletin* 125, pp. 1423–1441.

Deere, Don U (1963). "Technical description of rock cores for engineering purposes". In: *Felsmechanik und Ingenieurgeologie (Rock Mechanics and Engineering Geology)* 1.1, pp. 16–22.

Deere, Don U and Don W Deere (1989). *Rock quality designation (RQD) after twenty years*. Tech. rep. Washington, D.C.: United States Army Corps of Engineers, p. 101.

Deere, Don U, A J Hendron, F D Patton, and Edward J Cording (1967). "Design of surface and near surface constructions in rock". In: *Failure and breakage of rock*. Ed. by C Fairhurst. New York, New York: Society of Mining Engineers of the American Institute of Mining, Metallurgical, and Petroleum Engineers, pp. 237–302.

Deere, Don U and R P Miller (Dec. 1966). *Engineering classification and index properties for intact rock*. Tech. rep. Urbana, Illinois: University of Illinois, Urbana-Champaign; US Air Force Weapons Laboratory, p. 327.

Deere, Don U, Ralph B Peck, James Eugene Monsees, and B Schmidt (1969). *Design of Tunnel Liners and Support Systems*. Tech. rep. Washington, D.C.: Office of High Speed Ground Transportation, US Department of Transportation.

Deere, Don U, Ralph B Peck, H W Parker, J E Monsees, and B Schmidt (1970). "Design of tunnel support systems". In: *Highway Research Record* 339, pp. 26–33.

Diederichs, M S and P K Kaiser (Jan. 1999). "Stability of large excavations in laminated hard rock masses: the voussoir analogue revisited". In: *International Journal of Rock Mechanics and Mining Sciences* 36.1, pp. 97–117.

Diederichs, Mark Stephen (1999). "Instability of hard rockmasses, the role of tensile damage and relaxation". Doctor of Philosophy. Sudbury, Ontario, Canada: University of Waterloo.

Eberly, David (Nov. 2006). *3D Game Engine Design: A Practical Approach to Real-Time Computer Graphics*. CRC Press.

— (Sept. 2020). *Robust Computation of Distance Between Line Segments*. white paper. Redmond, WA: Geometric Tools, p. 14.

Efron, Nathaniel and Megan Read (Feb. 2012). *Analysing International Tunnel Costs*. Tech. rep. Worcester Polytechnic Institute, p. 108.

Einstein, Herbert H (2004a). *Decision Aids for Tunneling: SimJava*. Cambridge, MA: Massachusetts Institute of Technology.

— (2004b). "Decision Aids for Tunneling: Update". In: *Transportation Research Record* 1892, pp. 199–207.

Einstein, Herbert H, J-P. Dudt, V B Halabe, and Francois P Descoeudres (1992). *Decision Aids in Tunneling*. Tech. rep. November.

Einstein, Herbert H, Claude Indermitte, Joseph Sinfield, Francois P Descoeudres, and Jean-Paul Dudt (1999). "Decision Aids for Tunneling". In: *Transportation Research Record* 1656, pp. 6–13.

Einstein, Herbert H, Duane A Labreche, Michael J Markow, and Gregory B Baecher (1978). "Decision analysis applied to rock tunnel exploration". In: *Engineering Geology* 12.C, pp. 143–161.

Einstein, Herbert H, Guillermo F Salazar, Yeong W Kim, and Photios G Ioanou (1987). "Computer Based Decision Support Systems for Underground Construction". In: *Proceedings of the 1987 Rapid Excavation and Tunneling Conference*. New Orleans, LA: Society of Mining Engineers, pp. 1287–1308.

Einstein, Herbert H and S G Vick (1974). "Geological Model for a Tunnel Cost Model". In: *Proceedings of the 2nd Rapid Excavation and Tunneling Conference*. Vol. 2. San Francisco, CA: Society of Mining Engineers of the American Institute of Mining, Metallurgical, and Petroleum Engineers, pp. 1701–1720.

Eissa, Elsayed Ahmed (1980). "Stress analysis of underground excavations in isotropic and stratified rock using the boundary element method". PhD thesis. London, UK: Imperial College London.

Erslev, E A, S M Holdaway, S O'Meara, B Jurista, and B Selvig (2004). "Laramide minor faulting in the colorado front range". In: *New Mexico Bureau of Geology and Mineral Resources* 160, pp. 181–203.

ESRI (2019). *ArcMap*. Redlands, California.

Fossum, A F (Dec. 1985). "Effective elastic properties for a randomly jointed rock mass". In: *International Journal of Rock Mechanics and Mining Sciences & Geomechanics Abstracts* 22.6, pp. 467–470.

Galera, José M, M Álvarez, and Z.T. Bieniawski (2005). "Evaluation of the Deformation Modulus of Rock Masses: Comparison of Pressuremeter and Dilatometer Tests with RMR Prediction". In: *Proceedings of the ISP5-PRESSIO 2005*. Paris, France, p. 25.

Gardner, W S (1987). "Design of Drilled Piers in the Atlantic Piedmont". In: *Foundations and Excavations in Decomposed Rock of the Piedmont Province*. Geotechnical Special Publication (GSP) 9. Reston, Virginia: American Society of Civil Engineers (ASCE), pp. 62–86.

Gercek, H (2007). "Poisson's ratio values for rocks". In: *International Journal of Rock Mechanics and Mining Sciences* 44.1, pp. 1–13.

Ghamgosar, M, A Fahimifar, and V Rasouli (June 2010). "Estimation of rock mass deformation modulus from laboratory experiments in Karun dam". In: *Rock Mechanics in Civil and Environmental Engineering*. Lausanne, Switzerland: Taylor & Francis, pp. 805–808.

Gioi, Rafael Grompone von, Jérémie Jakubowicz, Jean-Michel Morel, and Gregory Randall (Mar. 2012). "LSD: a Line Segment Detector". In: *Image Processing On Line* 2, pp. 35–55.

Goel, R K (1994). "Correlations for Predicting Support Pressures and Closures in Tunnels". doctoral dissertation. Maharashtra, India: Nagpur University.

Goel, R K and J L Jethwa (1991). "Prediction of Support Pressure Using RMR Classification". In: *Proceedings of the Indian Geotechnical Conference*. Surat, India, pp. 203–205.

Goel, R K, J L Jethwa, and A G Paithankar (1995). "Indian Experiences with Q and RMR Systems". In: *Tunnelling and Underground Space Technology* 10.1, pp. 97–109.

— (1996). "Correlation between Barton's Q and Bieniawski's RMR - A new approach". In: *International Journal of Rock Mechanics and Mining Sciences & Geomechanics Abstracts* 33.2, pp. 179–181.

Gokceoglu, C, H Sonmez, and A Kayabasi (July 2003). "Predicting the deformation moduli of rock masses". In: *International Journal of Rock Mechanics and Mining Sciences* 40.5, pp. 701–710.

Goodfellow, Robert J F, Joe O'Carroll, and Spyridon Konstantis (2014). "Risk Registers and Their Use as a Contract Document". In: *North American Tunneling 2014 Proceedings*. Society for Mining, Metallurgy and Exploration Inc. (SME), pp. 670–680.

Gordian Group (2019). *Building Construction Costs with RSMeans Data*. Rockland, Massachusetts: Gordian Group.

Grimstad, E (1981). "Engineering-geology at the Holmestrand Tunnel". In: *Fjellsprengningsteknikk / Bergmekanikk / Geotecknikk*, pp. 30.1–30.8.

Grimstad, E and Nicholas Ryland Barton (1993). "Updating the Q-system for NMT". In: *Proceedings of the International Symposium on Sprayed Concrete*. Fagernes, Norway: Norwegian Concrete Association, p. 20.

Grimstad, Eystein (2007). "The Norwegian method of tunnelling - a challenge for support design." In: Madrid, Spain.

Grimstad, Eystein, Kalpana Kankes, Rajinder Bhasin, and Anette Wold Magnussen (2002). "Rock Mass Quality Q Used in Designing Reinforced Ribs of Sprayed Concrete and Energy Absorption". In: p. 19.

Gutierrez, Marte, Gunnar Vik, and Toralv Berre (Sept. 1996). "Shale Strength As Function of Stress History And Diagenesis". In: OnePetro.

Gutierrez, Marte S and C C Xia (2009). "Squeezing potential of tunnels in clays and clayshales from normalized undrained shear strength, unconfined compressive strength and seismic velocity". In: *Geotechnical Aspects of Underground Construction in Soft Ground: Proceedings of the 6th International Symposium (IS-Shanghai 2008)*. Shanghai, China: Taylor & Francis, pp. 537–543.

Haas, Christoph and Herbert H Einstein (2002). "Updating the Decision Aids for Tunneling". In: *Journal of Construction Engineering and Management* 128.1, pp. 40–48.

Hamidi, Jafar Khademi, Kourosh Shahriar, Bahram Rezai, and Jamal Rostami (July 2010). "Performance prediction of hard rock TBM using Rock Mass Rating (RMR) system". In: *Tunnelling and Underground Space Technology* 25.4, pp. 333–345.

Hasofer, Abraham M and Niels C Lind (Feb. 1974). "Exact and Invariant Second-Moment Code Format". In: *Proceedings of the American Society of Civil Engineers, Journal of the Engineering Mechanics Division* 100.EM1, pp. 111–121.

Hillier, M J et al. (2017). *Implicit 3-D modelling of geological surfaces with the generalized radial basis functions (GRBF) algorithm*. Open File 7814. Ottawa, Ontario, Canada: Geological Survey of Canada, pp. 1–15.

Hillier, Michael J, Ernst M Schetselaar, Eric A de Kemp, and Gervais Perron (2014). "Three-dimensional modelling of geological surfaces using generalized interpolation with radial basis functions". In: *Mathematical Geosciences* 46.8, pp. 931–953.

HM Treasury and Infrastructure UK (2010). *Infrastructure Cost Review*. London: HM Treasury.

Hoaglin, David C, Frederick Mosteller, and John Wilder Tukey, eds. (2000). *Understanding robust and exploratory data analysis*. Wiley clas. Wiley classics library. New York: Wiley.

Hoek, E and E T Brown (Aug. 2018). "The Hoek–Brown failure criterion and GSI – 2018 edition". In: *Journal of Rock Mechanics and Geotechnical Engineering*.

Hoek, Evert (1965). "Rock Fracture under Static Stress Conditions". PhD thesis. Cape Town, South Africa: University of Cape Town, p. 229.

— (1994). "Strength of rock and rock masses". In: *International Society for Rock Mechanics News Journal* 2.2, pp. 4–16.

— (2006). *Practical rock engineering*. North Vancouver, BC.

Hoek, Evert and E T Brown (1980). *Underground excavations in rock*. London, England: The Institution of Mining and Metallurgy.

— (1988). "The hoek brown failure criterion - a 1988 update". In: Toronto, Ontario: Canadian Rock Mechanics Association, pp. 31–38.

— (1997). "Practical Estimates of Rock Mass Strength". In: *International Journal of Rock Mechanics and Mining Sciences* 34.8, pp. 1165–1186.

Hoek, Evert, Carlos Carranza-Torres, and Brent Corkum (2002). "Hoek-brown failure criterion – 2002 edition". In: *Proceedings of the NARMS-TAC Conference*. Toronto, Ontario, pp. 267–273.

Hoek, Evert, Carlos Carranza-Torres, Mark S Diederichs, and Brent Corkum (2008). "Integration of geotechnical and structural design in tunneling". In: University of Minnesota 56th Annual Geotechnical Engineering Conference. Minneapolis, Minnesota.

Hoek, Evert, T G Carter, and M S Diederichs (2013). "Quantification of the geological strength index chart". In: Proceedings of the 47th US Rock Mechanics / Geomechanics Symposium. San Francisco, California: American Rock Mechanics Association.

Hoek, Evert and M S Diederichs (2005). "Empirical estimation of rock mass modulus". In: *International Journal of Rock Mechanics and Mining Sciences* 43.2, pp. 203–215.

Hoek, Evert, Peter K Kaiser, and W F Bawden (1995). *Support of underground excavations in hard rock*. 1st Editio. Rotterdam, Netherlands: A.A. Balkema Publishers.

Hoek, Evert and Paul G Marinos (Nov. 2000a). "Predicting tunnel squeezing problems in weak heterogeneous rock masses Part 1: Estimating Rock Mass Strength". In: *Tunnels and Tunnelling International*, p. 22.

Hoek, Evert and Paul G Marinos (Dec. 2000b). "Predicting tunnel squeezing problems in weak heterogeneous rock masses Part 2: Predicting Squeezing Problems in Deep Tunnels". In: *Tunnels and Tunnelling International*, p. 22.

Hoek, Evert, Paul G Marinos, and M Benissi (1998). "Applicability of the geological strength index (GSI) classification for very weak and sheared rock masses. The case of the Athens Schist Formation". In: *Bulletin of Engineering Geology and the Environment* 57, pp. 151–160.

Hogg, Robert V., Joseph W. McKean, and Allen T. Craig (2019). *Introduction to Mathematical Statistics*. 8th. Boston, Massachussetts: Pearson.

Hopper, R C, T A Lang, and A A Matthews (June 1972). "Construction of the Straight Creek Tunnel". In: *Proceedings of the North American Rapid Excavation and Tunneling Conference 1972*. Vol. 1. Proceedings of the North American Rapid Excavation and Tunneling Conference 1972. Chicago, Illinois: Society of Mining Engineers of the American Institute of Mining, Metallurgical, and Petroleum Engineers, pp. 501–538.

Hoskins, Earl, Jon White, Ted Nilssen, and Larry Messinger (Jan. 1974). *In-Situ Measurements of Stress and Modulus of Deformation in the Pioneer Bore of the Straight Creek Tunnel, Colorado*. Tech. rep. Rapid City, South Dakota: South Dakota School of Mines and Technology.

Huwaldt, Joseph A. (2015). *Plot Digitizer*.

Indraratna, B and P K Kaiser (1990). "Analytical model for the design of grouted rock bolts". In: *International Journal for Numerical and Analytical Methods in Geomechanics* 14.4, pp. 227–251.

Infrastructure and Projects Authority (Dec. 2018). *Case Study: Benchmarking tunnelling costs and production rates in the UK*. Tech. rep. HM Treasury, p. 14.

Innaurato, N, A Mancini, E Rondena, and A Zaninetti (Sept. 1991). "Forecasting And Effective TBM Performances In a Rapid Excavation of a Tunnel In Italy". In: International Society for Rock Mechanics and Rock Engineering (ISRM).

Innaurato, N, R Mancini, L Strangiotti, E Rondena, and A Sampaolo (Mar. 1988). "Several years of experience with TBM in the excavation of hydroelectric tunnels in Italy". In.

Isik, Nihat Sinan, Resat Ulusay, and Vedat Doyuran (Oct. 2008). "Deformation modulus of heavily jointed–sheared and blocky greywackes by pressuremeter tests: Numerical, experimental and empirical assessments". In: *Engineering Geology* 101.3-4, pp. 269–282.

ISRM (2007). *The complete ISRM suggested methods for characterization, testing and monitoring: 1974-2006*. Tech. rep. International Society for Rock Mechanics, p. 628.

Itasca (Jan. 2020). *FLAC*. Minneapolis, Minnesota.

ITIG (Jan. 2006). *A Code of Practice for Risk Management of Tunnel Works*. Tech. rep. International Tunnelling Insurance Group, p. 28.

Jackson, Henry M (Jan. 1970). *National Environmental Policy Act (NEPA)*.

Jaeger, J C (1960). "Shear failure of anisotropic rocks". In: *Geological Magazine* 97.1, pp. 65–72.

Jakubowski, Jacek (2011a). "Probabilistic Stability Analysis of a Tunnel in a Fracture Zone". In: *Archives of Mining Sciences* 56.3, pp. 405–413.

— (2011b). "The Stochastic Block Stability Simulation Method and Other Probabilistic Extensions of Block Theory". In: *Archives of Mining Sciences* 56.2, pp. 223–238.

Jasarevic, L and M S Kovacevic (1996). "Analyzing Applicability of Existing Classification For Hard Carbonate Rock In Mediterranean Aea". In: *ISRM-EUROCK-1996-101*. Turin, Italy: International Society for Rock Mechanics and Rock Engineering (ISRM), p. 8.

Jethwa, J L (1981). "Evaluation of rock pressures in tunnels through squeezing ground in lower himalayas". PhD thesis. Roorkee, India: University of Roorkee (IIT Roorkee).

Johnson, Lyndon B (Oct. 1966). *Department of Transportation Act*.

Jones, A, S Kramer, and P Arduino (Dec. 2002). *Estimation of uncertainty in geotechnical properties for performance-based earthquake engineering*. Tech. rep. Berkeley, California: Pacific Earthquake Engineering Research Center (PEER), p. 114.

Jumikis, Alfred R (Oct. 1964). *Mechanics of soils: Fundamentals for advanced study*. Princeton, New Jersey: Van Nostrand.

Kaiser, Peter K, C MacKay, and A D Gale (1986). "Evaluation of Rock Classifications at B.C. Rail Tumbler Ridge Tunnels". In: *Rock Mechanics and Rock Engineering* 19.4, pp. 205–234.

Kalamaras, George S and Z T Bieniawski (Sept. 1995). "A rock mass strength concept for coal seams incorporating the effect of time". In: Proceedings of the 8th ISRM International Congress on Rock Mechanics. Tokyo, Japan: International Society of Rock Mechanics, pp. 295–302.

Karam, Jad S (2005). "Decision aids for tunnel exploration". In: *Massachusetts Institute of Technology* Master of Science Thesis.

Kayabasi, A, C Gokceoglu, and M Ercanoglu (Jan. 2003). "Estimating the deformation modulus of rock masses: a comparative study". In: *International Journal of Rock Mechanics and Mining Sciences* 40.1, pp. 55–63.

Kellogg, K S, R R Shroba, B Bryant, and W R Premo (2008). *Geologic map of the Denver West 30' x 60' quadrangle, north-central Colorado*. geologic map. Washington, D.C.

Kirsch, Ernst Gustav (1898). "Die theorie der elastizität und die bedürfnisse der festigkeitslehre". In: *Zeitschrift des Vereines deutscher Ingenieure* 42, pp. 797–807.

Kotz, Samuel and Johan René Van Dorp (2004). *Beyond Beta: Other Continuous Families of Distributions with Bounded Support and Applications*. Hackensack, New Jersey: World Scientific.

Krajnovich, Ashton, Wendy Zhou, and Marte Gutierrez (2020). "Uncertainty assessment for 3D geologic modeling of fault zones based on geologic inputs and prior knowledge". In: *Solid Earth* 11.4, pp. 1457–1474.

Kulhawy, Fred H (Feb. 1978). "Geomechanical Model for Rock Foundation Settlement". In: *ASCE Journal of the Geotechnical Engineering Division* 104.GT2, pp. 211–227.

Ladd, Charles C. and Roger Foott (July 1974). "New design procedure for stability of soft clays". In: *ASCE Journal of the Geotechnical Engineering Division* 100.GT7, pp. 763–786.

Lambe, T William and Robert V Whitman (1969). *Soil Mechanics*. Series in soil engineering. Cambridge, Massachusetts: John Wiley and Sons.

Lauffer, H (1958). "Gebirgsklassifizierung fur den stollenbau". In: *Geologie und Bauwesen* 24.1, pp. 46–51.

Leapfrog (2014). *Unearthing 3D implicit modelling*.

Lee, Fitzhugh T and Thomas C Nichols (1966). "Rupture Phenomena in the Silver Plume Granite, Colorado". In: *Geological Survey Professional Paper* 550-C, pp. C29–C33.

Li, Charlie Chunlin (Jan. 2017). *Rockbolting*. Trondheim, Norway: Butterworth-Heinemann.

Logo, Benedek A and Balázs Vásárhelyi (2020). "Parametric Study on the Connection Between Poisson's Ratio, GSI and Environmental Stress". In.

Lovering, T S (1935). *Geology and Ore Deposits of the Montezuma Quadrangle, Colorado*. USGS Professional Paper 178. Washington, D.C.: United States Geological Survey, p. 119.

Low, B K and Wilson H Tang (Dec. 2007). "Efficient Spreadsheet Algorithm for First-Order Reliability Method". In: *Journal of Engineering Mechanics* 133.12, pp. 1378–1387.

— (June 2008). "New FORM algorithm with example applications". In: Hong Kong, pp. 221–226.

Lowson, A R and Z T Bieniawski (2013). "Critical Assessment of RMR-Based Tunnel Design Practices: A Practical Engineer's Approach". In: *Rapid Excavation and Tunneling Conference*. Society for Mining, Metallurgy, and Exploration, pp. 180–198.

Lowson, Alex (Mar. 2012). "The Support Capacity of Steel Ribs". In: *Tunnelling Journal*, pp. 18–20.

Lu, Hui (2020). "Uncertainty analysis in rock mass classification and its application to reliability evaluation in tunnel construction". PhD thesis. Golden, Colorado: Colorado School of Mines.

Lu, Hui, Eunhye Kim, and Marte Gutierrez (Dec. 2019). "Monte Carlo simulation (MCS)-based uncertainty analysis of rock mass quality Q in underground construction". In: *Tunnelling and Underground Space Technology* 94, p. 103089.

Lu, Hui, Eunhye Kim, and Marte S Gutierrez (June 2018). "A markovian rock mass quality q-based prediction model for tunneling". In: ARMA-2018-749. Seattle, Washington: American Rock Mechanics Association.

Marinos, Paul and Evert Hoek (July 2001). "Estimating the geotechnical properties of heterogeneous rock masses such as flysch". In: *Bulletin of Engineering Geology and the Environment* 60.2, pp. 85–92.

Marinos, Paul G and Evert Hoek (Nov. 2000). "GSI: A geologically friendly tool for rock mass strength estimation". In: *GeoEng2000*. Proccedings of the ISRM International Symposium. Melbourne, Australia: International Society for Rock Mechanics and Rock Engineering (ISRM), pp. 85–92.

Marinos, Vassilis P, Paul G Marinos, and Evert Hoek (2005). "The geological strength index: Applications and limitations". In: *Bulletin of Engineering Geology and the Environment* 64.1, pp. 55–65.

Marinos, Vassilis. and Trevor.G. Carter (2018). "Maintaining geological reality in application of GSI for design of engineering structures in rock". In: *Engineering Geology* 239, pp. 282–297.

MathWorks (2019). *MatLab*. Portola Valley, California.

Mattei, Fred A (1965). *Engineering and Construction Report of Straight Creek Pilot Tunnel*. Tech. rep. Denver, Colorado: Colorado Department of Highways.

McCormac, Jack C and R H Brown (2014). *Design of Reinforced Concrete*. Ninth Edit.

McOllough, P R (May 1981). "Eisenhower Memorial Tunnel - How Colorado Department of Highways Improved Contracting Practices and Management". In: *1981 Rapid Excavation and Tunneling Conference*. Vol. 2. San Francisco, California: American Institute of Mining, Metallurgical, and Petroleum Engineers, pp. 1651–1667.

Merten, Fred K (Apr. 1971). "Straight Creek Tunnel Construction, Route I-70, Colorado". In: *Proceedings of the 22nd Annual Highway Geology Symposium*. Ed. by Rosemary Kellner and William D Rose. Norman, Oklahoma: Oklahoma Geological Survey, pp. 71–76.

Microsoft (2008). *Excel*. Redmond, Washington.

Miles, George N and Fred A Mattei (1965). *Final Geologic Report of the Straight Creek Pioneer Tunnel*. Tech. rep. Denver, Colorado: Colorado Department of Highways.

Min, S Y, H H Einstein, J S Lee, and T K Kim (Sept. 2003). "Application of Decision Aids for Tunneling (DAT) to a drill & blast tunnel". In: *KSCE Journal of Civil Engineering* 7.5, pp. 619–628.

Min, S Y, H H Einstein, J S Lee, and H S Lee (July 2005). "Application of the Decision Aids for Tunneling (DAT) to update excavation cost/time information". In: *KSCE Journal of Civil Engineering* 9.4, pp. 335–346.

Min, S Y, T K Kim, J S Lee, and H H Einstein (Mar. 2008). "Design and construction of a road tunnel in Korea including application of the Decision Aids for Tunneling - A case study". In: *Tunnelling and Underground Space Technology* 23.2, pp. 91–102.

Min, Sangyoon (Aug. 2003). "The application of "Decision Aids for Tunneling (DAT)" to the Sucheon tunnel in Korea". Master of Science. Cambridge, Massachusetts: Massachusetts Institute of Technology.

— (Dec. 2007). "Development of the Resource Model for the Decision Aids for Tunneling (DAT)". Doctor of Philosophy. Cambridge, Massachusetts: Massachusetts Institute of Technology.

Min, Sangyoon and Herbert H Einstein (2016). "Resource scheduling and planning for tunneling with a new resource model of the Decision Aids for Tunneling (DAT)". In: *Tunnelling and Underground Space Technology* 51, pp. 212–225.

Min, Sanyoong (2014). "Risk Management Using the Decision Aids for Tunneling". In: *North American Tunneling 2014 Proceedings*. Ed. by Gregg Davidson, Alan Howard, Lonnie Jacobs, Robert Pintabona, and Brett Zernich. Englewood, Colorado: Society for Mining, Metallurgy and Exploration Inc. (SME), pp. 661–669.

Miro, S, M König, D Hartmann, and T Schanz (July 2015). "A probabilistic analysis of subsoil parameters uncertainty impacts on tunnel-induced ground movements with a back-analysis study". In: *Computers and Geotechnics* 68, pp. 38–53.

Mirzaeian, Yousef, Kourosh Shahriar, and Mostafa Sharifzadeh (2015). "Tunnel Probabilistic Structural Analysis Using the FORM". In: *Journal of Geological Research* 2015, pp. 1–9.

Mitri, H S, R Edrissi, and J Henning (1994). "Finite Element Modeling of Cablebolted Stopes in Hard Rock Ground Mines". In: Albuquerque, New Mexico: Society for Mining, Metallurgy, and Exploration, pp. 94–116.

Mohammadi, H and R Rahmannejad (2010). "The Estimation of Rock Mass Deformation Modulus Using Regression and Artificial Neural Networks Analysis". In: *Arabian Journal of Science and Engineering* 35, pp. 205–217.

Monk, Edward F and Richard A Farrow (1965). *Physical properties, dynamic and static test results, Straight Creek Tunnel pilot bore, Clear Creek and Summit Counties, Colorado.* USGS Open-File Report 65-111. United States Geological Survey (USGS), p. 1.

Monsees, James Eugene (1970). "Design of Support Systems for Tunnels in Rock". Doctor of Philosophy. Urbana, Illinois: University of Illinois at Urbana-Champaign.

Moré, J and D Sorensen (Sept. 1983). "Computing a Trust Region Step". In: *SIAM Journal on Scientific and Statistical Computing* 4.3, pp. 553–572.

Moreno Tallon, E (1980). "Aplicación de las Clasificaciones Geomecánicas a los Túneles de Pajares". In: *II Curso de Sostenimientos Activos en Galerías y Túneles*.

— (1982). "Comparison and application of geomechanics classification schemes in tunnel construction". In: *Proceedings of Tunneling '82*. Vol. 20. London, UK: Institution of Mining and Metallurgy.

Moret, Yvonne and Herbert H Einstein (2016). "Construction Cost and Duration Uncertainty Model: Application to High-Speed Rail Line Project". In: *Journal of Construction Engineering and Management* 142.10, p. 5016010.

Movinkel, Tore and Odd Johannessen (Apr. 1986). "Geological Parameters for Hard Rock Tunnel Boring". In: *Tunnels and Tunnelling International* 18.4, pp. 45–48.

Muskie, Edmund (Oct. 1972). *Clean Water Act (CWA)*.

Nelson, Priscilla P (1993). "TBM Performance Analysis with Reference to Rock Properties". In: *Comprehensive Rock Engineering Volume 4: Excavation, Support and Monitoring*. Ed. by John A Hudson. 1st Editio. Vol. 4. Oxford, England: Pergamon Press, pp. 261–291.

Nelson, Priscilla P, Y Abd Al-Jalil, and C Laughton (1994). *Tunnel boring machine project databases and construction simulation*. Geotechnical Engineering Center Report GR 94-4. Austin, Texas: University of Texas at Austin.

NGI (2015). *Using the Q-system*. Tech. rep. Oslo, Norway: Norwegian Geotechnical Institute.

Nguyen, Quang Phich, Van Manh Nguyen, and Ke Tuong Nguyen (Apr. 2018). "A new design concept of fully grouted rock bolts in underground construction". In: *IOP Conference Series: Earth and Environmental Science*. Vol. 143.

Nichols, Thomas C and Fitzhugh T Lee (1966). "Preliminary Appraisal of Applied Rock Mechanics Research on Silver Plume Granite, Colorado". In: *Geological Survey Professional Paper* 550-C, pp. C34–C38.

Nicholson, G A and Z T Bieniawski (1990). "A nonlinear deformation modulus based on rock mass classification". In: *International Journal of Mining and Geological Engineering* 8.3, pp. 181–202.

O'Neill, Michael W. and Lymon C. Reese (Aug. 1999). *Drilled shafts: Construction procedures and design methods*. Tech. rep. Washington, D.C.: Federal Highway Administration.

Öge, İbrahim Ferid (Dec. 2018). "Determination of deformation modulus in a weak rock mass by using menard pressuremeter". In: *International Journal of Rock Mechanics and Mining Sciences* 112, pp. 238–252.

Oggeri, Claudio and Pierpaolo Oreste (July 2012). "Tunnel Static Behavior Assessed by a Probabilistic Approach to the Back-Analysis". In: *American Journal of Applied Sciences* 9.7, pp. 1137–1144.

Oreste, Pierpaolo (2006). "Correlated Probabilistic Analysis of the Excavation Times and Costs in Tunneling". In: *Journal of Mining Science* 42.3, pp. 269–286.

— (2015). "Analysis of the Tunnel-Support Interaction Through a Probabilistic Approach". In: *American Journal of Applied Sciences* 15.2, pp. 121–129.

Osgoui, Reza R and Pierpaolo Oreste (2010). "Elasto-plastic analytical model for the design of grouted bolts in a Hoek–Brown medium". In: *International Journal for Numerical and Analytical Methods in Geomechanics* 34.16, pp. 1651–1686.

Ozdemir, Levent, R Miller, and F D Wang (1977). *Mechanical tunnel boring prediction and machine design. Annual report*. Tech. rep. Golden, Colorado: Excavation Engineering and Earth Mechanics Institute, Colorado School of Mines, p. 332.

Palmstrom, Arild (Feb. 1995a). "Characterizing the Strength of Rock Masses for Use in Design of Underground Structures". In: *Design and Construction of Underground Structures*. New Delhi, India, p. 10.

— (Aug. 1995b). "RMi - A Rock Mass Characterization System for Rock Engineering Purposes". doctoral dissertation. Oslo, Norway: University of Oslo.

— (July 1996). "RMi - a system for characterizing rock mass strength for use in rock engineering". In: *Journal of Rock Mechanics and Tunnelling Technology* 1.2, p. 40.

— (July 2005). "Measurements of and correlations between block size and rock quality designation (RQD)". In: *Tunnelling and Underground Space Technology* 20.4, pp. 362–377.

Palmstrom, Arild and Einar Broch (Nov. 2006). "Use and misuse of rock mass classification systems with particular reference to the Q-system". In: *Tunnelling and Underground Space Technology* 21.6, pp. 575–593.

Palmstrom, Arild and Rajbal Singh (2001). "The deformation modulus of rock masses - comparisons between in situ tests and indirect estimates". In: p. 17.

Pavlo, E Lionel (1960). *Interstate Highway Location Study Dotsero to Empire Junction*. Tech. rep. HPS-1-(20). New York, NY: Colorado Department of Highways, p. 243.

Pearson, Karl (Nov. 1893). "On the dissection of asymmetrical frequency curves". In: *Philosophical Transactions of the Royal Society of London*. A 185, pp. 71–110.

— (Jan. 1895). "Contributions to the Mathematical Theory of Evolution II: Skew variation in homogeneous material". In: *Philosophical Transactions of the Royal Society of London*. A 186, pp. 343–414.

Pells, P J N (2008). "What happened to the mechanics in rock mechanics and the geology in engineering geology?" In: *Journal of The Southern African Institute of Mining and Metallurgy* 108, pp. 309–323.

Pells, P. J., Z. T. Bieniawski, S. R. Hencher, and S. E. Pells (2017). "Rock quality designation (RQD): time to rest in peace". In: *Canadian Geotechnical Journal* 54.6, pp. 825–834.

Pells, Philip J N and R Bertuzzi (Apr. 2007). "Limitations of rock mass classification systems for tunnel support designs". In: *Tunnels and Tunnelling International*, p. 11.

Post, John D (Apr. 1973). *Rock Bolts and Rebar Anchors In the Straight Creek Tunnel*. Tech. rep. Denver, Colorado: Colorado Department of Transportation (CDOT), p. 26.

Post, John D and Al Eastwood (Apr. 1973). *Geological Report on the Straight Creek Tunnel*. Tech. rep. Denver, Colorado: Colorado Department of Transportation (CDOT), p. 36.

Priest, S D and J A Hudson (1976). "Discontinuity spacings in rock". In: *International Journal of Rock Mechanics and Mining Sciences & Geomechanics Abstracts* 13, pp. 135–148.

Proctor, Robert V, Thomas L White, and Karl Terzaghi (1946). *Rock Tunneling with Steel Supports*. Youngstown, Ohio: Commercial Shearing and Stamping Company.

Radhakrishnan, R and Chun F Leung (June 1989). "Load Transfer Behavior of Rock-Socketed Piles". In: *Journal of Geotechnical Engineering* 115.6, pp. 755–768.

Ramamurthy, T (Jan. 2004). "A geo-engineering classification for rocks and rock masses". In: *International Journal of Rock Mechanics and Mining Sciences* 41.1, pp. 89–101.

Ramamurthy, Temura (1993). "Strength and modulus responses of anisotropic rocks". In: *Comprehensive rock engineering: Principles, practice, and projects*. Ed. by Edwin T Brown. 1st ed. Vol. 1. Oxford ; Pergamon Press, pp. 313–329.

Ramezanzadeh, A, J Rostami, and D Tadic (2008). "Impact of Rock Mass Characteristics on Hard Rock Tunnel Boring Machine Performance". In: p. 8.

Raphael, Jerome M (1984). "Tensile Strength of Concrete". In: p. 8.

Read, S A L, N D Perrin, and L R Richards (Jan. 1999). "Applicability of the Hoek-Brown Failure Criterion to New Zealand Greywacke Rocks". In: *ISRM-9CONGRESS-1999-133*. Paris, France: International Society for Rock Mechanics and Rock Engineering, pp. 655–660.

Rehman, Hafeezur et al. (2018). "Review of rock-mass rating and tunneling quality index systems for tunnel design: Development, refinement, application and limitation". In: *Applied Sciences* 8.8, p. 1250.

Richards, David Barton (1963). "Engineering Geology of the Proposed Straight Creek Tunnel, Clear Creek and Summit Counties, Colorado". Master of Science. Golden, Colorado: Colorado School of Mines.

Robinson, Charles Sherwood et al. (1972). *Geological, Geophysical, and Engineering Investigations of the Loveland Basin Landslide, Clear Creek County, Colorado, 1963-1965*. USGS Professional Paper 673. Golden, Colorado: United States Geological Survey (USGS), p. 59.

Robinson, Charles Sherwood et al. (1974). *Engineering Geologic, Geophysical, Hydrologic, and Rock-Mechanics Investigations of the Straight Creek Tunnel Site and Pilot Bore, Colorado*. USGS Professional Paper 815. Washington, D.C.: United States Geological Survey (USGS), p. 165.

Rossum, Guido van (Apr. 1995). *Python Tutorial*. Tech. rep. CS-R9526 1995. Amsterdam, The Netherlands: Centrum voor Wiskunde en Informatica, p. 71.

Rossum, Guido van and Python Software Foundation (Dec. 2020). *Python*. Beaverton, Oregon.

Rostami, Jamal (Aug. 2016). "Performance prediction of hard rock Tunnel Boring Machines (TBMs) in difficult ground". In: *Tunnelling and Underground Space Technology* 57, pp. 173–182.

Rostami, Jamal and Levent Ozdemir (June 1993). "A New Model for Performance Prediciton of Hard Rock TBMs". In: *Proceedings of the Rapid Excavation and Tunneling Conference*. Boston, Massachusetts: Society for Mining, Metallurgy & Exploration (SME), p. 17.

Rostami, Jamal, Levent Ozdemir, and David M Neil (Nov. 1994). "Performance prediction: a key issue in mechanical hard rock mining". In: *Mining Engineering* November 1994, pp. 1263–1267.

Rostami, Jamal, Levent Ozdemir, and B Nilsen (1996). "Comparison Between CSM and NTH Hard Rock TBM Performance Prediction Models". In: *Proceedings of Annual Technical Meeting of the Insitute of Shaft Drilling Technology*. Las Vegas, Nevada.

Rostami, Jamal, Mahmoud Sepehrmanesh, Ehsan Alavi Gharahbagh, and Navid Mojtabai (Jan. 2013). "Planning level tunnel cost estimation based on statistical analysis of historical data". In: *Tunnelling and Underground Space Technology* 33, pp. 22–33.

Rousseeuw, Peter J and Christophe Croux (Dec. 1993). "Alternatives to the Median Absolute Deviation". In: *Journal of the American Statistical Association* 88.424, pp. 1273–1283.

Rowe, R K and H H Armitage (1984). *The Design of Piles Socketed Into Weak Rock*. Geotechnical research report. Faculty of Engineering Science, University of Western Ontario.

— (Feb. 1987). "A design method for drilled piers in soft rock". In: *Canadian Geotechnical Journal* 24.1, pp. 126–142.

Russo, G (2009). "A new rational method for calculating the GSI". In: *Tunnelling and Underground Space Technology* 24.1, pp. 103–111.

Rutledge, J C and R L Preston (1978). "New zealand experience with engineering classifications of rock for the prediction of tunnel support". In: Proceedings of the International Symposium on Tunneling. Tokyo, Japan: Japan Tunneling Society.

Santi, Paul M, Jason E Holschen, and Richard W Stephenson (Nov. 2000). "Improving elastic modulus measurements for rock based on geology". In: *Environmental and Engineering Geoscience* 6.4, pp. 333–346.

Sapigni, M, M Berti, E Bethaz, A Busillo, and G Cardone (Sept. 2002). "TBM performance estimation using rock mass classifications". In: *International Journal of Rock Mechanics and Mining Sciences* 39.6, pp. 771–788.

Seequent (2020). *Leapfrog Geo*. Christchurch, New Zealand.

Serafim, J Laginha and Jose Geraldo Pereira (1983). "Considerations of the Geomechanics Classification of Bieniawski". In: *Proceedings of the Symposium on Engineering Geology and Underground Openings*. Lisbon, Portugal, pp. 1133–1144.

Shaw, C A, K E Karlstrom, M L Williams, M J Jercinovic, and A M McCoy (2001). "Electron-microprobe monazite dating of ca. 1.71–1.63 Ga and ca. 1.45–1.38 Ga deformation in the Homestake shear zone, Colorado: Origin and early evolution of a persistent intracontinental tectonic zone". In: *Geology* 29.8, pp. 739–742.

Shen, Hong Qing (2012). "Non-deterministic analysis of slope stability based on numerical simulation". doctoral thesis. Freiberg, Germany: Technische Universität Bergakademie Freiberg.

Shen, Jiayi, Murat Karakus, and Chaoshui Xu (Nov. 2012). "A comparative study for empirical equations in estimating deformation modulus of rock masses". In: *Tunnelling and Underground Space Technology* 32, pp. 245–250.

Singh, Bhawani and R K Goel (2011). *Engineering rock mass classification: tunneling, foundations, and landslides*. Waltham, MA: Butterworth-Heinemann.

Singh, Bhawani, J L Jethwa, A K Dube, and B Singh (1992). "Correlation between Observed Support Pressure and Rock Mass Quality". In: 7.1, p. 16.

Smith, Kristina (Mar. 2012). "The GBR - Bible or Bane?" In: *Tunnelling Journal*, pp. 10–17.

Sonmez, H, C Gokceoglu, H A Nefeslioglu, and A Kayabasi (Feb. 2006). "Estimation of rock modulus: For intact rocks with an artificial neural network and for rock masses with a new empirical equation". In: *International Journal of Rock Mechanics and Mining Sciences* 43.2, pp. 224–235.

Sonmez, H, C Gokceoglu, and R Ulusay (July 2004). "Indirect determination of the modulus of deformation of rock masses based on the GSI system". In: *International Journal of Rock Mechanics and Mining Sciences* 41.5, pp. 849–857.

Sousa, Rita L and Herbert H Einstein (2012). "Risk analysis during tunnel construction using Bayesian Networks: Porto Metro case study". In: *Tunnelling and Underground Space Technology* 27.1, pp. 86–100.

Špačková, Olga and Daniel Straub (2013). "Dynamic bayesian network for probabilistic modeling of tunnel excavation processes". In: *Computer-Aided Civil and Infrastructure Engineering* 28.1, pp. 1–21.

Springer, Melvin Dale (1979). *The Algebra of Random Variables*. New York, New York: John Wiley & Sons, Inc.

Stillborg, E Bengt (1994). *Professional users handbook for rock bolting*. Series on rock and soil mechanics. Trans Tech Publications.

Sunday, Dan (2012). *Geometry Algorithms*.

Suorineni, Fidelis Tawiah (June 2014a). "Empirical methods in mining geomechanics – Reflections on current state-of-the-art". In: Lima, Peru.

— (Nov. 2014b). "Reflections on Empirical Methods in Geomechanics - The Unmentionables and Hidden Risks". In: *3rd Australasian Ground Control in Mining Conference*. Sydney, Australia, p. 15.

Tarkoy, P J (1979). "Predicting Raise and Tunnel Boring Machine Performance: State of the Art". In: *Proceedings of the 4th Rapid Excavation and Tunneling Conference*. Atlanta, Georgia, pp. 333–352.

Tarkoy, P J and A J Hendron (1975). *Rock Hardness Index Properties and Geotechnical Parameters for Predicting Tunnel Boring Machine Performance*. NSF Research Report PB-246-293. Urbana, Illinois: University of Illinois, Urbana-Champaign.

Technical Committee on Contracting Practices of the Underground Technology Research Council (1991). *Avoiding and Resolving Disputes During Construction*. New York, New York: American Society of Civil Engineers (ASCE).

Terzaghi, Karl (1946). "Rock Defects and Loads on Tunnel Supports". In: *Rock Tunneling with Steel Supports*. Youngstown, Ohio: Commercial Shearing and Stamping Company, pp. 17–99.

— (1950). "Tunnelman's Ground Classification". In: *Applied Sedimentation*. Ed. by Parker D Trask. Washington, D.C.: John Wiley & Sons, pp. 193–209.

Tien, Yong Ming and Ming Chuan Kuo (Apr. 2001). "A failure criterion for transversely isotropic rocks". In: *International Journal of Rock Mechanics and Mining Sciences* 38.3, pp. 399–412.

Tien, Yong Ming, Ming Chuan Kuo, and Charng Hsein Juang (Dec. 2006). "An experimental investigation of the failure mechanism of simulated transversely isotropic rocks". In: *International Journal of Rock Mechanics and Mining Sciences* 43.8, pp. 1163–1181.

Timoshenko, Stephen P and J N Goodier (1951). *Theory of Elasticity*. 2nd Editio. McGraw-Hill Book Company, Inc.

Trapani, Ralph, Jon Kaneshiro, David Jurich, Michael Salamon, and Steve Quick (June 2010). "Structural Inspections of Colorado's Eisenhower Johnson Memorial Tunnel, Hanging Lake Tunnel, and Reverse Curve Tunnel". In: *North American Tunneling 2010 Proceedings*. Portland, Oregon: Society for Mining, Metallurgy, and Exploration, pp. 224–232.

Tukey, John Wilder (1977). *Exploratory data analysis*. Addison-Wesley series in behavioral science. Reading, Massachusetts: Addison-Wesley Pub. Company.

Ueblacker, Horst (1971). *Straight Creek Tunnel Project I-70-3(34), Zone 2: Analysis of Horse-Shoe Shaped Tunnel Section with Straight Side Walls and Invert Arch*. Tech. rep. Rock Mechanics International, Inc.

Unal, Erdal (1983). "Development of Design Guidelines and Roof-Control Standards for Coal-Mine Roofs". Doctor of Philosophy. Ann Arbor: The Pennsylvania State University.

USGS (2016a). *USGS one meter x41y440 CO Central Western 2016*. Digital Elevation Model. Washington, D.C.

— (2016b). *USGS one meter x42y440 CO Central Western 2016*. Digital Elevation Model. Washington, D.C.

Vásárhelyi, B (July 2009). "A possible method for estimating the Poisson's rate values of the rock masses". In: *Acta Geodaetica et Geophysica Hungarica* 44.3, pp. 313–322.

Vásárhelyi, Balázs and Dorottya Kovács (2017). "Empirical methods of calculating the mechanical parameters of the rock mass". In: *Periodica Polytechnica Civil Engineering* 61.1, pp. 39–50.

Verman, M, B Singh, M N Viladkar, and J L Jethwa (1997). "Effect of tunnel depth on modulus of deformation of rock mass". In: *Rock Mechanics and Rock Engineering* 30.3, pp. 121–127.

Wellmann, Florian and Guillaume Caumon (2018). "3-D Structural geological models: Concepts, methods, and uncertainties". In: *Advances in geophysics*. 1st ed. Vol. 59. Elsevier Inc., pp. 1–121.

Whitmeyer, S J and K E Karlstrom (2007). "Tectonic model for the Proterozoic growth of North America". In: *Geosphere* 3, pp. 220–259.

Wickham, George E and Henry R Tiedemann (1972). *Ground support prediction model*. Tech. rep.

— (1974). *Ground support prediction model (RSR concept)*. Tech. rep. San Francisco, CA.

WSDOT (Feb. 2018). *Project Risk Management Guide*. Tech. rep. Spokane, Washington: Washington State Department of Transportation, p. 132.

Wu, Xuezhen, Yujing Jiang, Zhenchang Guan, and Bin Gong (Jan. 2019). "Influence of confining pressure-dependent Young's modulus on the convergence of underground excavation". In: *Tunnelling and Underground Space Technology* 83, pp. 135–144.

Yagiz, S, J Rostami, and L Ozdemir (May 2012). "Colorado School of Mines Approaches For Predicting TBM Performance". In: OnePetro.

Yang, Jianhua et al. (Feb. 2020). "Estimation of rock mass properties in excavation damage zones of rock slopes based on the Hoek-Brown criterion and acoustic testing". In: *International Journal of Rock Mechanics and Mining Sciences* 126, p. 104192.

Yang, Ke (May 2006). "Analysis of Laterally Loaded Drilled Shafts in Rock". Doctor of Philosophy. Akron, Ohio: The University of Akron.

Zare, S and A Bruland (May 2007). "Progress of drill and blast tunnelling efficiency with relation to excavation time and costs". In: *Underground Space – The 4th Dimension of Metropolises*. Taylor & Francis.

— (Jan. 2013). "Applications of NTNU/SINTEF Drillability Indices in Hard Rock Tunneling". In: *Rock Mechanics and Rock Engineering* 46.1, pp. 179–187.

Zare, Shokrollah and Amund Bruland (Nov. 2006). "Estimation Model for Advance Rate in Drill and Blast Tunnelling". In: Sharm El-Sheikh, Egypt, p. 7.

Zhang, Lianyang (July 2010). "Estimating the Strength of Jointed Rock Masses". In: *Rock Mechanics and Rock Engineering* 43.4, pp. 391–402.

— (Jan. 2017). *Engineering Properties of Rocks*. 2nd Editio. Butterworth-Heinemann.

Zhang, Lianyang and H H Einstein (Feb. 2004). "Using RQD to estimate the deformation modulus of rock masses". In: *International Journal of Rock Mechanics and Mining Sciences* 41.2, pp. 337–341.

Zhang, Wengang and Anthony T C Goh (Nov. 2012). "Reliability assessment on ultimate and serviceability limit states and determination of critical factor of safety for underground rock caverns". In: *Tunnelling and Underground Space Technology* 32, pp. 221–230.

Zhao, Yan-Gang and Tetsuro Ono (Jan. 1999a). "New Approximations for SORM: Part 1". In: *ASCE Journal of Engineering Mechanics* 125.1, pp. 79–85.

— (Jan. 1999b). "New Approximations for SORM: Part 2". In: *ASCE Journal of Engineering Mechanics* 125.1, pp. 79–85.

Zhao, Yan-gang and Tetsuro Ono (1999c). "General procedure for first/second-order reliability method (FORM/SORM)". In: *Structural Safety* 21, pp. 95–112.

APPENDIX A

SUPPLEMENTAL ELECTRONIC FILES

Table A.1: Supplemental Electronic Files

Filename	**Description**
EJMT_Data.zip	A data archive containing the input data used in the analyses presented in this thesis. Several of these data files are called directly by the subroutines contained in EJMT_Subroutines.zip. The files within EJMT_Data.zip should be placed within the "00 Data Files" folder after EJMT_Subroutines has been unpacked. This archive includes Microsoft Excel files and comma separated values files with tabulated data as well as Leapfrog block model files containing the summarized data from the Leapfrog geologic model used in this project.
EJMT_Subroutines.zip	A data archive containing the MatLab files which performed the bulk of these analyses, and which generated the FLAC input files for the numerical modeling.

APPENDIX B

HOW TO APPLY THE ALIGNMENT OPTIMIZATION METHODOLOGY

The application of the alignment optimization methodology developed in this thesis is quite straightforward.

1. Collect available data on the study area where a new tunnel is desired. Data should be digitized and a database system should be used to maintain these data. Spatial position metadata correlating to each data point are critical. Data should include:
   (a) Lithology, including observed locations of lithologic contacts;
   (b) Bedding and foliation orientations in each lithologic unit where such fabric is present;
   (c) Joint frequency, orientation, aperture, alteration, and weathering in each lithologic unit or in sub-units, if jointing varies within the unit;
   (d) Local groundwater conditions, e.g. the location of the groundwater table, piezometer data, sources of recharge, discharge quantities, direction of flow, etc;
   (e) Laboratory testing data on material parameters. Cast a wide net. Even seemingly irrelevant data may be useful later in the project, so digitize, spatially locate, and add to the database anything that you come across;
   (f) In-situ test data. This may include construction records, ongoing observations of previous infrastructure in the area, pilot bore data, test pits, and drill hole data.
   (g) If there are data from previous projects such as tunnels, mines, or quarries which are outside of the study area but potentially relevant, consider incorporating this data.
2. From the available data, develop probability density functions which describe the distribution of each type of data which is not spatially specific, i.e. a parameter that is dependent entirely on lithology rather than position within that lithology. This work was performed in MatLab for this study, but any calculation software capable of outputting tables of data to the three-dimensional (3D) implicit geologic modeling software could be used. Most commercial software packages are capable of importing data in comma-separated values (*.csv) format. For this research study, the non-spatially

distributed parameters were:

(a) Intact unconfined compressive strength or uniaxial compressive strength (UCS);
(b) Intact Young's modulus;
(c) Intact Poisson's ratio; and
(d) Drilling rate index (DRI).

3. For data which are spatially specific, define the uncertainty associated with each data point. For example, if joint spacing was measured on exposed surfaces at the surface or in test excavations, the measured value would be defined as the most likely value of the distribution, but a triangular distribution around that value might be defined around that value based on the possibility of field measurement error and the likely local variability of that value. Some uncertainties are easily quantified while others must be defined based on the best judgment of the team members preparing the study. As currently implemented, the alignment optimization algorithm requires all of the components of the rock mass quality index (Q) and rock mass rating (RMR) systems as well as the joint frequency data and anticipated groundwater flows:
   (a) The components of the RMR system (see Equation 2.2):
      i. UCS component
      ii. Joint frequency component (joints per meter)
      iii. Joint condition component
      iv. Groundwater component
      v. Alterability component
      vi. Stress component
   (b) The components of the Q system (see Equation 2.10):
      i. rock quality designation (RQD)
      ii. joint set number (J_n)
      iii. joint roughness (J_r)
      iv. joint alteration (J_a)
      v. joint water reduction factor (J_w)
      vi. stress reduction factor (SRF)
   (c) Joint frequency (joints per meter)
   (d) Anticipated groundwater flow (liters per minute)
4. When all data distributions have been been quantified, enter the distribution parameters into a 3D implicit geologic modeling software. For the purposes of this study, distributions were entered into the implicit geologic modeling software as lower bound, most likely, and upper bound estimates of each parameter. Use separate models for each distribution parameter. Other parameterizations are possible. For example, if the

data being modeled have a normal probability density function, the mean and standard deviation could be the parameters modeled. However, the alignment optimization algorithm as currently coded requires inputs of most likely, lower bound, and upper bound for each parameter. If a different distribution parameterization is desired, some recoding will be required.

5. Define the trends and radial basis functions for each parameter. For example, intact UCS is most closely linked to lithology and should thus follow lithologic trends in the geologic model. As a background estimate where no other trend is apparent, an isotropic (spherical) radial basis function may be assigned to a parameter. The trends used for each parameter in this study are shown in Table 3.10. Engineering judgement should be used in selecting the appropriate trend for each parameter.
6. The 3D implicit geologic model will calculate the likely value of each parameter at each point of the model. After each component of the RMR and Q systems has been estimated throughout the model, combine the components to estimate the RMR and Q scores throughout the model.
7. Output the results from the model on an appropriate regular spacing. For this study, parameters were evaluated on a 10 m 3D grid, also called a block model. The block model must not be too fine for practical calculation speed reasons and because the block model should not reflect a precision which is not justified by the precision of the underlying data. The block model must not be too coarse, or it loses relevance to future analyses.
8. Reimport the block model to the calculation software. The block model will consist of several 3D matrices of data. Each point within the 3D matrix represents a spatial coordinate. The data at that point represents a distribution parameter of interest, such as the most likely estimate of UCS.
9. Define the locations of the possible portals on the surface of the block model. The constraints for these portal locations are often governed by constructability, serviceability, and environmental constraints. An appropriately wide discretization density should be defined for the first iteration of the algorithm. For this study, a 100 m by 100 m grid was used, an even coarser grid may be warranted for larger study areas.
10. Run the alignment optimization algorithm using the defined portal locations and the block model (most likely, lower bound, and upper bound of each parameter). Ensure that all of the required input data files are in the same directory as the alignment optimization algorithm and the files are named as they are called in the algorithm. Note that the algorithm is currently coded in MatLab; a current license of this software is required. The input data files required by the alignment optimization algorithm are:

(a)

11. The overall highest scoring alignment output will be identified by the alignment optimization algorithm. Additionally, the alignments by several sub-metrics may be considered. Additional refinement of the portal grid density in areas of focused interest is likely warranted. However, avoid refining the portal grid density to a point not justified by the precision of the underlying data. For example, in this study, a 10 m block model was output from the implicit geologic model, therefore a portal grid finer than 10 m would provide no additional information.

For this study, MatLab was used for the probabilistic data reduction part of the analysis, the implementation of the alignment optimization algorithm, and the beam-spring modeling. However, any calculation software capable of handling large three- and four-dimensional data files could be used. For example, the MatLab files presented in Appendix A could be readily recoded into Python or C by someone with expertise in those codes.

The 3D implicit geologic modeling software used in this study was Leapfrog Geo. Other software packages may be available which can perform the same functions, or a custom piece of software could be implemented in another code platform (e.g., MatLab, Python, or C) to perform much the same functions.

APPENDIX C

ROCK MASS DEFORMATION MODULUS CORRELATIONS

Table C.1: Rock mass deformation modulus correlations

Reference	Equation	Notes
Bieniawski 1978	$E_{rm} = 2RMR - 100$	E_{rm} in GPa. Based on greywacke, phyllite, shale, mudstone, siltstone, sandstone, slate, quartzite, gneiss, and dolerite.
Coon and Merritt 1970 & Gardner 1987	$\alpha = 0.0231\text{RQD} - 1.32 >= 0.15$ $E_{rm} = \alpha E_i$	E_{rm} in same units as E_i. Based on granite, gneiss, limestone, sandstone, and Atlantic Piedmont. Coon and Merritt (1970) proposed the original equation based on data with RQD $\geq 57\%$. Gardner (1987) proposed the lower bound at $\frac{E_{rm}}{E_i} = 0.15$. This relationship was adopted by AASHTO in 1989.
Serafim and Pereira 1983	$E_{rm} = 10^{\frac{\text{RMR}-10}{40}}$	E_{rm} in GPa. Based on Bieniawski's data and several Portuguese dam projects. May be inaccurate at low values of $RMR < 25$, see Hoek and Brown (1997) and Zhang (2017).

Continued on next page

Table C.1 – continued from previous page

Reference	Rock Mass Deformation Modulus	Notes
Rowe and Armitage 1984	$E_{rm} = 215\sqrt{\sigma_c}$	E_{rm} in MPa, σ_c in MPa. Based on pile load tests in weak sedimentary rocks in Canada. See also Rowe and Armitage (1987) and Radhakrishnan and Leung (1989) who found good agreement between this correlation and tests on cast-in-drilled-shaft piles.
Nicholson and Bieniawski 1990	$E_{rm} = E_i(0.0028RMR^2 + 0.9e^{\frac{\text{RMR}}{22.82}})$	E_{rm} in same units as E_i. Based on simulated rock masses, empirically calibrated against data from shale, phyllite, sandstone, and mudstone. Nicholson & Bieniawski also offer a stress dependent formulation.
Grimstad and Barton 1993	$E_{rm} = 25\log_{10} Q$	E_{rm} in GPa. Based on a large database of projects, primarily European and especially Scandinavian. For $Q > 1$; suggested confidence interval is $E_{rm} = 10\log_{10} Q$ to $E_{rm} = 40\log_{10} Q$

Continued on next page

Table C.1 – continued from previous page

Reference	Rock Mass Deformation Modulus	Notes
Aydan et al. 1993 & Aydan et al. 1997	$E_{rm} = 9.7 \cdot 10^{-3} \cdot RMR^{3.54}$ $E_{rm} = 80\sigma_c^{1.4}$	E_{rm} in MPa, σ_c in MPa. Based on re-analysis of data from Bieniawski (1978) and Serafim and Pereira (1983), along with new data from Japanese projects.
Mitri et al. 1994	$E_{rm} = E_i \frac{1}{2}(1 - \cos(\pi \frac{RMR}{100}))$	E_{rm} in same units as E_i. Based on data from the Kidd Creek mine in Canada, a massive base-metal sulfide ore deposit
Jasarevic and Kovacevic 1996	$E_{rm} = e^{4.407+0.081\mathrm{RMR}}$ $E_{rm} = e^{7.971+0.729 \ln \mathrm{Q}}$	Based on fissured carbonate rocks on the Mediterranean coast (Adriatic limestone).
Aydan et al. 1997	$E_{rm} = 0.0097\mathrm{RMR}^{3.54}$	E_{rm} in MPa. Based on experimental data from sites in Japan.
Verman et al. 1997	$E_{rm} = 0.4H^{\alpha}10^{\frac{RMR-20}{38}}$ $H =$ depth below ground surface $\alpha = 0.16$ to 0.30 (higher for poorer rocks)	E_{rm} in GPa. Based on five water tunnels excavated in India by the drill-and-blast method
Hoek and Brown 1997	$E_{rm} = \sqrt{\frac{\sigma_c}{100}} \cdot 10^{\frac{GSI-10}{40}}$	E_{rm} in GPa. For $\sigma_c < 100$. No specific calibration database identified.

Continued on next page

Table C.1 – continued from previous page

Reference	Rock Mass Deformation Modulus	Notes
Read et al. 1999	$E_{rm} = 0.1(\frac{RMR}{10})^3$	E_{rm} in GPa. Based on New Zealand greywacke.
Diederichs 1999 & Diederichs and Kaiser 1999	$E_{rm} = 7\sqrt{Q'}$ $Q' = \frac{RQD}{J_n}\frac{J_r}{J_a}$ Suggested range $E_{rm} = (4\ to\ 10)\sqrt{Q'}$	E_{rm} in GPa. Diederichs states that this is not an engineering recommendation but rather a reasonable baseline assumption.
O'Neill and Reese 1999	RQD: 100 / 70 / 50 / 20 E_{rm}/E_i closed joints: 1.00 / 0.70 / 0.15 / 0.05 E_{rm}/E_i open joints: 0.60 / 0.10 / 0.10 / 0.05	Based on Carter and Kulhawy (1988) Kulhawy (1978), O'Neill & Reese proposed a relationship between RQD and $\frac{E_{rm}}{E_i}$ as a piecewise linear function with dependency on the closure of the rock mass joints. This correlation has been incorporated into more recent AASHTO specifications over the correlation proposed by Coon and Merritt (1970) and Gardner (1987) including in AASHTO (2017).
Aydan and Kawamoto 2000	$E_{rm} = E_i - \frac{E_i \cdot \mathrm{RMR}}{\mathrm{RMR}+6.0(100-\mathrm{RMR})}$	E_{rm} in same units as E_i. Based on experimental data from sites in Japan.

Continued on next page

Table C.1 – continued from previous page

Reference	Rock Mass Deformation Modulus	Notes
Palmstrom and Singh 2001	$E_{rm} = 8 * Q^{0.4}$	E_{rm} in GPa. Suggested range of applicability $1 < Q < 30$ and $sigma_{ci} > 150\ MPa$
Barton 2002	$Erm = 10 * \left(\frac{Q * sig_{ci}}{100}\right)^{\frac{1}{3}}$	E_{rm} in GPa and sig_{ci} in MPa
Hoek et al. 2002	$E_{rm} = \left(1 - \frac{D}{2}\right) \sqrt{\frac{\sigma_{ci}}{100}} \cdot 10^{\frac{GSI-10}{40}}$	E_{rm} in GPa, σ_{ci} in MPa. Slight modification of Hoek and Brown (1997) to include the damage parameter, D.
Kayabasi et al. 2003	$E_{rm} = 0.135 \cdot \left[\frac{E_i}{WD} \cdot \left(1 + \frac{RQD}{100}\right)\right]^{1.1811}$ $E_{rm} = 4.32 - 3.42WD + \left[0.19E_i \left(1 + \frac{RQD}{100}\right)\right]$	E_{rm} in GPa. One version based on simple linear regression, the second based on multiple linear regression. WD is a value between 1 and 4 indicating weathering degree. Note that the equations presented in the text of this paper do not match the equations presented on the figures in the paper. The equations shown here are from the figures and are also cited by Gokceoglu et al. (2003).
Gokceoglu et al. 2003	$E_{rm} = 0.001 \cdot \left[\frac{E_i}{UCS \cdot WD} \left(1 + \frac{RQD}{100}\right)\right]^{1.5528}$	E_{rm} in GPa. Contains a good summary of previous correlations plus two new equations.

Continued on next page

Table C.1 – continued from previous page

Reference	Rock Mass Deformation Modulus	Notes
Ramamurthy 2004	$E_{rm} = E_i \cdot e^{\frac{RMR-100}{17.4}}$ $E_{rm} = E_i \cdot e^{0.8625 \log_{10} Q - 2.875}$	E_{rm} in same units as E_i.
Sonmez et al. 2004	$E_{rm} = E_i \cdot (s^a)^{0.4}$	E_{rm} in same units as E_i
Carvalho 2004	$E_{rm} = E_i \cdot s^{0.25}$	E_{rm} in same units as E_i. Not actually published, but referenced by Hoek and Diederichs (2005) as personal communication.
Zhang and Einstein 2004	$E_{rm} = E_i \cdot 10^{0.0186\text{RQD}-1.91}$ upper bound $= 1.8 \cdot E_i \cdot 10^{0.0186\text{RQD}-1.91}$ lower bound $= 0.2 \cdot E_i \cdot 10^{0.0186\text{RQD}-1.91}$	E_{rm} in same units as E_i. Based on data from mudstone, siltstone, sandstone, shale, dolerite, granite, limestone, greywacke, gneiss.
Hoek and Diederichs 2005	$E_{rm} = E_i \left[0.02 \cdot \frac{1-\frac{D}{2}}{1+e^{\frac{60+15D-GSI}{11}}} \right]$	E_{rm} in same units as E_i.
Galera et al. 2005	$E_{rm} = 0.0876 \; for \; \text{RMR} \leq 50$ $E_{rm} = 0.0876\text{RMR} + 1.056(\text{RMR} - 50) + 0.015(\text{RMR} - 50)^2 \; for \; \text{RMR} > 50$ $E_{rm} = E_i e^{\frac{RMR-100}{36}}$	E_{rm} in GPa.

Continued on next page

Table C.1 – continued from previous page

Reference	Rock Mass Deformation Modulus	Notes
Yang 2006	$E_{rm} = \frac{E_i}{100} e^{\frac{GSI}{21.7}}$	E_{rm} in same units as E_i.
Sonmez et al. 2006	$E_{rm} = E_i 10^{\frac{(\mathrm{RMR}-100)(100-\mathrm{RMR})}{4000}} e^{-\frac{\mathrm{RMR}}{100}}$	E_{rm} in same units as E_i. Based on a broad range of rock types including diabase, granite, basalt, limestone, dolomite, sandstone, shale, quartzite, gneiss, marble, schist, greywacke, and agglomerate
Chun et al. 2006	$E_{rm} = 0.3228 e^{0.0485\mathrm{RMRb}}$	E_{rm} in GPa. Based on granite, gneiss, andesite, tuff, sandstone, and shale. Note that this correlation uses RMRb, indicating that the RMR value has not been modified for joint orientation.
Isik et al. 2008	$E_{rm} = 6.7\mathrm{RMR} - 103$ $E_{rm} = 5.57\mathrm{GSI}$ $\mathrm{RMR} \geq 27$	E_{rm} in MPa. Based on greywacke.
Mohammadi and Rahmannejad 2010	$E_{rm} = 0.0003\mathrm{RMR}^3 - 0.0193\mathrm{RMR}^2 + 0.3157\mathrm{RMR} + 3.4064$	E_{rm} in GPa. Based on limestone and marble.

Continued on next page

Table C.1 – continued from previous page

Reference	Rock Mass Deformation Modulus	Notes
Beiki et al. 2010	$E_{rm} = \sqrt[3]{\sigma_c} \cdot \tan\left(\sqrt{1.56 + \ln \mathrm{GSI}^2}\right)$	E_{rm} in GPa. Based on shale, sandstone-quartzite, limestone, marl-limestone (with silica veins), sandstone, siltstone, and mudstone.
Ghamgosar et al. 2010	$E_{rm} = 0.0912e^{0.0866\mathrm{GSI}}$	E_{rm} in GPa. Based on limestone, schist, and shale.
Shen et al. 2012	$E_{rm} = 110e^{-(\frac{\mathrm{RMR}-110}{37})^2}$ $E_{rm} = 1.14E_i e^{-(\frac{\mathrm{RMR}-116}{41})^2}$	E_{rm} in GPa. Based on mudstone, siltstone, sandstone, shale, dolerite, granite, gneiss.
Alemdag et al. 2015	$E_{rm} = 0.058e^{0.0785\mathrm{RMR}}$	E_{rm} in GPa. Based on basalt, tuffite, diabase, and siltstone.
Alemdag et al. 2016	$E_{rm} = 6.7 \cdot 10^{-4}\left[RQD^2 + RQD \cdot \sigma_c + \frac{RQD \cdot \sigma_c + \sigma_c^2}{RQD + 99.5}\right]$	E_{rm} in GPa. Based on siltstone. Alemdag et al. developed 6 different correlations using a genetic algorithm approach (regression using machine learning). The best fit was given by the presented equation incorporating RQD and UCS.

Continued on next page

Table C.1 – continued from previous page

Reference	Rock Mass Deformation Modulus	Notes
Öge 2018	$E_{rm} = (\text{RQD} + 10)^{0.648124} \cdot \sigma_{ci}^{1.06661} + \text{RMR}(\text{JCond})^{2.23513}$ $E_{rm} = 100 \left(\frac{\text{RQD}+1+\text{RMR}(\text{JCond}) \cdot 11.7478}{20} \right)^{1.1056} \left(\frac{\sigma_{ci}}{100} \right)^{0.251}$ $E_{rm} = \left(\frac{H}{10} \right)^{0.4797} (RQD + 1)^{0.6496} \sigma_{ci}^{1.038} \text{RMR}(\text{JCond})^{2.229}$ $E_{rm} =$ $1.25 \, (RQD + 5)^{0.75} \, (0.075\sigma_{ci})^{2.25} + (2\text{RMR89}(\text{JCond}))^{1.5}$	E_{rm} in MPa, σ_{ci} in MPa, depth H in meters. Oge developed four correlations for rock mass modulus by comparing results from in-situ pressuremeter testing with rock mass classifications in heavilty jointed andesitic rock (41 test points in 7 boreholes). Equation C is highly inaccurate for deep points. Equation D is proposed by Oge as a lower bound. Calibration bounds of these equations are generally shallow (20 to 100 m).

Continued on next page

Table C.1 – continued from previous page

Reference	Rock Mass Deformation Modulus	Notes
Wu et al. 2019	$E_{rm} = E_{max} - (E_{max} - E_0)\, e^{-\alpha\sigma_3}$	E_{rm} in GPa. This generates a curve of Young's moduli as a function of minor principal stress (confining stress), σ_3. E_{max} is the maximum Young's modulus at the critical confining pressure, e.g. the in-situ stress state. E_0 is the unconfined Young's modulus at the excavation surface. The curvature parameter α was suggested to range from 0.001 to 1, with fits to test data on amphibolite, gneiss, sandstone, and limestone showing values ranging 0.041 to 0.062.

Continued on next page

Table C.1 – continued from previous page

Reference	Rock Mass Deformation Modulus	Notes
Yang et al. 2020	$E_{rm} = E_i \left(1 - \frac{D_0}{2} + \frac{D_0}{2} \frac{d}{d_{EDZ}}\right)$	E_{rm} in GPa. D is the disturbance factor from 0 (undisturbed) to 1 (completely disturbed). D_0 is the disturbance factor at the excavated or blasted surface. d is the depth of interest, limited to the depth of the excavation damage zone. d_{edz} is the depth of the excavation damage zone, as measured by in-situ geophysical testing. For cases where E_0 is unknown, Yang et al. suggest using their calculated term times the rock mass modulus of Hoek et al. (2002).